

NO-A176 287

EVALUATION AND VALIDATION OF THE PRINCETON UNIVERSITY  
EFFECTIVE STRESS MODEL(U) NAVAL CIVIL ENGINEERING LAB  
PORT HUENEME CA J H PREVOST ET AL DEC 86

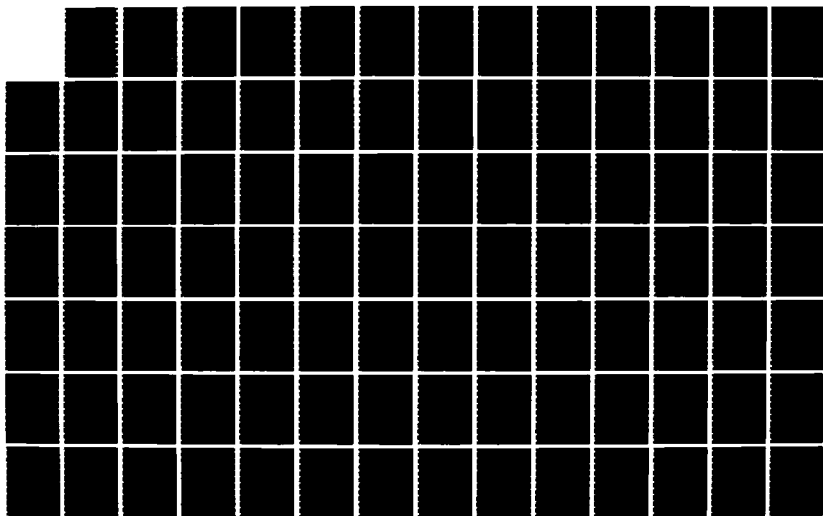
1/2

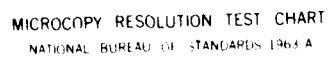
UNCLASSIFIED

NCEL-TR-R-919

F/G 8/13

NL





12

R-919

December 1986

# NCEL

Technical Report

By Professor J.H. Prevost, Princeton University and  
John M. Ferritto and Robert J. Slyh, NCEL

Sponsored By Naval Facilities Engineering Command

AD-A176 207

## EVALUATION AND VALIDATION OF THE PRINCETON UNIVERSITY EFFECTIVE STRESS MODEL

**ABSTRACT** An efficient finite element procedure to analyze transient phenomena in dry and/or fluid-saturated porous media is presented. The saturated porous medium is modeled as a two-phase system consisting of a solid and a fluid phase. Time integration of the resulting semidiscrete finite element equations is performed by an implicit-explicit algorithm. In order to remove the time step size restriction associated with the presence of the stiff fluid in the mixture, the fluid contribution to the equations of motion is always treated implicitly. The procedure allows an optimal selection of the time step size independently of the fluid. Depending upon the particular intended applications (e.g., seismic, blast loading), the fluid may be assumed incompressible or compressible.

Accuracy and versatility of the proposed procedure are demonstrated by applying it to analyze a number of dynamic soil and/or soil-structure interaction tests and quasi-static consolidation tests performed in centrifuges.

DTIC  
ELECTE  
JAN 29 1987  
S E D

DTIC FILE COPY

NAVAL CIVIL ENGINEERING LABORATORY PORT HUENEME, CALIFORNIA 93043

Approved for public release; distribution is unlimited

87 1 20 001

# METRIC CONVERSION FACTORS

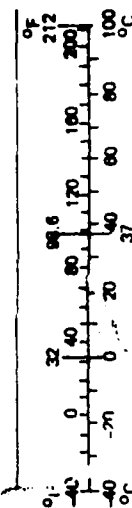
## Approximate Conversions to Metric Measures

Symbol	When You Know	Multiply by	To Find	Symbol
in ft yd mi	inches feet yards miles	2.5 30 0.9 1.6	centimeters	cm
			centimeters	cm
			meters	m
			kilometers	km
in <sup>2</sup> ft <sup>2</sup> yd <sup>2</sup> mi <sup>2</sup>	square inches square feet square yards square miles acres	6.5 0.09 0.8 2.6 0.4	square centimeters	cm <sup>2</sup>
			square meters	m <sup>2</sup>
			square kilometers	km <sup>2</sup>
			hectares	ha
oz lb	ounces pounds short tons (2,000 lb)	28 0.45 0.9	grams	g
			kilograms	kg
			tonnes	t
tsp Tbsp fl oz c pt qt gal ft <sup>3</sup> yd <sup>3</sup>	teaspoons tablespoons fluid ounces cups pints quarts gallons cubic feet cubic yards	5 15 30 0.24 0.47 0.95 3.8 0.03 0.76	milliliters	ml
			milliliters	ml
			milliliters	ml
			liters	l
			liters	l
			liters	l
			cubic meters	m <sup>3</sup>
			cubic meters	m <sup>3</sup>
°F	Fahrenheit temperature	5/9 (after subtracting 32)	Celsius temperature	°C
			Celsius temperature	°C

\*1 in = 2.54 (exactly). For other exact conversions and more detailed tables, see NBS Misc Publ 286, Units of Weights and Measures, Price \$2.25, SD Catalog No. C13 10 286.

## Approximate Conversions from Metric Measures

Symbol	When You Know	Multiply by	To Find	Symbol
mm cm m km	millimeters centimeters meters kilometers	0.04 0.4 3.3 0.6	inches	in
			inches	in
			feet	ft
			yards	yd
m <sup>2</sup> km <sup>2</sup> ha	square centimeters square meters square kilometers hectares (10,000 m <sup>2</sup> )	0.16 1.2 0.4 2.5	square inches	in <sup>2</sup>
			square yards	yd <sup>2</sup>
			square miles	mi <sup>2</sup>
			acres	
g kg t	grams kilograms tonnes (1,000 kg)	0.035 2.2 1.1	ounces	oz
			pounds	lb
			short tons	
ml l l l m <sup>3</sup> m <sup>3</sup>	milliliters liters liters liters cubic meters cubic meters	0.03 2.1 1.06 0.26 35 1.3	fluid ounces	fl oz
			pints	pt
			quarts	qt
			gallons	gal
			cubic feet	ft <sup>3</sup>
			cubic yards	yd <sup>3</sup>
°C	Celsius temperature	9/5 (then add 32)	Fahrenheit temperature	°F
			Fahrenheit temperature	°F



Unclassified

AD-A176207

SECURITY CLASSIFICATION OF THIS PAGE (When Data Entered)

REPORT DOCUMENTATION PAGE		READ INSTRUCTIONS BEFORE COMPLETING FORM
1 REPORT NUMBER TR-919	2 GOVT ACCESSION NO. DN387338	3 RECIPIENT'S CATALOG NUMBER
4 TITLE (and Subtitle) EVALUATION AND VALIDATION OF THE PRINCETON UNIVERSITY EFFECTIVE STRESS SOIL MODEL		5 TYPE OF REPORT & PERIOD COVERED Final; Oct 1984 - Sep 1986
		6 PERFORMING ORG. REPORT NUMBER
7 AUTHOR(s) Professor J.H. Prevost    John M. Ferritto & Robert Slyh Princeton University    Naval Civil Engineering Lab. Princeton, New Jersey    Port Hueneme, California		8 CONTRACT OR GRANT NUMBER(s)
9 PERFORMING ORGANIZATION NAME AND ADDRESS NAVAL CIVIL ENGINEERING LABORATORY Port Hueneme, California 93043-5003		10 PROGRAM ELEMENT, PROJECT, TASK AREA & WORK UNIT NUMBERS 62760N; YY60.534.091.01.310
11 CONTROLLING OFFICE NAME AND ADDRESS Naval Facilities Engineering Command Alexandria, Virginia 22332		12 REPORT DATE December 1986
		13 NUMBER OF PAGES 174
14 MONITORING AGENCY NAME & ADDRESS (if different from Controlling Office)		15 SECURITY CLASS (of this report) Unclassified
		15a DECLASSIFICATION/DOWNGRADING SCHEDULE
16 DISTRIBUTION STATEMENT (of this Report)  Approved for public release; distribution unlimited.		
17 DISTRIBUTION STATEMENT (of the abstract entered in Block 20, if different from Report)		
18 SUPPLEMENTARY NOTES		
19 KEY WORDS (Continue on reverse side if necessary and identify by block number)  Effective stress, soil model testing, finite elements		
20 ABSTRACT (Continue on reverse side if necessary and identify by block number)  An efficient finite element procedure to analyze dynamic transient phenomena in dry and/or fluid-saturated porous media is presented. The saturated porous medium is modeled as a two-phase system consisting of a solid and a fluid phase. Time integration of the resulting semidiscrete finite element equations is performed by an implicit-explicit algorithm. In order to remove the time step size restriction associated with the presence of the stiff fluid in the continued		

DD FORM 1473

EDITION OF 1 NOV 65 IS OBSOLETE

Unclassified

SECURITY CLASSIFICATION OF THIS PAGE (When Data Entered)

Unclassified

SECURITY CLASSIFICATION OF THIS PAGE (When Data Entered)

20. Continued

mixture, the fluid contribution to the equations of motion is always treated implicitly. The procedure allows an optimal selection of the time step size independently of the fluid. Depending upon the particular intended applications (e.g., seismic, blast loading), the fluid may be assumed incompressible or compressible.

Accuracy and versatility of the proposed procedure are demonstrated by applying it to analyze a number of dynamic soil and/or soil-structure interaction tests and quasi-static consolidation tests performed in centrifuges.

7



Library Card

Naval Civil Engineering Laboratory  
EVALUATION AND VALIDATION OF THE PRINCETON UNIVERSITY  
EFFECTIVE STRESS SOIL MODEL (Final), by Prevost, Ferritto & Slyh  
TR-919 174 pp illus December 1986 Unclassified

1. Effective stress 2. Soil model testing I. YY60.534.091.01.310

An efficient finite element procedure to analyze dynamic transient phenomena in dry and/or fluid-saturated porous media is presented. The saturated porous medium is modeled as a two-phase system consisting of a solid and a fluid phase. Time integration of the resulting semidiscrete finite element equations is performed by an implicit-explicit algorithm. In order to remove the time step size restriction associated with the presence of the stiff fluid in the mixture, the fluid contribution to the equations of motion is always treated implicitly. The procedure allows an optimal selection of the time step size independently of the fluid. Depending upon the particular intended applications (e.g., seismic, blast loading), the fluid may be assumed incompressible or compressible.

Accuracy and versatility of the proposed procedure are demonstrated by applying it to analyze a number of dynamic soil and/or soil-structure interaction tests and quasi-static consolidation tests performed in centrifuges.

Unclassified

SECURITY CLASSIFICATION OF THIS PAGE (When Data Entered)

# CONTENTS

	Page
INTRODUCTION AND PROBLEM . . . . .	1
TECHNICAL BACKGROUND . . . . .	4
THE PRINCETON UNIVERSITY EFFECTIVE STRESS FINITE ELEMENT PROCEDURE . . . . .	6
Governing Equations . . . . .	6
Balance of Mass . . . . .	6
Balance of Linear Momentum . . . . .	7
Equations of State . . . . .	8
Constitutive Assumptions . . . . .	9
Field Equations . . . . .	11
Weak Form - Semi-Discrete Finite Element Equations . . . . .	11
Time Integration . . . . .	14
Implementation . . . . .	16
Program DYNAFLOW . . . . .	22
Post-Dynamic Event Simulation . . . . .	24
THE PRINCETON UNIVERSITY EFFECTIVE STRESS SOIL MODEL . . . . .	24
Theory . . . . .	24
LABORATORY TRIAXIAL TEST SIMULATION - COHESIONLESS SOILS . . . . .	28
Test Program . . . . .	28
Monterey "0" Sand . . . . .	29
Leighton-Buzzard Sand . . . . .	35
Silica Sand . . . . .	35
Miesers Bluff Sand . . . . .	48
SENSITIVITY OF PARAMETERS . . . . .	48
Critical Stress Ratio . . . . .	48
Elastic Moduli . . . . .	49
Plastic Moduli . . . . .	49
Yield Surface Size . . . . .	50
Yield Surface Position . . . . .	66
LABORATORY TESTS - COHESIVE SOILS . . . . .	66
Kaolinite I . . . . .	66
Kaolinite II . . . . .	67
LABORATORY CENTRIFUGE TESTS . . . . .	74
Analysis of Model Tests . . . . .	74
Monterey Soil Column Test . . . . .	75
Leighton-Buzzard Soil Column Test . . . . .	81

	Page
Brass Footing Test . . . . .	87
Retaining Wall Test . . . . .	94
Storage Tank Test . . . . .	102
DYNAFLOW ADINA COMPARISON . . . . .	105
PILE AND PIER FOUNDATIONS . . . . .	113
Load Capacity . . . . .	113
Cyclic Behavior of Piles . . . . .	123
Friction Between Calcareous Sand and Building Materials . . . . .	125
Piles in Calcareous Sands . . . . .	130
CONCLUSIONS/RECOMMENDATIONS . . . . .	154
REFERENCES . . . . .	155



## INTRODUCTION AND PROBLEM

The Navy has \$25 billion worth of facilities in seismically active regions. Each year \$200 million of new facilities are added to those in seismically active areas. The Navy, because of its mission, must locate at the waterfront with a high watertable and often on marginal land. Seismically induced liquefaction is a major threat to the Navy. Presently, procedures do not exist to analyze the effect of liquefaction on structures. Developing an effective stress soil model will provide a tool for such analysis of waterfront structures.

To understand the significance of liquefaction, it is important to note the damage caused in recent earthquakes. The following summarizes recent experiences during major earthquakes.

### 1960 Chilean Earthquake (Magnitude 6-8.3)

Most spectacular damage occurred in Puerto Montt, to quay walls, steel sheet piles, and sea walls. Liquefaction of the loose fine sandy soils was the primary cause of the failures.

### 1964 Alaska Earthquake (Magnitude 8.4)

Severe damage at Anchorage, Cordova, Homer, Kodiak, Seldovia, Seward, Valdez, Klawock, and Whittier. Large-scale land slides and liquefaction induced most of the extremely heavy damage and total destruction.

1964 Niigata Earthquake (Magnitude 7.5)

Severe damage in Niigata Port (West Harbor). Areas affected were Additional Harbor, Yamanoshita Wharf, North Wharf, East Wharf, Central Wharf, South Wharf, Kurinoki River Landings, Bandai Island Wharf, Shinano River Left Bank Bulkhead, and West Coast Bulkheads. Liquefaction caused most of the heavy damage.

1968 Tokachi-Oki Earthquake (Magnitude 7.8)

Ports affected were Hachinohe, Aomori, Hakodate, and Muroran. Damage was relatively light compared to that caused by Niigata Earthquake. Most of the damage occurred to structures of smaller scale. Liquefaction was not the primary cause of damage even though spouting sand sediments were seen at several waterfront areas near the damaged structures.

1973 Nemuro-Hanto-Oki Earthquake (Magnitude 7.4)

Severe damage occurred mainly in Hanasaki and Kiritappu Ports. Nemuro Port situated only 6 km away from Hanasaki Port sustained very slight damage. The damage was attributed to soil liquefaction.

1978 Mivagi-Ken-Oki Earthquake (Magnitude 7.4)

Areas affected were Shiogama, Sendai, and Ishinomaki Ports, and Ishinomaki and Yuriage Fishing Ports. The damage in Ishinomaki Port accounted for approximately 90 percent of the total damage costs at port and harbor facilities caused by this earthquake. Gravity quay walls and piers suffered various degrees of damage. Sheet pile quay walls damaged were primarily due to liquefaction of fill materials. Liquefaction again played a significant role in this earthquake. At sites where liquefaction did occur, the

damage to the port and harbor structures was very severe. Conversely, the damage to port and harbor structures was small at sites where no liquefaction occurred.

As can be seen, liquefaction played a major role in waterfront damage, most of the time being the single cause of widespread losses. Fortunately the United States has not suffered a devastating earthquake in recent years. However, the seismic risk is great, particularly in the West where it is estimated that there is a 5 percent annual probability of a major event in Southern California that could affect a number of Naval bases. This problem has been noted in an ONR sponsored study evaluating the Navy's seismic vulnerability. The experience noted in recent earthquakes is that liquefaction greatly increased the amount of damage observed in waterfront facilities. Particular problems exist with sheet piles, quay walls, wharfs, and embedded structures. Conventional buildings also suffer severe damage.

The Navy's experience has been limited to damage inflicted in the 1964 Alaskan earthquake., heavy damage was noted in the seawall at the Kodiak Naval Station. One foot of differential settlement was noted beneath aircraft hangars. Compaction of fill occurred under asphalt aircraft ramps. It is significant to note that these facilities were constructed on 15 to 20 feet of engineered fill where seismically induced pore pressure increases would be expected to reduce soil stiffness and shear strength. The damage noted was caused by soil failure, and in addition, substantial damage was caused by the seismic sea wave. The United States has not had a large number of events exposing Navy facilities to damage. However, the Japanese have had a number of events and their experience illustrates that seismic liquefaction was responsible for most waterfront damage.

The conclusions from this are:

- (1) Seismic liquefaction causes severe damage to waterfront structures.

(2) The Navy, located in seismically active areas having numerous waterfront structures on marginal land, is vulnerable to substantial damage.

(3) Techniques presently do not exist to accurately analyze the response of a large complex waterfront structure on soil in which seismically induced pore pressures cause loss of soil stiffness and shear strength (liquefaction).

The most promising solution to this problem is developing a constitutive soil relationship that is capable of accurately predicting soil behavior under generalized loading conditions. Implementing this effective stress soil model into a finite element computer program would allow analysis of soil and structure together.

#### TECHNICAL BACKGROUND

The analysis of dynamic transient phenomena in fluid-saturated porous media is of great interest in geophysics and geotechnical engineering. Fluid saturation of an otherwise inviscid porous solid skeleton introduces a time dependence into the response to applied loads. Biot (Ref 1) first considered the propagation of harmonic waves in a fluid-saturated porous medium. Since then, his theory and results have been the standard reference and basis for most of the investigations in acoustics, geophysics, and geomechanics. Many one-dimensional wave propagation theories have since been proposed (see Ref 2 and 3) for recent surveys of western and Russian literature), and one-dimensional wave propagation numerical results were first presented in References 4 and 5. The need for a general multidimensional formulation and solution technique has become important in recent years because of the increased concern with the dynamic behavior of saturated soil deposits and associated liquefaction of saturated sand deposits (see Ref 6 and 7) under seismic loading conditions. Also concern in marine foundation engineering with water wave induced dynamic pore pressures in saturated marine deposits has spurred interest in the subject matter (see Ref 8 and 9

for related analytical solutions). Most of the solution procedures reported in the literature are restricted to linear systems. Ghaboussi and Wilson (Ref 10) first proposed a multidimensional finite element numerical scheme to solve the linear coupled governing equations. Despite the extensive literature published in soil dynamics (see Reference 11 for extensive references) no general technique capable of accounting for all present nonlinear effects (large deformations, strains; nonlinear material behavior) has yet been fully developed and implemented, although attempts at presenting a suitable general framework have been reported (see Ref 12, 13, 14, 15, 16, and 17).

Professor J.H. Prevost of Princeton University (Ref 13) has developed an efficient finite element numerical procedure to analyze transient phenomena in fluid saturated porous media. The saturated porous medium is modeled as a two-phase system consisting of a solid and a fluid phase. The solid skeleton may be linear, or nonlinear and hysteretic. Large deformations may also be included. The fluid may be compressible or incompressible depending upon the intended applications (e.g., seismic, blast loading). Time integration of the resulting semi-discrete finite element equations is performed by using an implicit-explicit algorithm (Ref 18 and 19). In order to remove the time step size restriction associated with the presence of the stiff fluid in the mixture, the fluid contribution is always treated implicitly.

This study is directed toward examining the predictive capabilities of the numerical procedure proposed in Reference 20. Of particular interest is the validity of the proposed numerical model in capturing adequately the generation and dissipation of excess pore-water pressures in saturated sand deposits during (and after) earthquakes, and its performance in dynamic soil-structure interaction problems. The most appropriate method for such a validation study would be to utilize field data from instrumented prototype situations. However such a study is preempted by the paucity and scarcity of the field data. In the absence of actual prototype earthquake field data, an alternate method of validation is provided by analyzing centrifuge soil model test data. Although imperfect in many respects, it is felt that dynamic centrifuge soil model tests can still provide a data base for calibration of numerical procedures. A number of dynamic centrifuge soil model tests

have been reported. The last two test results in this study have been reported in Reference 25. The test results have been developed to illustrate the effects of the pore pressure on the behavior of the soil.

The test results are presented in the form of a plot of the pore pressure ratio,  $u/\sigma_v$ , versus the vertical stress ratio,  $\sigma_v/\sigma_v^0$ , for the two test results. The test results are shown in Figure 1.

The test results are presented in the form of a plot of the pore pressure ratio,  $u/\sigma_v$ , versus the vertical stress ratio,  $\sigma_v/\sigma_v^0$ , for the two test results. The test results are shown in Figure 1.

The test results are presented in the form of a plot of the pore pressure ratio,  $u/\sigma_v$ , versus the vertical stress ratio,  $\sigma_v/\sigma_v^0$ , for the two test results. The test results are shown in Figure 1.

where  $N = N_0 + N_1 \sigma_v$  and  $N_0$  and  $N_1$  are constants to be determined.

## Governing Equations

The saturated porous medium is viewed as a representative two-phase system consisting of a solid and a fluid phase, each of which is regarded as a continuum, and each following its own motion. Biot (Ref. 24) early in the 1950's extending the work of Terzaghi (Ref. 25) on soil consolidation, first formulated linear governing equations for the interaction of two such phases. The required formalism for the development of general nonlinear equations was later introduced through the theory of mixtures (Ref. 26, 27, and 28). General mixture results can be shown through formal linearization of the field and constitutive equations, to reduce to Biot linear poroelastic model (see Ref. 29). The balance laws for the two-phase mixture are summarized in this report.

## Balance of Mass

$$\frac{Dn^\alpha}{Dt} + n^\alpha \nabla \cdot \mathbf{v}^\alpha = - \frac{n^\alpha}{\rho_\alpha} \frac{D}{Dt} (\rho_\alpha) \quad (\alpha = s, w) \quad (1)$$

### Balance of Linear Momentum

$$\nabla \cdot \underline{\sigma}^\alpha + \hat{\underline{p}}^\alpha + \rho^\alpha \underline{b} = \rho^\alpha \underline{a}^\alpha \quad (\alpha = s, w) \quad (2)$$

where:  $\frac{D}{Dt} = \frac{d}{dt} + \underline{v} \cdot \nabla$  = material derivative following the motion of the  $\alpha$ -phase

$\rho^\alpha = n^\alpha \rho_\alpha$  = macroscopic average mass density

$\rho_\alpha$  = microscopic mass density

$n^\alpha$  = fraction of elemental volume,  $dV$ , occupied by  $\alpha$ -phase (i.e.,  $n^\alpha = dV^\alpha/dV$ ).

Clearly,  $\sum n^\alpha = n^s + n^w = 1$ ,

where:  $s$  and  $w$  = solid and fluid phases, respectively

$n^w$  = porosity

$\underline{v}^\alpha$  = velocity (spatial) of  $\alpha$ -phase

$\underline{a}^\alpha$  = acceleration of  $\alpha$ -phase

$\underline{b}$  = body force per unit mass

$\hat{\underline{p}}^\alpha$  = momentum supply to the  $\alpha$ -phase from the other phase, subject to  $\sum_\alpha \hat{\underline{p}}^\alpha = \hat{\underline{p}}^s + \hat{\underline{p}}^w = 0$ .

In the following, momentum interaction consists of diffusive and dilatational contributions, viz.,

$$\hat{\underline{p}}^s = - \hat{\underline{p}}^w = - \xi \cdot (\underline{v}^s - \underline{v}^w) - p_w \nabla n^w \quad (3)$$

where:  $\xi$  = symmetric, positive definite second-order tensor

$p_w$  = fluid pressure

The first term is sometimes called the "Stokes drag" (see Ref 26).

In Equation 2,  $\underline{\sigma}^\alpha$  = partial (Cauchy) stress tensor corresponding to the  $\alpha$ -phase. The partial stress tensor  $\underline{\sigma}^w$  corresponding to the fluid phase is equal to  $n^w$  times the pore fluid stress  $\underline{\sigma}_w$ , i.e.,

$$\sigma^w = n^w \underline{\sigma}_w \quad (4)$$

However, the partial stress tensor  $\underline{\sigma}^s$  corresponding to the solid phase is not the effective stress  $\underline{\sigma}'^s$  of classical soil mechanics (Ref 25), but rather is

$$\underline{\sigma}^s = \underline{\sigma}'^s + n^s \underline{\sigma}_w \quad (5)$$

where  $n^s \underline{\sigma}_w$  accounts for the effects of the pore fluid stress on the individual solid grains which constitute the solid skeleton. The global stress,  $\underline{\sigma}$ , is the sum of the partial stresses, and is equal to (from Equations 4 and 5)

$$\underline{\sigma} = \underline{\sigma}^s + \underline{\sigma}^w + \underline{\sigma}'^s + \underline{\sigma}_w \quad (6)$$

as postulated in classical soil mechanics (Ref 25).

#### Equations of State

For all practical applications of interest in soil dynamics, the soil grains may always be assumed to be incompressible, and in the following  $\rho_s$  constant. Equation 1 for the solid phase then simplifies to

$$\frac{Dn^w}{Dt} = (1 - n^w) \underline{\nabla} \cdot \underline{v}^s \quad (7)$$

and Equations 1 and 7 may be combined to yield the so called "storage equation," viz.,

$$\underline{\nabla} \cdot [n^w \underline{v}^w] + \underline{\nabla} \cdot [(1 - n^w) \underline{v}^s] = - \frac{n^w}{\rho_w} \frac{D}{Dt} (\rho_w) \quad (8)$$



### Constitutive Assumptions

A rate-type constitutive equation describes the behavior of the porous solid skeleton, of the following form:

$$\frac{D}{Dt} (\underline{\sigma}'^s) = \underline{D}^s : \underline{v}^s_{( )} + \underline{D}^G : \underline{v}^s_{[ ]} - (\underline{\sigma}'^s \times \underline{\delta}'^s) : \underline{\dot{v}}_{( )} \quad (9a)$$

where:  $\underline{v}^s_{( )}$  = symmetric parts of the solid velocity gradient

$\underline{v}^s_{[ ]}$  = skew-symmetric parts of the solid velocity gradient

$\underline{D}^s$  = material constitutive tensor, an objective tensor valued function of possible  $\underline{\sigma}'^s$  and the solid deformation gradient

$\underline{D}^G$  = contribution from the rotational component of the stress rate.

Namely,

$$D^G_{ijkl} = \frac{1}{2} [\sigma'^s_{il} \delta_{jk} + \sigma'^s_{jl} \delta_{ik} - \sigma'^s_{ik} \delta_{jl} - \sigma'^s_{jk} \delta_{il}] \quad (9b)$$

The last term on the right-hand side in Equation 9a is introduced to ensure that the tangent stiffness operator obtained through linearization of the momentum equations possesses the major symmetry as the  $\underline{D}^s$  tensor. Many nonlinear material models of interest can be put in the above form (e.g., all nonlinear elastic and many elastic-plastic material models). The particular form of the constitutive equation (Equation 13) adopted here was first proposed by Hill (Ref 30) within the context of plasticity theory. Appropriate expressions for the effective modulus tensor,  $\underline{D}^s$ , for soil media are given in References 31 and 32. For a linear isotropic elastic porous skeleton:

$$D^s_{ijkl} = \lambda^s \delta_{ij} \delta_{kl} + \nu^s (\delta_{ik} \delta_{jl} + \delta_{il} \delta_{jk}) \quad (10)$$

where:  $\lambda^s, \nu^s$  = effective Lamé's moduli

$\delta_{ij}$  = Kronecker delta

The following constitutive equation is assumed to describe the behavior of the fluid phase

$$\underline{\sigma}_w = - p_w \underline{\delta} \quad (11)$$

where:  $p_w$  = pore-fluid pressure

We assumed that the fluid has no average shear viscosity. Further, the fluid flow is assumed barotropic so that the fluid kinetic equation of state is independent of the temperature, viz.,

$$F(p_w, \rho_w) = 0 \quad (12)$$

from which it follows that

$$\frac{1}{p_w} \frac{D}{Dt} (\rho_w) = \frac{1}{\lambda^w} \frac{D}{Dt} (p_w) \quad (13)$$

where:  $\lambda^w = \rho_w \partial p_w / \partial \rho_w$  = bulk modulus of the fluid phase.

The fluid pressure can thus be determined from Equation 8, which now writes:

$$\frac{D}{Dt} (p_w) = \frac{\lambda^w}{\nu^w} \{ \underline{\nabla} \cdot (n^w \underline{\nu}^w) + \underline{\nabla} \cdot [(1 - n^w) \underline{\nu}^s] \} \quad (14)$$

For soil media, the compressibility of the fluid phase is often no smaller than the compressibility of the solid skeleton. Therefore, the fluid phase may, in some soil dynamics applications, be regarded as incompressible, and Equation 8 reduces to:

$$\underline{\nabla} \cdot [n^w \underline{\nu}^w] + \underline{\nabla} \cdot [(1 - n^w) \underline{\nu}^s] = 0 \quad (15)$$

## Field Equations

Under the assumptions described above, the linear momentum equations (Equation 2) simplify to.

$$\rho^s \underline{\underline{a}}^s = \underline{\underline{\nabla}} \cdot \underline{\underline{\sigma}}^s - n^s \underline{\underline{\nabla}} p_w - \underline{\underline{\xi}} \cdot (\underline{\underline{v}}^s - \underline{\underline{v}}^w) + \rho^s \underline{\underline{b}} \quad (16a)$$

$$\begin{aligned} \rho^w \frac{D}{Dt} (\underline{\underline{v}}^w) &= \rho^w (\underline{\underline{v}}^w - \underline{\underline{v}}^w) \cdot \underline{\underline{\nabla}} \underline{\underline{v}}^w - n \underline{\underline{\nabla}} p_w \\ &+ \underline{\underline{\xi}} \cdot (\underline{\underline{v}}^s - \underline{\underline{v}}^w) + \rho^w \underline{\underline{b}} \end{aligned} \quad (16b)$$

when the movement of the solid phase is used as the reference motion. When inertia and convective terms are neglected, Equation 16b reduces to Darcy's law as:

$$n^w (\underline{\underline{v}}^w - \underline{\underline{v}}^s) = - (n^w)^2 \underline{\underline{\xi}}^{-1} \cdot (\underline{\underline{\nabla}} p - \rho \underline{\underline{b}}) \quad (17)$$

and thus  $\underline{\underline{k}} = (n^w)^2 \gamma_w \underline{\underline{\xi}}^{-1}$  = Darcy permeability tensor (symmetric, positive definite), (units. L/T),  $\gamma_w = g \rho_w$  = unit weight of the fluid;  $g$  = acceleration of gravity.

## Weak Form - Semi-Discrete Finite Element Equations

The initial boundary value problem consists of finding the solid displacement,  $\underline{\underline{v}}^s$ , the fluid velocity,  $\underline{\underline{v}}^w$ , and the fluid pressure,  $p_w$ , (all functions of position and time) satisfying the field equations (Equation 16a and 16b) together with the constitutive relations and continuity conditions subject to appropriate initial and boundary conditions. In order to reduce the number of unknowns, the fluid pressure is eliminated from the formulation, thereby producing a most efficient scheme. In the case of a compressible fluid, the fluid pressure is determined from the computed velocities through time integration of Equation 14. In the case of an incompressible fluid, a

penalty-function formulation of the continuity constraint expressed by the storage equation (Equation 15) is used to compute the fluid pressure as:

$$p_w = -\frac{\lambda^w}{n^w} \{ \underline{\nabla} \cdot [n^w \underline{v}^w] + \underline{\nabla} \cdot [(1 - n^w) \underline{v}^s] \} \quad (18)$$

where  $\lambda^w > 0$  is a penalty parameter, not the effective bulk modulus appearing in Equation 14. The penalty parameter is selected as a large number. This parameter is further discussed later.

The weak formulation associated with the initial boundary value problem is obtained by proceeding along standard lines (see Ref 33). The associated matrix problem is obtained by discretizing the domain occupied by the porous medium into nonoverlapping finite elements. Associated with this discretization are nodal points at which shape functions are prescribed. Two sets of shape functions will be required for the solid displacement and the fluid velocity fields, respectively. However, since attention in the following is restricted to low order (i.e., four-node plane., eight-node brick) finite elements, which are the most efficient in nonlinear analysis, the same shape functions are used for both the solid and the fluid. The shape functions for the solid displacement and fluid velocity associated with node A are denoted by  $N^A$ . They satisfy the relations  $N^A(\underline{x}^B) = \delta_{AB}$  in which  $\underline{x}^B$  denotes the position vector of node B,  $\delta_{AB}$  = Kronecker delta. The solution of the Galerkin counterpart of the weak formulation is then expressed in terms of the shape functions and gives rise to the following system of equations

$$\begin{bmatrix} \underline{M}^s & \underline{0} \\ \underline{0} & \underline{M}^w \end{bmatrix} \begin{bmatrix} \underline{a}^s \\ \underline{a}^w \end{bmatrix} = \begin{bmatrix} \underline{F}^s \\ \underline{F}^w \end{bmatrix} - \begin{bmatrix} \underline{Z} & -\underline{Z} \\ -\underline{Z}^T & \underline{Z} \end{bmatrix} \begin{bmatrix} \underline{v}^s \\ \underline{v}^w \end{bmatrix} \quad (19)$$

where:  $\underline{M}^\alpha$  = mass matrix

$\underline{a}^\alpha$  = acceleration vector

$\underline{v}^\alpha$  = velocity vector

$\underline{F}^\alpha$  = force vector

Several computational simplifications result in using a diagonal mass matrix, and a "lumped" mass matrix is used throughout. For the two-dimensional (three-dimensional), four- (eight-) node bilinear (trilinear) isoparametric element,

$$(M_{ij}^{AB})^\alpha = \delta_{ij} \delta^{AB} \int_{\Omega^e} \rho^\alpha N^A d\Omega \quad (\text{no sum on } A) \quad (20)$$

where:  $M_{ij}^{AB}$  = the elemental mass contribution to node A from node B for directions i and j to the global mass matrix  $\Omega^e$  = spatial domain occupied by element e.

In Equation 19,  $\underline{Z}$  is a damping matrix arising from the momentum transfer terms in Equations 16 and 17 as:

$$Z_{ij}^{AB} = \int_{\Omega^e} N_{ij}^A \xi N^B d\Omega \quad (21)$$

The solid force vector  $\underline{F}^s$  is:

$$\underline{F}^s = (\underline{F}^{\text{ext}})^s - \underline{N}^s \quad (22)$$

where:  $(\underline{F}^{\text{ext}})^s$  = vector of external solid forces (i.e., body force, surface tractions)

$\underline{N}^s$  = vector of solid stress forces, viz.,

$$N_i^A{}^s = \int_{\Omega^e} N_{,j}^A (\sigma_{ij}^{s} - n^s p_w \delta_{ij}) d\Omega \quad (23)$$

The fluid force vector  $\underline{F}^w$  is:

$$\underline{F}^w = (\underline{F}^{\text{ext}})^w - \underline{N}^w \quad (24)$$

where:  $(\underline{F}^{\text{ext}})^w$  = vector of external fluid forces

$\underline{N}^w$  = vector of convective and fluid stress forces, viz.,

$$\left( \underline{N}_i^A \right)^w = \int_{\Omega^e} \rho^w N_i^A (v_j^w - v_j^s) v_{i,j}^w d\Omega - \int_{\Omega^e} N_{,i}^A n^w p_w d\Omega \quad (25)$$

### Time Integration

Time integration of the semidiscrete finite element equations (Equation 19) is performed by using a finite difference time stepping algorithm. Many types of time stepping algorithms and algorithmic strategies are presently available (see Ref 34 for a description of most widely used computational transient analysis methodologies). Broadly speaking, implicit or explicit procedures are available. Explicit procedures are the most computationally efficient procedures since they do not require (for a diagonal mass matrix) equation solving to advance the solution. However, stability restricts the size of the allowable time step. On the other hand, unconditional stability can usually be achieved in implicit procedures but they do require solution of a system of equations at each time step. First and foremost, it must be pointed out that a purely explicit procedure is not appropriate for the problem at hand because of the unreasonably stringent time step restriction resulting from the presence of the overly stiff fluid in the mixture (even for highly nonlinear solid material models). Methods that combine the attractive features of explicit and implicit integrations have recently been developed. The methods used here fall under the category of "split operator methods." In operator splitting methods, an implicit integrator is selected as the starting point and the integrand (right-hand side in Equation 19) is split so that the system of equations solved is reduced. The specific choice made is obviously problem dependent as discussed further.

Symbolically, the discretized equations of motion (Equation 19) can be written as:

$$\underline{M} \underline{\ddot{a}} + \underline{C} \underline{\dot{v}} + \underline{N}(\underline{d}, \underline{v}) = \underline{F}^{\text{ext}} \quad (26)$$

where  $\underline{M}$ ,  $\underline{C}$ ,  $\underline{N}$ ,  $\underline{\ddot{a}}$ ,  $\underline{\dot{v}}$ , and  $\underline{d}$  are defined by Equation 19 in an obvious manner. Time integration is performed by using the implicit-explicit algorithm of References 35, 18, and 19, which consists of satisfying the following equations:

$$\underline{M} \underline{\ddot{a}}_{n+1} + \underline{C}^I \underline{\dot{v}}_{n+1} + \underline{C}^E \underline{\tilde{v}}_{n+1} + \underline{N}^I(\underline{d}_{n+1}, \underline{v}_{n+1}) \quad (27)$$

$$+ \underline{N}^E(\underline{\tilde{d}}_{n+1}, \underline{\tilde{v}}_{n+1}) = \underline{F}_{n+1}^{\text{ext}}$$

$$\underline{d}_{n+1} = \underline{\tilde{d}}_{n+1} + \alpha \Delta t^2 \underline{\ddot{a}}_{n+1}$$

$$\underline{v}_{n+1} = \underline{\tilde{v}}_{n+1} + \beta \Delta t \underline{\ddot{a}}_{n+1}$$

where:

$$\underline{\tilde{d}}_{n+1} = \underline{d}_n + \Delta t \underline{\dot{v}}_n + (1 - 2\beta) \frac{\Delta t^2}{2} \underline{\ddot{a}}_n$$

$$\underline{\tilde{v}}_{n+1} = \underline{v}_n + (1 - \alpha) \Delta t \underline{\ddot{a}}_n$$

and the superscript I and E refer to the parts of  $\underline{C}$  and  $\underline{N}$  that are treated as implicit or explicit, respectively. The notation is:  $\Delta t$  = time step;  $\underline{F}^{\text{ext}} = \underline{F}^{\text{ext}}(t_n)$ ;  $\underline{d}_n$ ,  $\underline{v}_n$ , and  $\underline{\ddot{a}}_n$  are the approximations to  $\underline{d}(t_n)$ ,  $\underline{v}(t_n)$ , and  $\underline{\ddot{a}}(t_n)$ ;  $\alpha$  and  $\beta$  = algorithmic parameters that control accuracy and stability of the method. It may be recognized that Equations 27 and 28 correspond to the Newmark formulas (Ref 36). The quantities,  $\underline{\tilde{d}}_{n+1}$  and  $\underline{\tilde{v}}_{n+1}$ , are referred to as "predictor" values, while  $\underline{d}_{n+1}$  and  $\underline{v}_{n+1}$  are referred to as "corrector" values. From Equations 26 through 28, it is apparent that the calculations are rendered partly explicit by evaluating part of the viscous contribution  $\underline{C}^E \underline{\tilde{v}}_{n+1}$ , and the force,  $\underline{N}^E$ , in terms of data known from the previous step.

Calculations commence with the given initial data (i.e.,  $\underline{d}_0$  and  $\underline{v}_0$ ) and  $\underline{\ddot{a}}_0$ , which is defined by.

$$\underline{M} \underline{\dot{a}}_0 = \underline{F}_0^{\text{ext}} - \underline{C}_0 \underline{v}_0 - \underline{N}(\underline{d}_0, \underline{v}_0) \quad (28)$$

since  $\underline{M}$  is diagonal, the solution of Equation 28 is rendered trivial.

### Implementation

At each time step, Equations 26 through 28 constitute a nonlinear algebraic problem that is solved by a Newton-Raphson type iterative procedure. The most useful and versatile implementation is to form an "effective static problem" from Equations 26 through 28 in terms of the unknown  $\underline{a}_{n+1}$ , which is in turn linearized. Within each time step, the calculations are performed as summarized in Table 1 in which  $\underline{C}^I$  and  $\underline{K}^I$  denote the parts of the damping and tangent stiffness operators, respectively, to be treated implicitly.

The following choices have been found most appropriate:

Incompressible Fluid (Penalty Formulation). In this case,  $\underline{C}^I$  is selected to contain both the momentum transfer and the penalty term

$$\underline{C}^I = \begin{bmatrix} \underline{Z} + \underline{C}^{ss} & -\underline{Z} + \underline{C}^{sw} \\ -\underline{Z}^T + \underline{C}^{ws} & \underline{Z} + \underline{C}^{ww} \end{bmatrix} \quad (29)$$

where:  $\underline{C}^{\alpha\beta}$  ( $\alpha, \beta = s, w$ ) = damping matrices arising from the penalty treatment of the fluid contribution as.

$$(\underline{C}_{ij}^{AB})^{\alpha\beta} = \int_{\Omega^e} \lambda^w \frac{n^\alpha n^\beta}{n^w} N^A_{,i} N^B_{,j} d\Omega \quad (30)$$

The convective fluid force (see Equation 24) is usually small and is treated explicitly with no resulting computational difficulty. Note that since  $\underline{C}^{sw} = (\underline{C}^{ws})^T$  the resulting  $\underline{C}^I$  is symmetric for the choice adopted here.

As for the solid stress force (Equation 23) contribution to the equations of motion, three options are possible: "implicit," "explicit," or "implicit-explicit" treatment. The choice is made as follows:



Wave Propagation Type Calculations. Very short time scale (and high frequency) solutions are sought and an explicit treatment of the solid effective stress contribution is usually found most appropriate in this case. The time step size restriction resulting from stability considerations, is of the same order as the one resulting from accuracy considerations for nonlinear material models. Further, the specific implicit treatment adopted for the fluid contribution allows the calculations to be carried out at a time step usually close to the time step corresponding to the propagation of the solid compressional wave through the solid phase of the critical element.

Vibration Type Calculations. Since the frequencies captured are usually much higher than above, an implicit treatment of the solid effective stress contribution is usually convenient in this case since it allows the time step to be selected following accuracy considerations only. Unconditional stability is achieved by selecting the proper algorithmic parameters as discussed later. However, for nonlinear analyses, a purely implicit treatment requires a maxtrix reform/factorize at each time step (and for every iteration to be performed, in general), thus producing a considerable computational burden. It is therefore convenient, in the nonlinear case, to adopt an implicit-explicit treatment of the effective stress contribution as follows: The linear part of the stiffness is treated implicitly while the remaining nonlinear part is treated explicitly. For that purpose, a solid stiffness operator is defined from Equations 9 and 23 through linearization as:

$$\tilde{K}_s = \begin{bmatrix} \tilde{K}^S + \tilde{K}^G & 0 \\ 0 & 0 \end{bmatrix} \quad (31)$$

where:  $\tilde{K}^S$  = material tangent part

$\tilde{K}^G$  = "initial stress" or geometric part, formed from the tensors  $\tilde{D}^S$  and  $\tilde{D}^G$  (Equation 9) in the usual manner (see Ref 16).

Table 1. Flow Chart

1. Initialization:

$$i = 0$$

$$Q1 = Q2 = 0$$

2. Predictor Phase:

$$\tilde{d}_{n+1}^{(i)} = \tilde{d}_{n+1}$$

$$\tilde{v}_{n+1}^{(i)} = \tilde{v}_{n+1}$$

$$\tilde{a}_{n+1}^{(i)} = 0_{n+1}$$

3. Form Effective Mass: (Reform and factorize only if required)

$$\tilde{M}^* = \tilde{M} + \Delta t \alpha \tilde{C}^I + \Delta t^2 \beta \tilde{K}^I$$

4. Form Residual Force:

$$\Delta \tilde{F}^{(i)} = \tilde{F}_{n+1}^{ext} - \tilde{M} \tilde{a}_{n+1}^{(i)} - \tilde{C} \tilde{v}_{n+1}^{(i)} - \tilde{N}(\tilde{d}_{n+1}^{(i)}, \tilde{v}_{n+1}^{(i)})$$

5. Solution Phase:

$$\tilde{M}^* \Delta \tilde{a}^{(i)} = \Delta \tilde{F}^{(i)}$$

6. Corrector Phase:

$$\tilde{a}_{n+1}^{(i+1)} = \tilde{a}_{n+1}^{(i)} + \Delta \tilde{a}^{(i)}$$

$$\tilde{v}_{n+1}^{(i+1)} = \tilde{v}_{n+1} + \Delta t \alpha \tilde{a}_{n+1}^{(i+1)}$$

$$\tilde{d}_{n+1}^{(i+1)} = \tilde{d}_{n+1} + \Delta t^2 \beta \tilde{a}_{n+1}^{(i+1)}$$

Table 1. Continued

7. Convergence Check: (only if  $i > 0$ )

$$Q2 = Q1$$

$$Q1 = \left\| \frac{\Delta a^{(i)}}{\Delta a^{(i-1)}} \right\|$$

$$Q = \text{AMAX}(Q1, Q2)$$

$$\text{If } \left\| \frac{\Delta F^{(i)}}{\Delta F^{(0)}} \right\| \leq \text{TOL}^* \text{ .AND.}$$

$$Q \left\| \frac{\Delta a^{(i)}}{\Delta a^{(0)}} \right\| \leq (1-Q)\text{TOL}^* \text{ GOTO 9}$$

Otherwise; continue

8.  $i \leftarrow i + 1$  ; GOTO 3

9.  $n \leftarrow n + 1$  ; GOTO 1

\*Typically,  $\text{TOL} = 10^{-3}$

In the implicit-explicit procedure:

$$K^I = \begin{bmatrix} \tilde{K}^S_E & 0 \\ 0 & \tilde{0} \end{bmatrix} \quad (32)$$

where:  $\tilde{K}^S$  = linear elastic contribution to the material tangent stiffness (from Equation 10).

Such a choice does not always lead to unconditional stability. The difficulty is not usually associated with the explicit treatment of  $\tilde{K}^G$  (which contains terms of the stress order and therefore usually has a negligible impact on stability), but rather from the explicit treatment of the nonlinear term  $(\tilde{K}^S \quad \tilde{K}^S_E)$  for materials with a locking tendency. In that case, care must be exercised in selecting a time step smaller than the one associated with the fastest expected wave speed corresponding to the subsequent stress histories to be followed by the material elements.

Diffusion Type Calculations. It is sometimes desirable to capture the purely diffusive part ("consolidation" part) of the solution "dynamically." Such a necessity arises in situations in which both short and long time solutions to a dynamical problem are sought (such as in seismic or blast induced liquefaction simulations). As shown in References 14 and 16, by switching to an appropriate choice of the Newmark parameters,  $\alpha = 3/2$  and  $\beta = 1$ , and by using the implicit-explicit option described above, all dynamic transients can be damped out, and purely diffusive (consolidation) solutions can be obtained "dynamically" by solving the dynamic equations.

The penalty treatment of the storage equation constraint requires that  $\lambda^w$  be selected as a "large number" capable of predominating the other moduli. It should be picked according to the relation:

$$\lambda^w = C \text{ Max} \left[ \frac{n^w}{\epsilon} \cdot \frac{\gamma_w}{2} \cdot \frac{1}{2} \Delta t (\lambda^S + 2 \nu^S) \right] \quad (33)$$

where:  $C$  = a constant that depends only on the computer word length. Numerical studies reveal that for floating-point word lengths of 60 to 64 bits,  $C \approx 10^7$ .

It has been determined, on the basis of numerical experiments, that it is better to use reduced integration of the penalty terms and of the solid volumetric stiffness ( $\text{div } \underline{v}^s$  contribution) to alleviate potential mesh locking phenomena.

Compressible Fluid. In this case,  $\underline{C}^I$  contains the momentum transfer term contribution to the equations of motion, viz.,

$$\underline{C}^I = \begin{bmatrix} \underline{Z} & -\underline{Z} \\ -\underline{Z}^T & -\underline{Z} \end{bmatrix} \quad (34)$$

and the convective fluid force is treated explicitly.

Again, the fluid pressure contribution is treated implicitly. For this purpose, a fluid stiffness operator is defined from Equations 14 and 19 through linearization as

$$\underline{K}_w = \begin{bmatrix} \underline{C} & \underline{C} \\ \underline{C}^{ws} & \underline{C}^{ww} \end{bmatrix} \quad (35)$$

Where  $\underline{C}^{\alpha\beta}$  ( $\alpha, \beta = s, w$ ) are the same matrices as previously defined in Equation 31. However, note that in this case, the matrices contribute to the stiffness matrix rather than to the damping matrix.

The same options as described previously for the solid stress force contribution to the equations are used. Note that in the implicit-explicit procedures,

$$\underline{K}^I = \begin{bmatrix} \underline{K}_E^s + \underline{C}^{ss} & \underline{C}^{sw} \\ \underline{C}^{ws} & \underline{C}^{ww} \end{bmatrix} \quad (36)$$

which again is a symmetric matrix.

Stability. The resulting stability conditions (Ref 35) are summarized: In all cases  $\alpha \geq 1/2$ :

1. Implicit Treatment: Unconditional stability is achieved if  $\beta \geq \alpha/2$  and it is recommended that (Ref 37):

$$\beta = \frac{\left(\alpha + \frac{1}{2}\right)^2}{4} \quad (37a)$$

2. Implicit-Explicit Treatment: The time step restriction is

$$\omega \Delta t < \frac{2}{\left(\alpha + \frac{1}{2}\right)} \quad (37b)$$

to maximize high-frequency numerical dissipation.,  $\omega$  = highest natural frequency associated with the explicit part of the stiffness operator. The maximum expected frequency may be bounded by the frequency of the smallest element, viz., for a rectangular four node bilinear element,

$$\omega = 2 \frac{C}{L} \quad (37c)$$

where:  $L$  = smallest dimension of the element

$C$  = wave speed ( $= \sqrt{(\lambda^s + 2 \mu^s)/\rho^s}$  for the linear model).

#### Program DYNAFLOW

Equations 19 through 37 have been incorporated into the finite element computer program DYNAFLOW (Ref 38). Numerical results that illustrate the performance of the proposed numerical schemes in analyzing the propagation of plane progressive waves (Ref 39, 1, 29, 26, 40, and 41) in fluidsaturated porous soil media have been reported in Reference 13. In Reference 13 both compressible and incompressible fluid cases are considered. In the following, attention is restricted to vibration calculations in soil-structure interacting systems associated with seismic events in which the pore fluid may be assumed to be incompressible (compared to the compressibility of the soil skeleton).

In the calculation reported the four-node bilinear isoparametric element (see Ref 43 and 33 for a detailed description) is used with the standard selective integrations scheme (Ref 43). Also, the Newark algorithmic parameters are always selected such that  $\alpha \geq 1/2$  and  $\beta = (\alpha + 1/2)^2/4$  to maximize high-frequency numerical dissipation (Ref 37).

Time integration of the semi-discrete finite element equations is performed by using the implicit-explicit, predictor-(multi) corrector option. The structural domains and the fluid phase are always treated implicitly, whereas the solid skeleton phase is treated partly implicitly, partly explicitly. Specifically, the "elastic" part of the solid stiffness is treated implicitly, whereas the elastic-plastic part of the stiffness is treated explicitly. Such a choice allows time integration to be performed most efficiently for cases in which many load/unload cycles occur, such as during dynamic events.

In order to simulate realistic initial conditions for the stresses and strains in the soil deposits before input of the earthquake like ground motions, in all the example problems reported, the numerical simulation was carried in at least two sequential steps:

1. Installation of Soil Deposit. This step in the numerical simulation was designed to simulate realistic initial conditions. The computed gravitational stresses/displacements/pore-water pressures were used as initial conditions for the ground motion calculations.

2. Ground Motion Simulation: The computed gravitational stresses/displacements/pore-water pressures computed in the first sequence were used as initial conditions for the ground motion calculations. In order to avoid the initial propagations of any spurious noises, the acceleration array was first cleared before activating the ground motion. Also, the algorithmic parameters were reset to  $\alpha = 0.65$ ,  $\beta = 0.33$  (slightly diffusive), the time to zero, and the time step,  $\Delta t$ , selected to properly follow the details of the stresses (and pore-water pressures) "at rest" before input of the ground shaking. For that purpose, small initial stresses were first input in the soil deposit and gravity was

turned on. A number of steps (and iterations) were used to apply gravity with a large enough time step,  $\Delta t$ , to ensure: (1) that no excess pore-water pressures (over steady state conditions) would build-up., (2) full development of effective stresses in the foundation soil would occur; and (3) that no transients would occur. For that purpose, a backward scheme with high numerical dissipation was used to damp out all transients setting  $\alpha = 1.50$  and  $\beta = 1.00$ . Iterations (Newton-Raphson or modified Newton-Raphson) were used to ensure proper convergence of the solution at each time step.

#### Post-Dynamic Event Simulation

In saturated soil deposits, excess pore-water pressures usually buildup and do not have time to fully dissipate within the time frame of the earthquake. Subsequent redistribution and diffusion of these excess pore-water pressures following the dynamic event are often of interest since they may lead to failures (e.g., in earth dams where failures have been recorded in the field several minutes to several hours following the earthquake). It is, however, usually inefficient (costwise) to capture numerically the post-event behavior with a time step designed to follow the details of an earthquake motion. Therefore, in the following, post-dynamic events have been calculated by resetting  $\alpha = 1.5$  and  $\beta = 1.00$  (highly diffusive backward) and by selecting the appropriate time step,  $\Delta t$ , for capturing the post-event diffusion part of the solution. (Note. Either constant  $\Delta t$  or geometrically growing  $\Delta t$  were used for this sequence.)

### PRINCETON UNIVERSITY EFFECTIVE STRESS SOIL MODEL

#### Theory

The hysteretic stress-strain behavior of the soil skeleton modeled by using the effective-stress elastic-plastic model reported by Professor Prevost (Ref 31). The model is an extension of the simple



multi-surface  $J_2$ -plasticity theory and uses conical yield surfaces. The model has been developed for cohesionless soils and tailored to:

1. Retain the extreme versatility and accuracy of the multi-surface  $J_2$ -theory in describing observed shear nonlinear hysteretic behavior, shear stress-induced anisotropy effects.
2. Reflect the strong dependency of the shear dilatancy on the effective stress ratio in granular cohesionless soils.

The model is applicable to general three-dimensional stress-strain conditions, but its parameters can be derived entirely from the results of conventional triaxial soil tests.

Yield Function. The yield function selected is of the following form:

$$f = \frac{3}{2}(\underline{s} - p \underline{\alpha}) : (\underline{s} - p \underline{\alpha}) - m^2 p^2 = 0 \quad (38)$$

where:  $\underline{s} = \underline{\sigma} - p \underline{\delta}$  = deviatoric stress tensor

$p = 1/3 \text{ tr } \underline{\delta}$  = effective mean normal stress

$\underline{\delta}$  = effective stress tensor

$\underline{\alpha}$  = kinematic deviatoric tensor defining the coordinates of the yield surface center in deviatoric stress subspace ("the back stress")

$m$  = material parameter

tr = trace

The yield function plots as a conical yield surface (Drucker-Prager) in stress space, with its apex at the origin, and is shown in Figure 1. Unless  $\underline{\alpha} = \underline{0}$ , the axis of the cone does not coincide with the space diagonal. The cross section of the yield surface by any deviatoric plane ( $p = \text{constant}$ ) is circular. Its center does not generally coincide with the origin, but is shifted by the amount  $p \underline{\alpha}$ . This is illustrated in Figure 1 in the principal stress space.

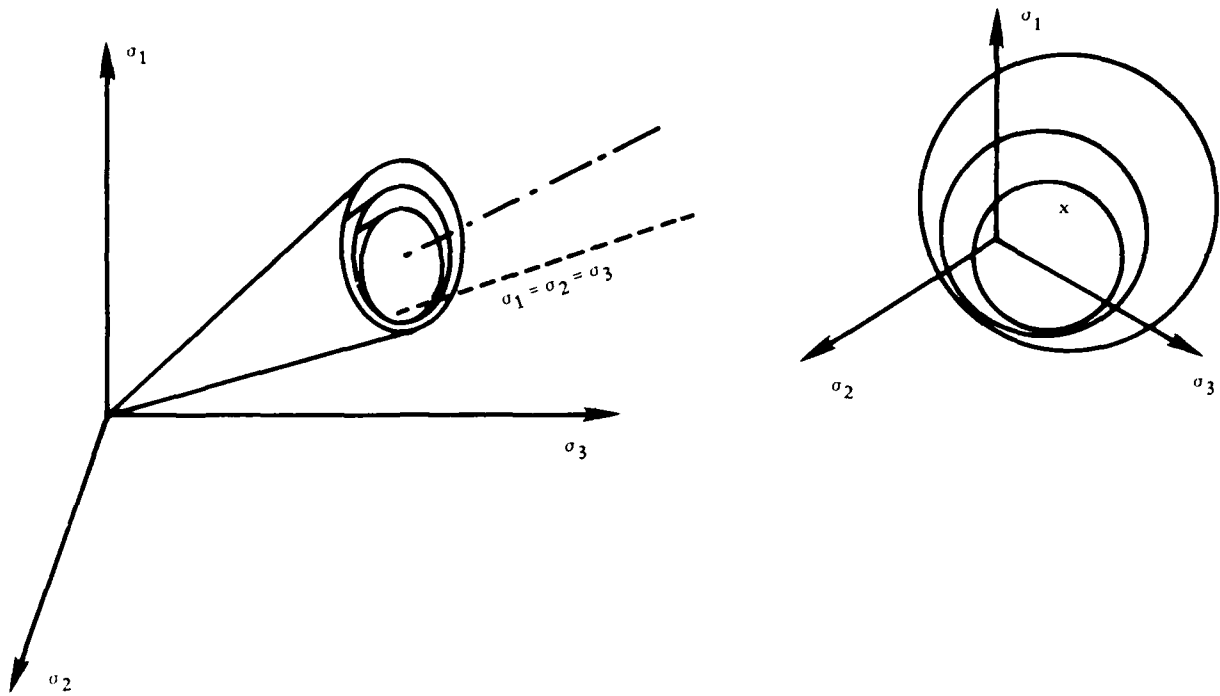


Figure 1. Yield surfaces in principal stress space.

Flow Rule. The plastic potential is selected such that the deviatoric plastic flow be associative. However, a non-associative flow rule is used for its dilatational component, and in the following:

$$\text{tr } \underline{\underline{p}} = \frac{(\eta \bar{\eta}^2) - 1}{(\eta \bar{\eta}^2) + 1} \quad (39)$$

where:  $\text{tr}$  = trace

$\underline{\underline{p}}$  = symmetric second-order tensor which defines (in stress-space) the "direction" of plastic deformations

$\bar{\eta} = (3/2 \underline{\underline{s}} : \underline{\underline{s}})^{1/2} / p$  = stress ratio

$\eta$  = material parameter.

When  $\eta < \bar{\eta}$ , the trace of  $\underline{\underline{p}}$  is less than zero and plastic compaction takes place, whereas when  $\eta > \bar{\eta}$ , the trace of  $\underline{\underline{p}}$  is greater than zero and plastic dilation takes place. The case  $\eta = \bar{\eta}$  corresponds to no plastic volumetric strains. In the following,  $\bar{\eta} = \bar{\eta}_C$  when  $\text{tr } \underline{\underline{s}}^3 < 0$ , and  $\bar{\eta} = \bar{\eta}_E$  when  $\text{tr } \underline{\underline{s}}^3 > 0$ .

Hardening Rules. In order to allow for the adjustment of the plastic hardening rule to any kind of experimental data, a collection of nested yield surfaces is used. The yield surfaces are all similar conical surfaces (Equation 1), and a purely kinematic hardening rule is adopted. Upon contact, the yield surfaces are translated by the stress point and the direction of translation is selected so that no overlapping of the surfaces can take place (see Reference 31 for more details).

Each yield surface is associated with a plastic modulus  $H'$ . The dependence of the plastic modulus upon the deviatoric stress is assumed to be in the following form:

$$H' = \frac{H'_C - H'_E}{2} \frac{E}{C} \theta + \frac{H'_C + H'_E}{2} \frac{E}{C} \quad (40)$$

where:

$$\theta = \frac{1}{m_p} \frac{\text{tr } \bar{\underline{s}}^3}{\text{tr } \bar{\underline{s}}^2} \quad \bar{\underline{s}} = 3(\underline{s} - p \underline{\alpha})$$

and  $H'_C, H'_E$  = material parameters.

Effects of the Effective Mean Confining Stress. The dependence of the material moduli upon the effective mean confining stress is:

$$G = G_1 \left( \frac{p}{p_1} \right)^n \quad B = B_1 \left( \frac{p}{p_1} \right)^n \quad H' = H'_1 \left( \frac{p}{p_1} \right)^n \quad (41)$$

where:  $G$  = elastic shear modulus

$B$  = elastic bulk modulus

$H'$  = plastic modulus

$n$  = experimental parameter ( $n = 0.5$  for most cohesionless soils)

$G_1, B_1, H'_1$  = moduli at reference effective mean normal stress  $p_1$ .

## LABORATORY TRIAXIAL TEST SIMULATION - COHESIONLESS SOILS

### Test Program

To validate the Princeton University Effective Stress Soil Model, a series of sands were evaluated in both drained and undrained triaxial tests. The tests were carried out in both extension and compression, and over a range of confining cell pressures and relative densities. To eliminate some of the uncertainty as to the effects of sample preparation and testing procedure on the model's sensitivity, the test data were obtained from different university experts and the Waterways Experiment Station.

The material parameters for the Princeton University soil model are derived from drained triaxial compression and extension data, defined by shear stress, shear strain, mean stress, and volume strain information. This information forms the input for the computer Program MUD, which is an automated procedure to derive the material model moduli and yield surface parameters. The material model has been implemented into a one-point equilibrium solution procedure, Program TEST A, to provide a quick and easy means to evaluate a particular soil model in various stress states for direct comparisons and evaluation of laboratory tests. TEST A was used for this portion of the evaluation, which is the simulation of the triaxial test data.

The basic steps performed to evaluate the laboratory test data were:

1. Select a representative set of drained triaxial tests for which both compression and extension results are available.
2. Use the results from step one as input to Program MUD to determine model parameters.
3. Construct the TEST A input, with the output from Program MUD to evaluate the models representation of input test data.

4. Analyze the stress ratio value in the model parameters to determine a reasonable estimate of the critical stress ratio value. The critical stress ratio parameters control the compactive-dilative characteristics of the model, and thus the volumetric strain.

5. Adjust the critical stress ratios through successive TEST A analysis to optimize the drained model versus undrained prediction agreement.

6. Once soil model agreement is achieved with the original test data, the parameters determined to quantify the soil behavior may be used to predict behavior at different confining pressures and along different stress paths without further modification.

#### Monterey "0" Sand

The University of California, Davis, under contract with the Naval Civil Engineering Laboratory (NCEL) performed triaxial tests on Monterey "0" sand. Figures 2(a) and 2(b) present the drained compression and extension results from the triaxial test data that were used to formulate the model, and the generated results from Program TEST A. As noted, agreement is nearly exact. In Figures 3(a) and 3(b) the model parameters determined at an initial confining stress of  $1 \text{ kg/cm}^2$  are used to simulate drained compression and extension tests at an initial confining stress of  $3 \text{ kg/cm}^2$ . Again, the agreement between predicted versus observed behavior is very good.

Figures 4(a) and 4(b) present the shear stress-strain and effective stress path for an undrained compression test. The undrained stress path agrees almost perfectly, which is a direct indication of the model's ability to capture correctly, the soils compactive-dilative characteristics. This in turn generates the positive and negative pore pressures, and hence the changes in effective stress, which agree very well with those observed in the actual test. In Figure 4(a) the shear stress-shear strain comparisons for the undrained analysis are again in good agreement.

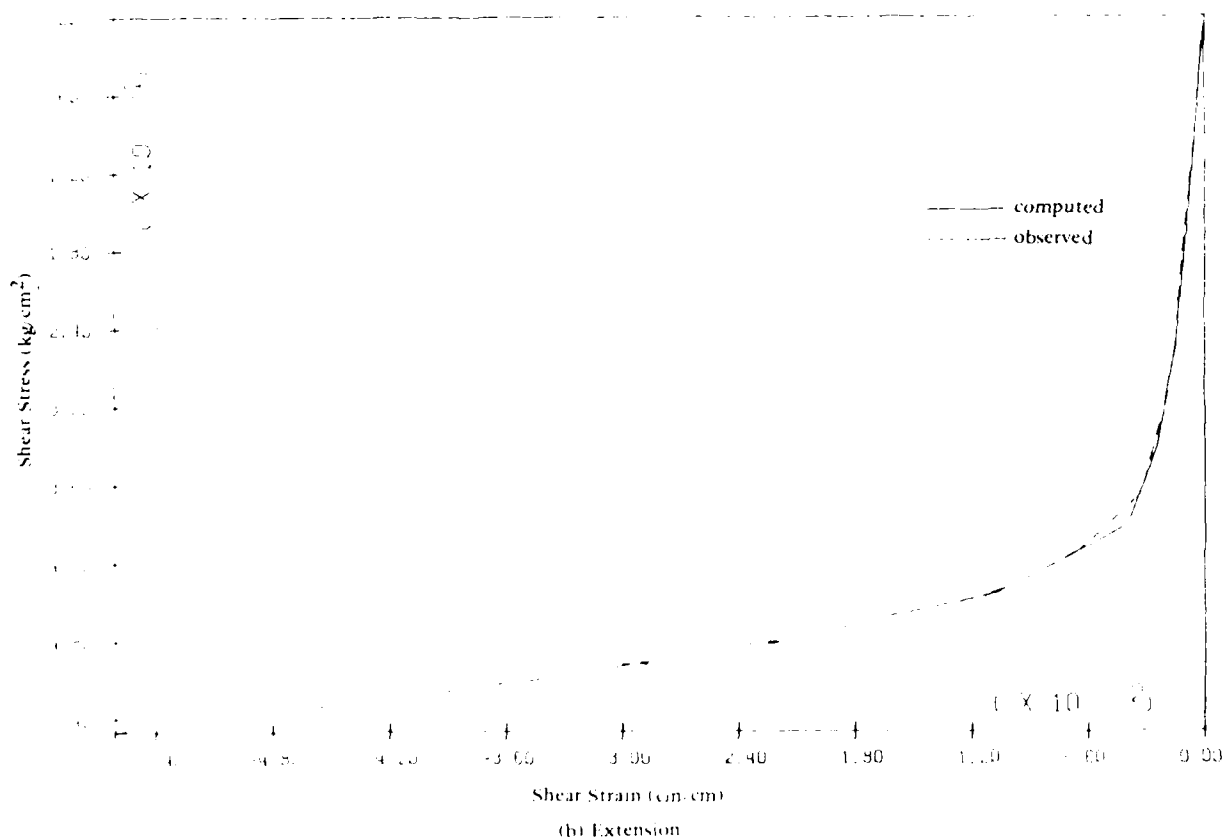
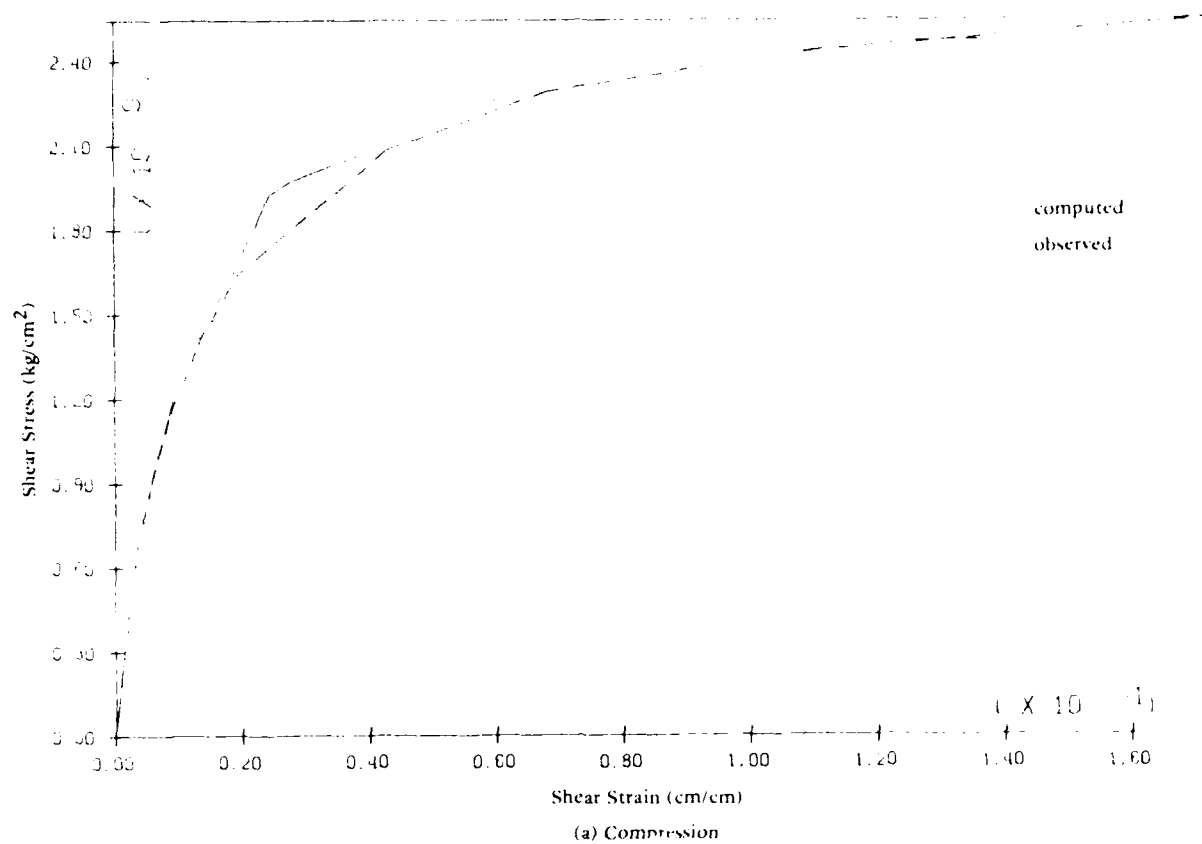


Figure 2. Drained compression and extension Monterey "0" sand, confining cell pressure =  $1 \text{ kg/cm}^2$ .

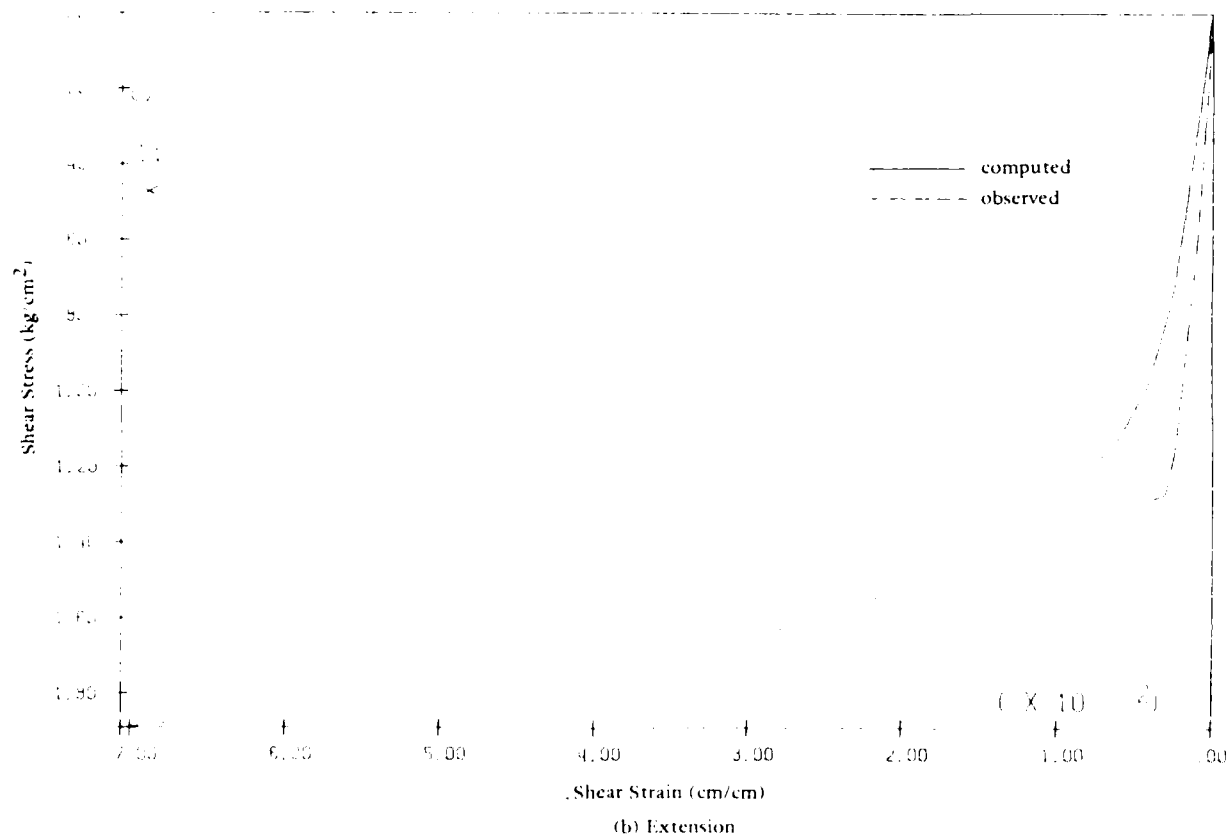
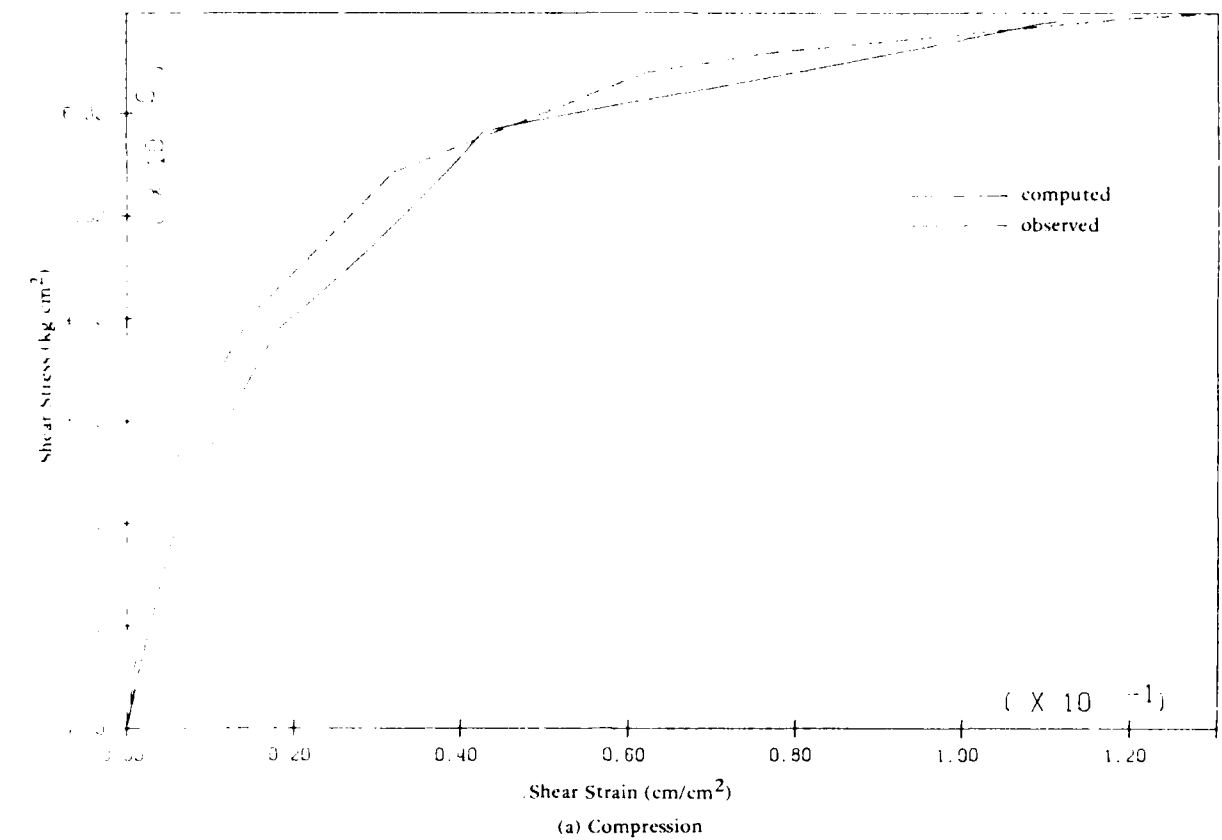


Figure 3. Drained compression and extension Monterey "0" sand, confining cell pressure = 3 kg/cm<sup>2</sup>.

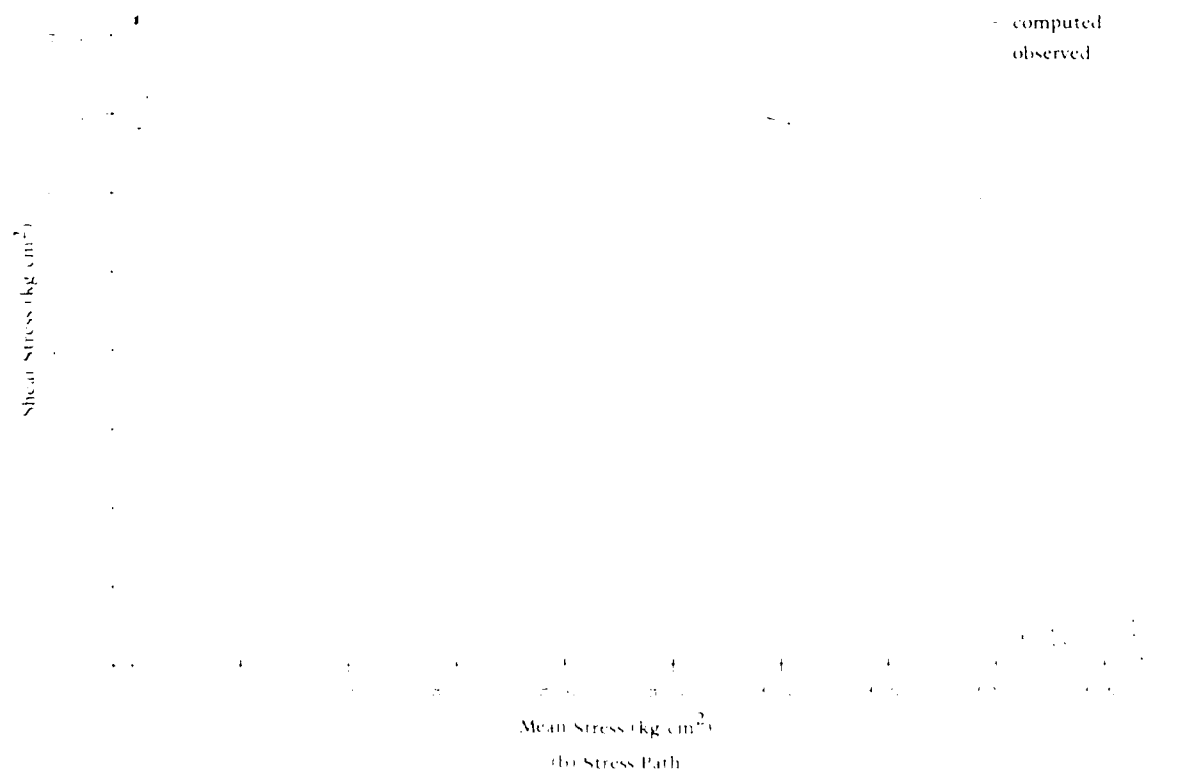
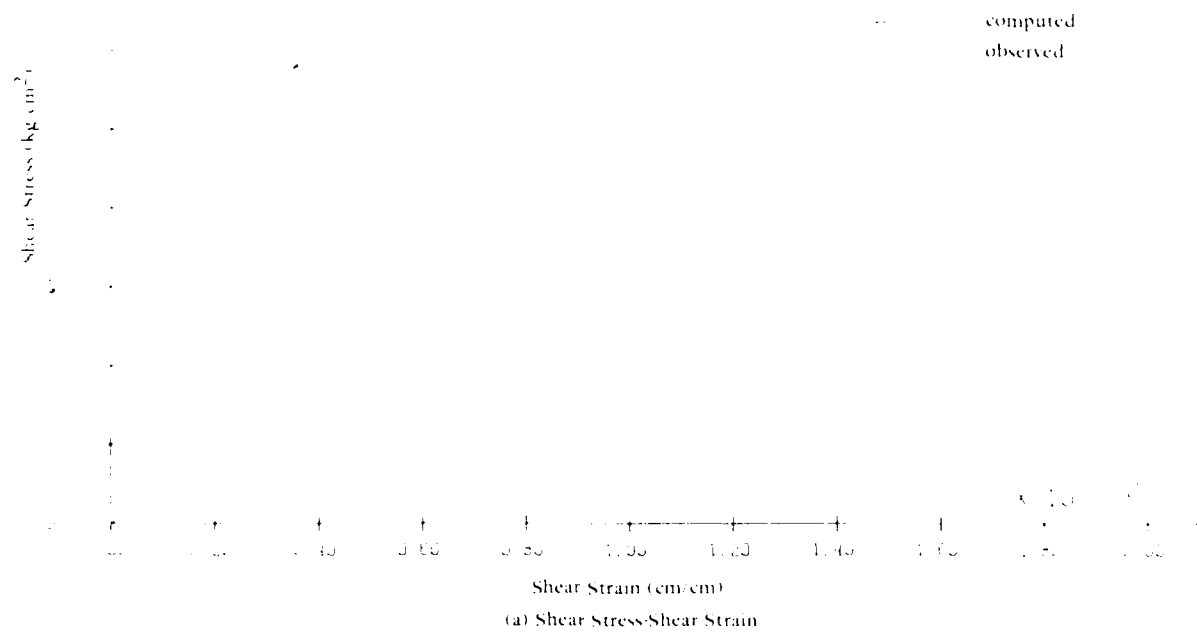


Figure 4. Undrained compression Monterey "0" sand, confining cell pressure = 1 kg/cm<sup>2</sup>.



Figures 5, 6(a) and 6(b) are a demonstration of the same material model derived from drained monotonic triaxial data, predicting an undrained cyclic triaxial test. As can be seen in Figure 5, the model does an adequate job of predicting the observed hysteretic behavior. There is a minor difference in initial stiffnesses between predicted and observed behavior caused by a discrepancy in tracking initial volumetric test data. This could have been improved by providing added definition to the initial portion of the test data but was judged satisfactory as it is. Note the general agreement between the stiffnesses in both loading and unloading, which demonstrates correct energy dissipation in each cycle. In the stress path plot in Figure 6(a) the same degradation per cycle is demonstrated. Note the number of predicted cycles to failure is 4.5, this agrees well with the observed 5.5 cycles. The overall generation of pore water pressure is in good agreement as well, which is shown both in the decline in effective stress to failure in Figure 6(a), as well as in the maximum level attained, Figure 6(b).

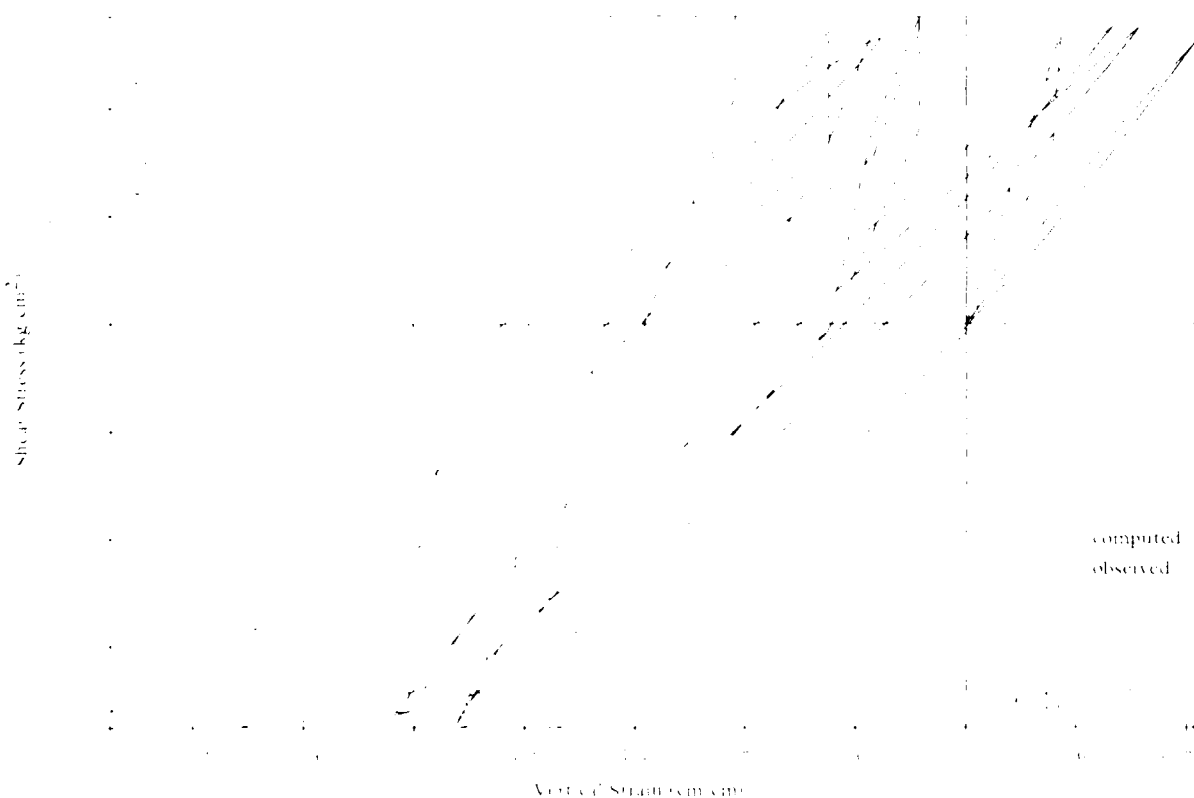


Figure 5. Undrained cyclic analysis Monterey "0" sand confining cell pressure = 1 kg/cm<sup>2</sup>, shear stress-vertical strain.

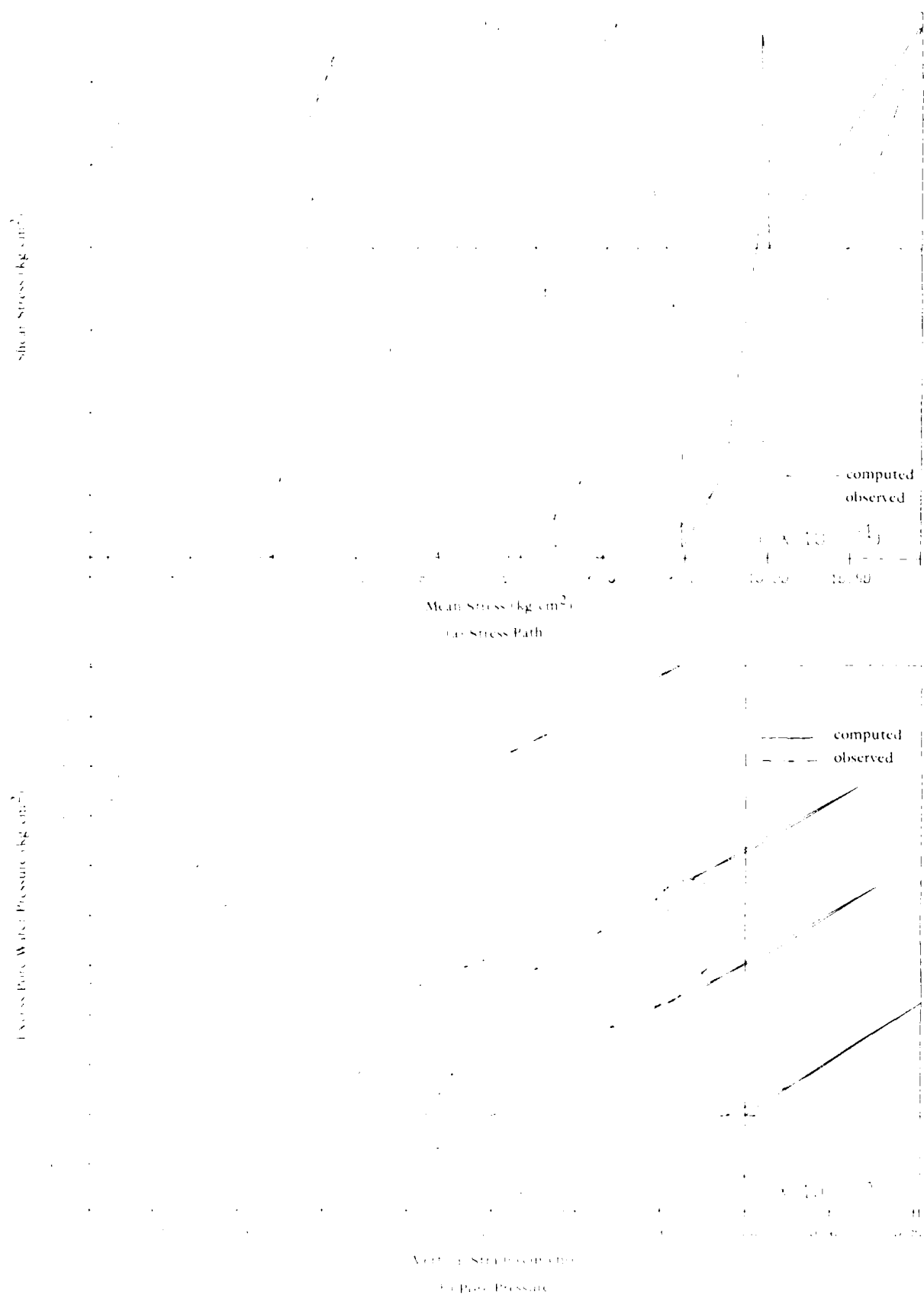


Figure 6. Undrained cyclic analysis Monterey "0" sand, confining cell pressure = 1 kg/cm², stress path and pore pressure.

### Leighton-Buzzard Sand

Triaxial tests on Leighton-Buzzard sand were performed by the University of California, Davis, under contract to NCEL. Figures 7(a) and 7(b) show the drained, monotonic compression and extension comparisons. Figure 8(a) shows the undrained shear stress-shear strain data, and Figure 8(b) shows the undrained stress path from the same test. The model in this example predicts a softer initial response with a smaller generation of pore water pressure than the recorded test data, but these differences are well within the ranges of acceptable differences between two laboratory tests.

The simulation of the undrained cyclic test from the monotonic model again shows good agreement in producing an accurate assessment of energy dissipation and failure state. The model in this case predicted 1.75 cycles to failure compared to the observed failure at 2.75, (Figures 9, 10(a) and 10(b)). The final effective stress values and pore water pressures are in good agreement as well.

### Silica Sand

Silica sand was tested at the University of California at Los Angeles, under contract with NCEL. Figures 11(a) and 11(b) show the reproduction of the drained triaxial compression and extension data used to generate the material model. As would be expected agreement is very good. To demonstrate the model's ability to predict tests at different confining cell pressures, simulations were run at  $5 \text{ kg/cm}^2$  and  $1 \text{ kg/cm}^2$ , the results are plotted on Figures 12(a) and 12(b), respectively. Again generated curves are in very good agreement with the observed results.

Figures 13(a) and 13(b) show the model's ability to simulate a substantially different stress path. The data plotted in these figures is from a drained uniaxial test ( $k_0$ ) where vertical stress is increased while holding horizontal strain at zero. The model uses the same parameters used to predict the standard drained and undrained tests for the

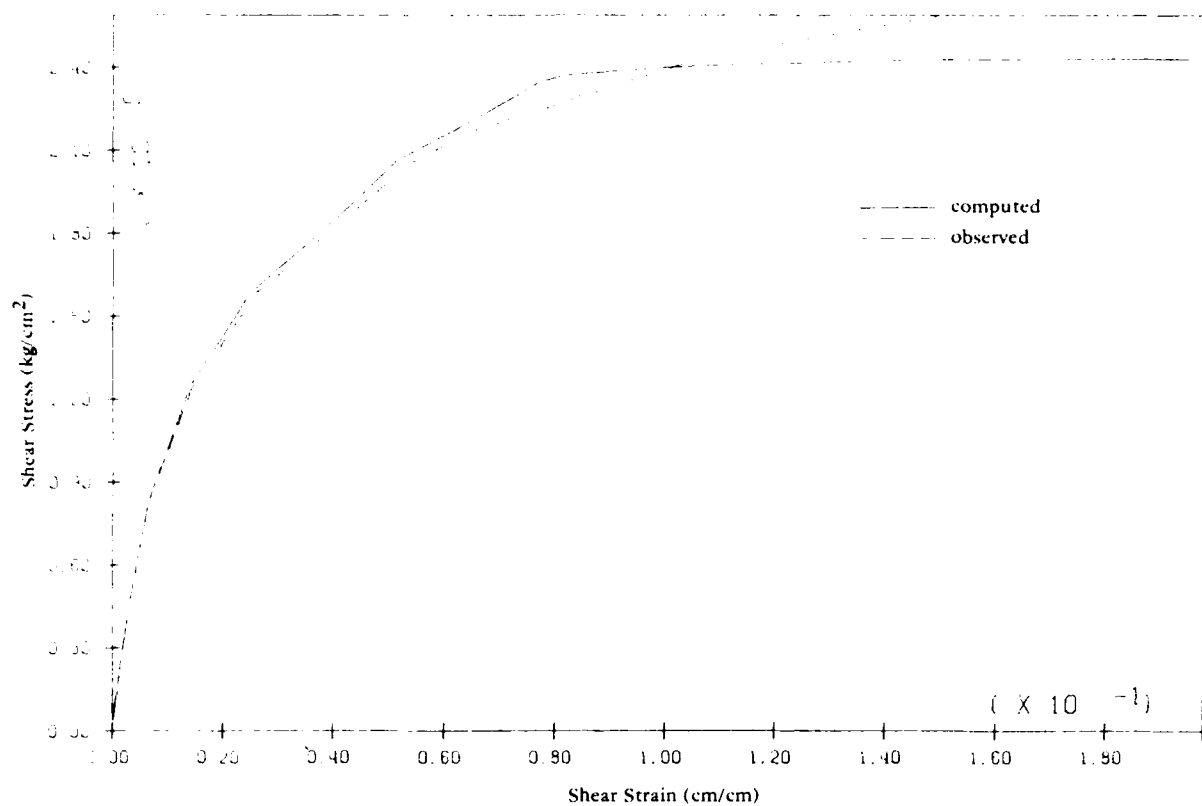
silica sand. Shear stress-vertical strain agreement and volume stress-volume strain agreement are very good. In addition to the uniaxial test, a proportional loading test was run. The results are presented in Figures 14(a) and 14(b). The initial computed stress path deviates slightly from the observed data, however, the results do present a reasonable simulation of the actual test once the initial anisotropic stability is reached.

Figures 15, 16(a), and 16(b) present an undrained cyclic triaxial simulation using the same drained monotonic model used throughout the analysis of the silica sand. The model predicts liquefaction in 4.7 cycles as compared to measured values of 5.7 and 3.4 in two identical laboratory tests. Rates of energy dissipation and pore water pressure generation are again in reasonable agreement, and as in prior analysis, the failure state of the soil is captured quite well.

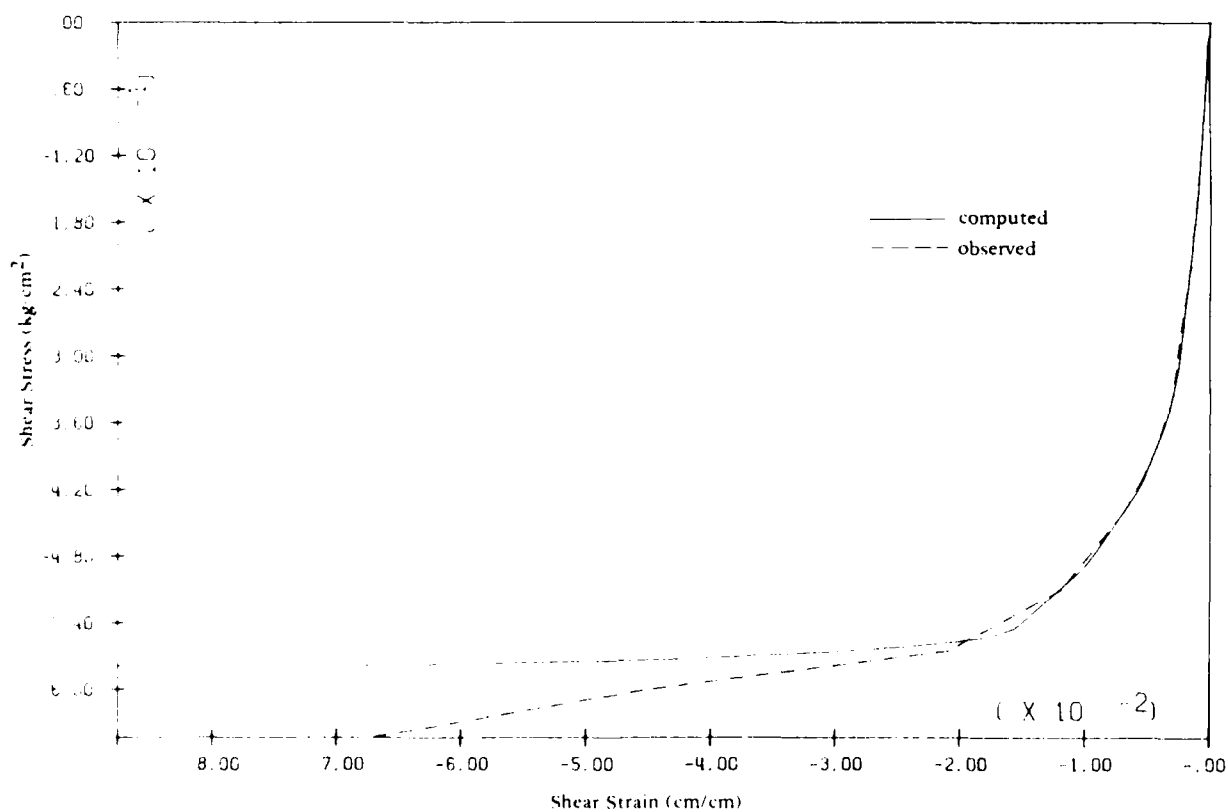
In addition to the determination of model parameters from the consolidated drained tests where volume strains are measured, analyses were performed to predict drained and undrained tests from an undrained model. In an undrained test, the volume strain is held constant (i.e., to zero) and excess pore water pressure is developed. This pore water pressure is a result of the skeletal deformation, which is an indication of the degree of skeletal volume strain.

Program MUD was used with undrained test data to develop the model parameters. (Previously drained data was used.) These parameters were then used to predict drained tests. The results of the undrained model for silica sand are presented in Figures 17(a) and 17(b). The compression and extension results both agree very well with the actual test data, and the previous results calculated using the model formulated from drained data (Figures 11(a) and 11(b)).

The undrained model predicting undrained compression is in good agreement with the data and drained model predictions. There is a slightly larger pore pressure build up in the undrained model (Figures 17(a) and 17(b)) shown by the larger decrease in effective stress presented in the stress path plot (Figure 17(b)).

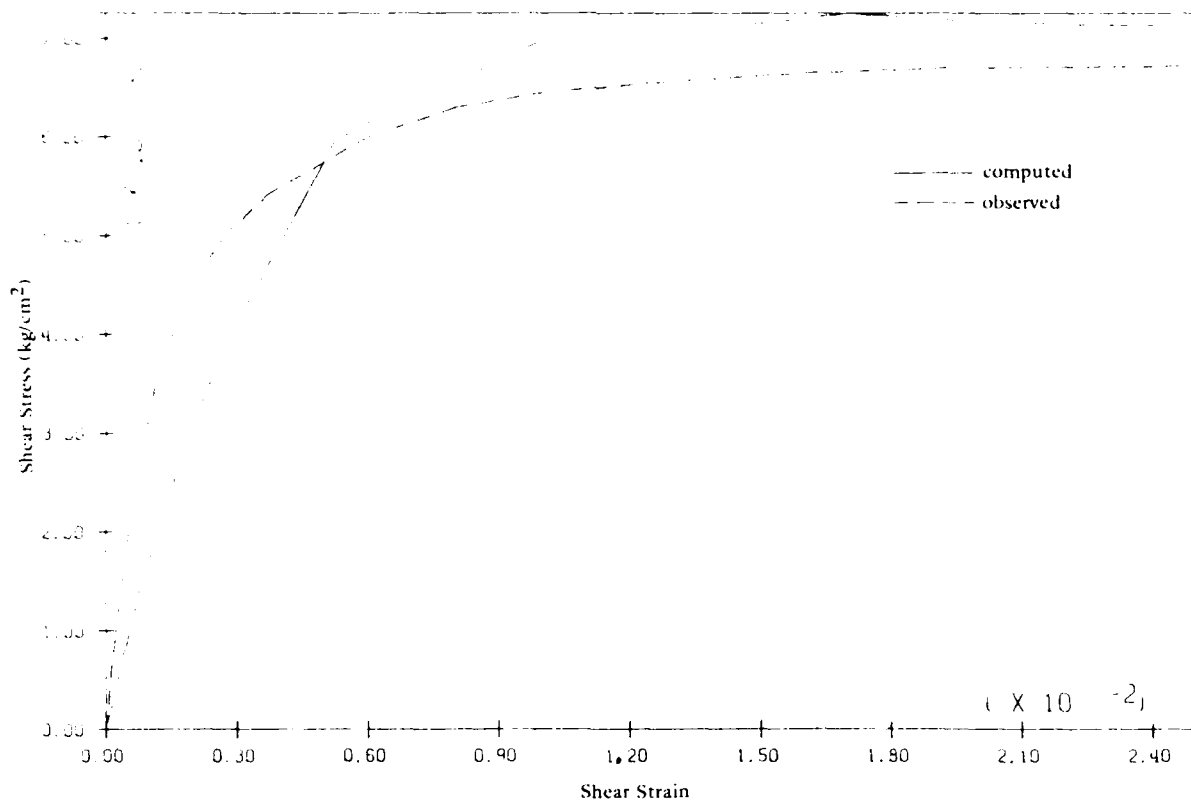


(a) Compression

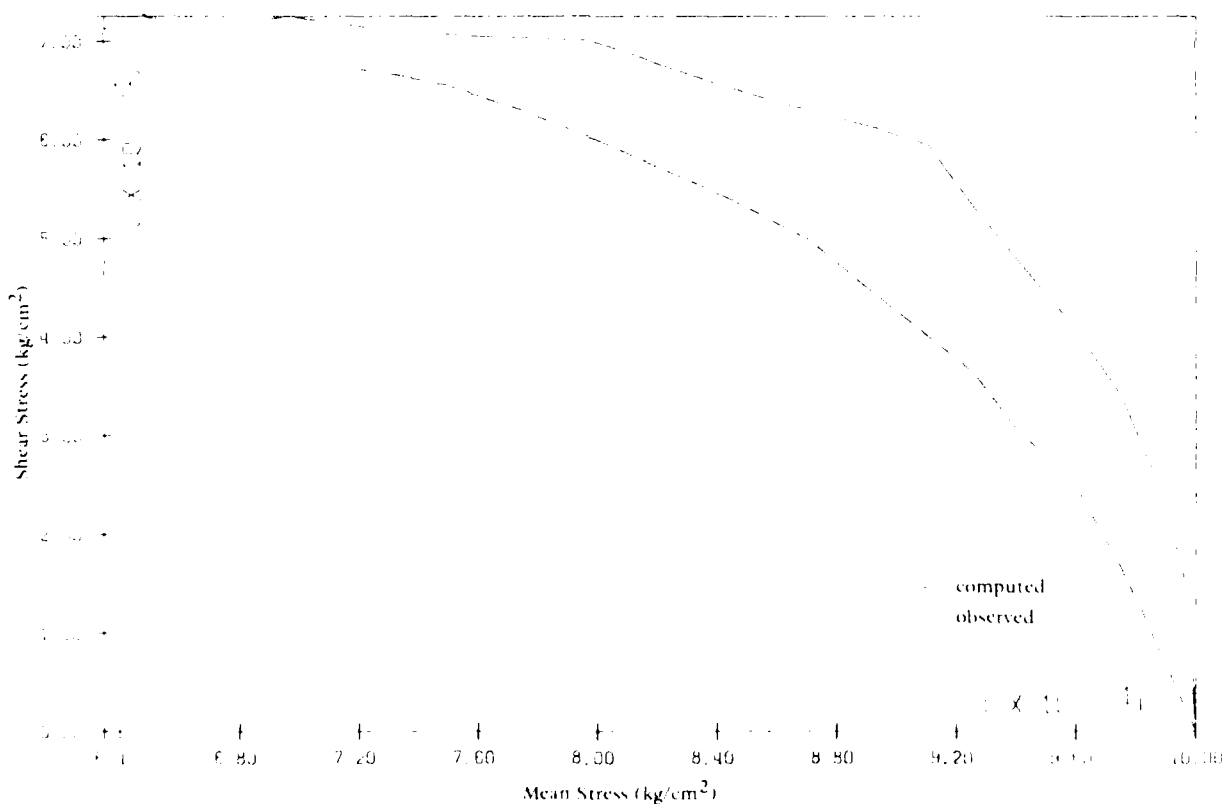


(b) Extension

Figure 7. Drained compression and extension Leighton-Buzzard sand, confining cell pressure = 1  $\text{kg/cm}^2$ .



(a) Shear Stress-Shear Strain



(b) Stress Path

Figure 8. Undrained compression Leighton-Buzzard sand confining cell pressure = 1 kg/cm<sup>2</sup>.

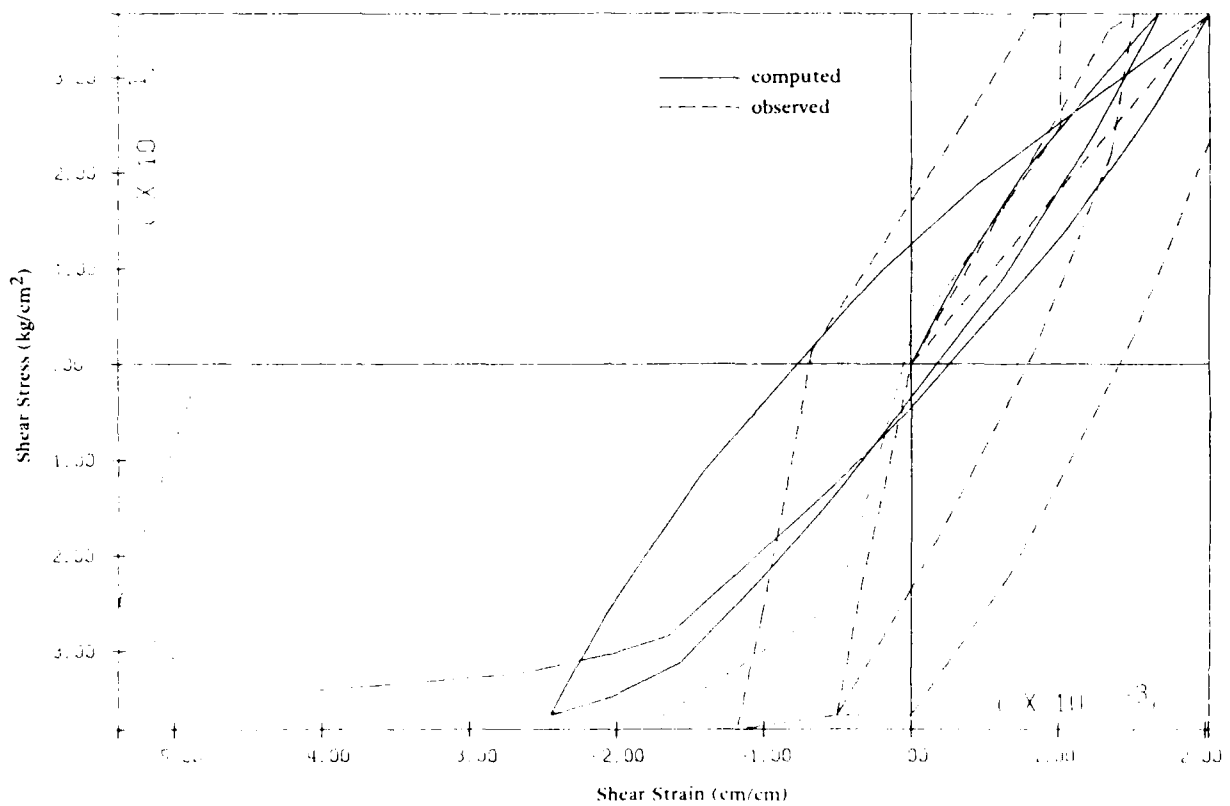


Figure 9. Undrained cyclic analysis Leighton-Buzzard sand, confining cell pressure = 1.0 kg/cm<sup>2</sup>, shear stress-shear strain.

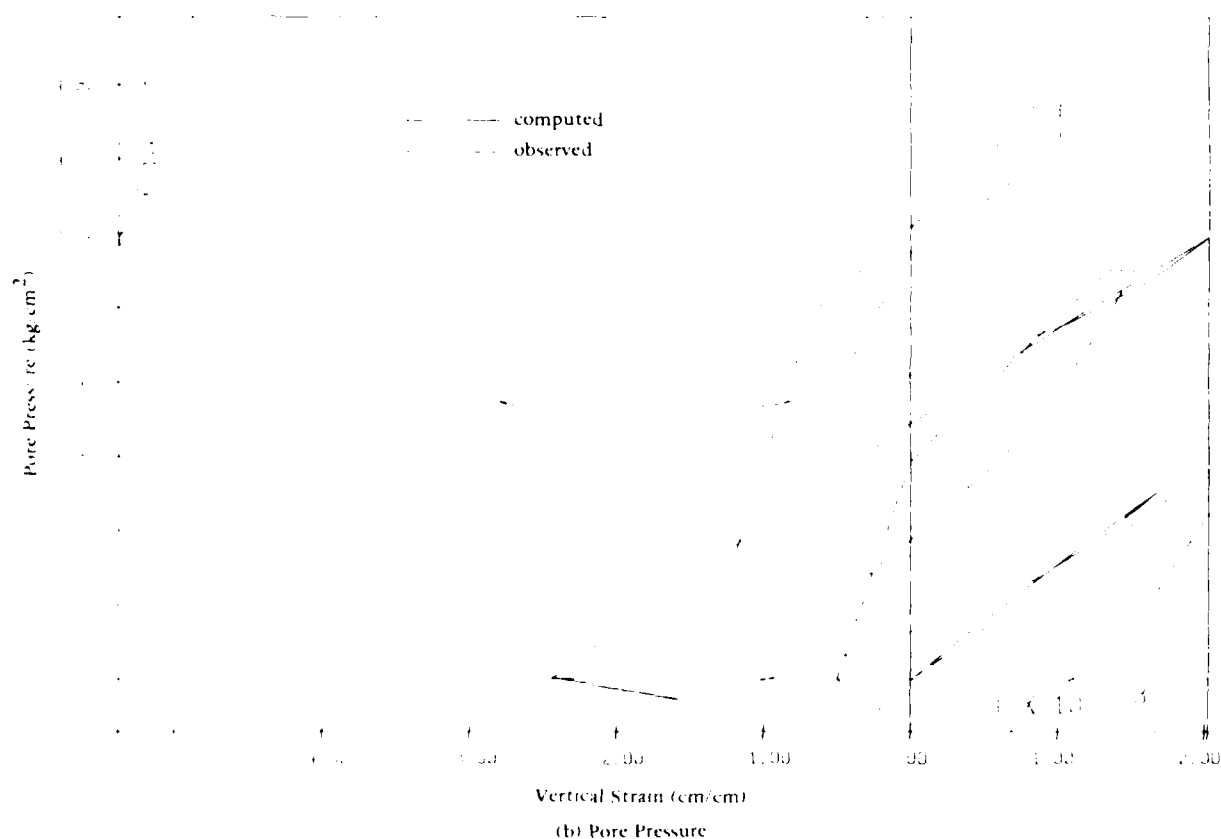
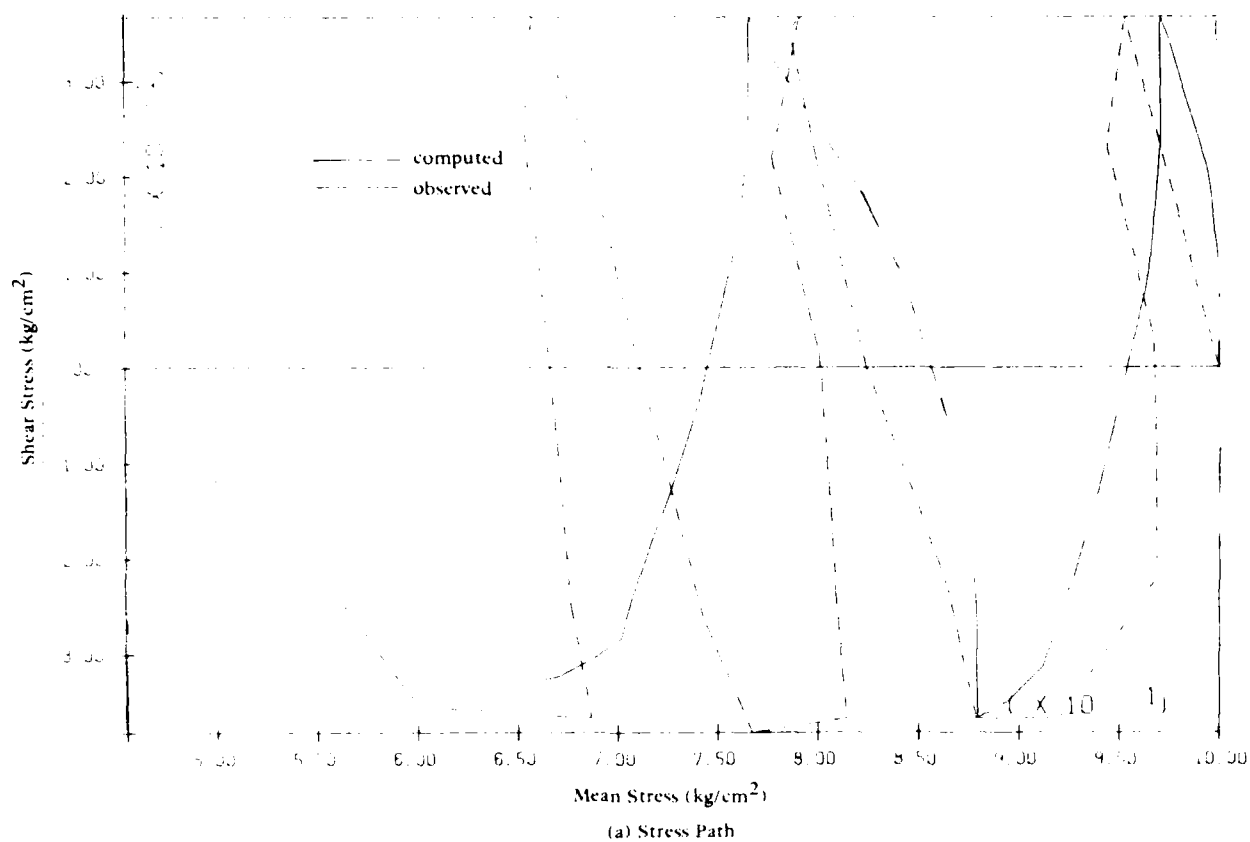


Figure 10. Undrained cyclic analysis Leighton-Buzzard sand, confining cell pressure =  $1.0 \text{ kg/cm}^2$ , stress path and pore pressure.



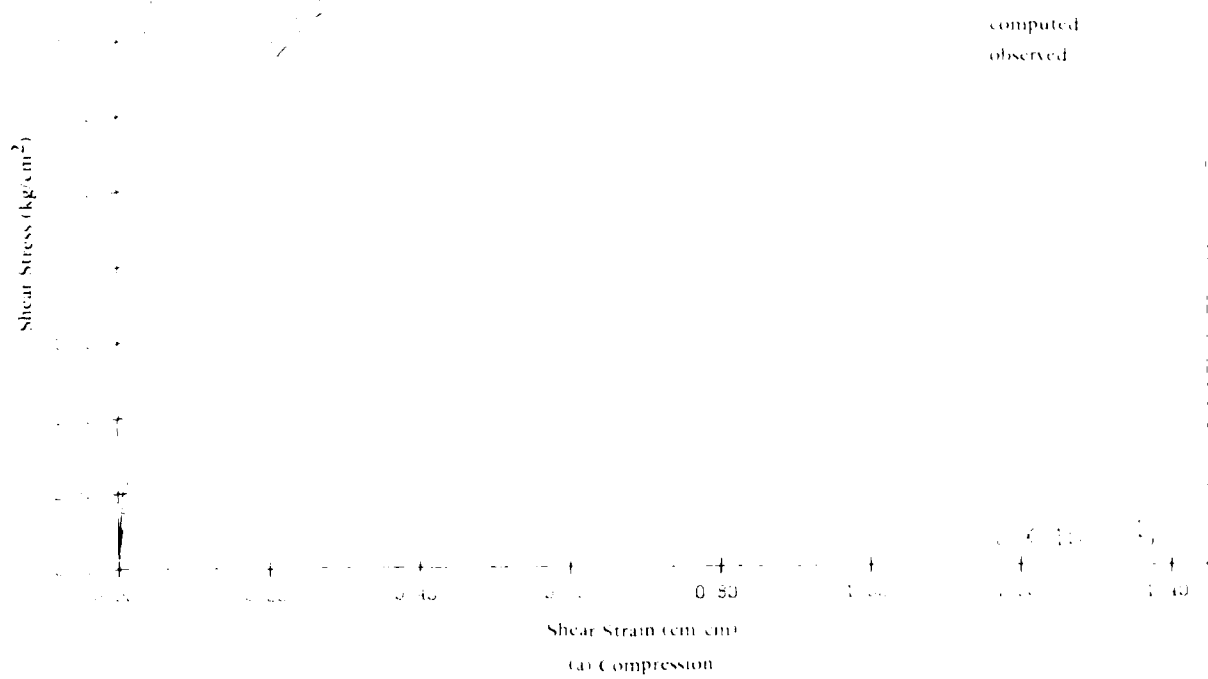


Figure 11. Drained compression and extension silica sand, confining cell pressure = 2 kg/cm<sup>2</sup>.

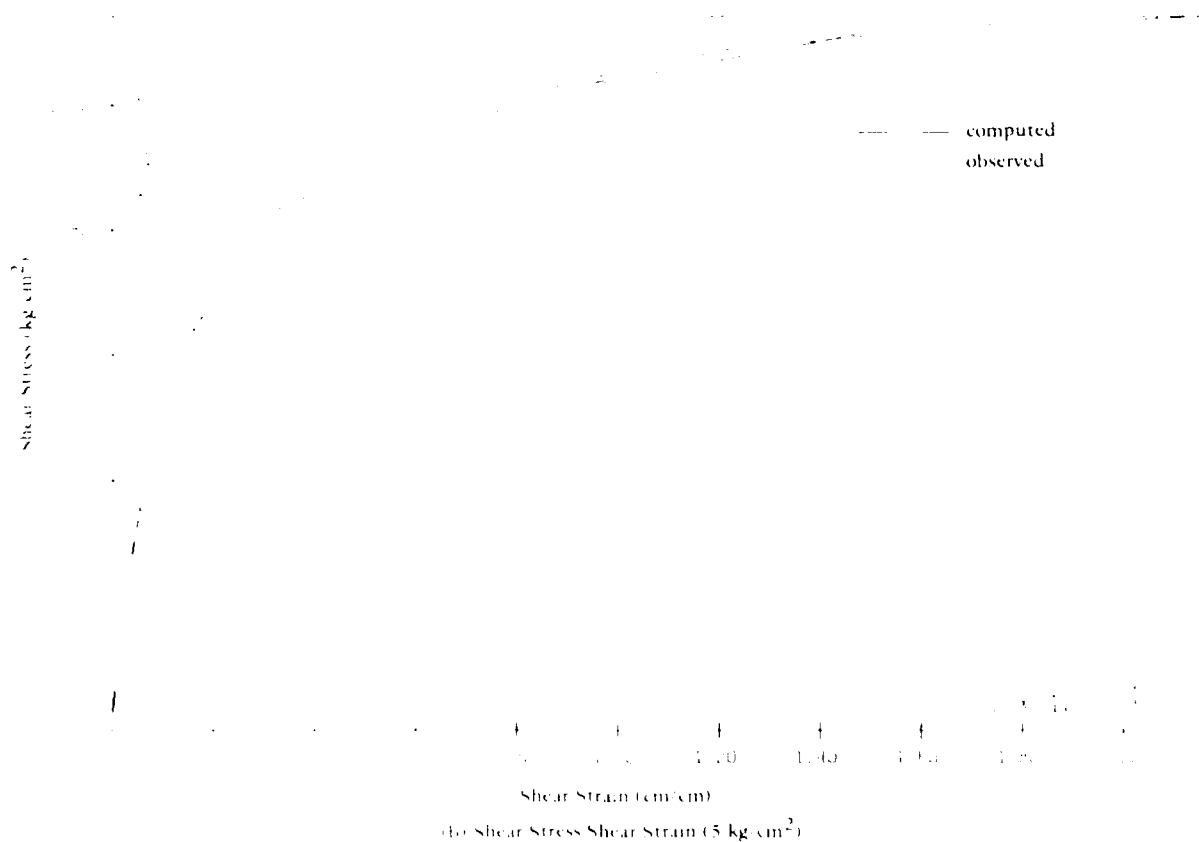
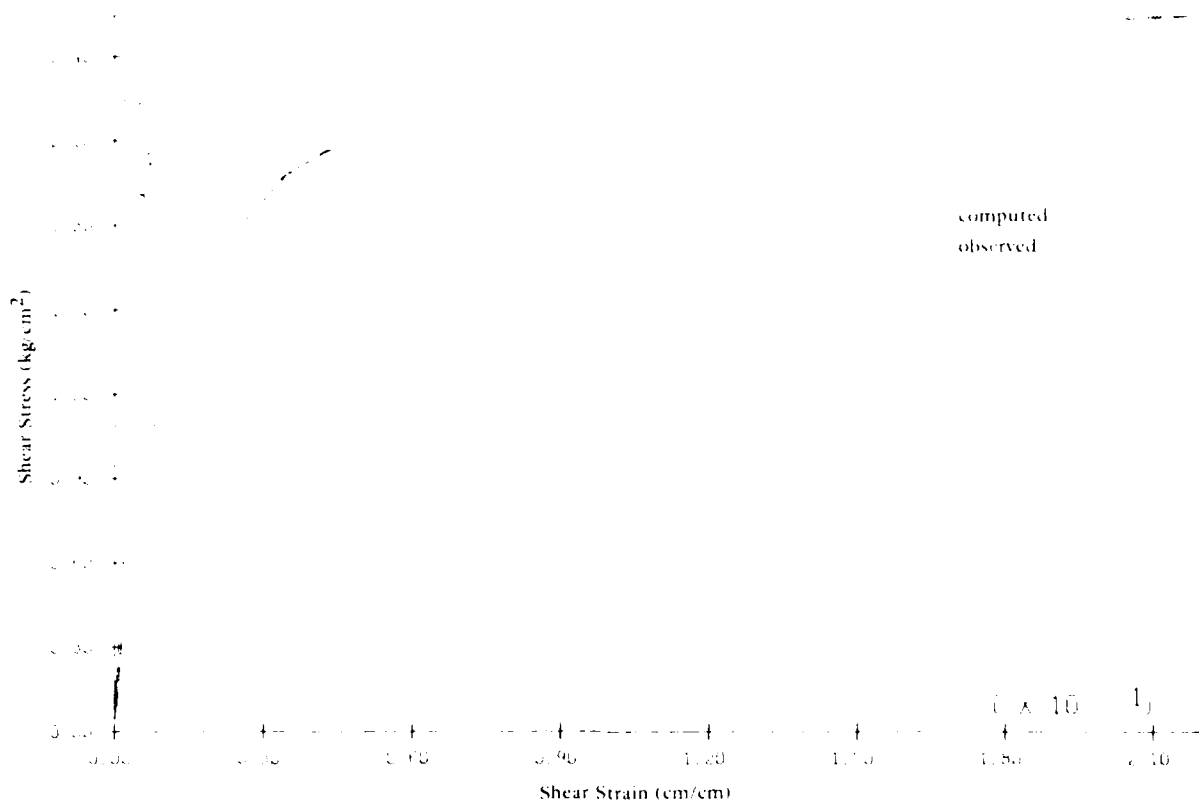


Figure 12. Drained compression silica sand, confining cell pressure = 1.0 and 5.0 kg/cm<sup>2</sup>.

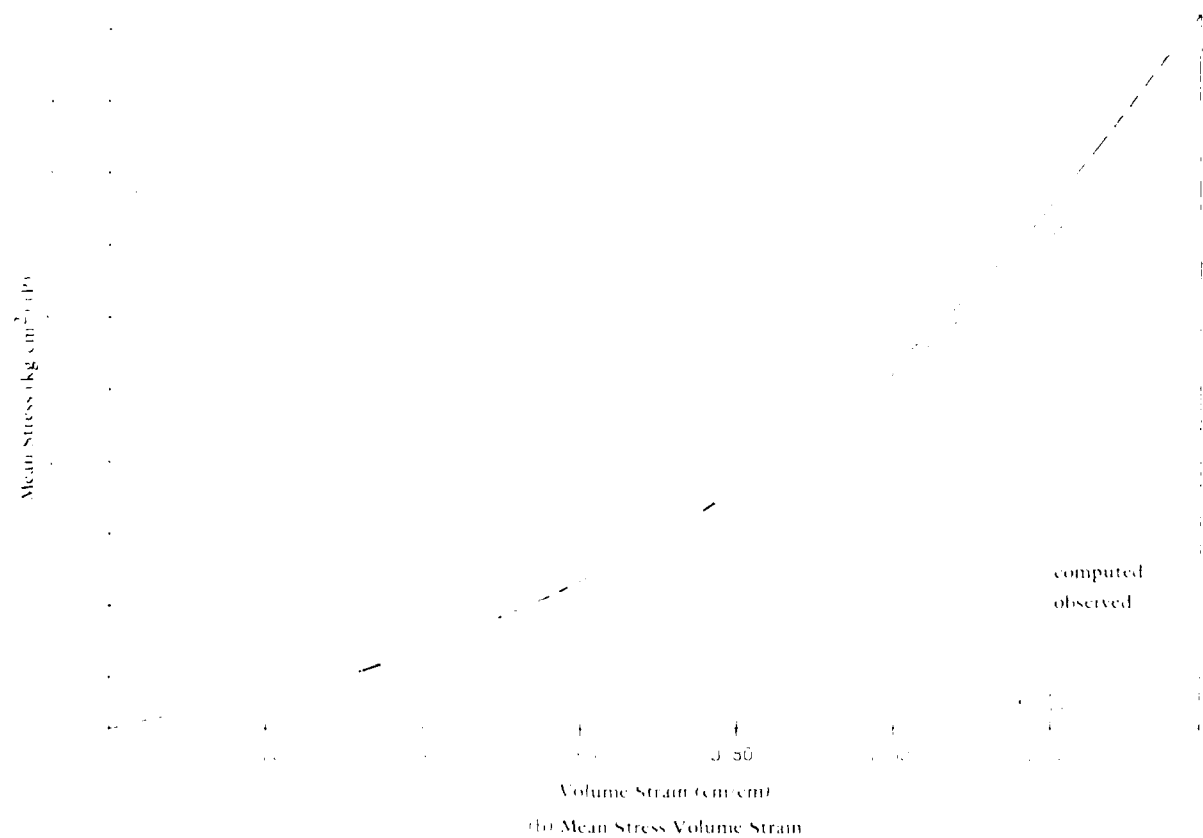
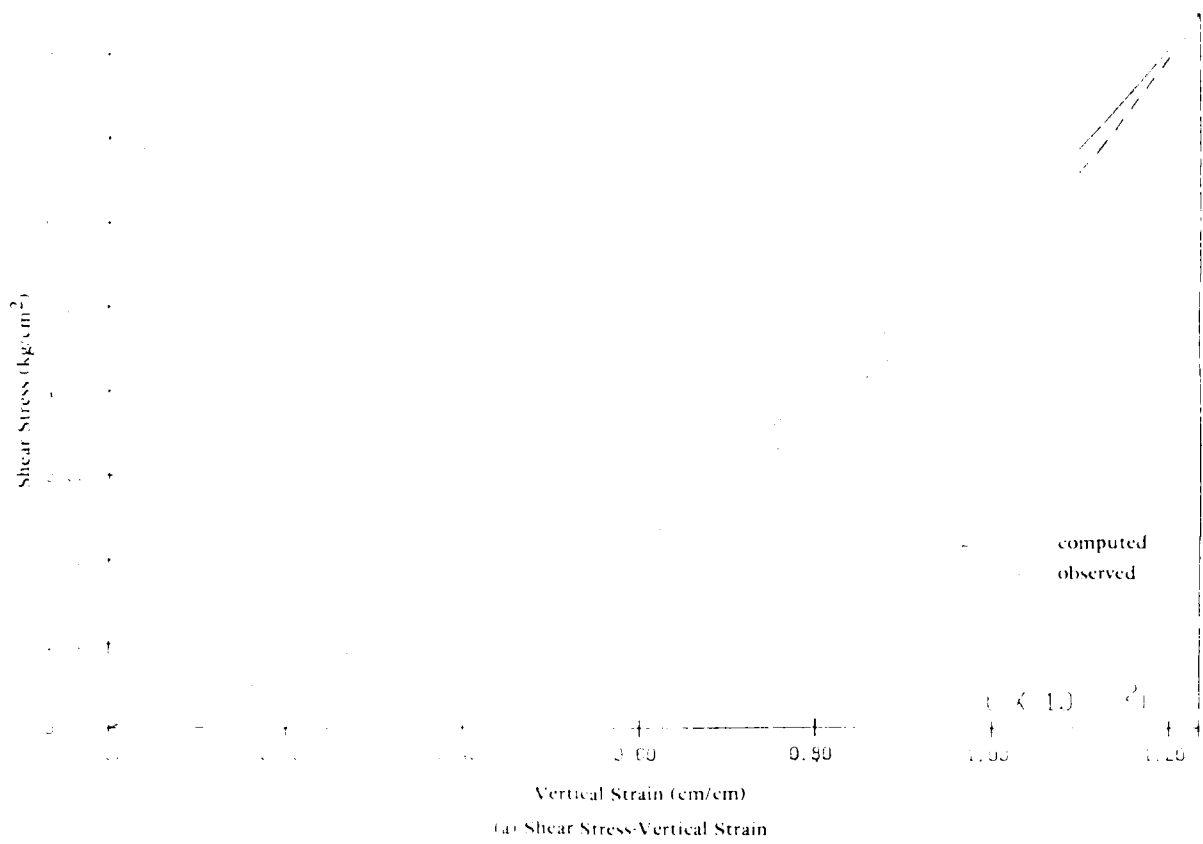
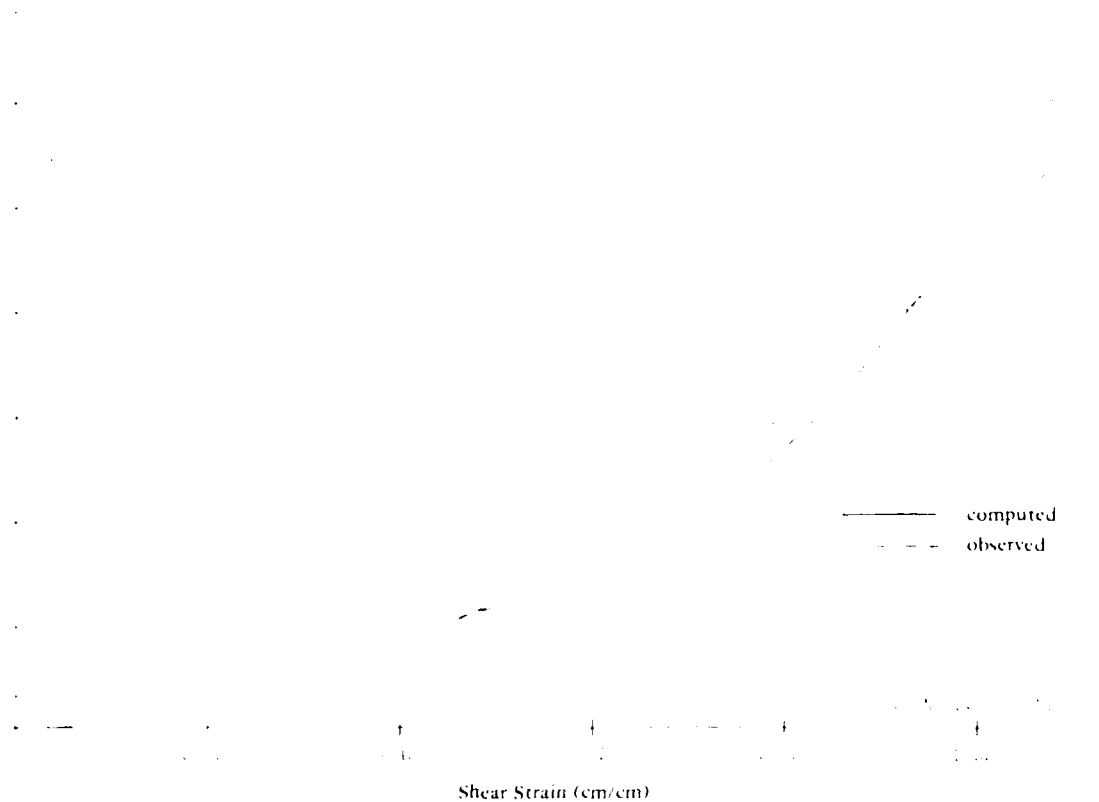


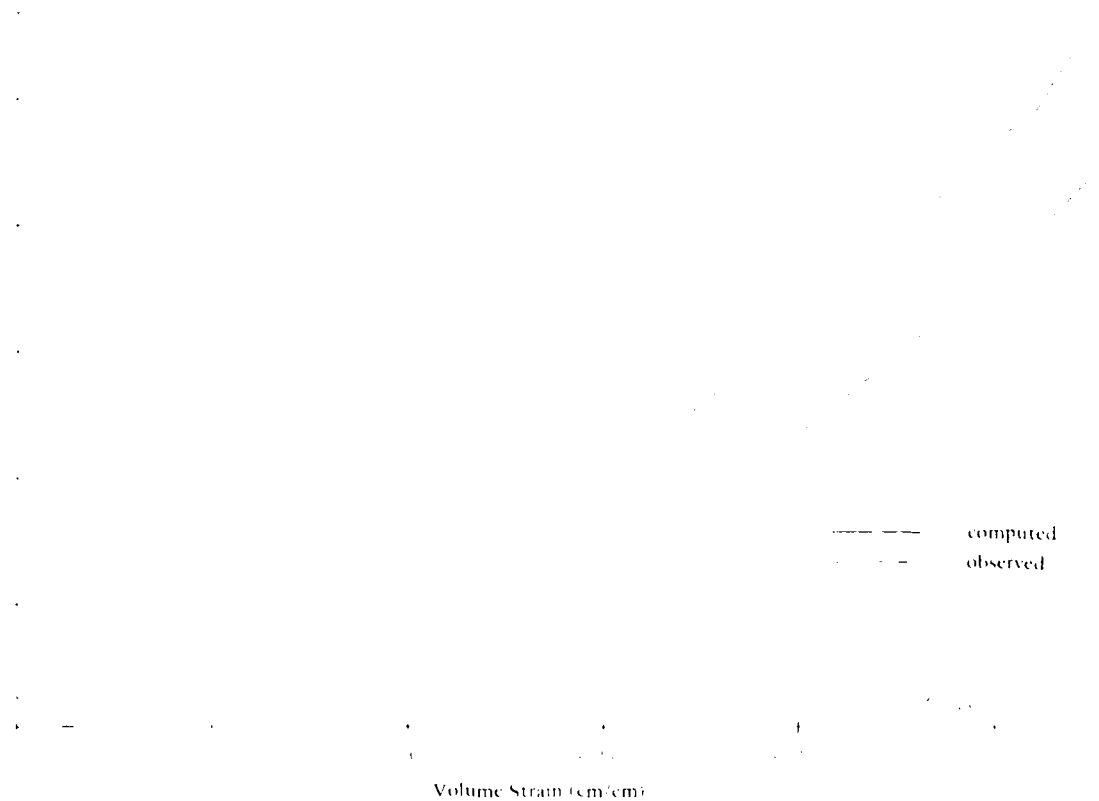
Figure 13. Uniaxial compression test with silica sand.

Shear Stress ( $\text{kg/cm}^2$ )



(a) Shear Stress-Shear Strain

Mean Stress ( $\text{kg/cm}^2$ )



(b) Mean Stress Volume Strain

Figure 14. Proportional loading test with silica sand.

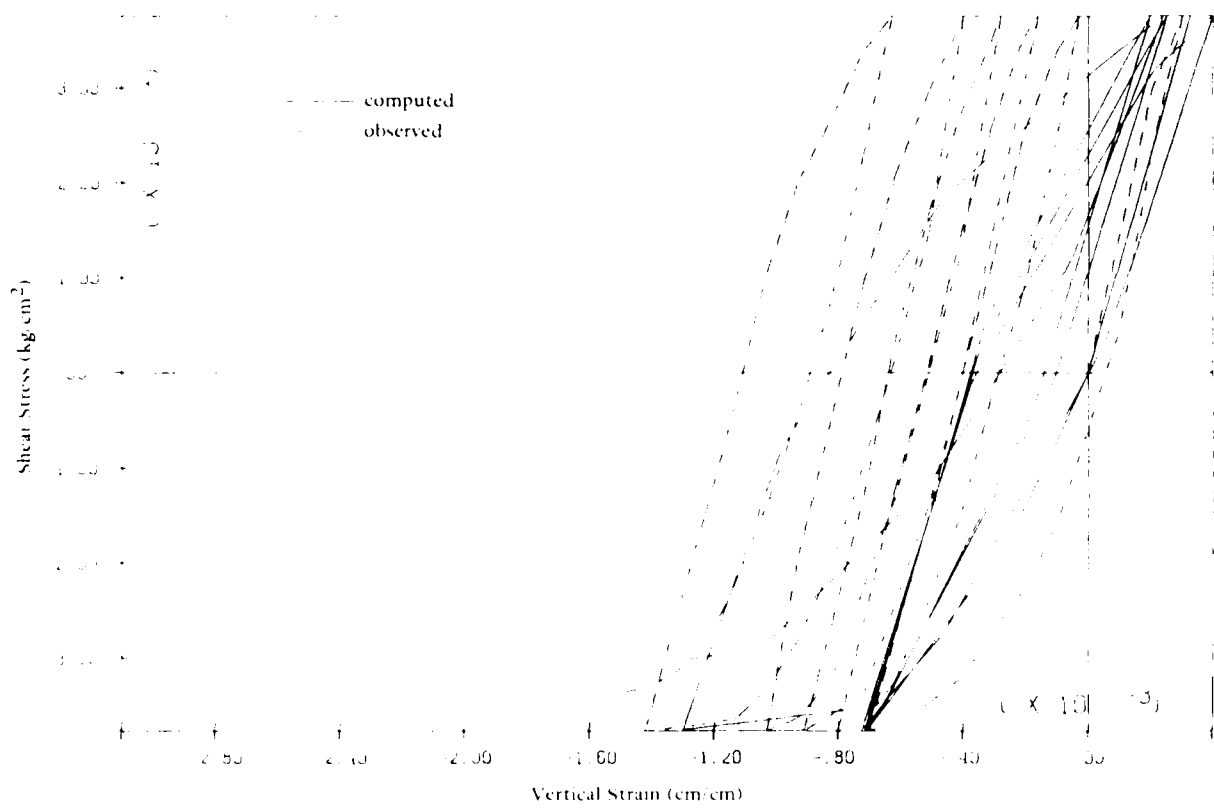


Figure 15. Undrained compression silica sand, confining cell pressure = 2.0 kg/cm<sup>2</sup>.

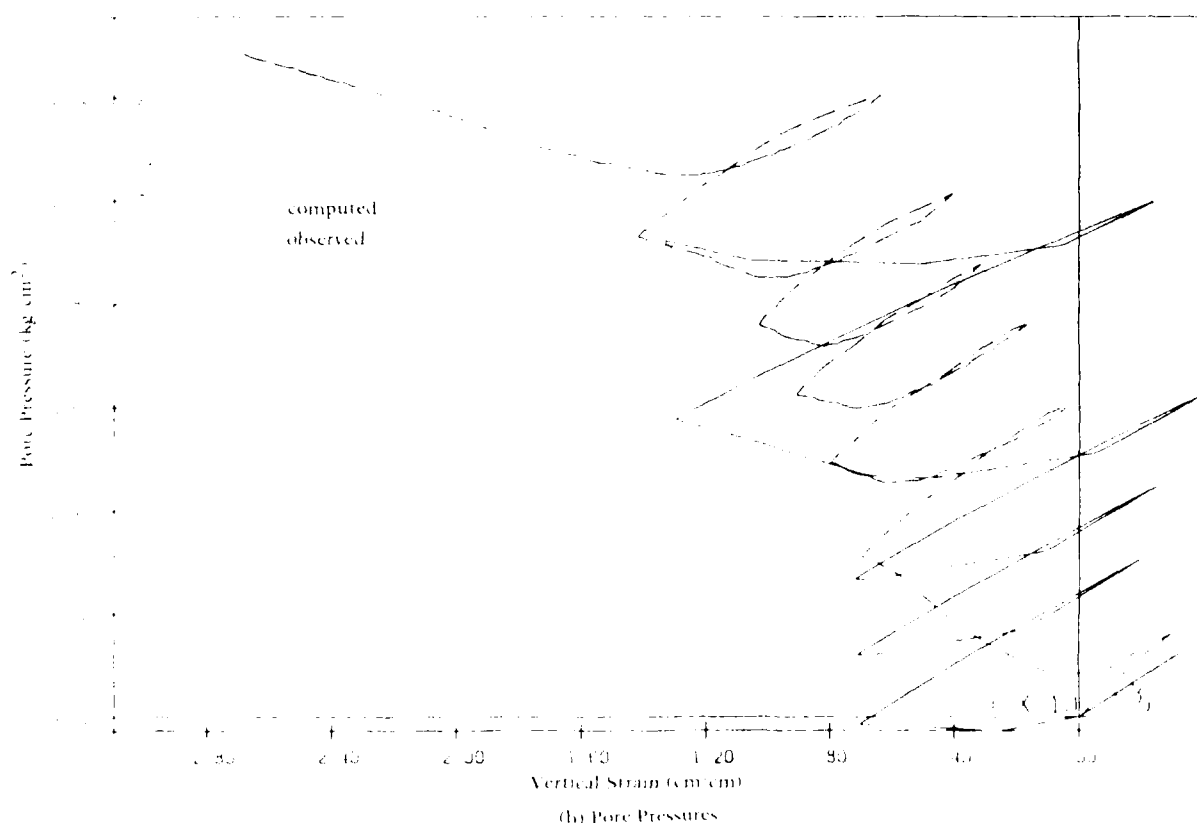
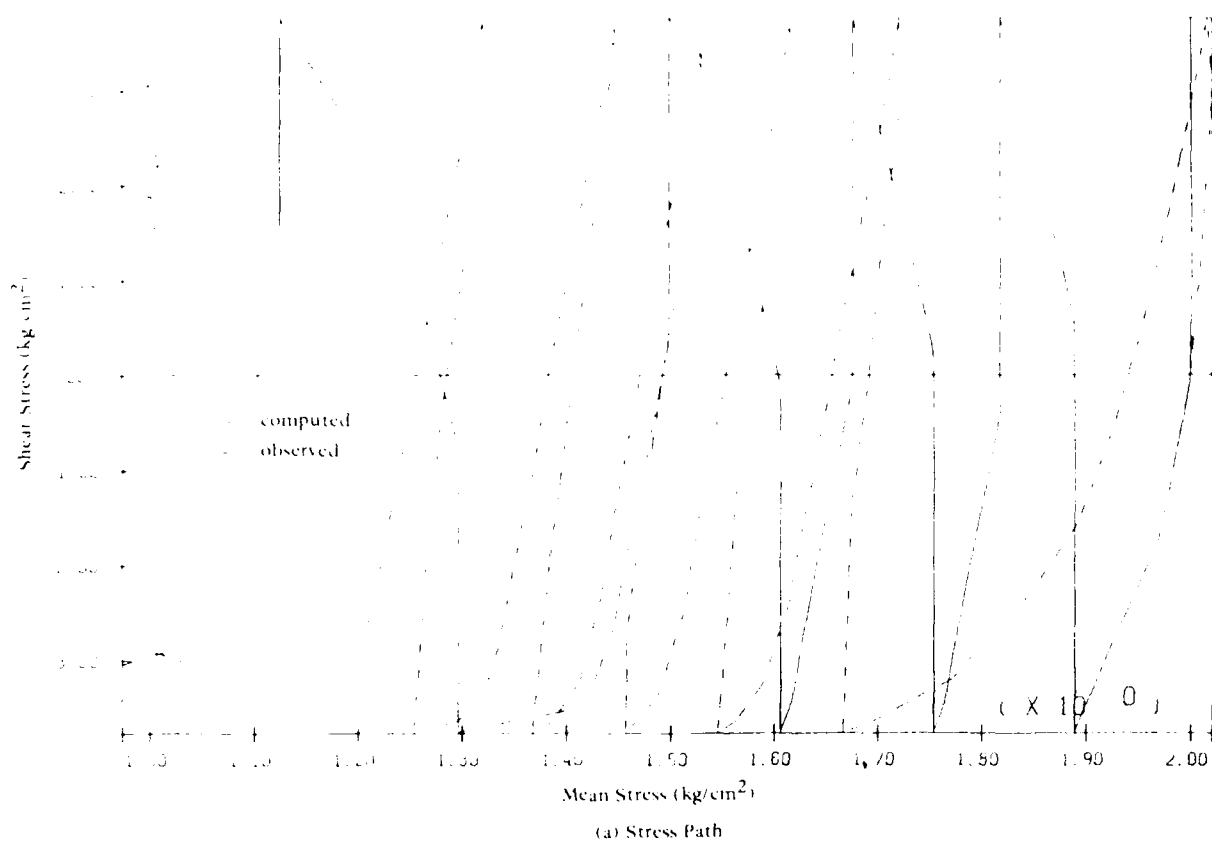


Figure 16. Undrained cyclic analysis silica sand, confining cell pressure =  $2.0 \text{ kg/cm}^2$ , shear stress-vertical strain.

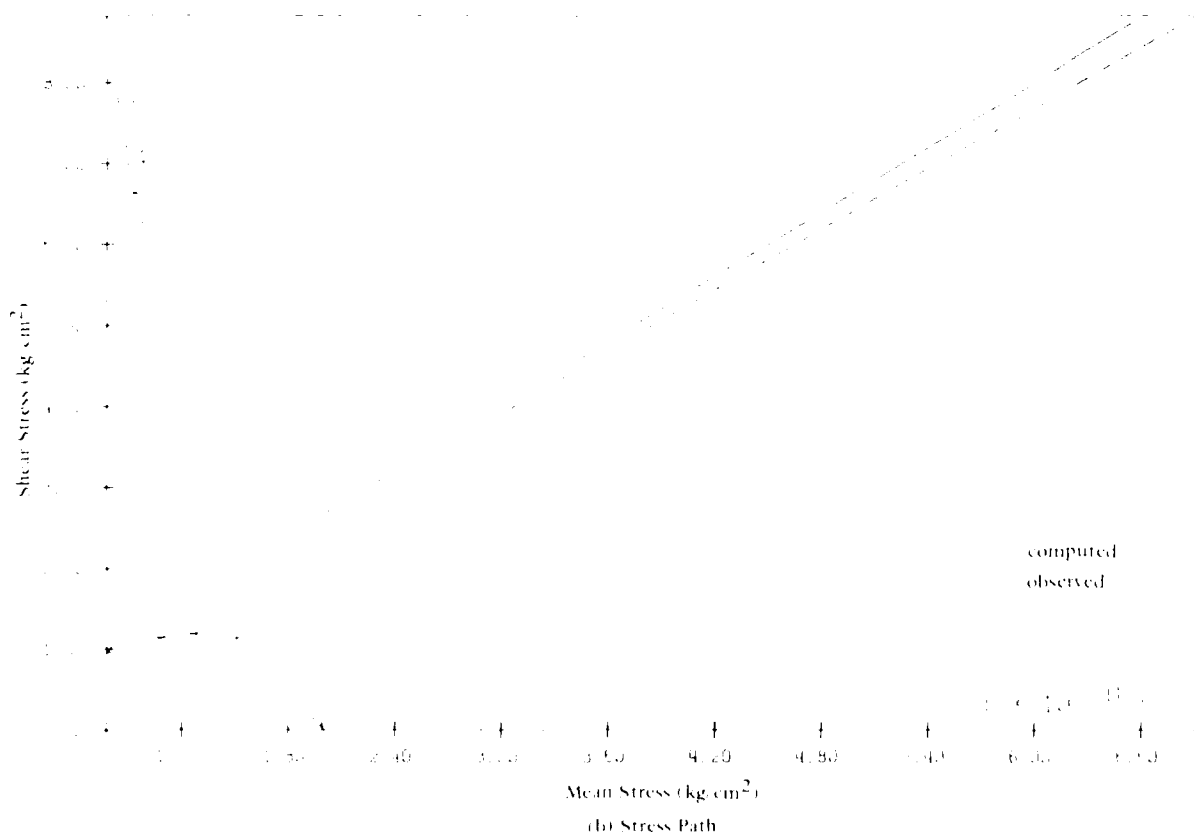
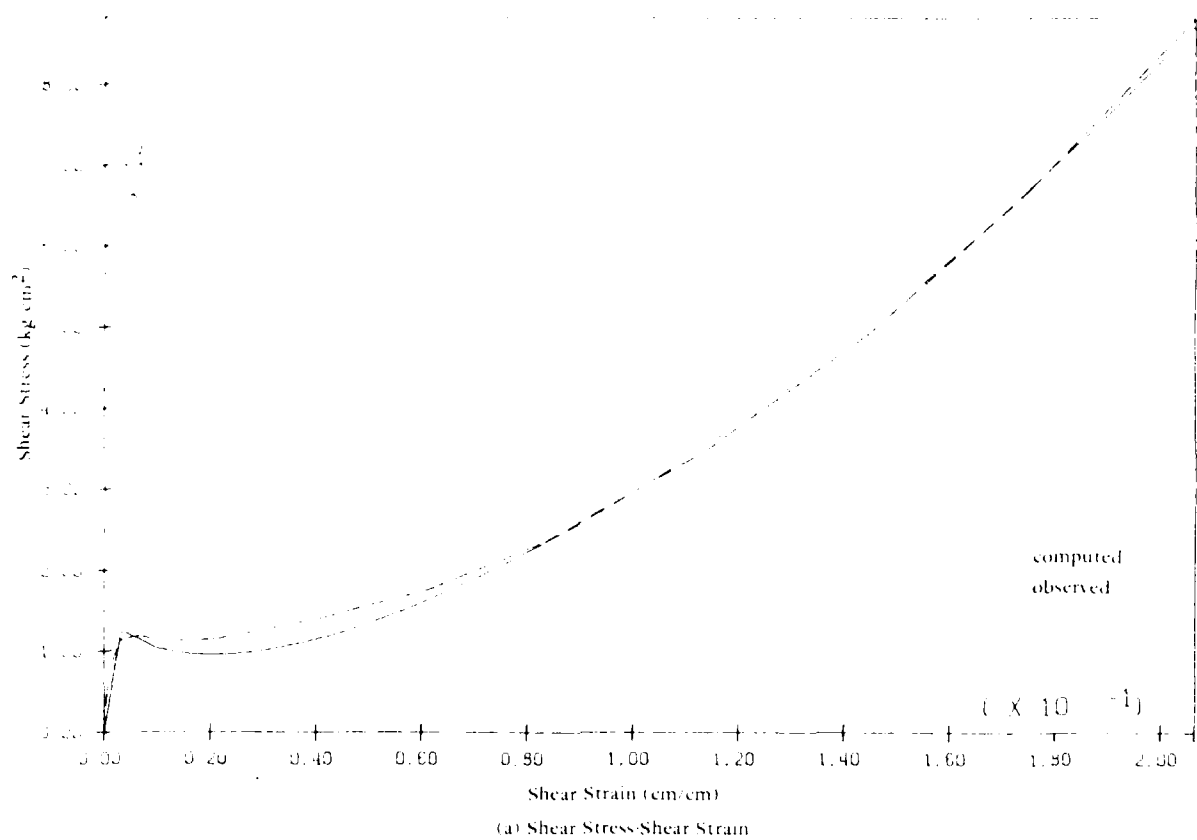


Figure 17. Undrained cyclic analysis, silica sand, confining cell pressure = 2.0kg/cm<sup>2</sup>, stress path and pore pressure.

### Miesers Bluff Sand

The Miesers Bluff sand was tested at the Waterways Experiment Station Geotechnical Laboratory. Figures 18(a) and 18(b) show the drained test data used to generate the model and the computed results. Figures 19(a), 19(b), and 20 present the model's ability to predict the drained response of the material over a range of confining pressures from 0.14 MPA to 6.9 MPA based upon the model parameters determined at 3.45 MPA. Again agreement is very good across the entire range of the drained analysis. Unfortunately, many of the reference curves lack definition, because the test data used for this series had to be digitized from hard copy plots.

Figures 21(a) and 21(b) present an undrained simulation run at a confining stress of 3.45 MPA. Note that the trends of this particular sand are well modeled with reasonable accuracy, but due again to the coarseness of the digitizing process, both the test data and, therefore, model predictions of stress strain behavior may be somewhat in error. Figures 22(a) and 22(b) present the results of an additional undrained test run at 1.72 MPA. Again, note the agreement between the predicted and observed behavior.

Figures 23 and 24 represent an undrained cyclic triaxial simulation of the Miesers Bluff sand. Cyclic test data were not available for this analysis but the simulation was included for completeness.

### SENSITIVITY OF PARAMETERS

#### Critical Stress Ratio

The critical stress ratio (CSR) is the parameter in extension or compression which determines the stress state at which there is a change between compactive and dilative volume strains. Adjustment of this parameter has little effect on the shear stress-strain curves in the drained simulation, but does make significant changes in the amount of volume strain generated by the model. An example of varying the critical



stress ratio by  $\pm 6\%$  is presented for a drained test using the silica sand model (Figures 25(a) and 25(b)).

Figures 26(a) and 26(b) present the results of the same modification in the critical stress ratio during an undrained simulation. Note the significant changes in strength caused by the 10% increase in critical stress ratio leading to a prediction of near total loss of strength. Decreasing the value of the stress ratio by 6% more than doubles the amount of shear strength developed. Figure 26(b) presents the stress paths associated with each of the modifications. Note that each of the models follows essentially the same path up to the point of contacting the critical state line. At this point, if the sample has not begun to dilate, it then loses strength by moving toward zero effective stress.

#### Elastic Moduli

Figures 27(a) and 27(b) demonstrate the effects of varying the elastic moduli for all surfaces in the drained material model by  $\pm 25\%$ . The effects on the shear stress-strain curves are minimal; however, there is a more significant change in the degree of compactive volume strain generated. Note as well, the changes in volume strain are not equivalent for both cases. This is caused by an increase in plasticity associated with the decreased elastic stiffness necessary to reach the same load level. The increased elastic stiffness in turn, allows the given load to be reached at a smaller strain level, but does not decrease the plastic strain to the same degree. Figures 28(a) and 28(b) present the effects of the same variation on the undrained simulation.

#### Plastic Moduli

Varying the plastic moduli for all surfaces has significant effects on both the drained and undrained simulations (Figures 29 and 30). A greater change appears as a result of increasing the plastic moduli for each yield surface than by decreasing it. The effect is two-fold in

that it not only increases the overall stiffness of the system in the drained simulation (Figure 29(a)), but decreases the overall compactive volumetric strain as well (Figure 29(b)). These factors both contribute to the greatly enhanced stiffness in the undrained simulation (Figure 30(a)) by improving the skeletal response while at the same time decreasing the excess pore water pressure generation.

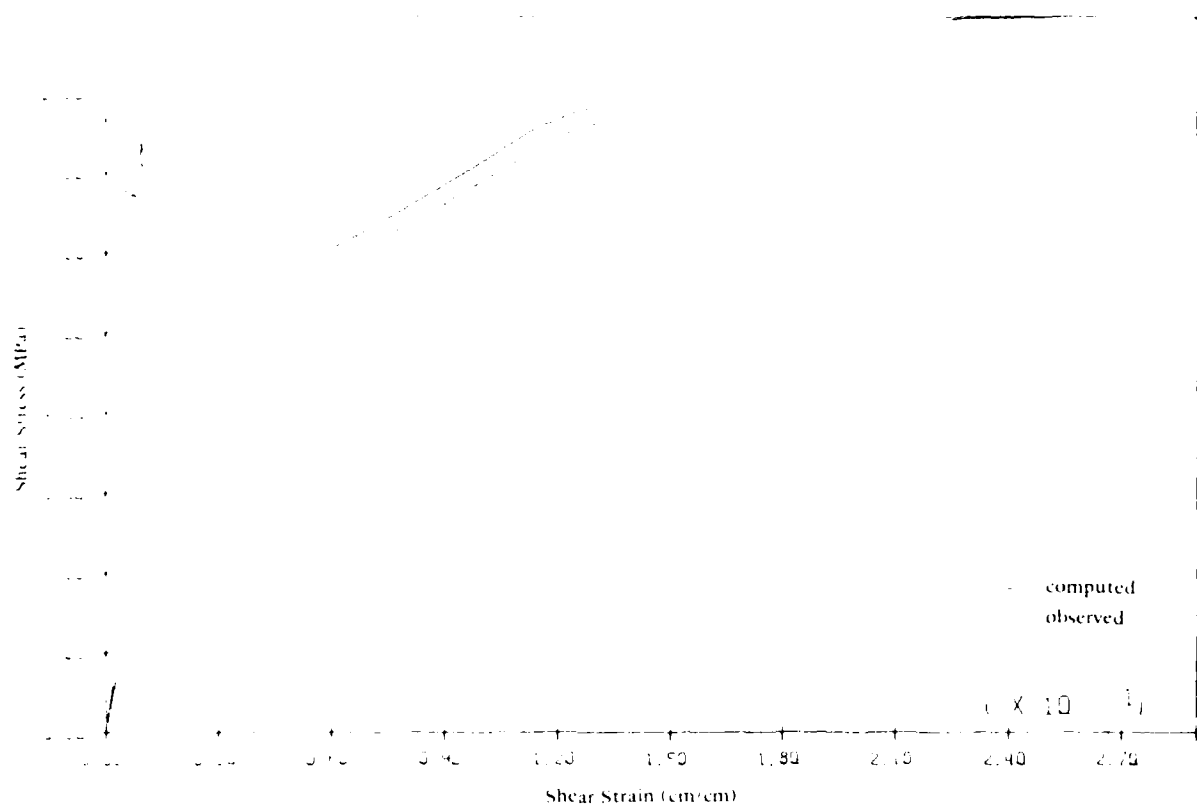
Reducing the plastic moduli has less effect in both drained and undrained simulations causing a slightly larger amount of compaction before dilation begins. This produces a moderately softer system in both the drained and undrained environments.

#### Yield Surface Size

Changing the yield surface size changes the shear strength values which may be achieved at a particular strain level. Figures 31 and 32 clearly demonstrate this property of the model.

In the drained analysis (Figures 31(a) and 31(b)), increasing the yield surface size decreases the shear strain at a particular level of shear stress, and reduces volumetric strains not by a change in moduli values, but rather as a result of changing the position of compactive-dilative interchange in relation to the original critical surface position. Reducing the yield surface size results in the reaching of the various surfaces earlier, at reduced stress levels, and induces greater amounts of plasticity. At the same time, the reduction also moves the compactivedilative point outside the outermost surface, allowing large compactive volumetric strains to occur (Figure 31(b)).

In the undrained simulation (Figures 32(a) and 32(b)) the two-fold effect of a stiffer skeleton and reduced volumetric strains are present. The increase in yield surface size produces a stiffer system with a reduction in positive pore water pressure generation before dilation begins. The reduction in size causes an early generation of volume strains and positive pore water pressures, coupled with a softer system resulting in the zero effective stress condition.

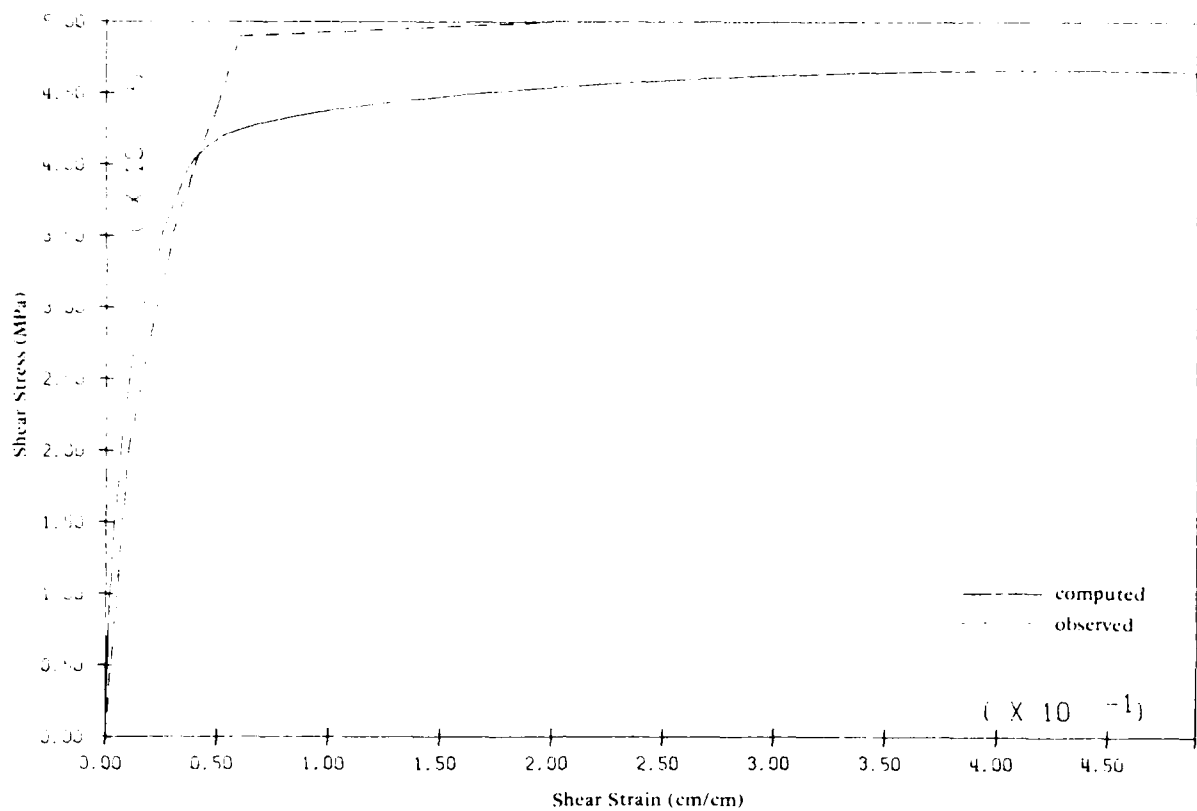


(a) Compression

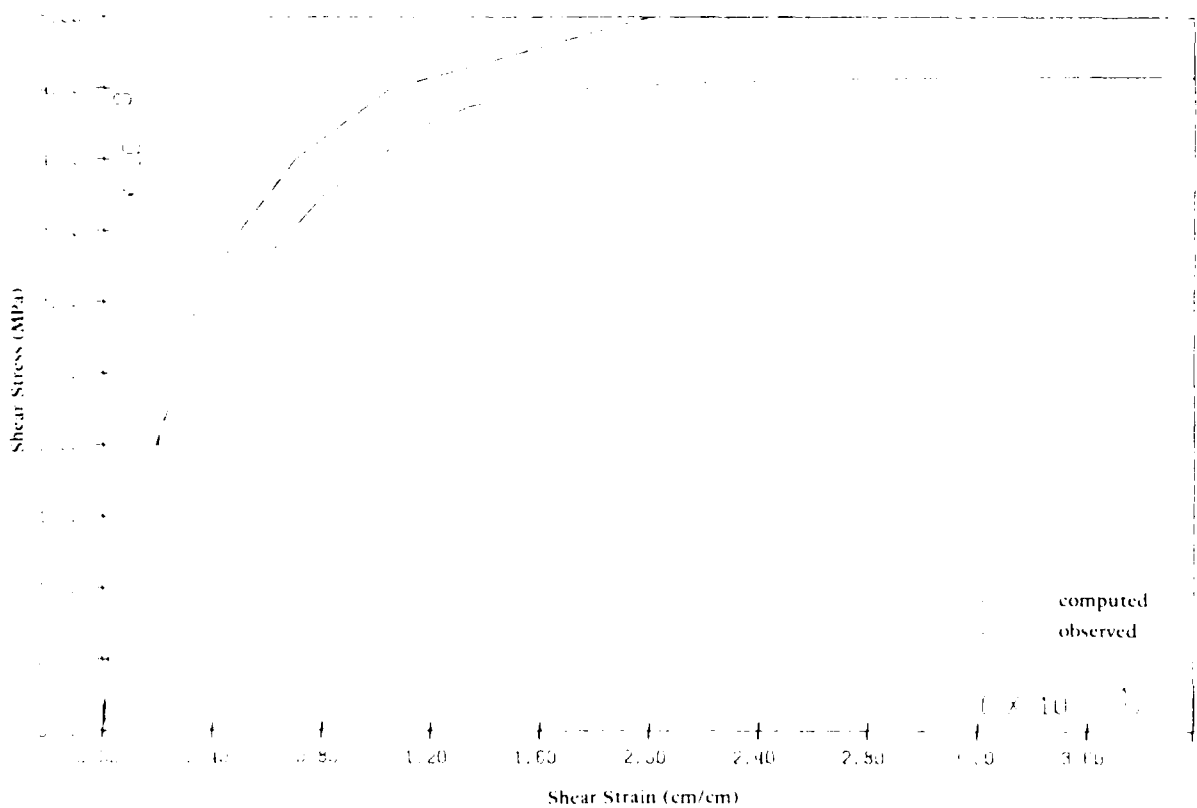


(b) Extension

Figure 18. Drained compression and extension Mieser-Bluff sand, confining cell pressure = 3.45 MPa.



(a) Shear Stress-Shear Strain (0.14 MPa)



(b) Shear Stress-Shear Strain (1.72 MPa)

Figure 19. Drained compression Mieser-Bluff sand, confining cell pressures = 0.14 and 1.72 MPa.

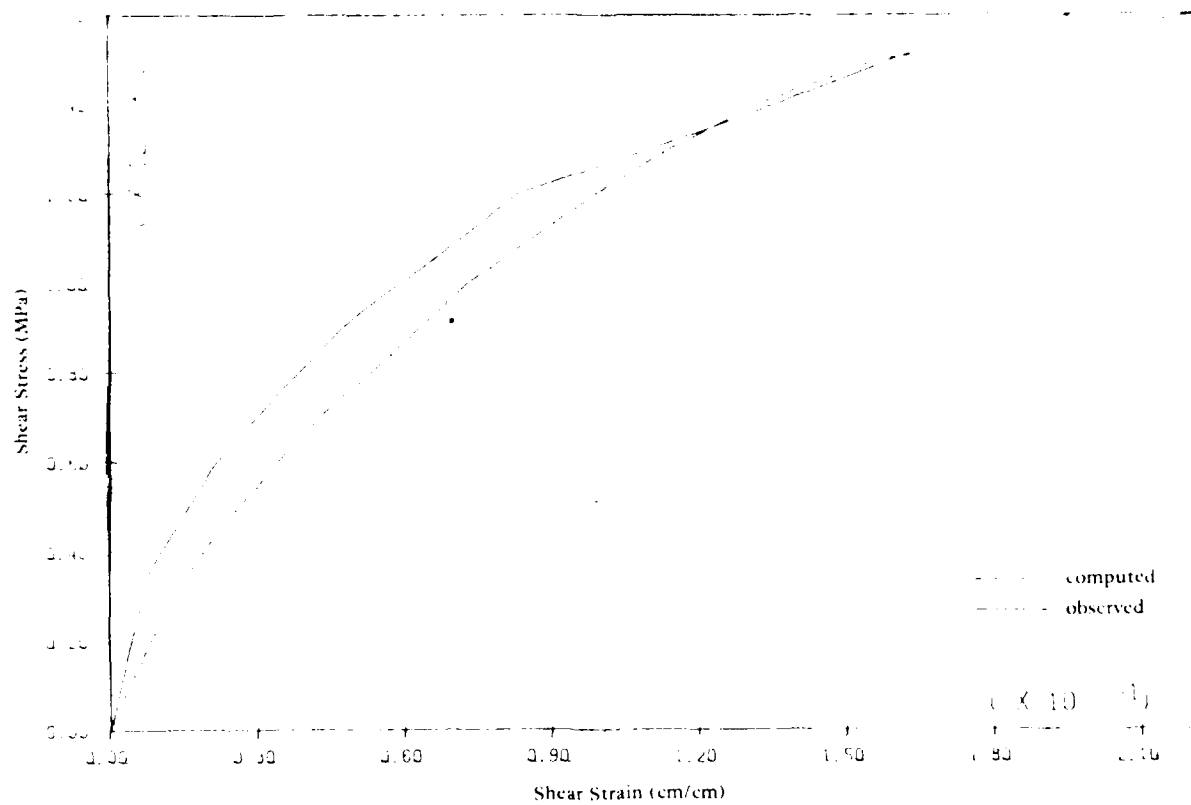
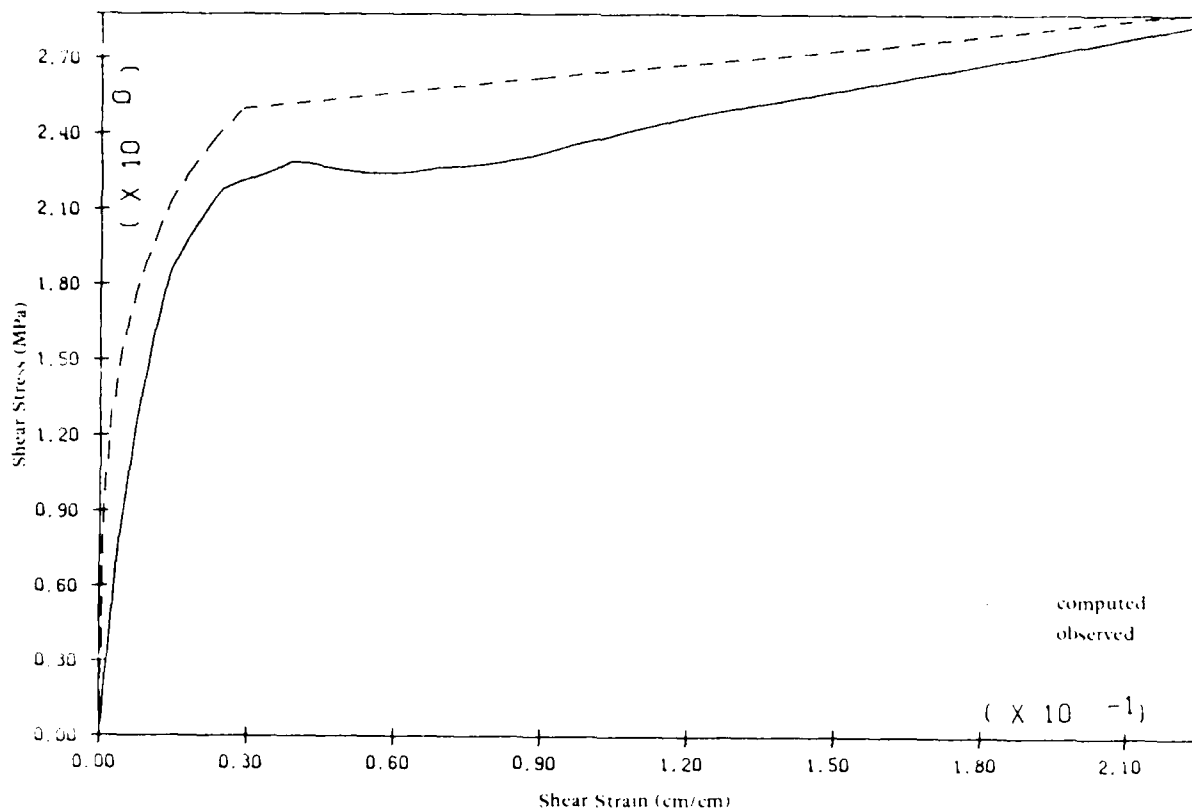
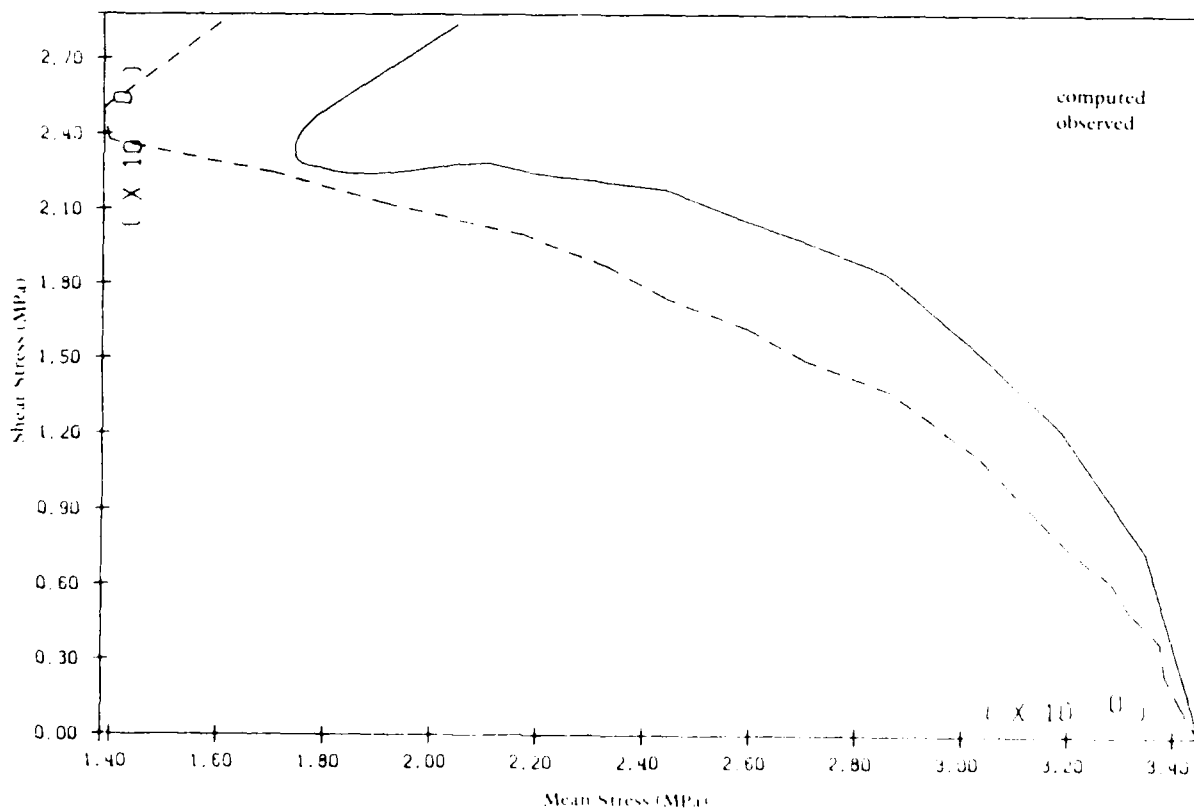


Figure 20. Drained compression Mieser-Bluff sand, confining cell pressure = 6.90 MPa.



(a) Shear Stress-Shear Strain



(b) Stress Path

Figure 21. Undrained compression Mieser-Bluff sand, confining cell pressure = 3.45 MPa.

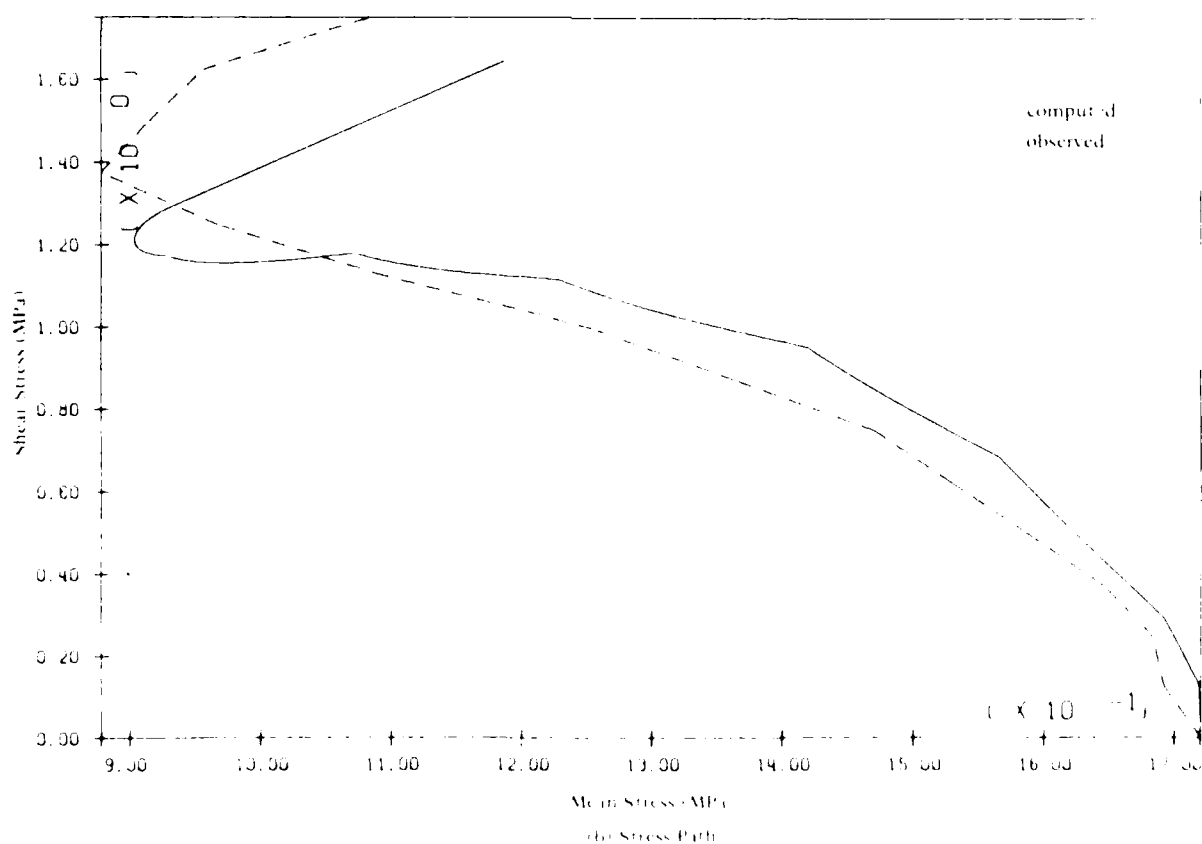
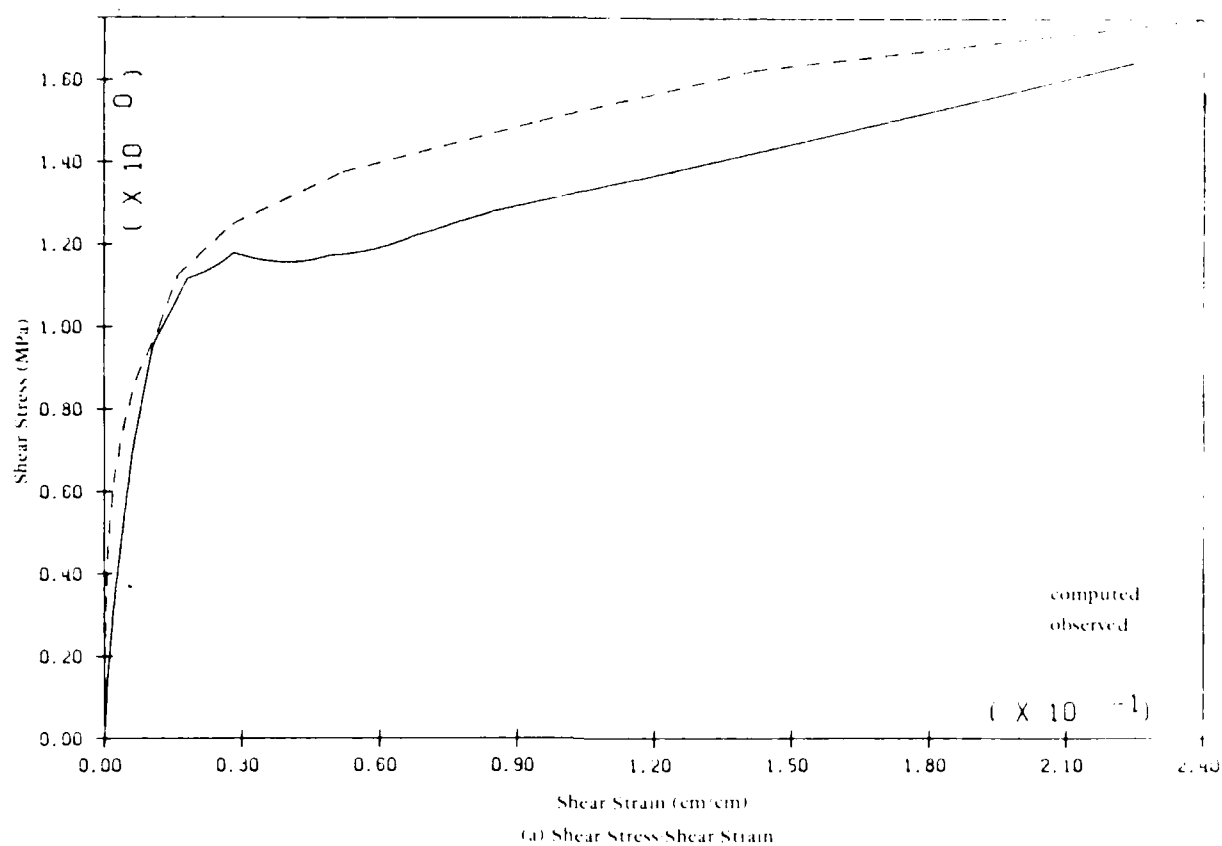


Figure 22. Undrained compression Mieser-Bluff sand, confining cell pressure = 1.72 MPa.

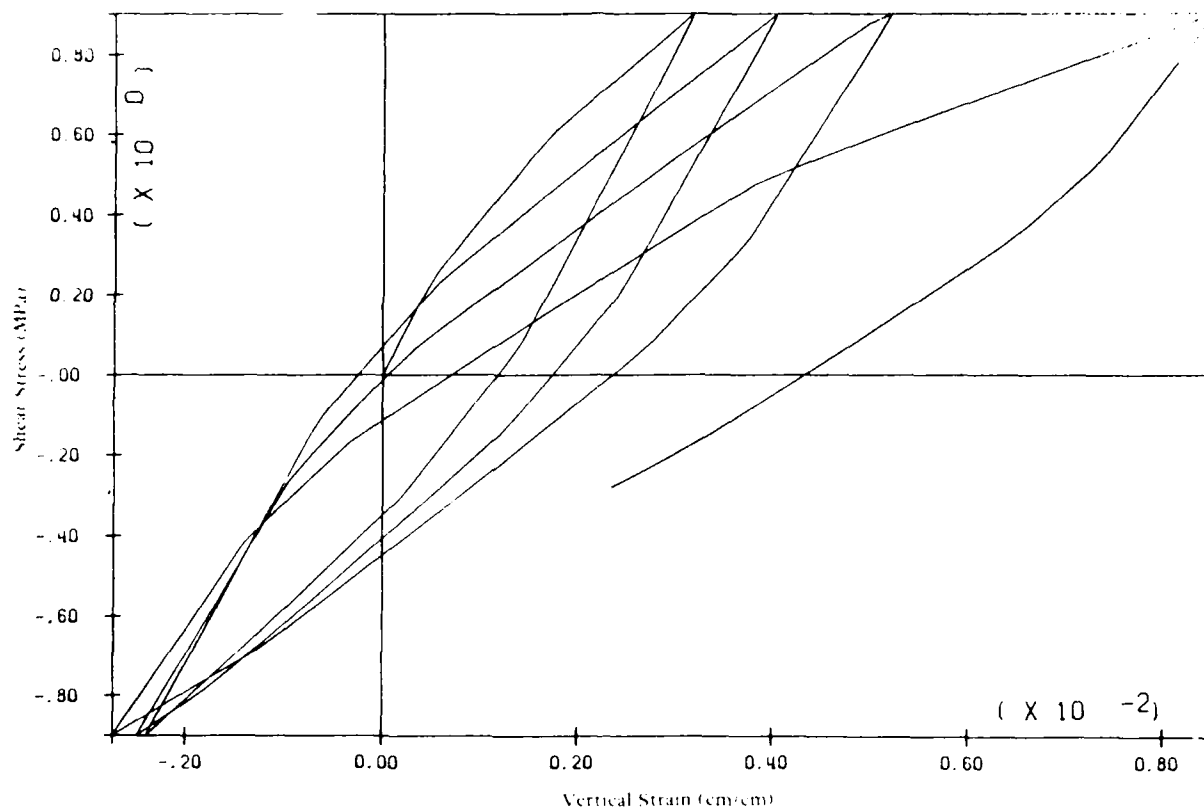


Figure 23. Undrained cyclic simulation Mieser-Bluff sand, confining cell pressure = 3.45 MPa, shear stress-shear strain.



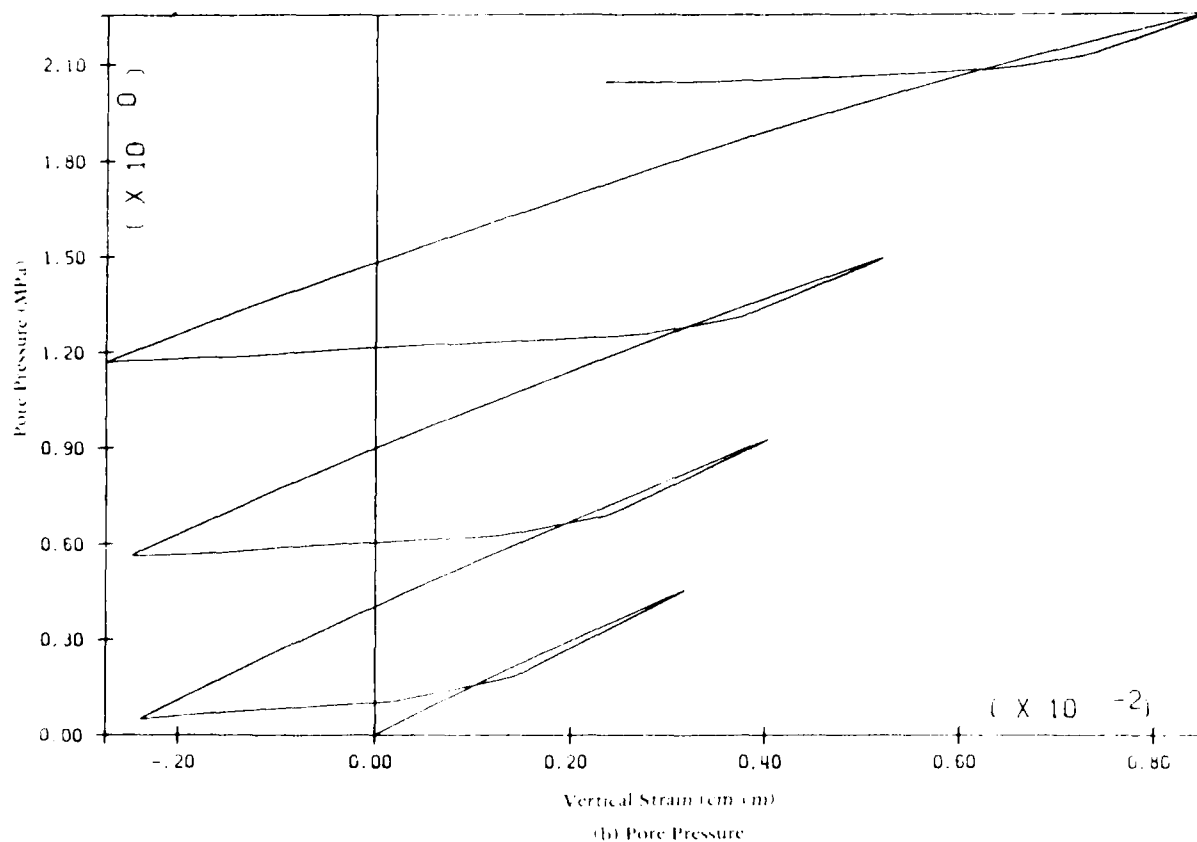
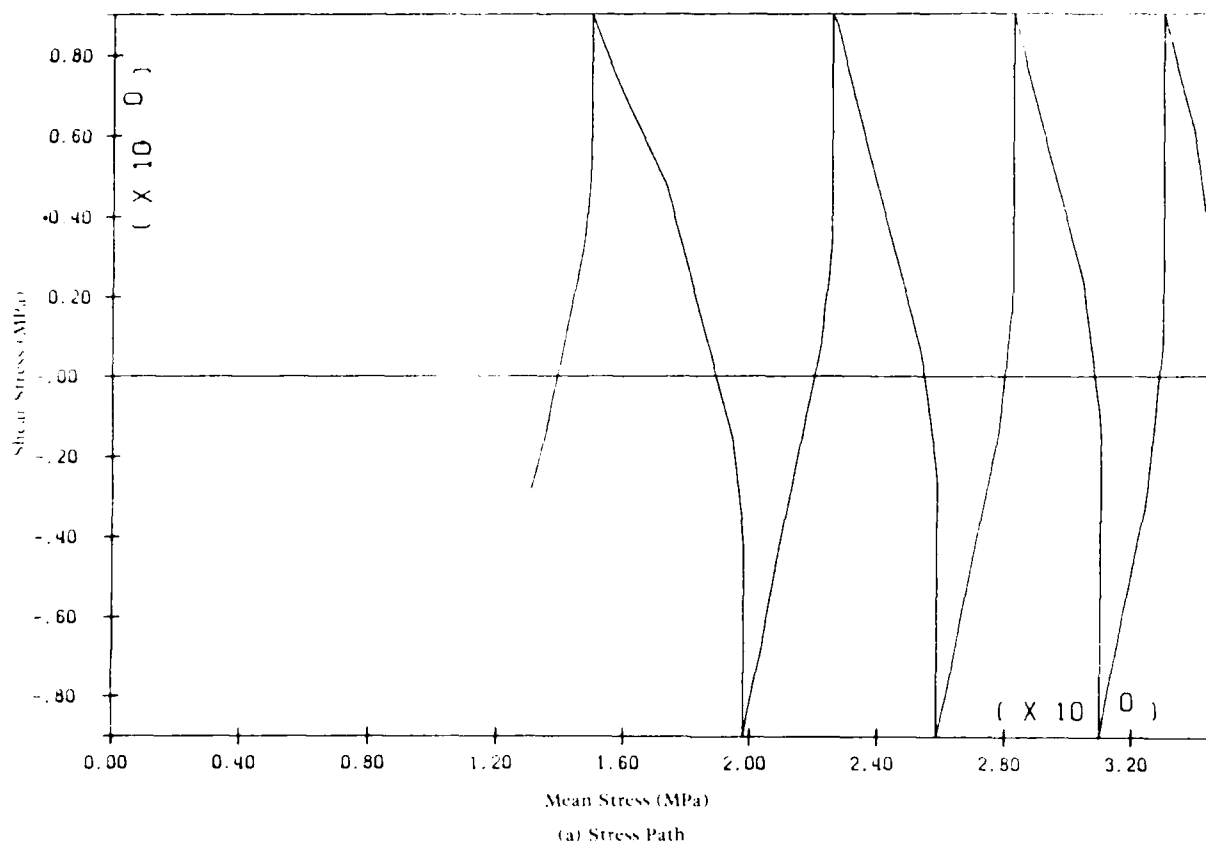
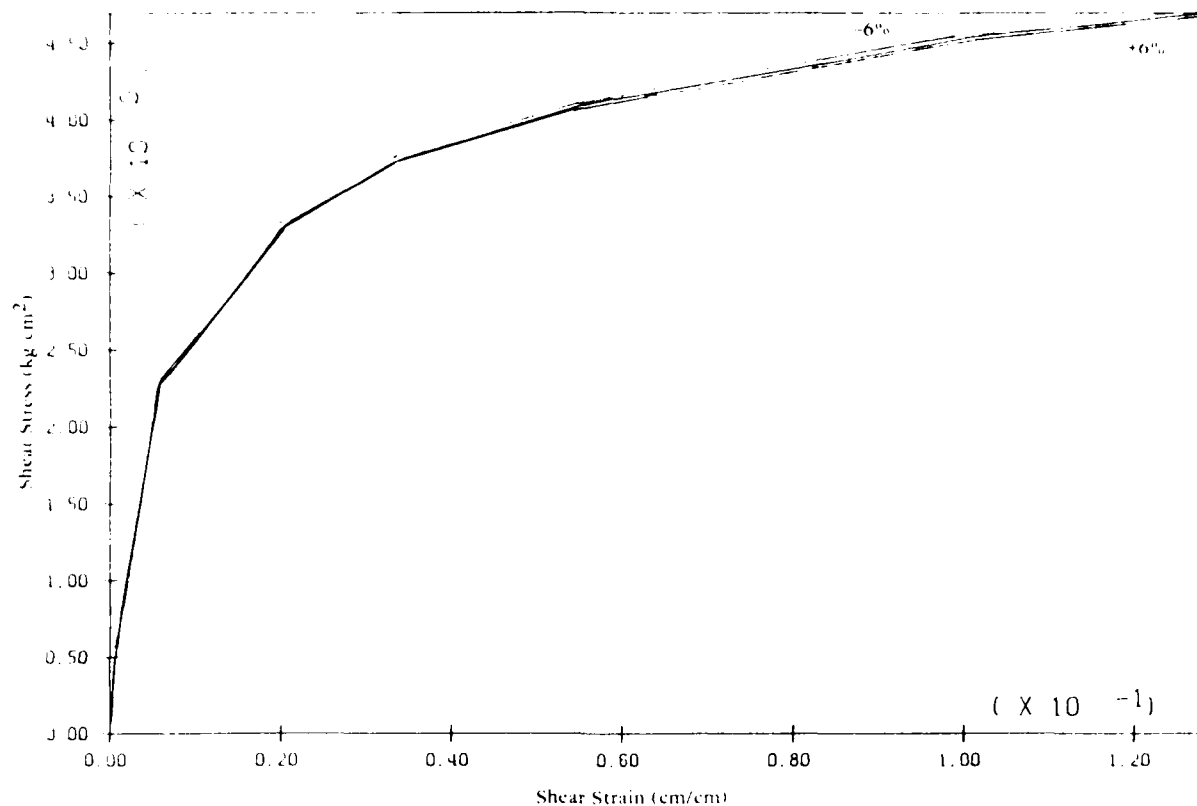
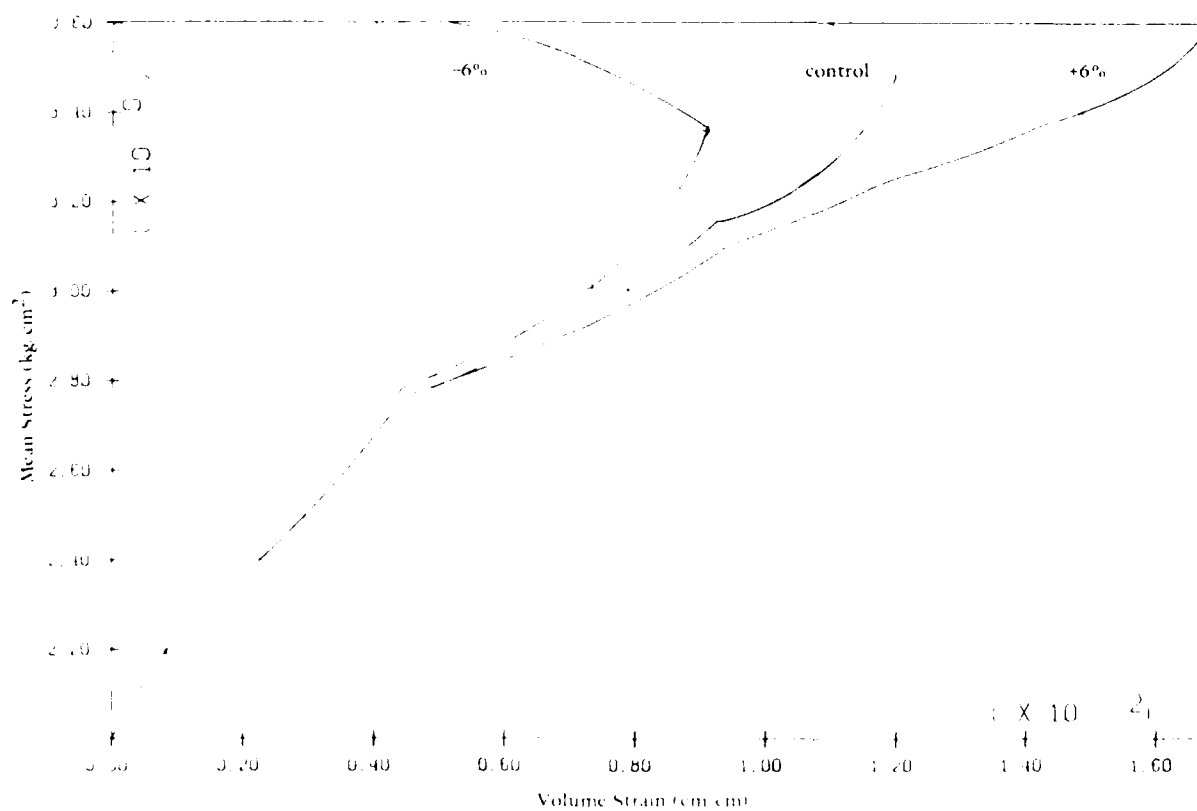


Figure 24. Undrained cyclic simulation Mieser-Bluff sand, confining cell pressure = 3.45 MPa, stress path pore pressure.



(a) Shear Stress-Shear Strain



(b) Mean Stress Volume Strain

Figure 25. Critical stress ratio variation  $\pm 6\%$  drained compression shear stress-strain, mean stress-volume strain.

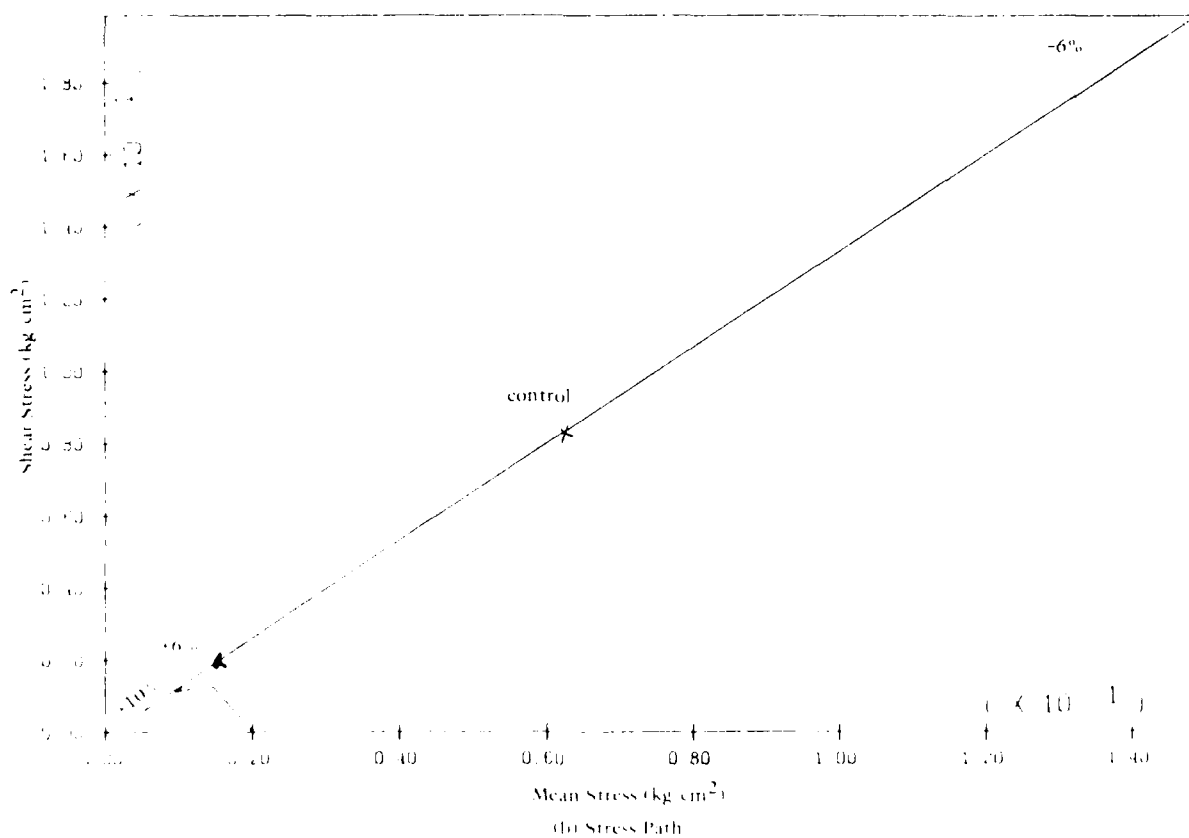
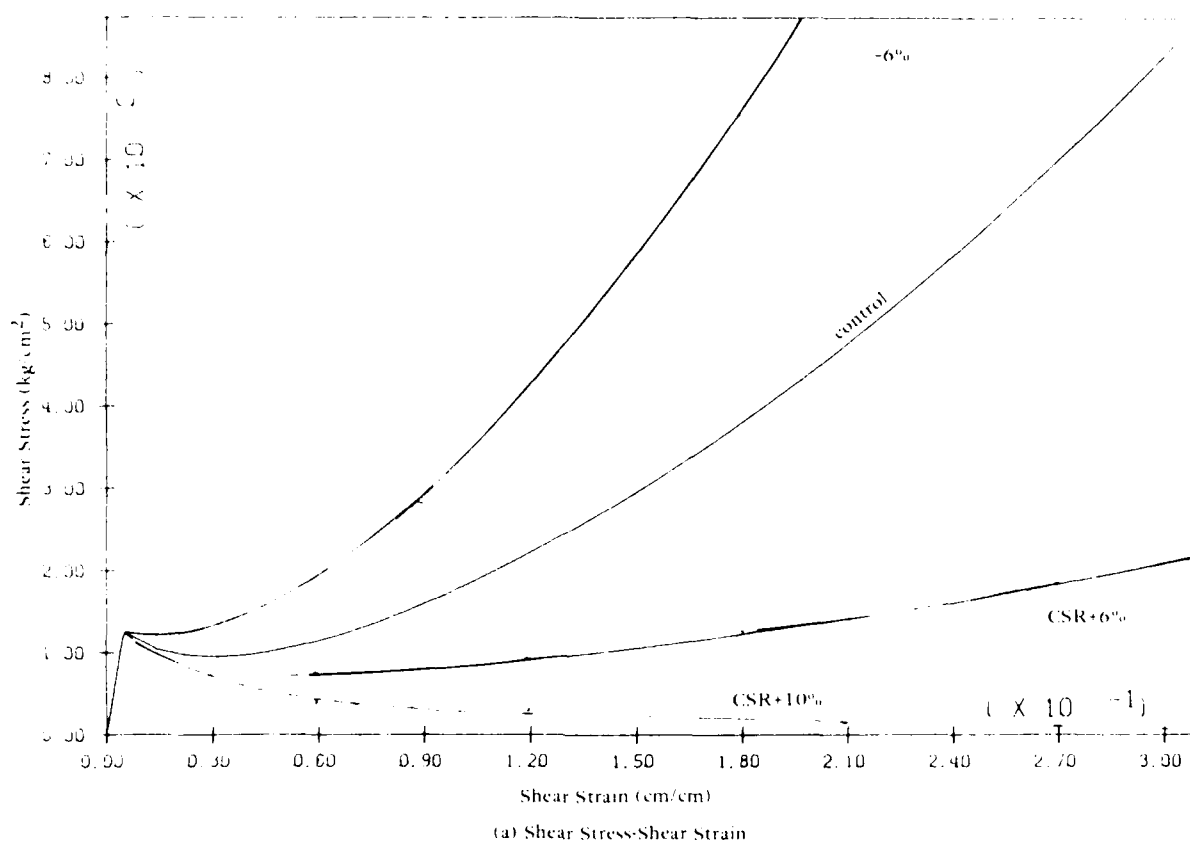
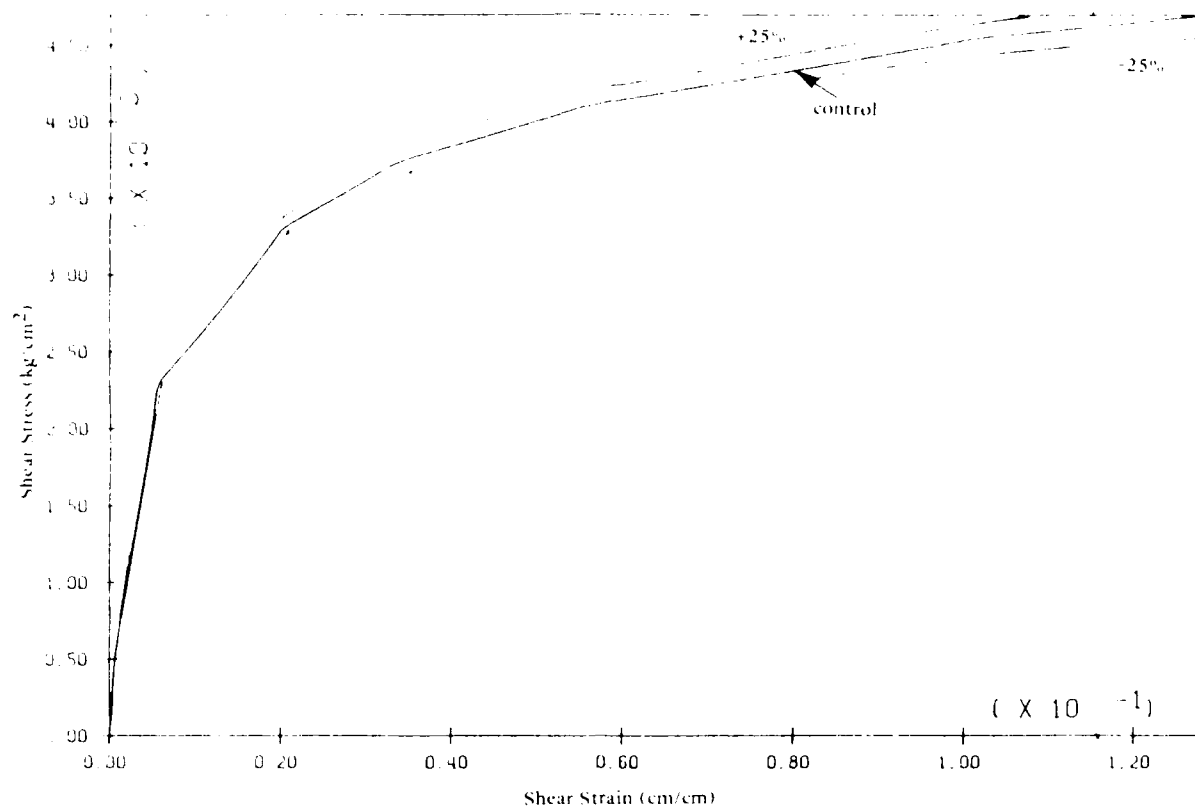
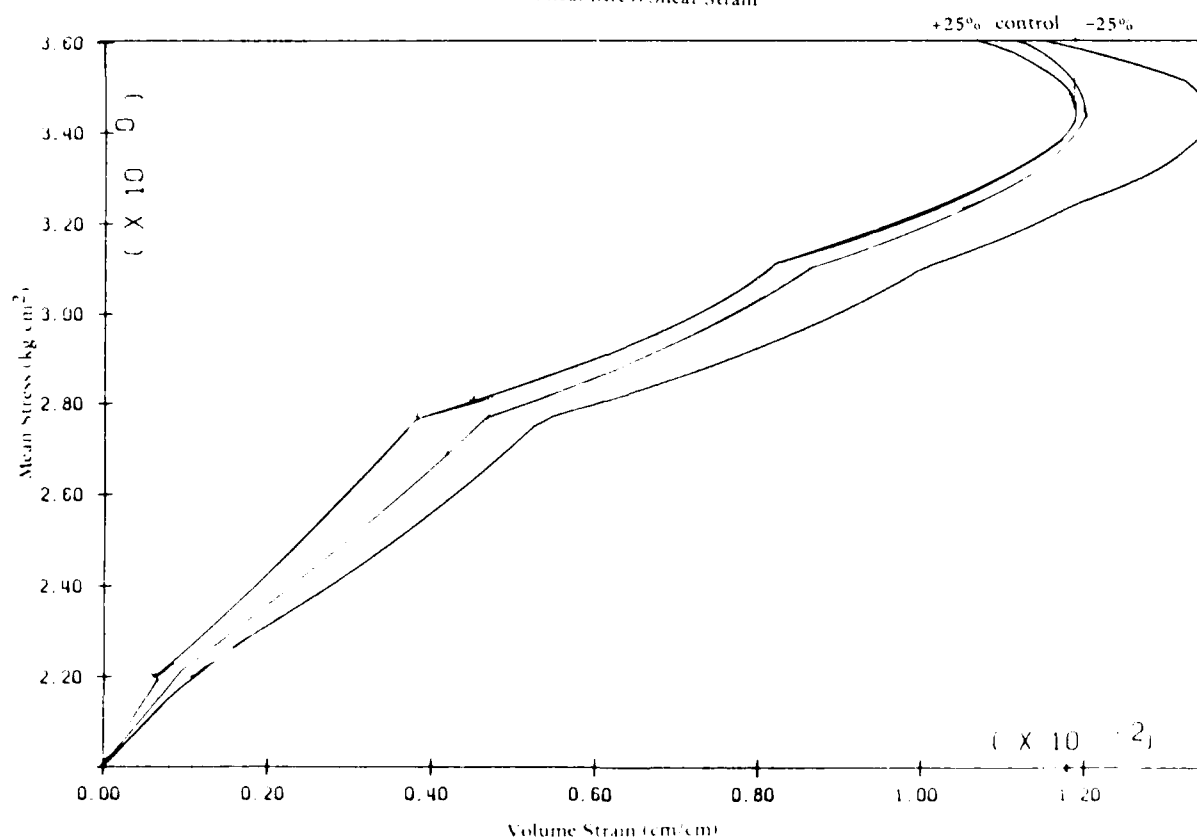


Figure 26. Critical stress ratio variation  $\pm 6\%$ ,  $+10\%$ , undrained compression shear stress-strain, stress path.



(a) Shear Stress-Shear Strain



(b) Mean Stress Volume Strain

Figure 27. Elastic moduli variation  $\pm 25\%$  drained compression shear stress-strain, mean stress-volume strain.

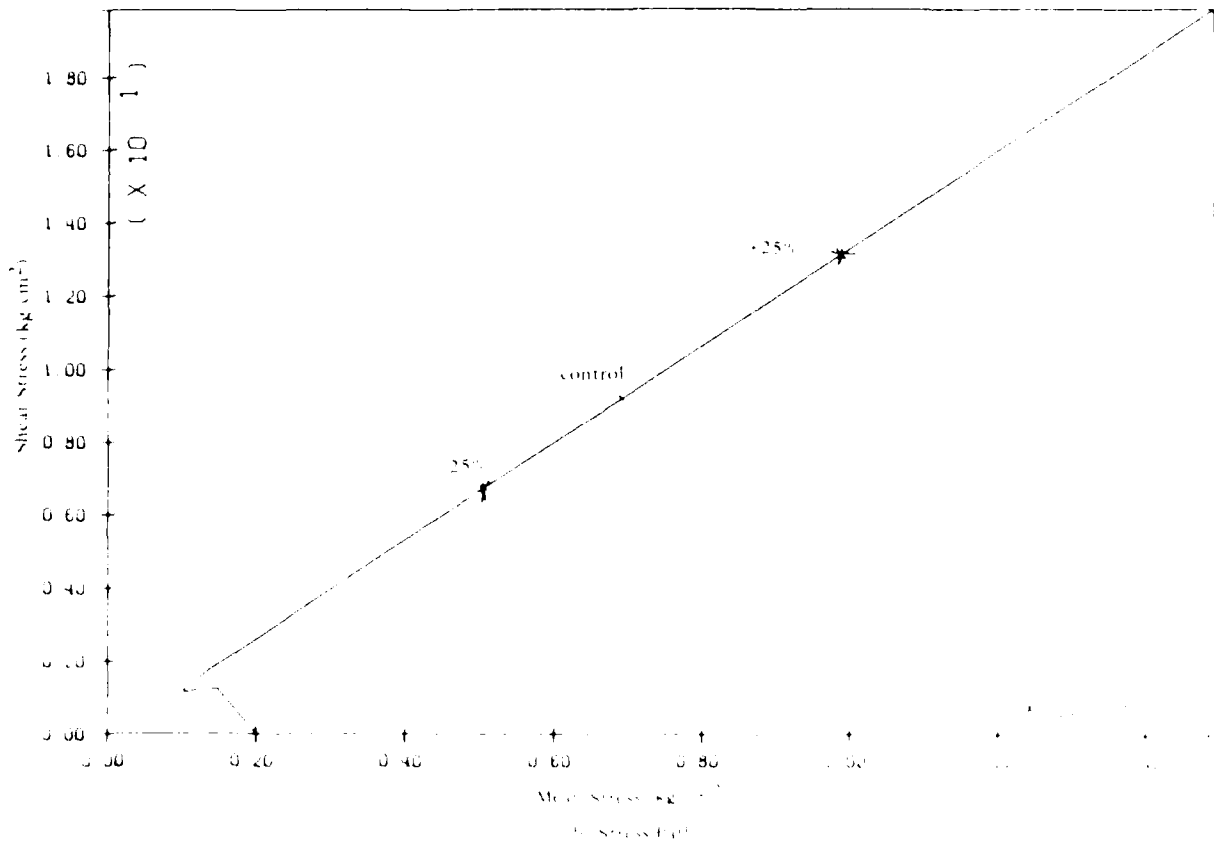
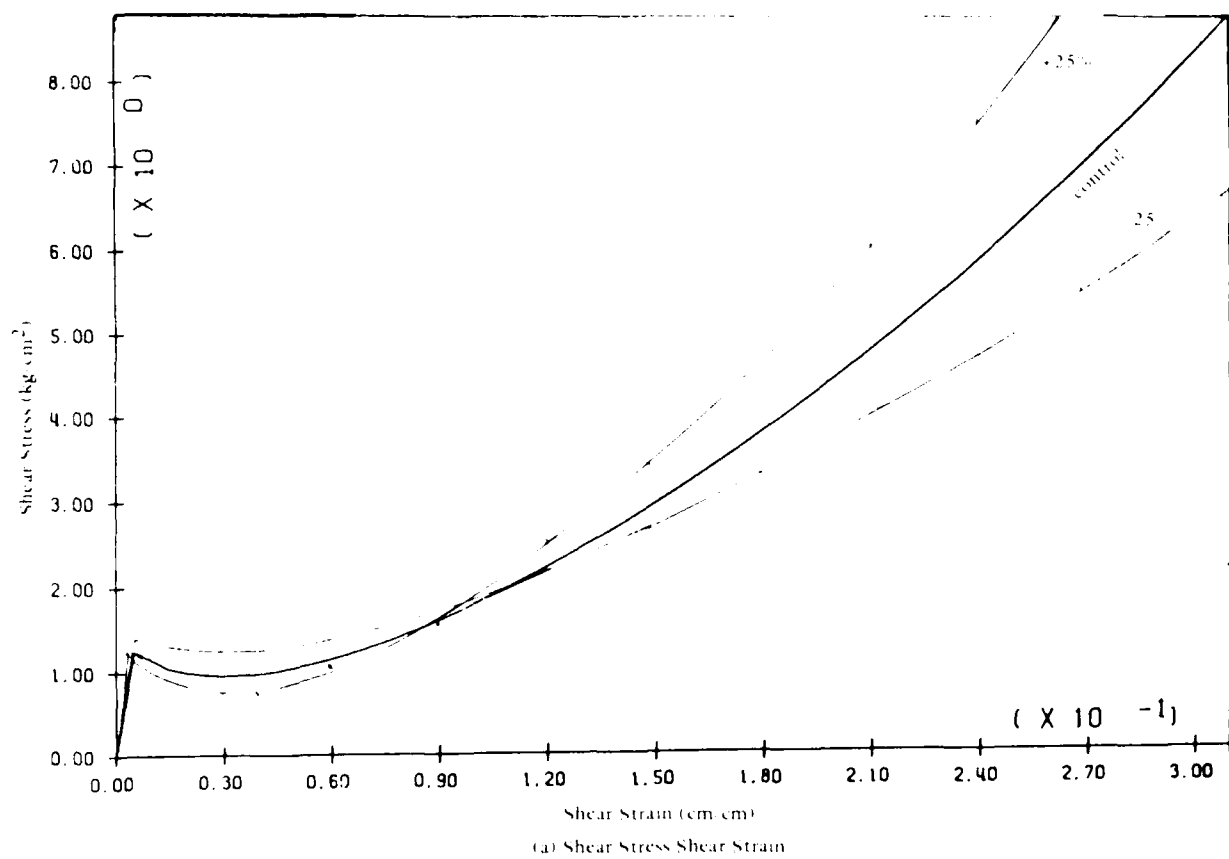


Figure 28. Elastic moduli variation  $\pm 25\%$  undrained compression shear stress-strain, stress path.

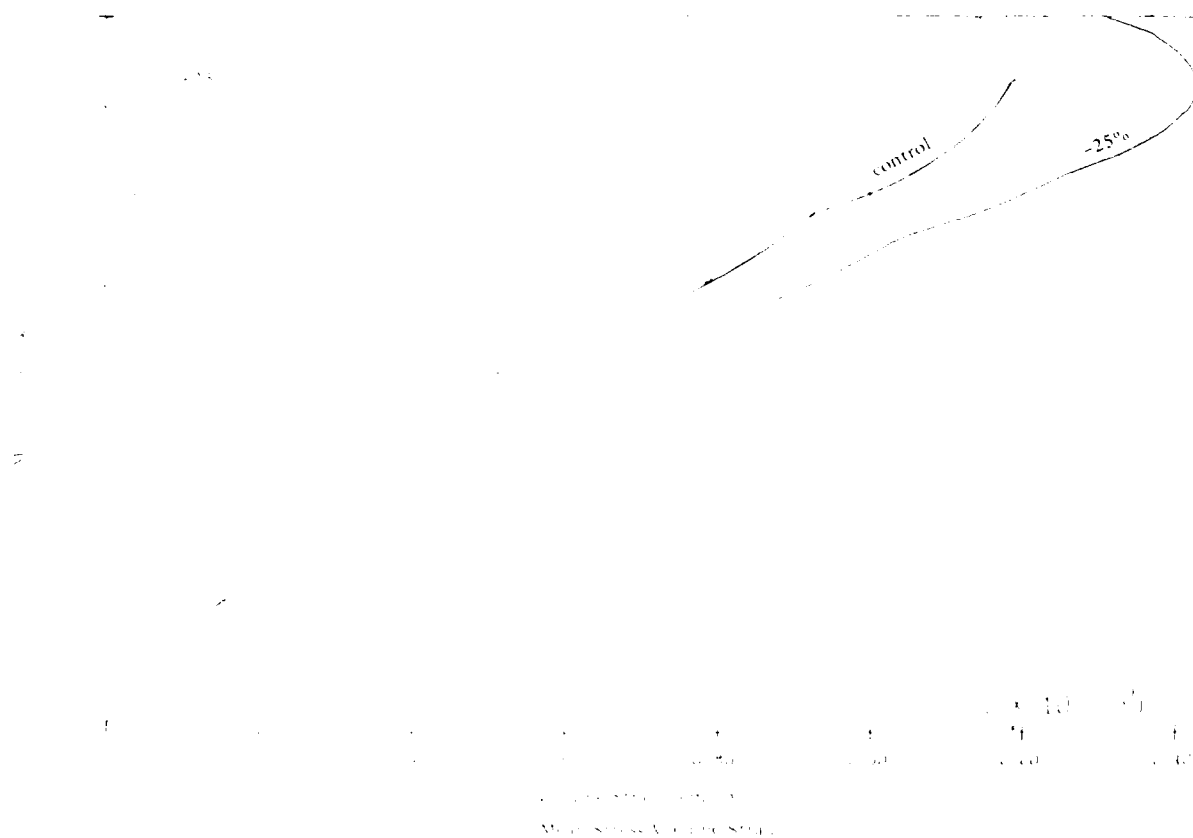
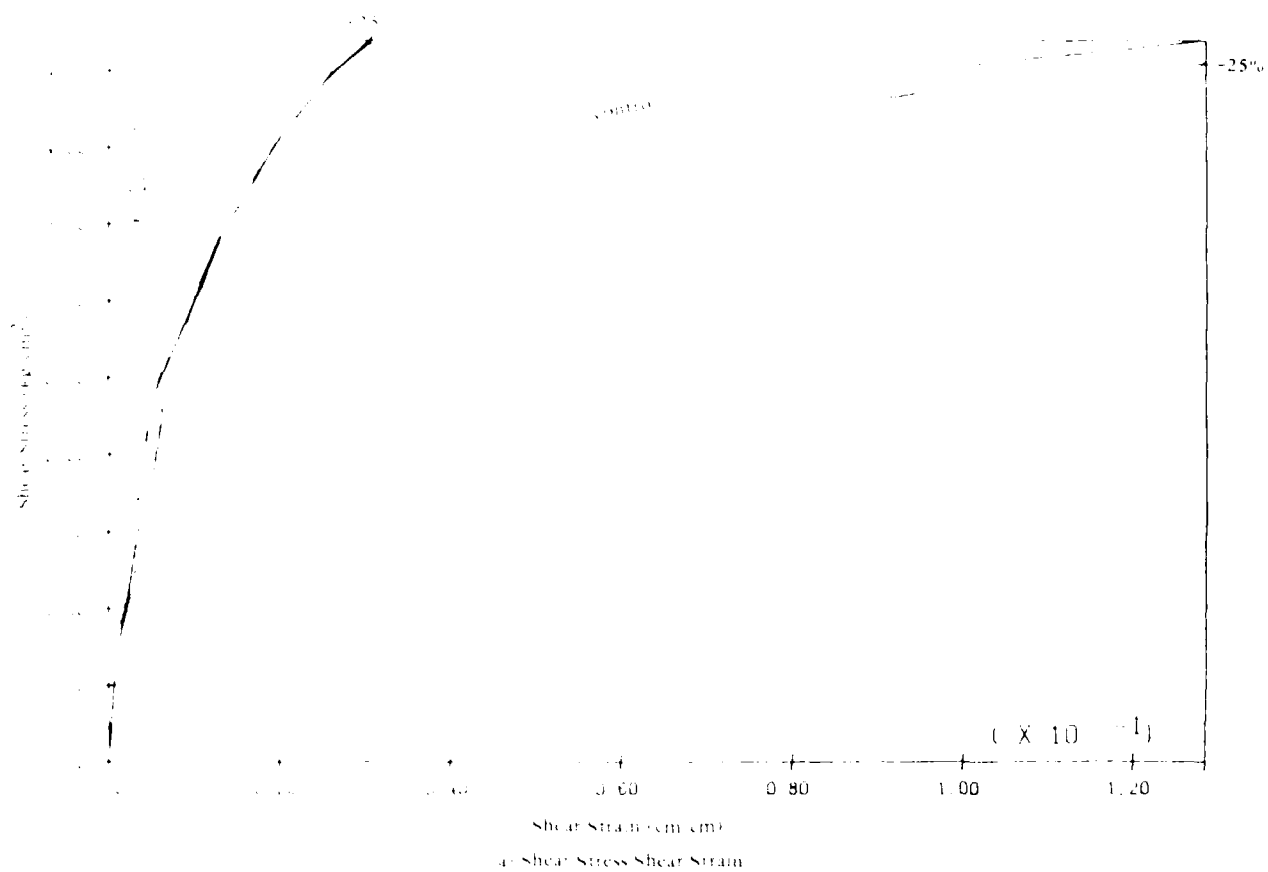


Figure 29 Plastic moduli variation  $\pm 25\%$  drained compression shear stress-strain, mean stress-volume strain.

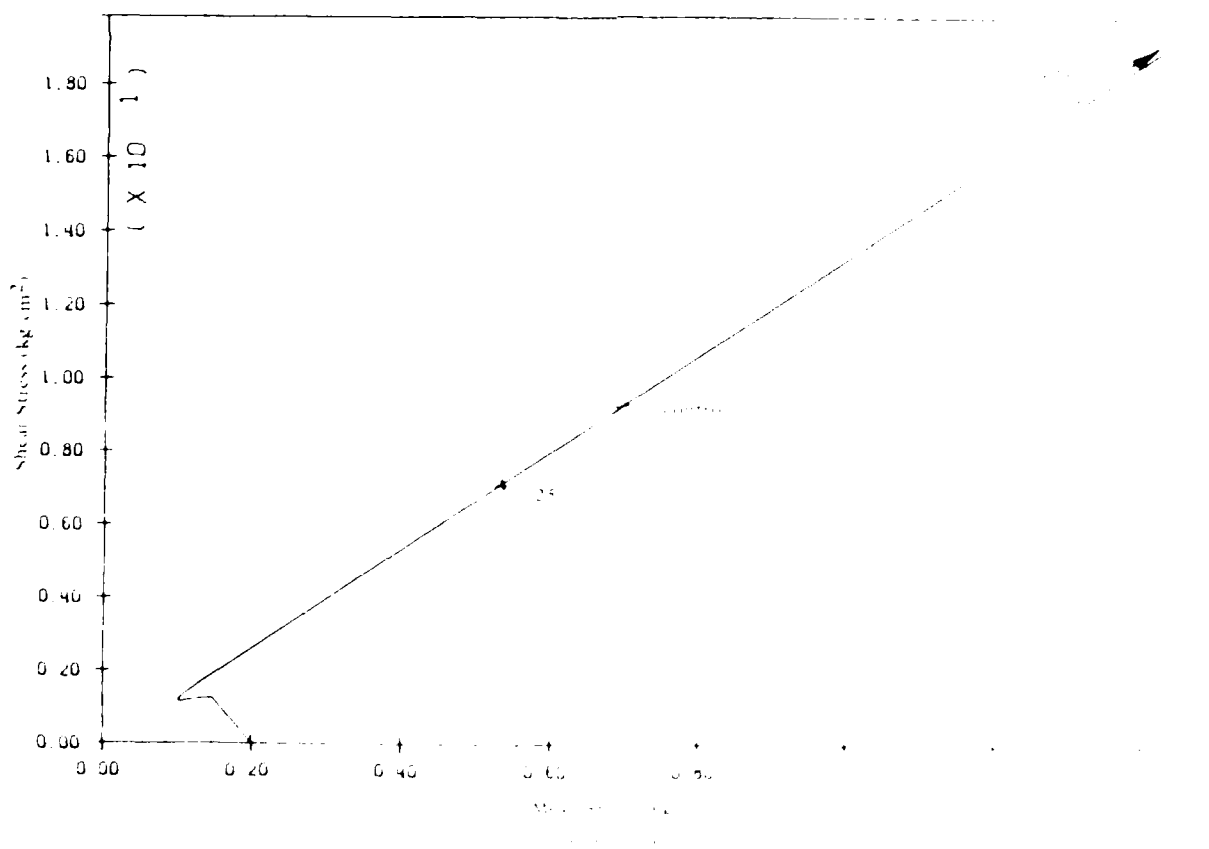
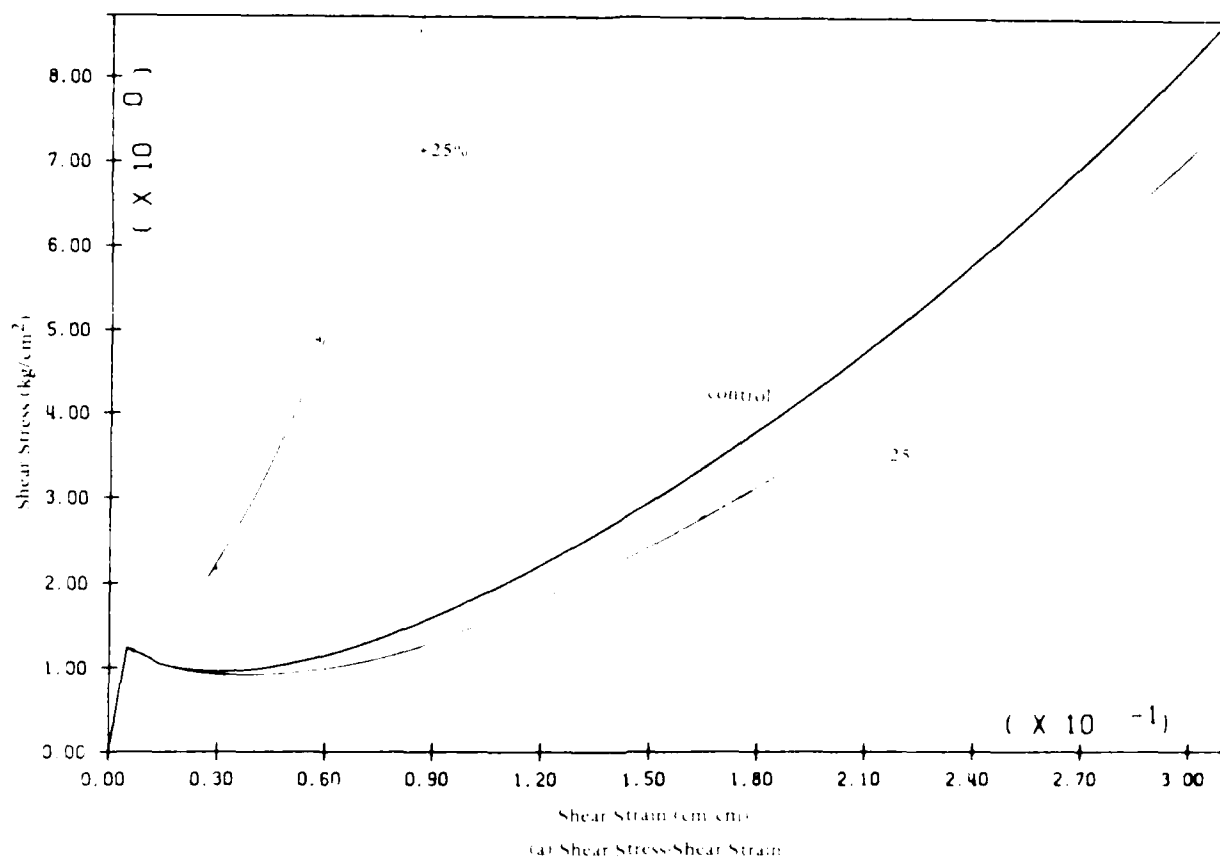
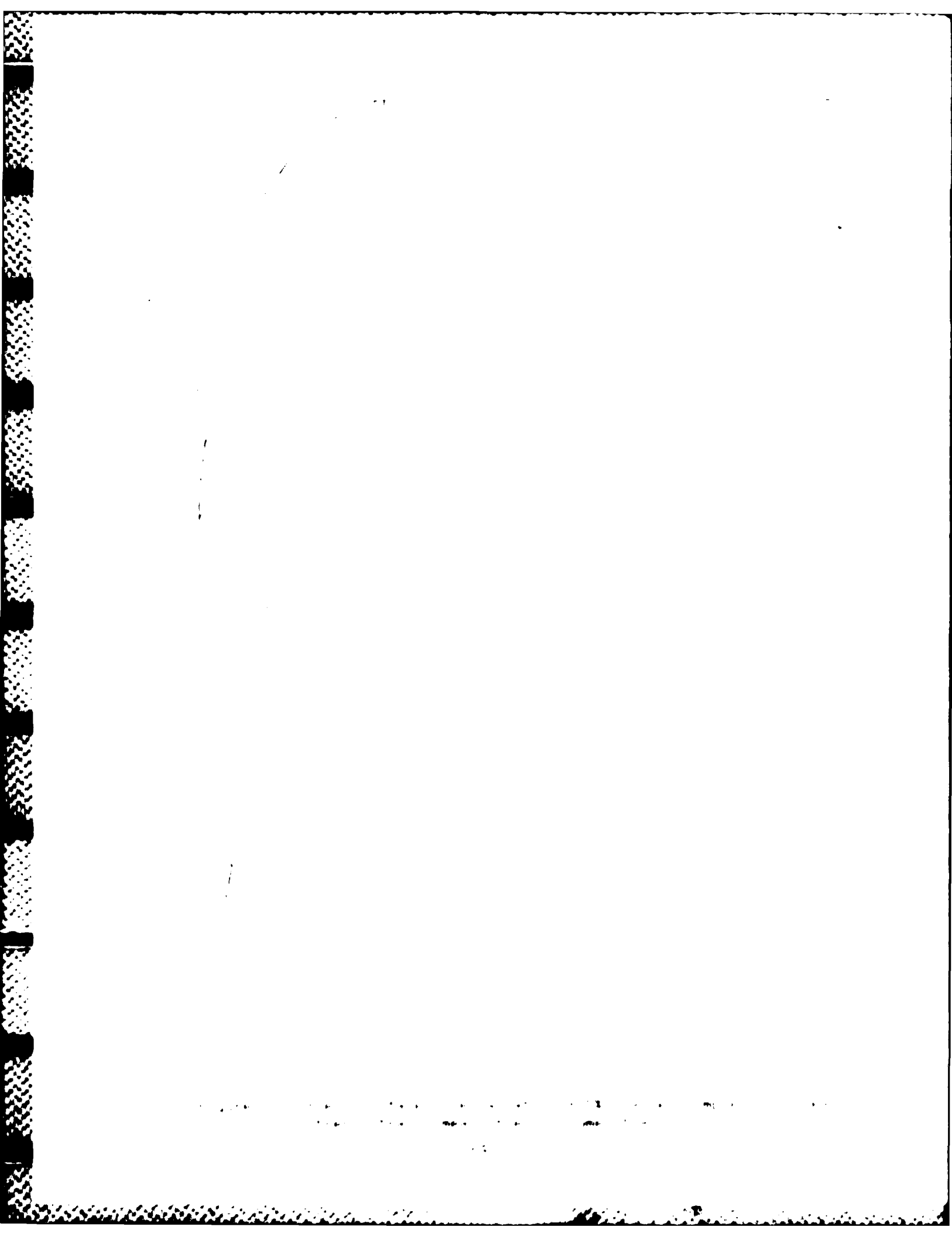


Figure 30. Plastic moduli variation  $\pm 25\%$  undrained compression shear stress-strain, stress path





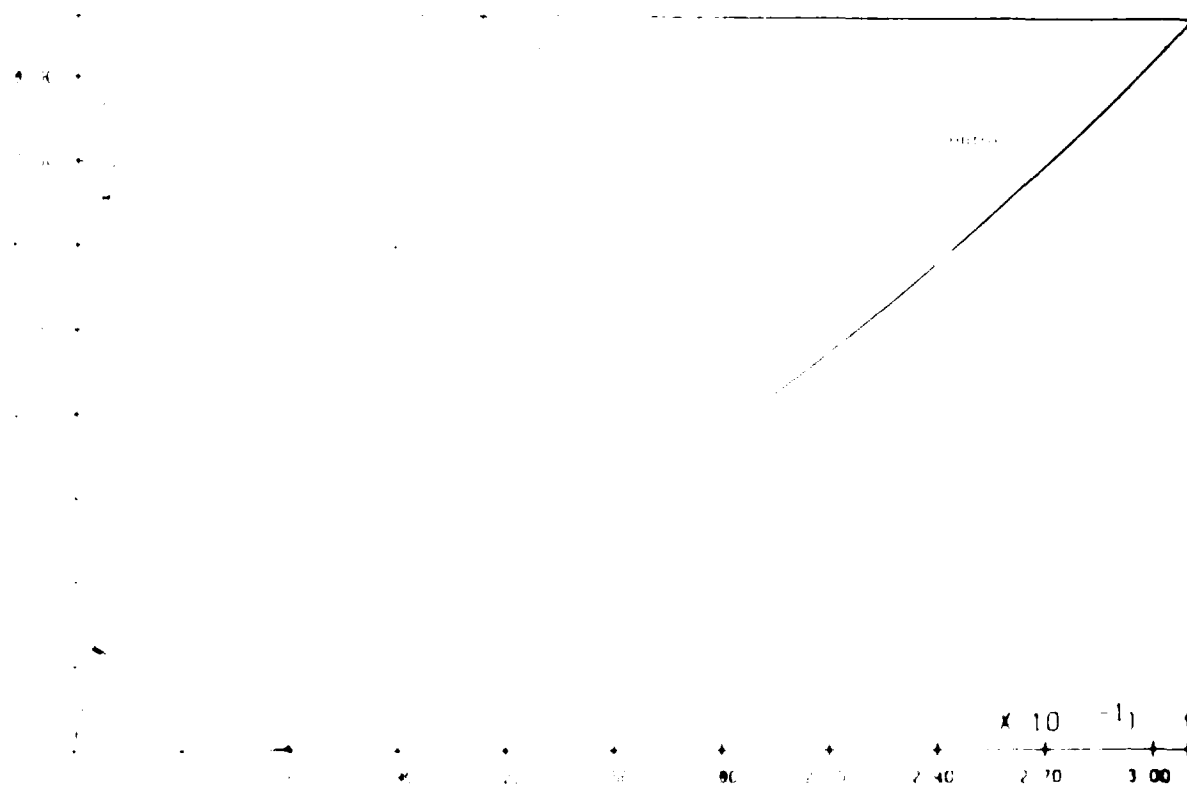


Figure 1. Shear stress-shear strain relationship for (25% - 10% undrained compression) shear strain stress path

### Yield Surface Position

Variation of yield surface position has equal effects in both drained and undrained simulations (Figures 33 and 34). By moving the surfaces in a positive direction, the system is stiffened by changing the points at which the load path intercepts a particular surface, i.e., the path achieves greater stress levels with less plasticity before impacting the next surface, thereby, remaining at a given stiffness through a larger strain increment. By moving the surface position in a negative direction, the load path then intercepts a particular surface at a smaller stress increment, and induces greater amounts of plasticity, effectively softening the system.

Effects on the undrained simulation are presented in Figures 34(a) and 34(b). Qualitatively, the changes produce the same response as demonstrated in the drained simulation.

## LABORATORY TESTS - COHESIVE SOILS

### Kaolinite I

The triaxial tests for the kaolinite clay fitted in Figure 35 were performed at the University of California, Davis. The model parameters for the kaolinite were derived from the consolidated undrained triaxial compression and extension tests. Figures 35(a) and 35(c) present the predictions for shear stress versus shear strain. There is some discrepancy in the predicted ultimate strength in compression which may be attributed to the error involved in digitizing the data points for the effective volume stress based on the stress path plots of the original data. The extension predictions in Figure 35(c) are in excellent agreement with the measured values. The stress path predictions presented in Figures 35(c) and 35(d) show the same behavior as were demonstrated in the shear stress strain plots, with acceptable agreement in both cases. Better agreement may be achieved by increasing the

number of yield surfaces in the initial portion of the loading. This requires better data definition and a much finer digitizing process.

### Kaolinite II

The soil data used in this section are part of the data which were collected by the organizing committee of the National Science Foundation North American Workshop in soil engineering held May 28-30, 1980 at McGill University, Montreal, Canada and reported in Reference 40. Axial test data on the laboratory prepared kaolinite clay had been provided. Predictions about the constitutive behavior of the soil subjected to loading stress paths not identified in the data had been requested and their analysis compares the model predictions with observed behavior in the tests.

The dashed lines in Figure 36 show the experimental results obtained in conventional triaxial undrained monotonic axial compression/extension soil tests and the solid lines show the design curves used to determine the model parameters for that clay. Some data close to failure have been ignored in selecting the design curves because they are not consistent with the rest of the data. This inconsistency may be due to experimental difficulties in capturing failure states in stress-controlled testing devices.

The experimental tests had been conducted on cylindrical samples in a torsional shear testing device. All samples had been unisotropically consolidated to insitu conditions and all the tests were stress controlled and performed under undrained conditions.

Figure 37 shows model predictions for a torsional shear test in which the major principal stress was inclined at  $\theta = 15$  degrees, relative to the vertical axis of the soil specimen (Ref 40). Figure 37 also shows a comparison between predicted and observed behavior of the soil in these tests. Note that all the model predictions agree well with the experimental test results (Ref 40).

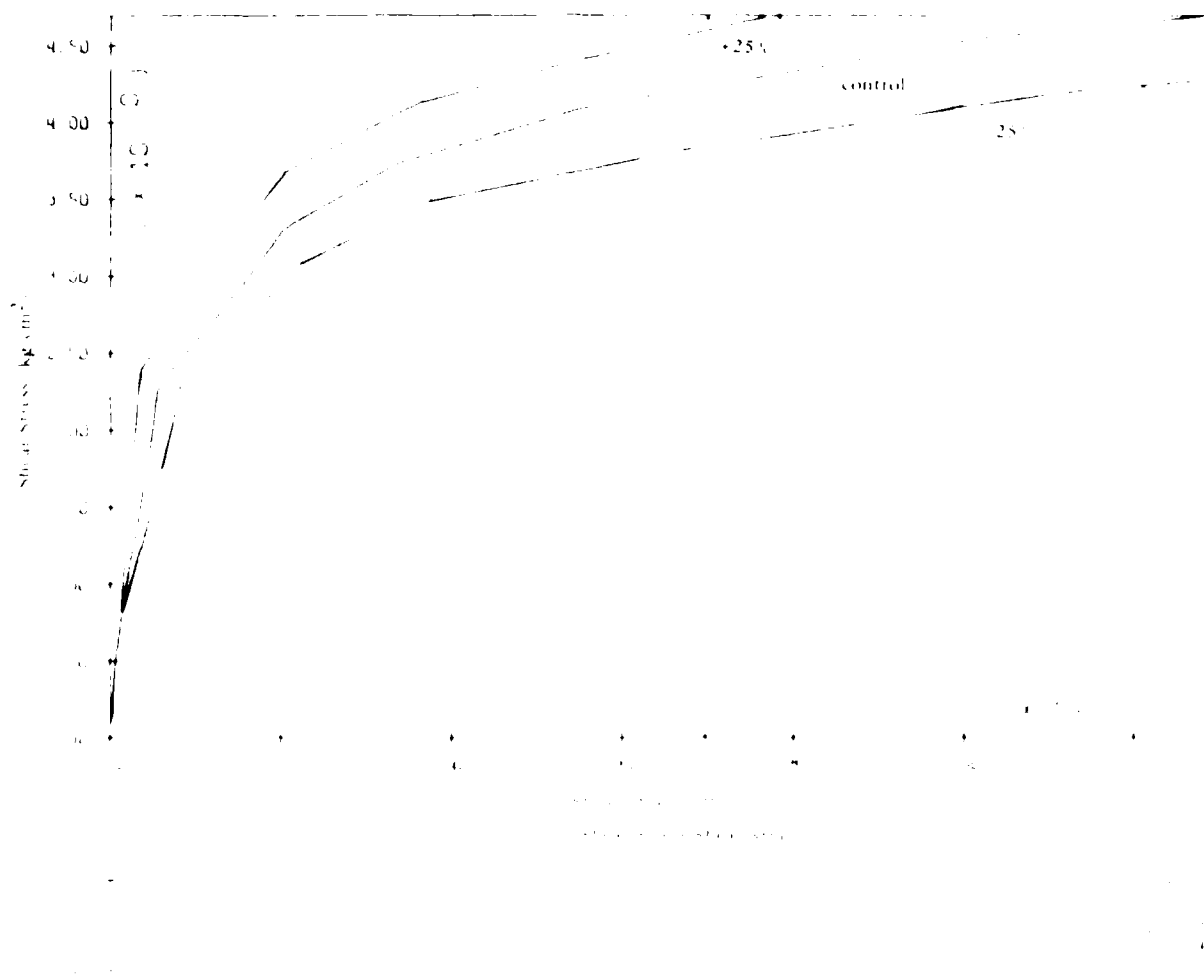


Figure 33 Yield surface position variation  $\pm 25\%$  drained compression  
shear stress-strain, mean stress-volume strain

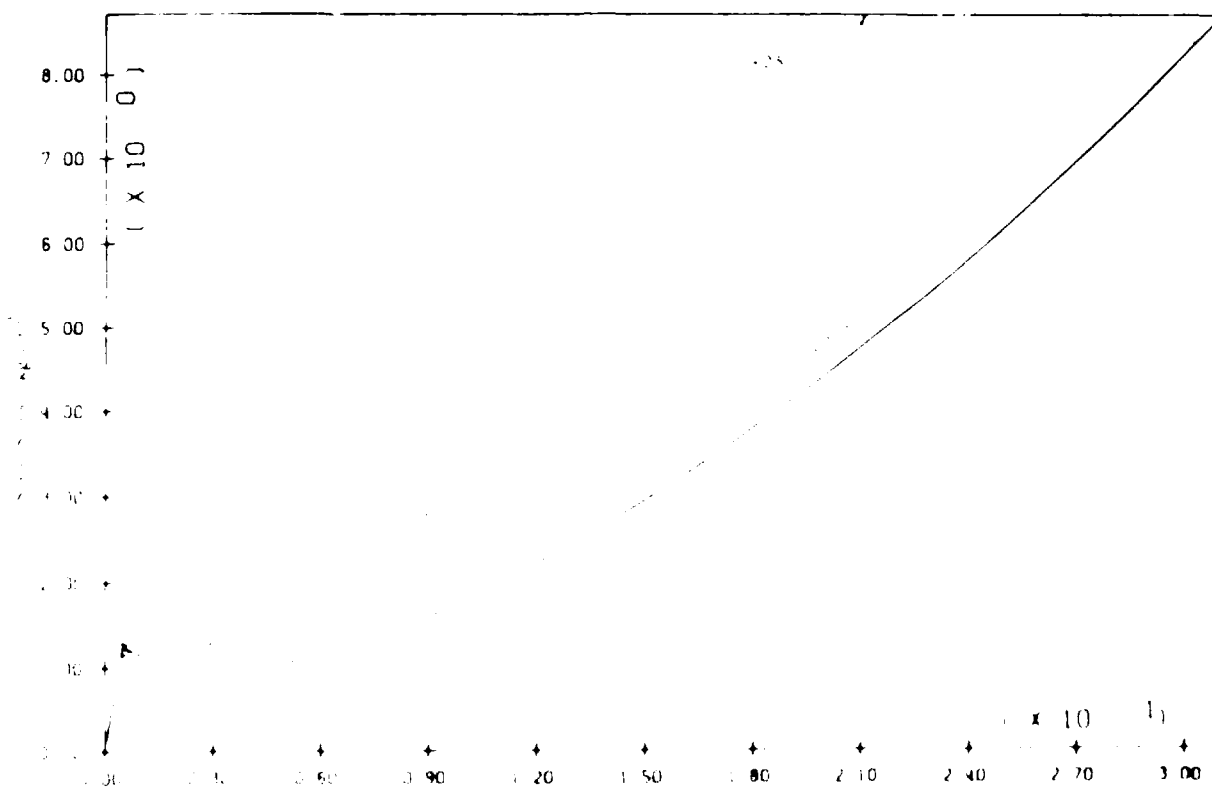


Figure 34 yield surface position 25% undrained compression shear stress-strain, stress path



Figure 35 Undrained shear stress-shear strain kaolinite clay, compression and extension

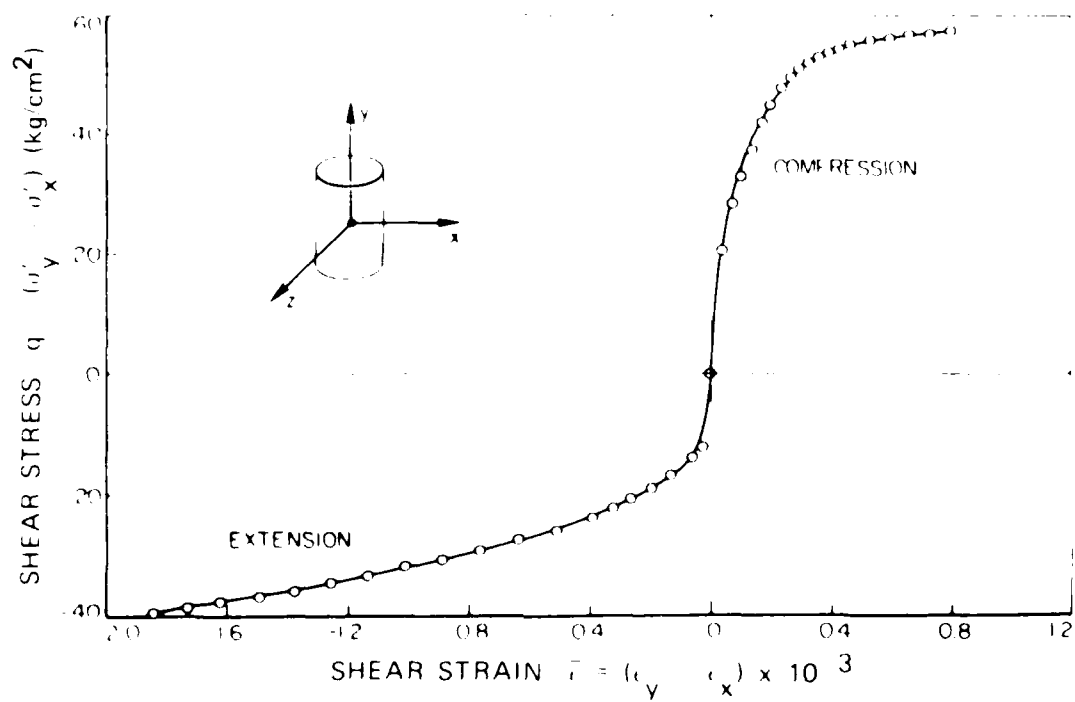


Shear Stress (KPa)

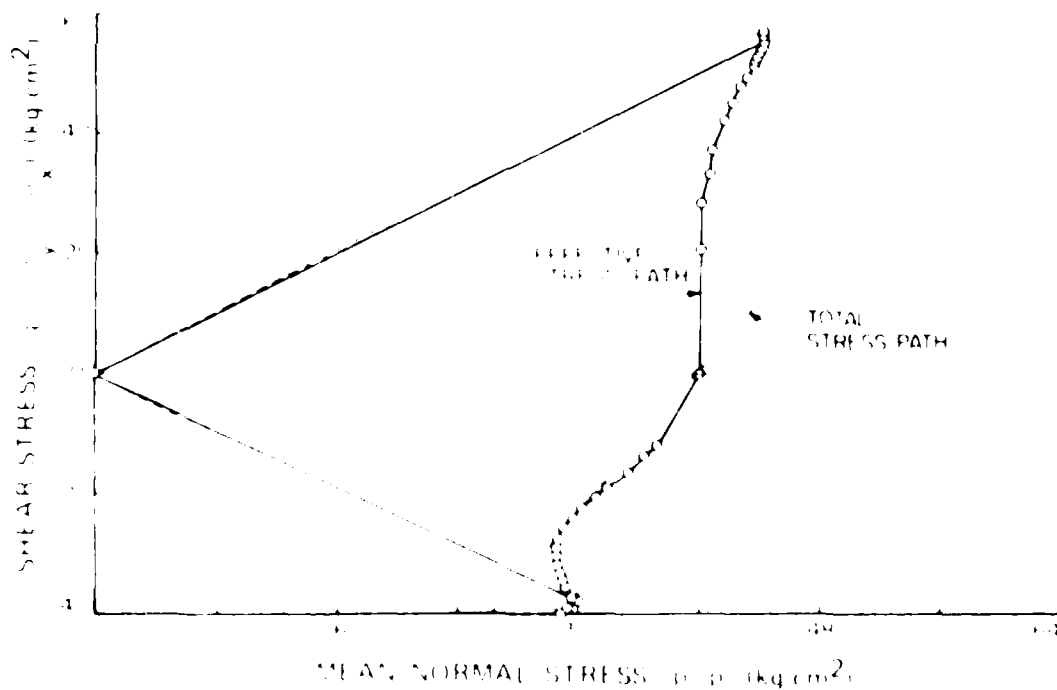
Figure 35(a) Extension of Shear Stress Shear Strain

completed  
observed

Figure 35 Continued



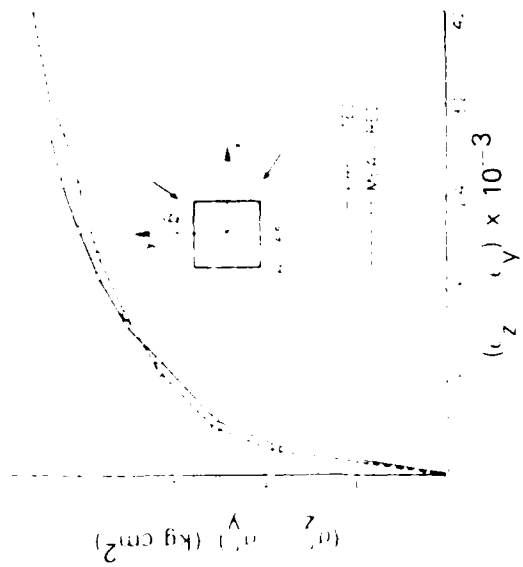
(a) Shear stress versus shear strain.



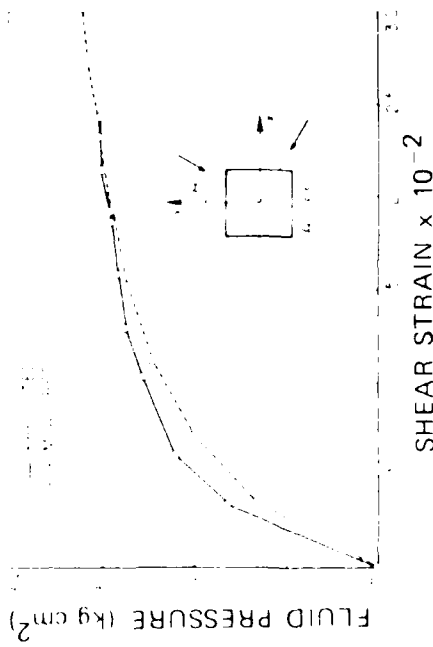
(b) Shear stress versus mean normal effective stress

Figure 36 Undrained compression and extension, kaolinite clay, confining cell pressure = 40 kg/cm<sup>2</sup>





(b) Stress difference versus strain difference  $(y-z)$   $(\sigma_y - \sigma_z)$  versus  $(\epsilon_y - \epsilon_z)$ .



(d) Fluid pressure versus shear strain. 
$$\frac{1}{2} \sqrt{(\epsilon_x - \epsilon_y)^2 + (\epsilon_y - \epsilon_z)^2 + (\epsilon_z - \epsilon_x)^2}$$

Figure 37 Undrained simple shear test with kaolinite clay.

## LABORATORY CENTRIFUGE TESTS

### Analysis of Model Tests

The objective of this work was directed at examining the predictive capabilities of the Princeton University Effective Stress Soil model. Of particular interest are the validity of the numerical model in capturing the generation and dissipation of excess pore-water pressures in saturated sand deposits during and after earthquakes, and its performance in dynamic soil-structure interaction problems. The most appropriate method for such a validation study would be to field data from instrumented prototype situations. However such a study is pre-empted by the nonavailability of field data. In the absence of actual prototype earthquake field data, an alternate method of validation is provided by analyzing centrifugal soil model tests. Although imperfect in many respects, it is felt that dynamic centrifuge soil model tests can still provide a valuable data base for calibration of numerical procedures. A number of dynamic centrifuge soil model tests have been reported in the literature. The particular tests selected for this calibration study have been reported in References 21, 22, 23, and 24. Monterey and the Leighton-Buzzard sands were used in these tests. The basic plan developed to achieve the research objective is summarized as follows:

1. Select a particular constitutive model which most appropriately fits observed soil behavior from conventional triaxial soil tests.
2. Determine the soil model parameters for each particular soil (Monterey and Leighton-Buzzard sands) following the results of conventional triaxial soil tests.
3. Analyze the boundary value problem of a dynamic soil-structure centrifuge test to determine the soil model parameters which best describe the dynamic soil behavior.



Table 2. Summary of Analysis Cases

Test	Time Step Size, $\Delta$ (sec)	NTS	$\alpha$ (Newmark Integration Parameter)	ALGO* (Solution Algorithm)	NITER (Maximum)	NFAC
<b>Monterey Soil Column</b>						
Gravity Load	1800.0	15	1.5	1	10	-
Shaking (285 g, 5.0 Hz)	0.025	200	0.65	0	5	10
Resonance	0.025- 0.500	35	1.5	1	10	-
<b>Lighter Buzzard Soil Column</b>						
Gravity Load	1800.0	15	1.5	1	10	-
Shaking (20 g, 1.0 Hz)	0.07267	160	0.65	0	5	5
<b>Brass Footing</b>						
Dead Loads	1000.0	20	1.5	1	10	-
Shaking (20 g, 1.0 Hz)	0.125	80	0.65	1	10	-
Resonance	0.125	40	1.5	1	10	-
<b>Retaining Wall</b>						
Gravity Load	1000.0	1	1.5	0	10	1
Shaking (20 g, 1.0 Hz)	0.08333	192	0.65	0	5	1

## NOTE

\*ALGO Modified Newton-Raphson

1. Newton-Raphson

2. BFGS

3. Broyden

NT Number of time steps

NITER Number of iterations per time step

NFAC Number of iterations between stiffness matrix reformations.

Table 3. Soil Parameters

Monterey "0" Sand - Dr = 40%

$\rho_s = 2.64 \times 10^3 \text{ kg/m}^3$	(mass density, solid grains)
$\rho_w = 1.00 \times 10^3 \text{ kg/m}^3$	(mass density, fluid phase)
$n^w = 0.43$	(porosity)
$k = 5 \times 10^{-4} \text{ m/sec}$	(permeability)
$\psi'_c = 34^\circ$	(friction angle; compression case)
$\psi'_E = 17.6^\circ$	(friction angle; extension case)
$g_1/p_1 = 800.00$	(elastic shear modulus)
$B_1/p_1 = 533.33$	(elastic bulk modulus)
$p_1 = 9.81 \times 10^4 \text{ N/m}^2$	(reference pressure)
$\eta = 0.50$	(power exponent)
$\eta_c = 1.20$	
$\eta_E = 0.60$	

Yield Surface Number	$\alpha$	$m$	$(H'_c)_1/p_1$	$(H'_E)_1/p_1$
1	0.08937	0.08937	1181.00	1581.00
2	0.18613	0.18610	524.40	813.60
3	0.14217	0.40800	116.90	210.50
4	0.19995	0.49770	69.15	142.40
	0.26444	0.63710	23.46	57.76
	0.36570	0.81520	3.14	10.08
	0.49060	0.90910	1.11	4.21
	0.63990	0.96990	0.52	2.17

Table 4 Soil Parameters

Leighton-Buzzard 120/200 Sand -  $D_r = 55\%$

$\rho_s = 2.73 \times 10^3 \text{ kg/m}^3$	(mass density, solid grains)
$\rho_w = 1.00 \times 10^3 \text{ kg/m}^3$	(mass density, fluid phase)
$n^w = 0.47$	(porosity)
$k = 2.5 \times 10^{-3} \text{ m/sec}$	(permeability)
$\psi'_c = 34.35^\circ$	(friction angle; compression case)
$\psi'_E = 21.14^\circ$	(friction angle; extension case)
$g_1/p_1 = 500.$	(elastic shear modulus)
$B_1/p_1 = 333.33$	(elastic bulk modulus)
$p_1 = 9.81 \times 10^4 \text{ N/m}^2$	(reference pressure)
$\eta = 0.50$	(power exponent)
$\eta_c = 1.30$	
$\eta_E = 0.80$	

Yield Surface Number	$\alpha$	$m$	$(H'_c)_1/p_1$	$(H'_E)_1/p_1$
1	0.03099	0.06582	966.80	1168.00
2	0.06261	0.14300	357.70	459.20
3	0.09681	0.26590	219.40	337.30
4	0.08969	0.32670	162.00	265.40
5	0.15857	0.50160	42.03	81.95
6	0.23864	0.63800	17.47	41.31
7	0.27796	0.76120	7.60	21.99
8	0.32030	0.9023	3.78	13.21
9	0.32580	0.9930	1.17	4.47

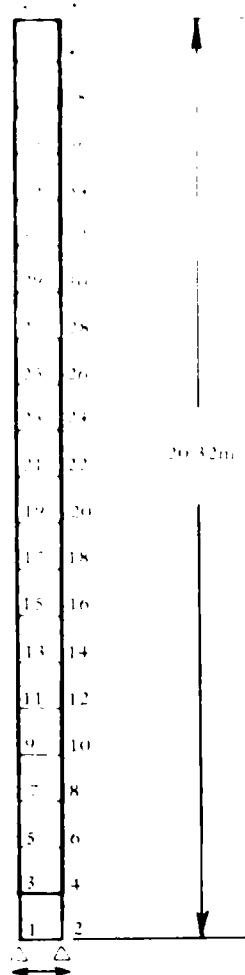
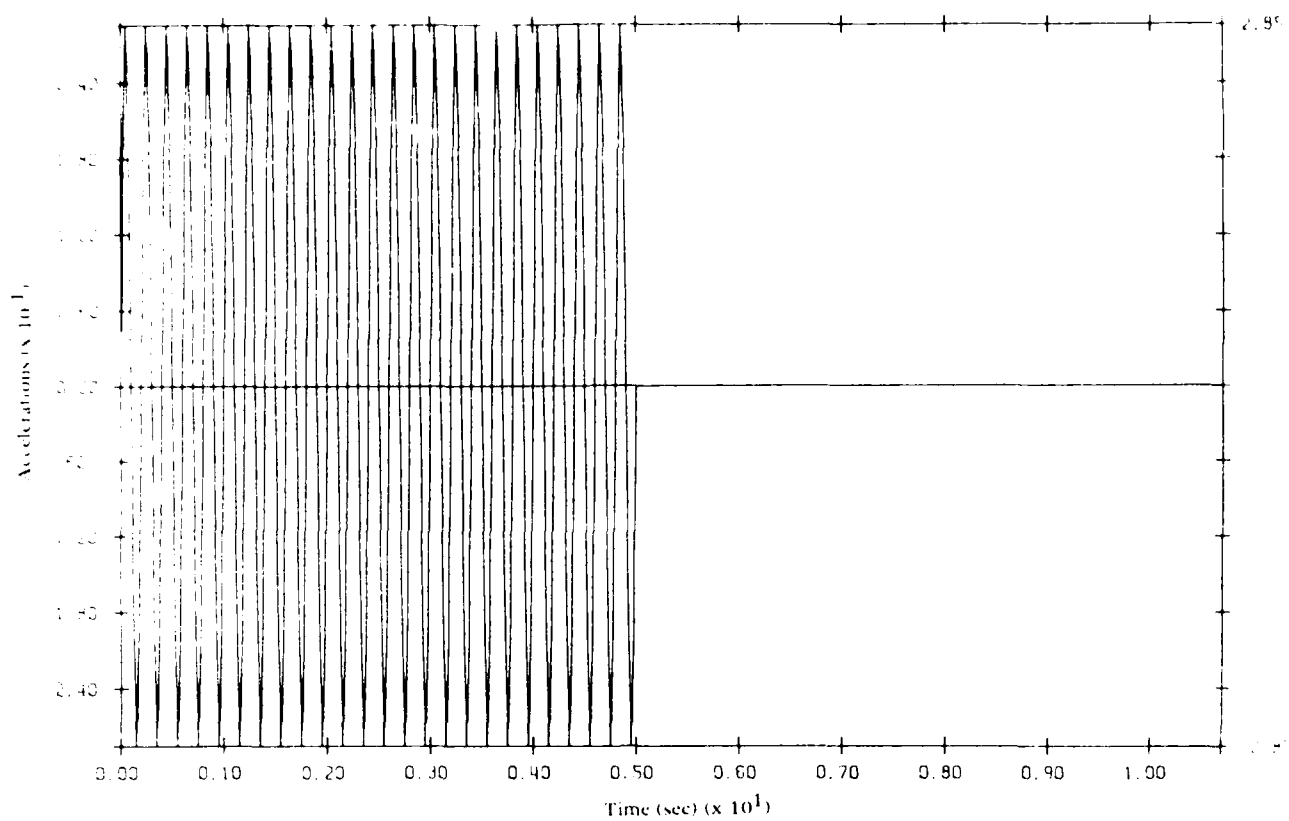


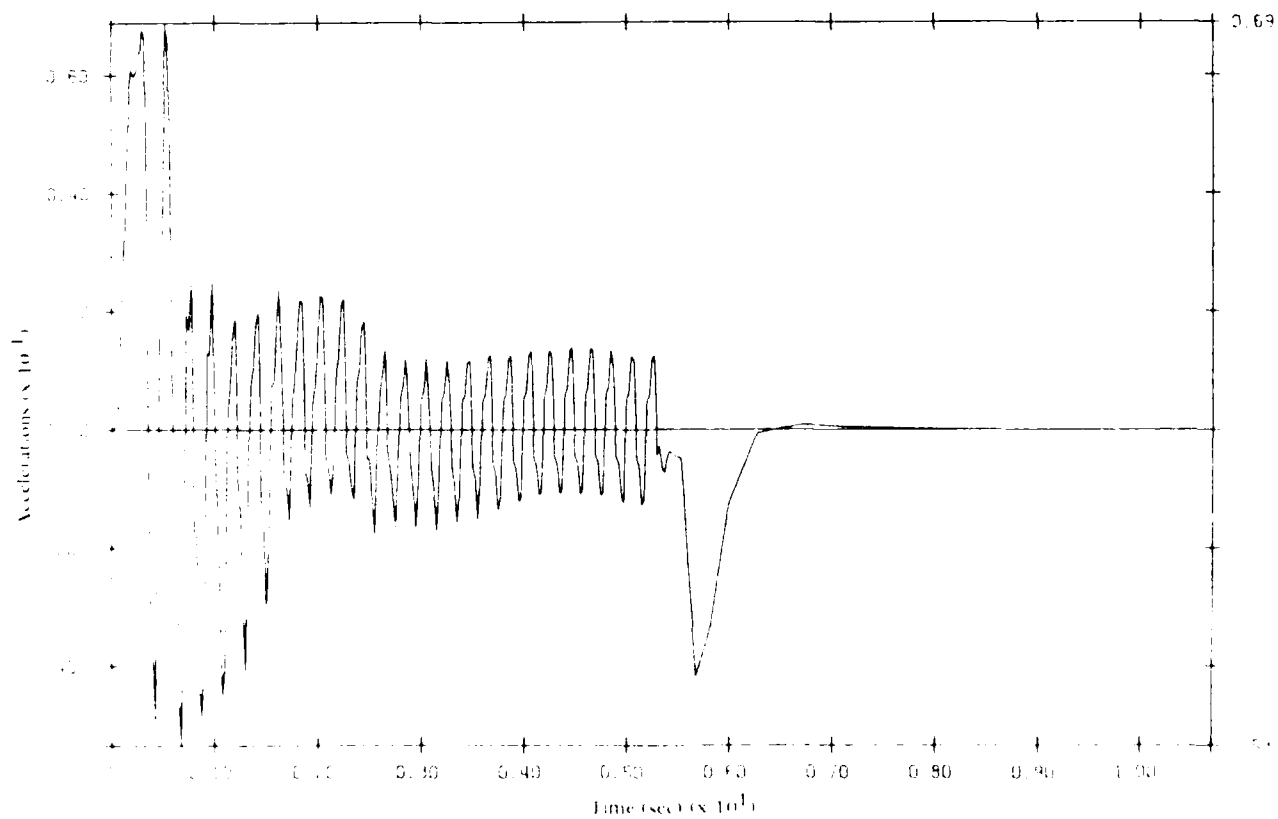
Figure 38. Undeformed mesh soil column (Monterey "0" sand).

pore-fluid is allowed to take place through the rigid bottom boundary (nor the side boundaries) and the ground shaking is applied as a horizontal sinusoidal input acceleration at the bottom boundary nodes. The permeability (Table 3) used in the simulation  $k = 5 \times 10^4 \times 100 \text{ m/sec}$  in order to correct for the fact that in the centrifuge (at 100 gs) diffusion of pore-water takes place 100 times faster than in the corresponding prototype.

Figure 39 shows the computed horizontal acceleration time histories at the bottom (Figure 39(a)) and at the top (Figure 39(b)) of the soil column for an input horizontal base acceleration with an amplitude 0.285 gs and a frequency of 5 Hz. The results for 25 cycles of loading (5 seconds of shaking) are reported in Figure 39. Note the strong modification of the signal computed at the surface as a result of its passage through the saturated soil deposit. The computed maximum surface acceleration compares favorably with the recorded value in the test.



(a)



(b)

Figure 39. Horizontal accelerations at bottom and top of column (Monterey "0" sand).



Figure 40 shows the computed vertical motion at the surface. As a result of the shaking, excess pore-water pressures build up and partly dissipate in the soil column. These in turn generalize vertical motions (via volumetric strains in the soil skeleton). Although small, the computed vertical acceleration (Figure 40(b)) at the top (0.0377 g) is not negligible and is about one-half the horizontal peak acceleration. Figure 40(a) shows the resulting settlement of the soil column that accumulated during and after the shaking as excess pore-water pressure is being dissipated from the column. The computed ultimate settlement = 24 cm.

Figure 41 shows the computed excess pore-water pressures, vertical effective stress, and shear stress time histories at various depths. The plots have been normalized by dividing the quantities of interest by the initial vertical effective stress. In Figure 41(a),  $h = 0.51$  meter and in Figure 41(b),  $h = 10.66$  meters where  $h =$  distance from the bottom boundary (close to points B and A in Reference 21. Note the computed increases in pore-water pressures. In Figure 41(a),  $\Delta u/\sigma'_{v0} \approx 0.69$  and in Figure 41(b),  $\Delta u/\sigma'_{v0} = 0.85$  compares most favorably with recorded values in the test (0.74 and 0.86, respectively). Note the diffusion taking place after the base motion has stopped.

#### Leighton-Buzzard Soil Column Test

The test procedures and test results are reported in Reference 23. The sand was rained in water, in a stacked-ring apparatus. The model was tested on a centrifuge at a centrifugal acceleration of 35.5 gs, and subjected to a decaying sinusoidal base acceleration. The corresponding prototype situation is analyzed. The particular test selected for analysis is referred to as PL-3A in Reference 23.

As in the previous section, the test is intended to simulate free-field conditions in a horizontally layered soil deposit, and the same analysis procedure was used. Figure 42 shows the finite element mesh. Ten equally spaced elements are used to simulate the 10.8 meters of the sand column (12-inch model at 35.5 gs). The water table is located at the ground surface. No drainage of the pore fluid is allowed to take

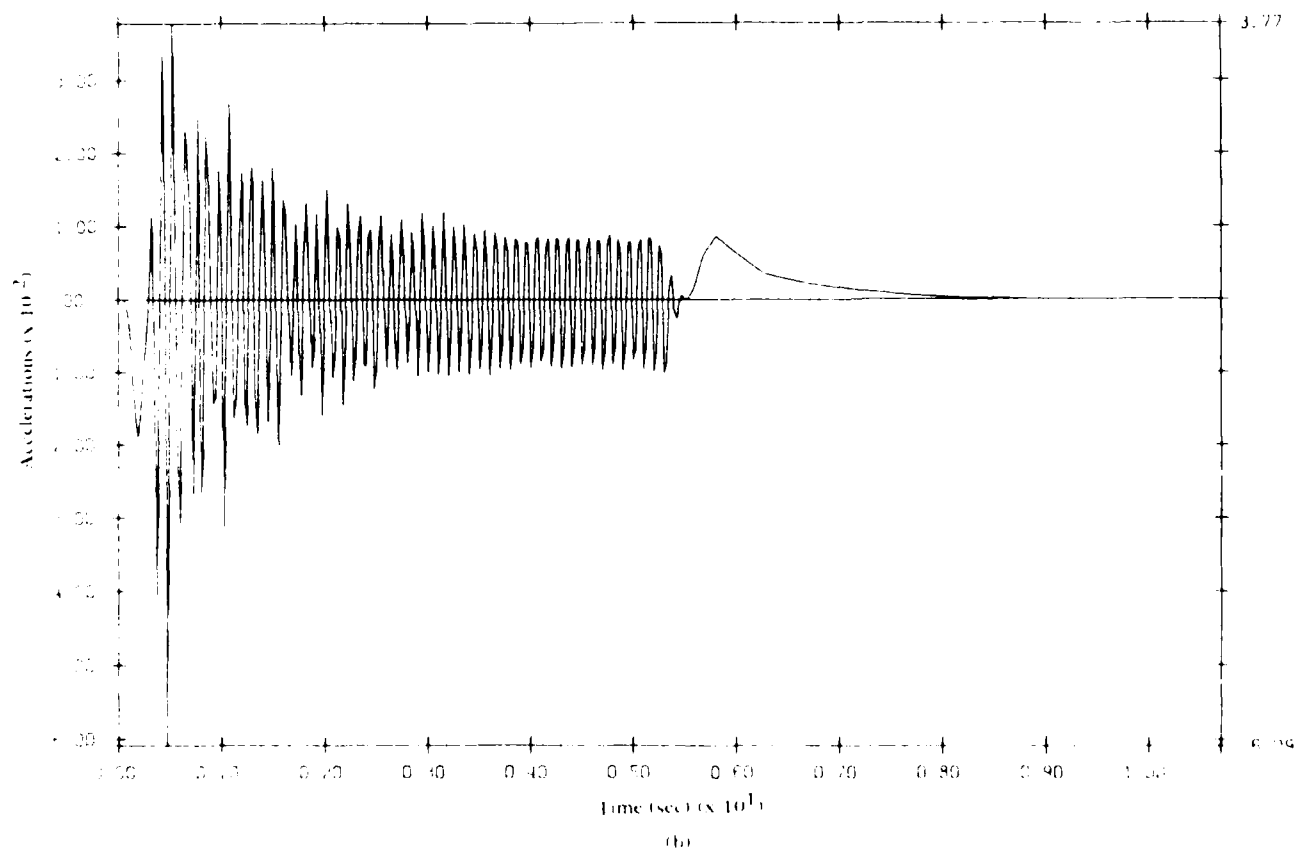
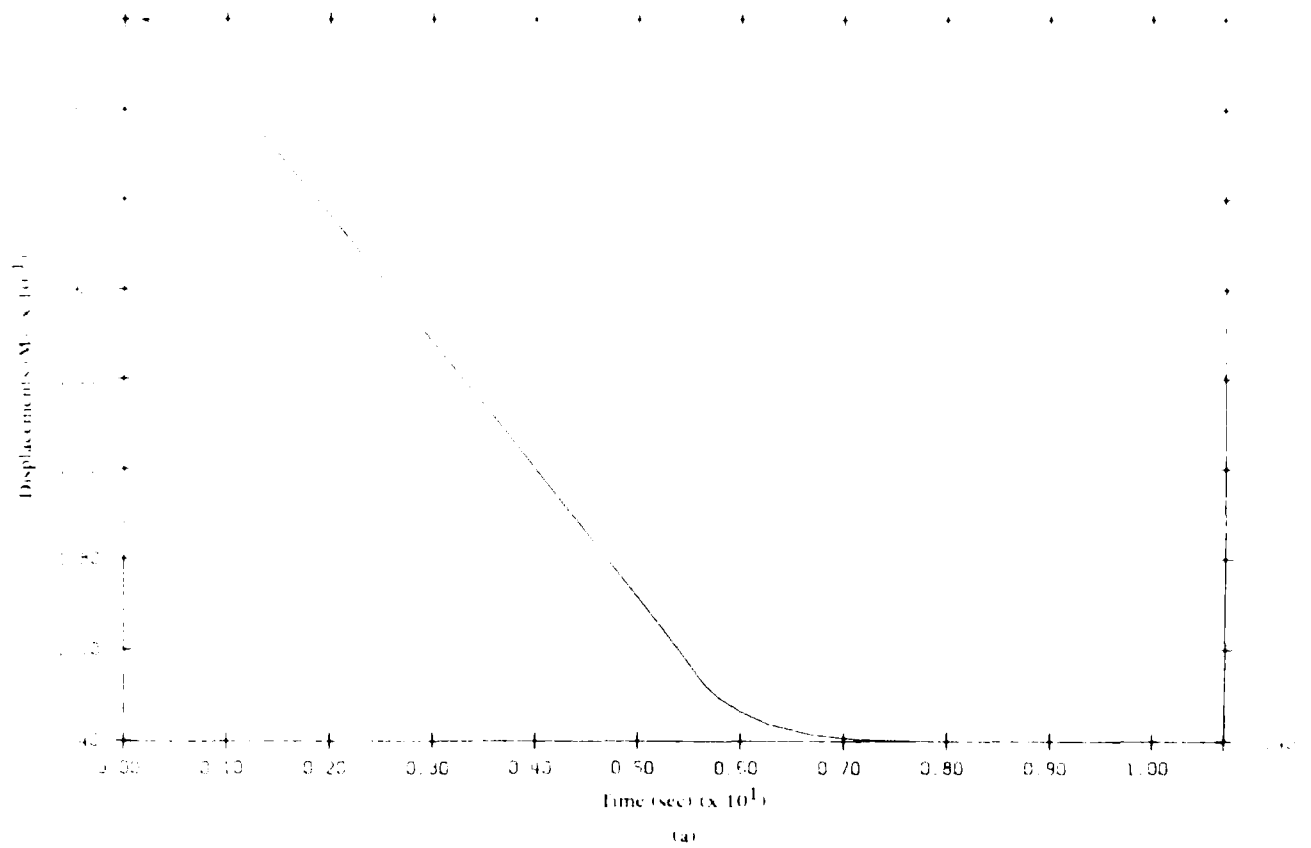


Figure 40. Vertical displacement and accelerations at top of column (Monterey "0" sand).

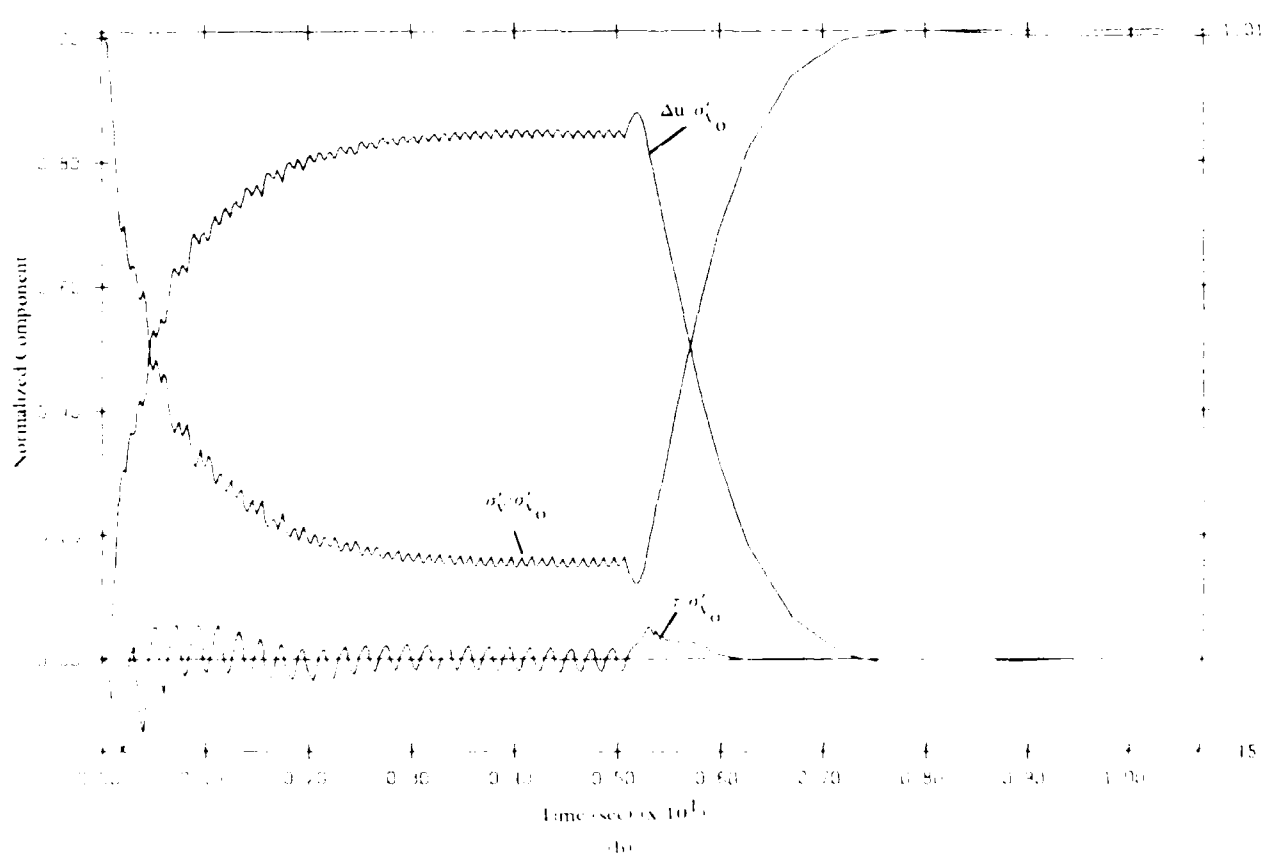
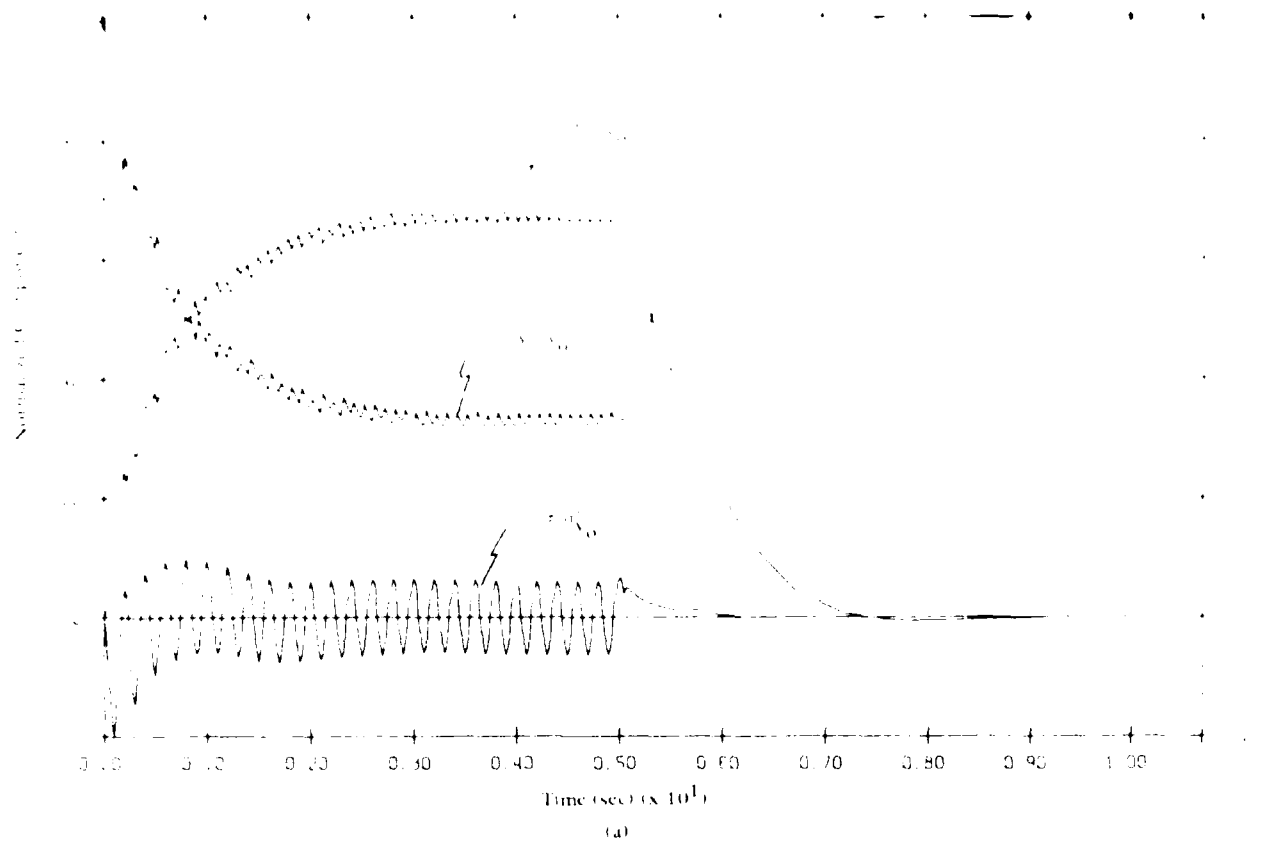


Figure 41. Normalized pore pressure, vertical stress, and shear stress (Monterey "0" sand).

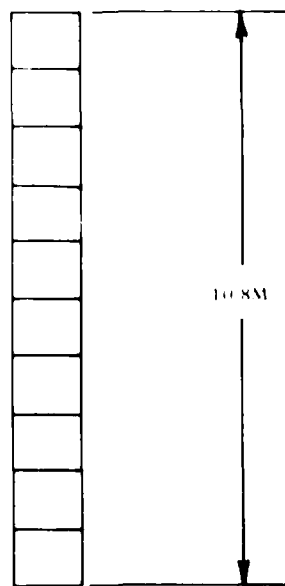


Figure 42. Undeformed mesh soil column (Leighton Buzzard sand).

place through the rigid bottom boundary or the side boundaries, and the ground shaking is applied as a horizontal input acceleration at the bottom boundary nodes. The permeability (Table 4) used in the simulation is  $k = 2.5 \times 10^3 \times 35.5$  m/sec to correct for the fact that in the centrifuge (at 35.5 gs) diffusion of the pore water takes place 35.5 times faster than in the corresponding prototype.

Figure 43 shows the computed horizontal acceleration time histories at the bottom (Figure 42(a)) and at the top (Figure 42(b)) of the soil column for an input horizontal base acceleration with a peak amplitude of 0.20 g and a frequency of 1.72 Hz. The results for 15 cycles of loading (9 seconds of shaking) are reported in Figure 42. Note that as a result of the massive liquefaction occurring in the underlying strata, the motion is not transmitted to the surface after about 2 seconds of shaking (1.16 cycles of loading) as observed in the test. Surface accelerations were not measured in the test, which make direct comparison with the predicted time history shown in Figure 43(b) impossible.

Figure 44 shows the computed vertical motion at the surface. Very little diffusion takes place and the resulting vertical motions and settlement are very small (7.3 cm).

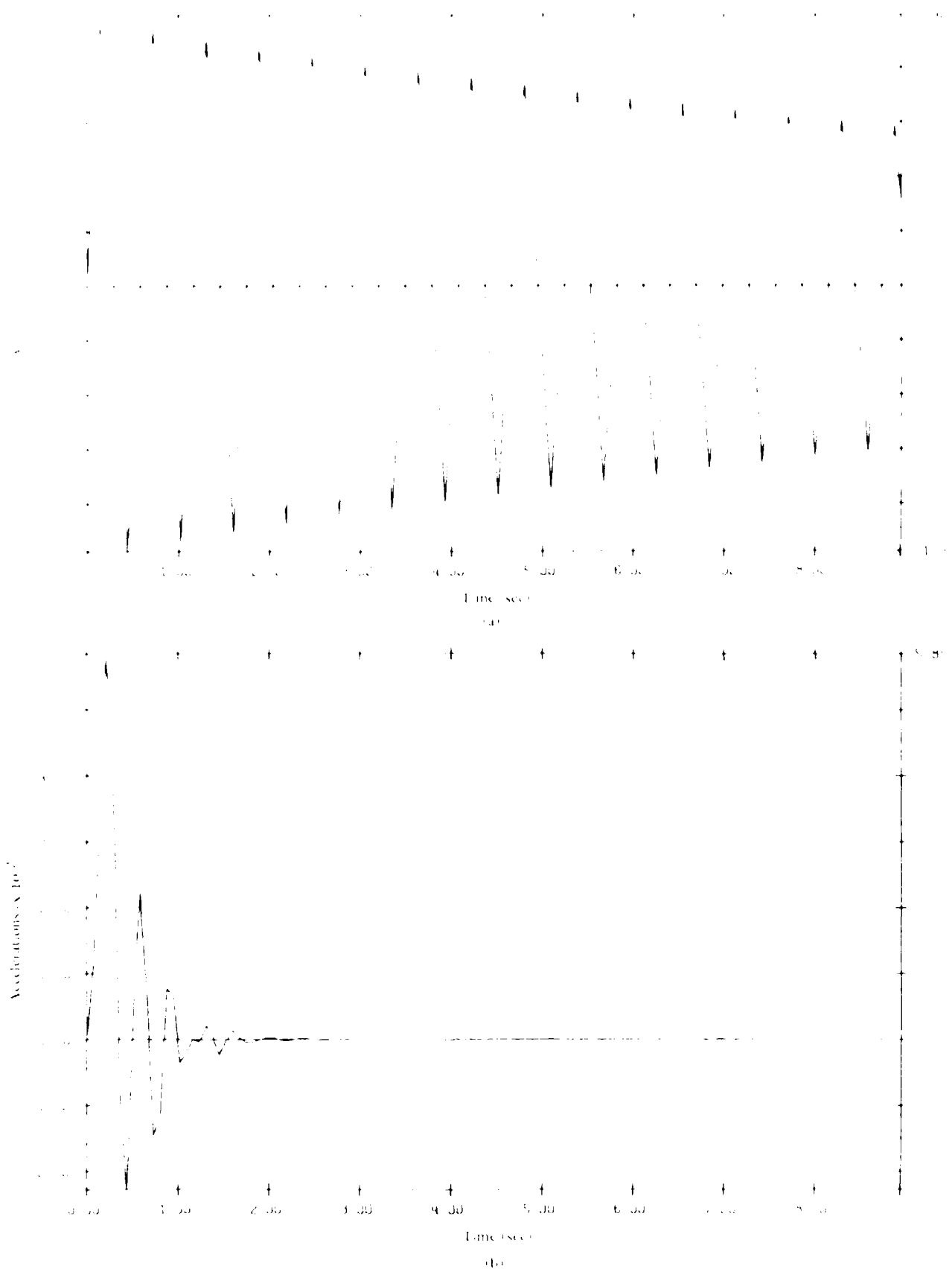


Figure 43. Horizontal accelerations at bottom and top of column (Leighton-Buzzard sand).

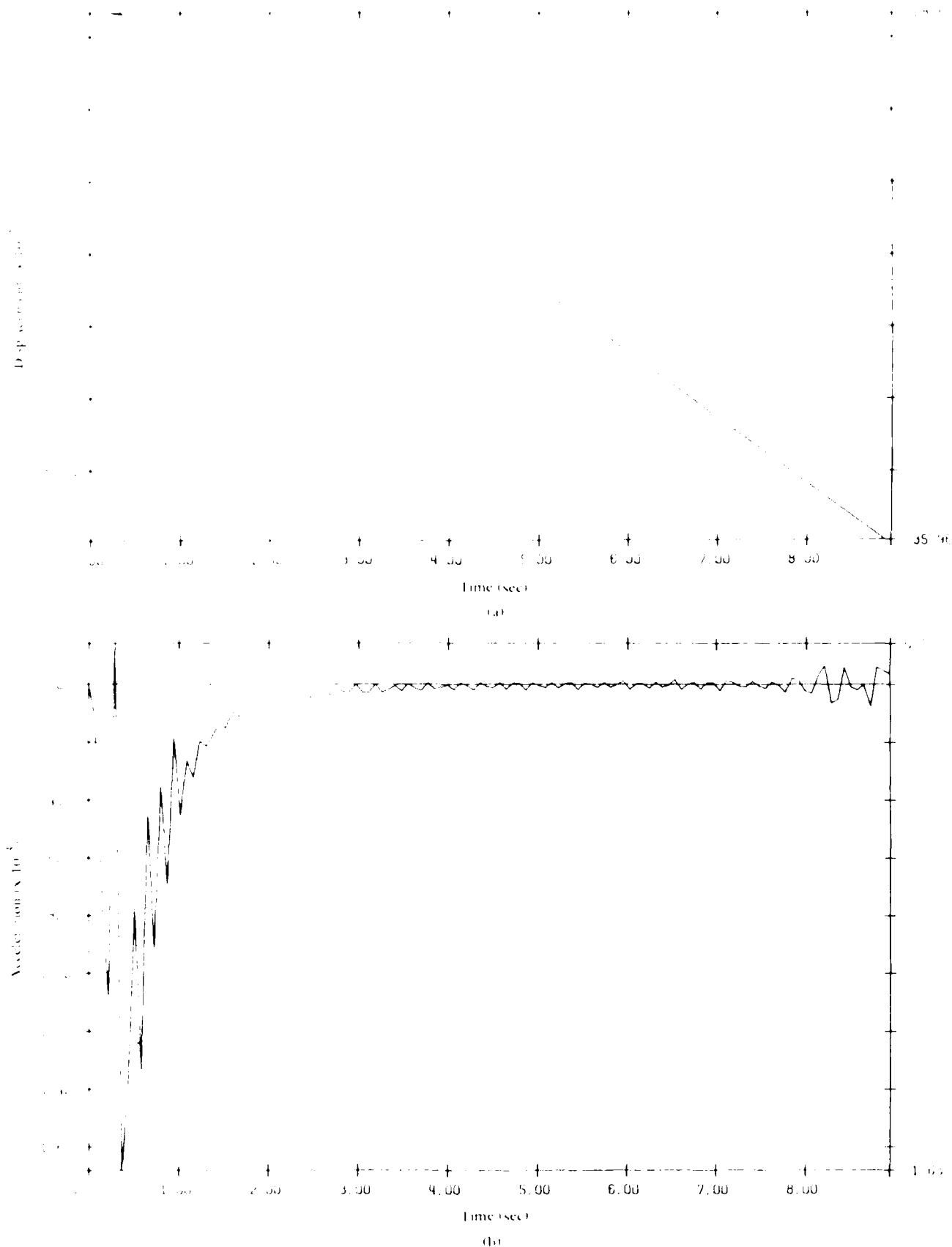


Figure 44. Vertical displacements and accelerations at top of column (Leighton-Buzzard sand).

Figure 45 shows the computed excess pore-water pressure, vertical effective stress, and shear stress time histories at various depths. The plots have been normalized by dividing the quantities of interest by the initial vertical effective stress. In Figure 45(a),  $h = H/3$  and in Figure 45(b),  $h = 2H/3$  from the bottom boundary, where  $H = 10.8$  meters = height of soil column. Note the rapid increase (in almost one cycle of loading) in pore-water pressures and associated liquefaction of the soil column, which result in no shear being transmitted through the column. The predicted massive liquefaction of the column was actually recorded at the test of the same time, and resulted in failure of the stack-ring apparatus.

#### Brass Footing Test

The test procedures and test results are reported in Reference 24. The soil was Leighton-Buzzard 120/200 sand. The soil deposit was placed in a stacked-ring apparatus by pluviating the sand in layers into water and then rodding to achieve the desired density. A brass footing with a diameter of 113 mm was placed on top of the saturated sand deposit (height = 151 mm, diameter = 406 mm) and tested on a centrifuge at a centrifugal acceleration of 80 gs. The deposit was then subjected to sinusoidal base acceleration. The corresponding prototype situation was analyzed.

Figure 46 shows the finite-element mesh used for analysis, pore-pressures, and vertical stresses at measured points and a comparison of measured and computed results. The soil is discretized by using 240 elements and the brass footing by using two rows of 10 elements each. The soil parameters are given in Table 4, and in the analysis  $k = 2.5 \times 10^{-3} \times 80$  m/sec to properly scale diffusion time. The brass footing is modeled as a one-phase elastic solid with  $\rho = 8.5 \times 10^3$  kg/m<sup>3</sup> (mass density);  $E = 10^{12}$  N/m<sup>2</sup> (Young's modulus), and  $\nu = 0.0$  (Poisson's ratio). A static pressure is applied to the top of the footing to achieve a static bearing pressure of  $1.30 \times 10^5$  N/m<sup>2</sup> in the test (at 80 gs).

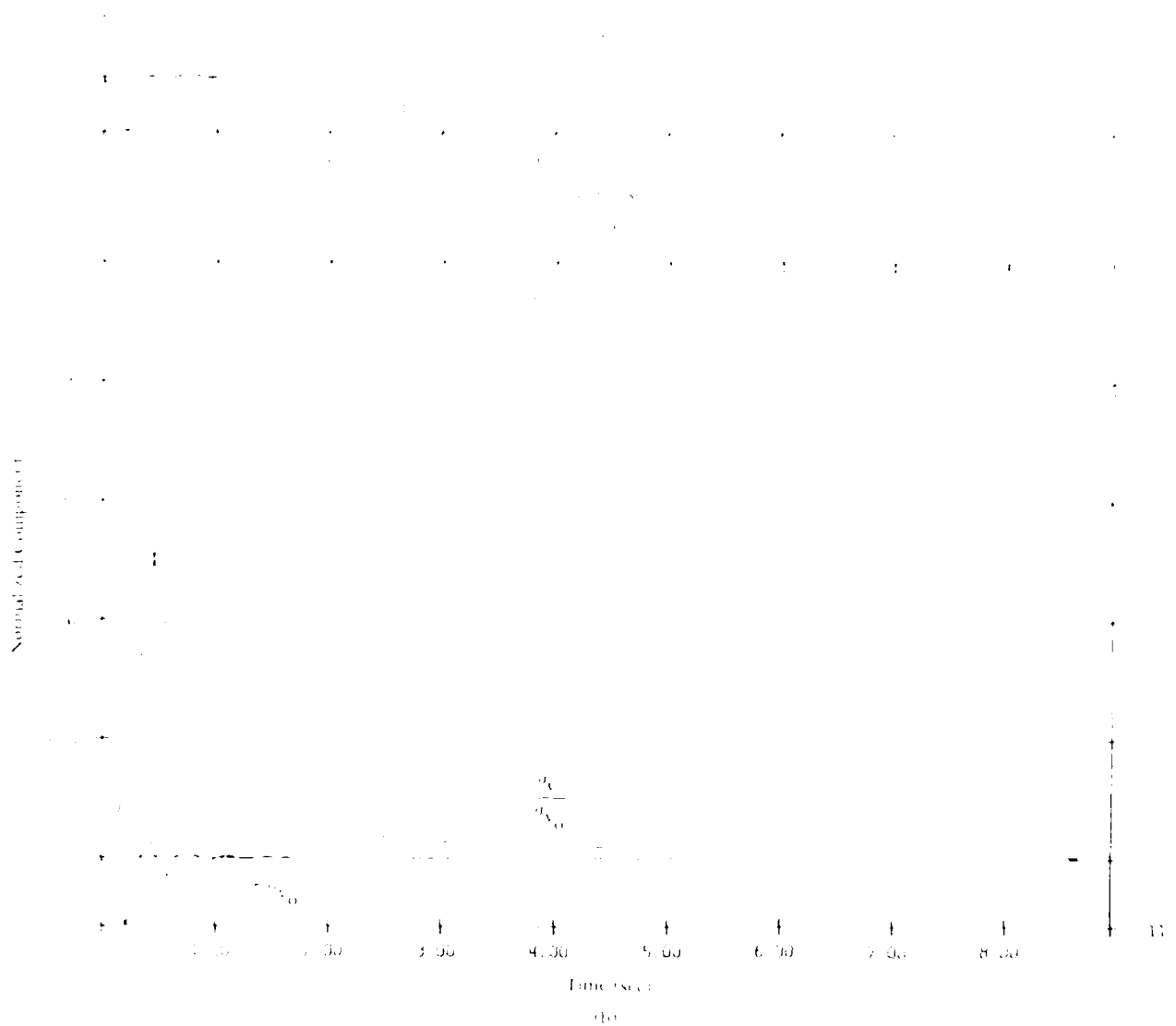
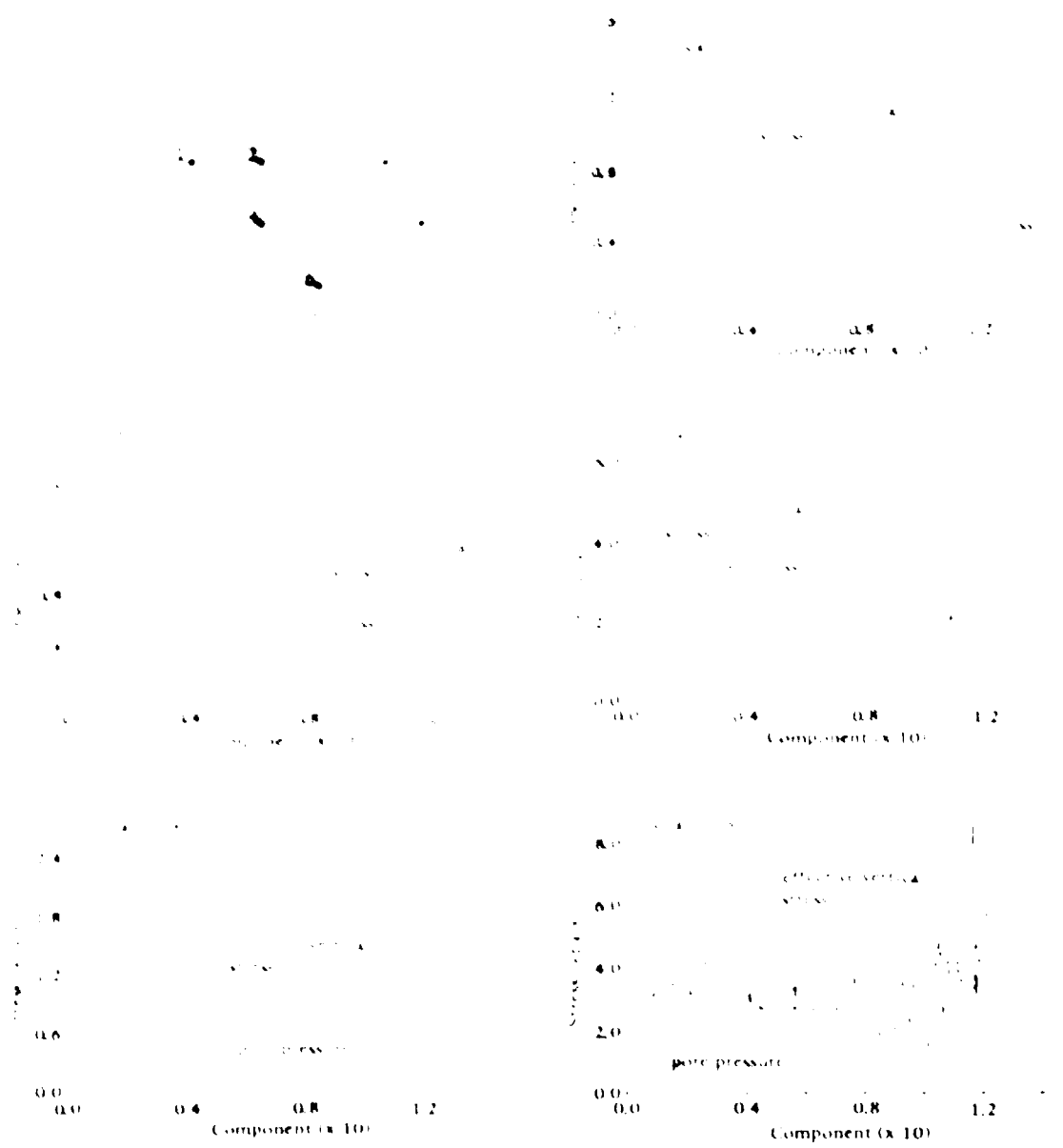


Figure 45. Normalized pore pressures, vertical stress, and shear stress (Leighton-Buzzard sand).





Peak Pore Pressure (kpa)

Location	Computer	Measured
1	20	20
2	30	30
3	30	25
4	15	12
5	50	65
6	40	60

Figure 46. Undeformed mesh, brass footing, computed vertical stress, and pore pressure.

The water table is located at the ground surface. Drainage of the pore fluid is not allowed to take place through the rigid bottom boundary or the lateral side boundaries. A ground shaking is applied as a horizontal sinusoidal input acceleration at the bottom boundary nodes, with a maximum acceleration = 0.17 g and a frequency of 1 Hz for 10 seconds (10 cycles).

The stacked-ring apparatus is used to simulate free-field conditions, therefore, the same procedure as used previously in the soil column test simulations was used. Specifically, the same equation number was assigned to each nodal degree of freedom on the same horizontal plane for the two side boundaries.

Figure 47 shows the computed horizontal acceleration time history at the bottom (Figure 47(a), node 131) of the soil deposit and at the top (Figure 47(b), node 285) of the brass footing on the center line. Note that as a result of the dynamic soil-structure interaction, the recorded motion on the footing is different from the input motion at the base.

Figure 48 shows the computed vertical acceleration time history at the left corner (Figure 48(a), node 275), center (Figure 48(b), node 285), and right corner (Figure 48(c), node 295) of the footing. Note that as a result of the horizontal base motion, vertical accelerations are imparted to the footing. Figure 49 shows the computed vertical displacements at the left corner (Figure 49(a)), center (Figure 49(b)), and right corner (Figure 49(c)) of the footing. During the test, the settlement increased as the shaking continued. Further settlement occurred after the shaking stopped. However, the computed maximum settlement amount was measured experimentally.

The Navy is sponsoring a centrifuge test to determine axial test results for the program. The program is currently in progress.

AD-A176 207

EVALUATION AND VALIDATION OF THE PRINCETON UNIVERSITY  
EFFECTIVE STRESS MODEL(U) NAVAL CIVIL ENGINEERING LAB  
PORT HUENEME CA J H PREVOST ET AL DEC 86

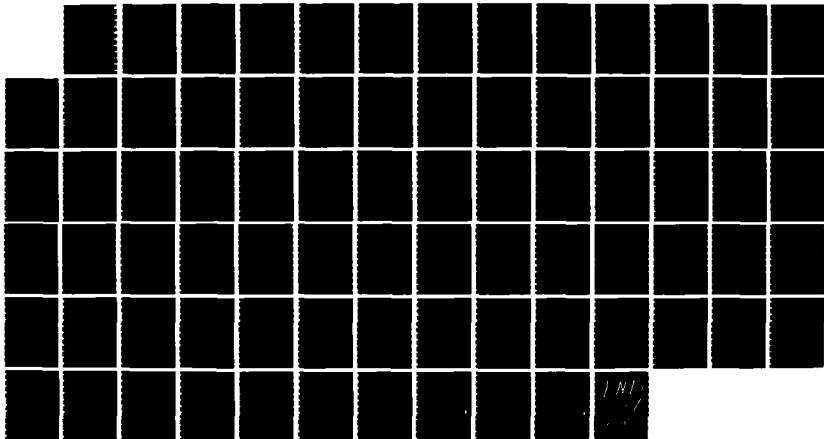
2/2

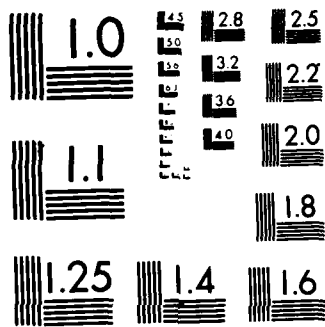
UNCLASSIFIED

NCEL-TR-R-919

F/G 8/13

NL





MICROCOPY RESOLUTION TEST CHART  
NATIONAL BUREAU OF STANDARDS-1963-A

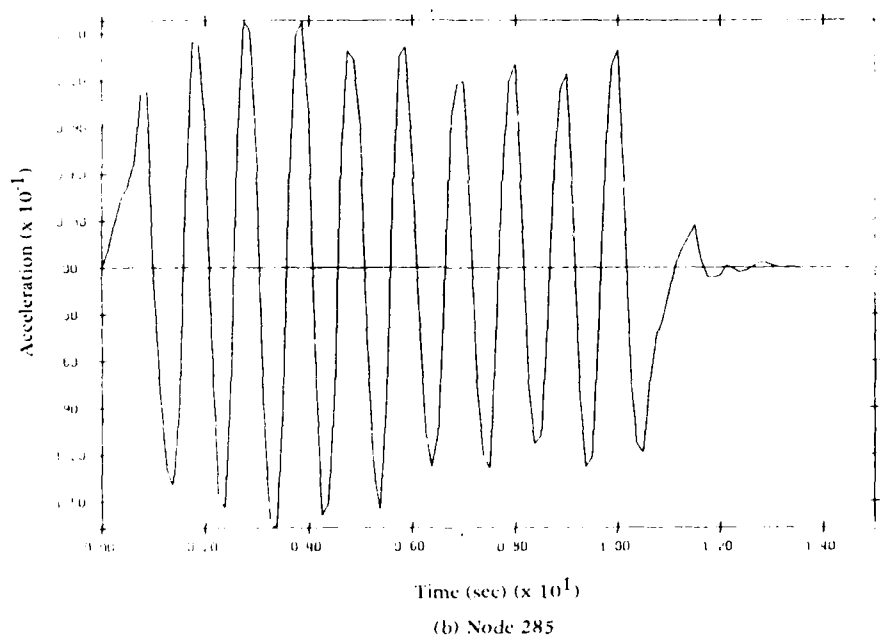
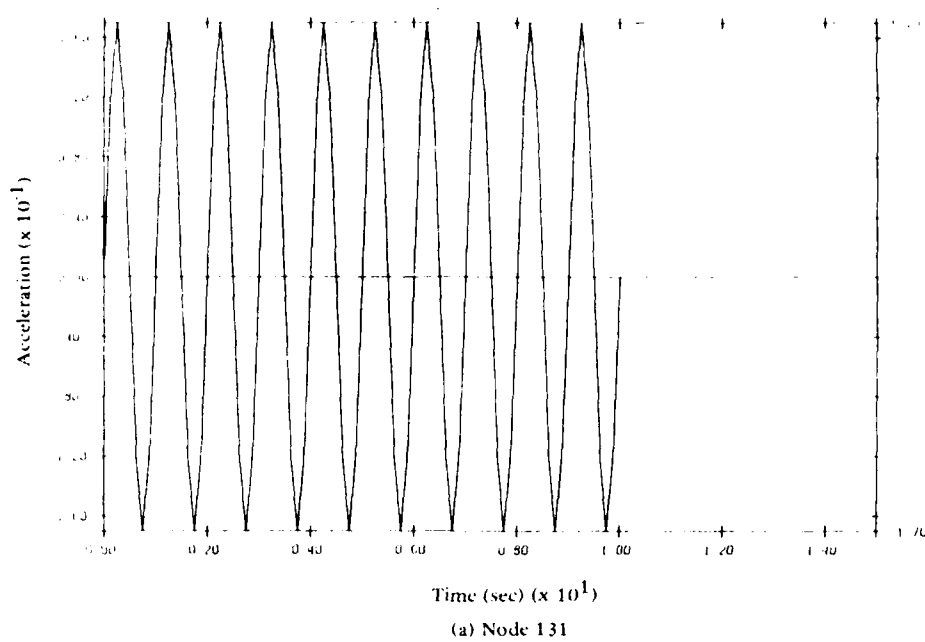


Figure 47. Input horizontal accelerations and resultant accelerations at center of the footing.

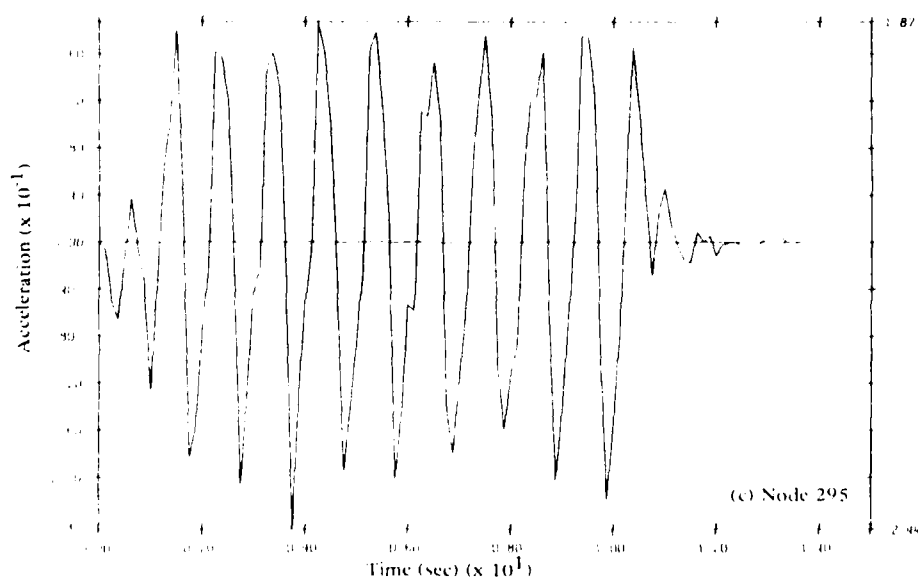
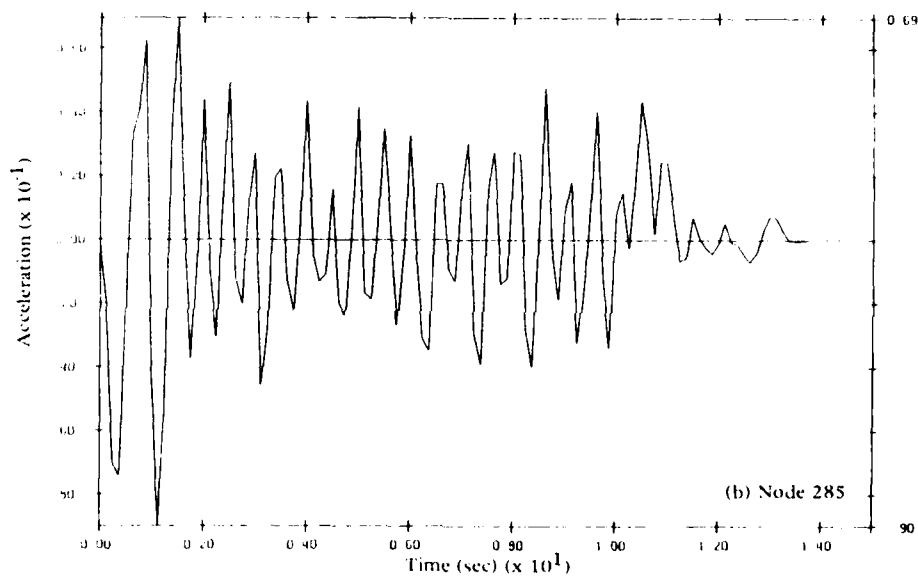
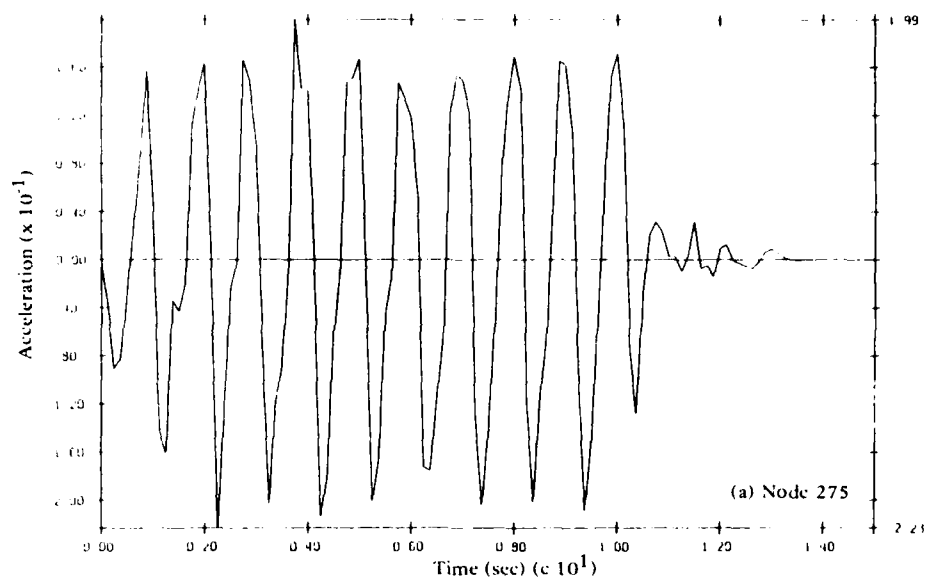
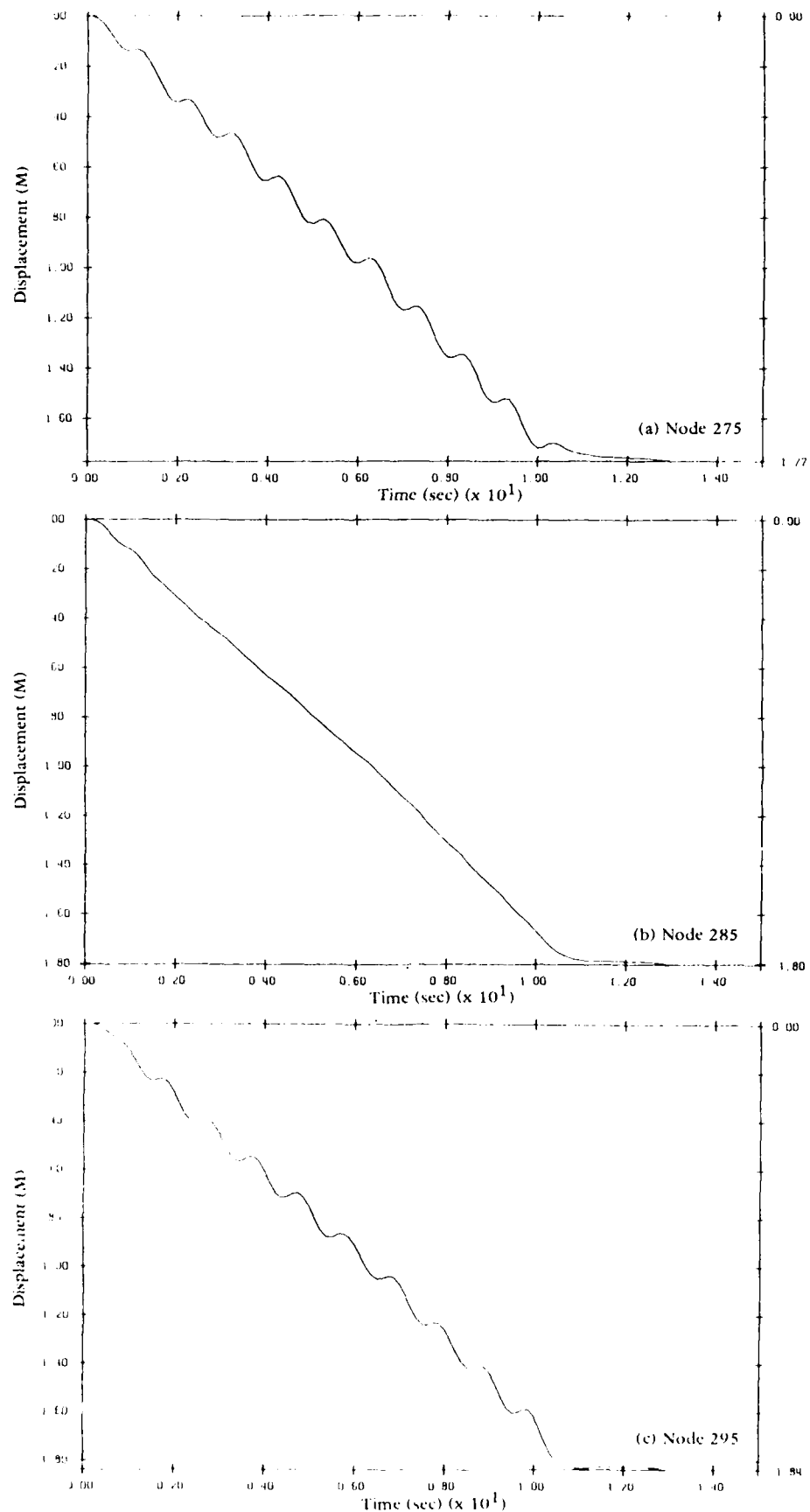


Figure 48. Vertical footing accelerations.



different preparation techniques, resulted in differences in void ratios for the respective soils. This factor effects the soils ultimate strength and moduli. The computed results showed stress levels on the relatively flat yield portion of the stress-strain diagram where small increases in loading results in large increases in displacement. The actual centrifuge loading conditions remained slightly below those which would generate "flow-type" strains and large displacements. In addition, the authors (Ref 24) acknowledged difficulties in precisely controlling the properties of the centrifuge soil deposit.

These factors combined to generate computer simulation which, though only moderately weaker in ultimate strength, caused much larger strains, hence, displacements to be generated to reach an equilibrium state of stress.

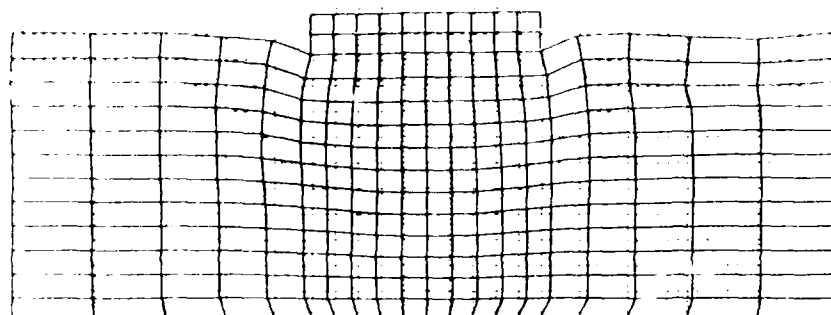
Figure 50(a, b, and c) shows the deformed mesh at  $t = 5$  seconds, 10 seconds, and 15 seconds.

Figure 51 shows the contour of the pore-water pressures at  $t = 0$  seconds, 10 seconds, and 15 seconds. Note that as observed in the test, in the "free-field" close to the sides, the pore-water pressure rises quickly (Figures 51(b),(c)). Directly under the structure, the pore-water pressure increase is slower and always remains smaller than the pore-water pressure in the free-field at the same elevation (Figures 51(b), (c)). Immediately following the shaking, the excess pore-water pressures dissipate rapidly and reach their steady state conditions 5 seconds after the end of shaking (Figure 51(d)). This condition was further illustrated in Figure 46, which shows time histories for the vertical effective stress and excess pore-water pressures for the points shown on the mesh (Figure 45(a)).

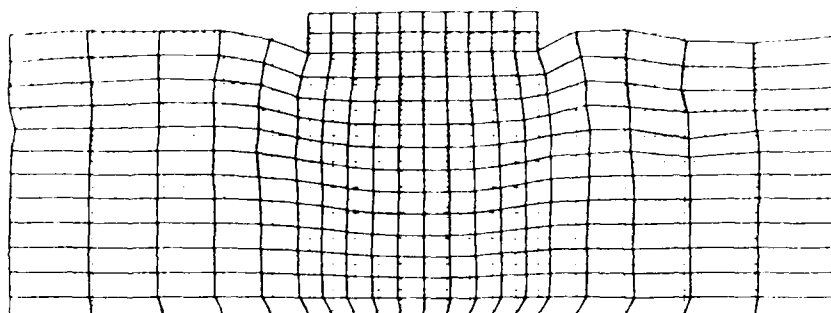
#### Retaining Wall Test

The test procedures and test results are reported in Reference 22. Leighton-Buzzard sand was used and was poured dry from a hopper behind the wall. Density was adjusted by altering the rate of flow and height of the drop. The loose backfill case ( $D_r = 55\%$ ) was selected for this analysis. A reinforced micro-concrete wall model, 175 mm high with a

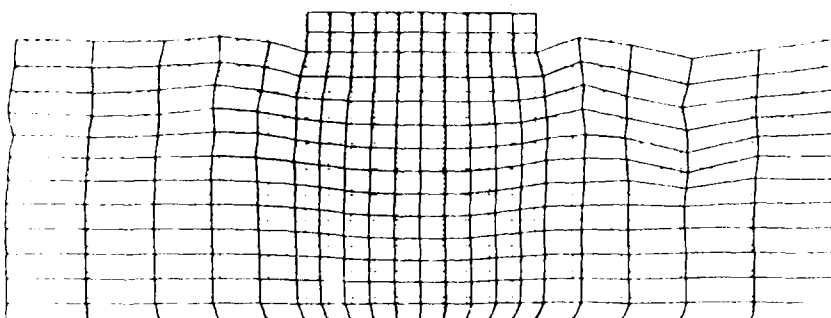




(a)  $t = 5$  seconds

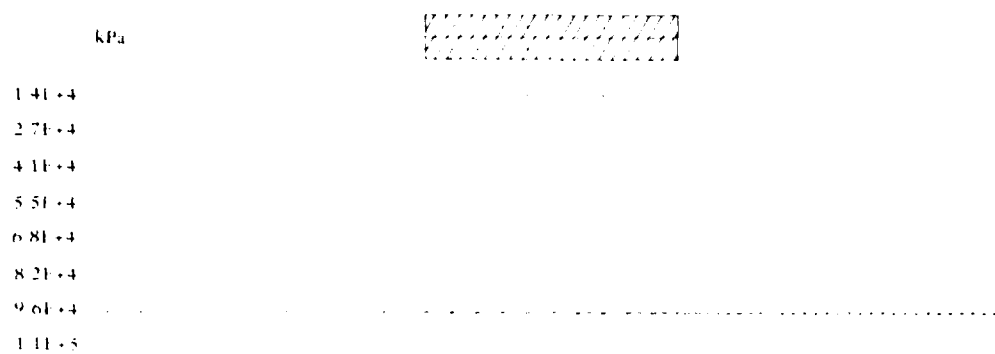


(b)  $t = 10$  seconds

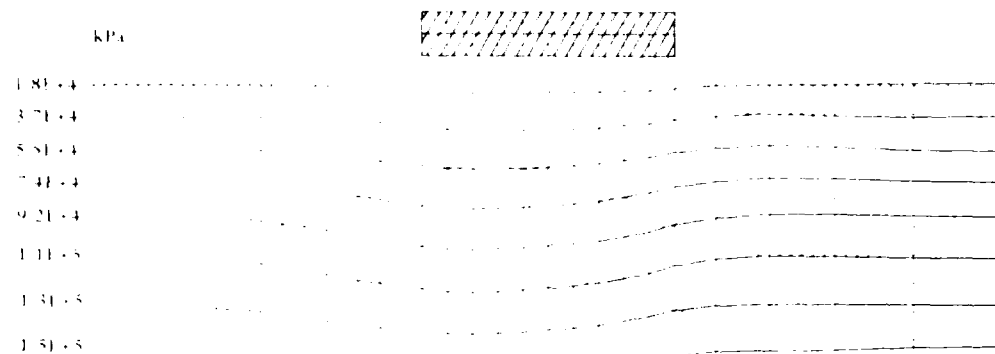


(c)  $t = 15$  seconds

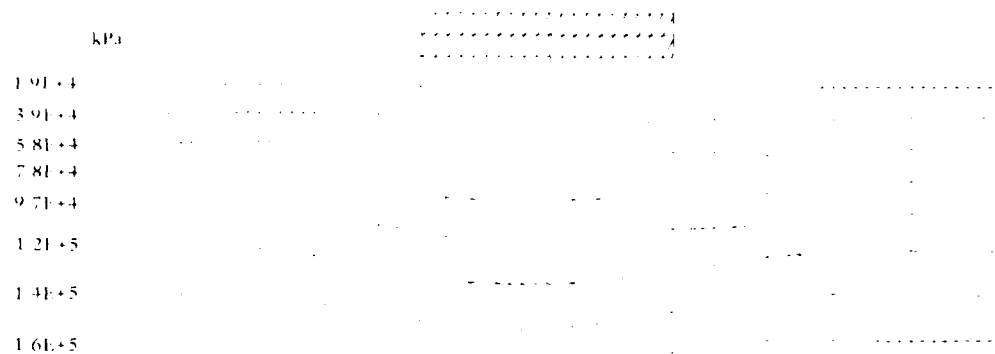
Figure 50. Deformed mesh



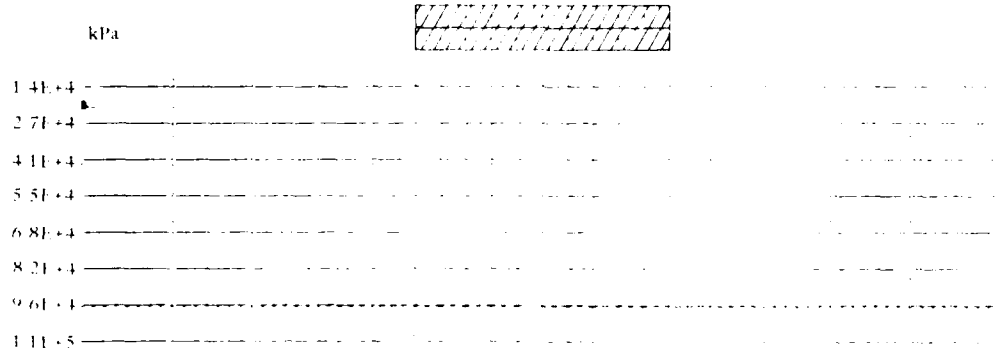
(a)  $t = 0$  second



(b)  $t = 5$  seconds



(c)  $t = 10$  seconds



(d)  $t = 15$  seconds

Figure 51. Pore pressure contours.

stem thickness of 15 mm was bolted rigidly to the test container with the sand backfill placed behind it. The model was then placed on board a centrifuge and "spun up" to a centrifugal acceleration of 80 gs. The container was then subjected to a sinusoidal input acceleration motion perpendicular to the plane of the wall. The corresponding prototype situation is analyzed hereafter.

Figure 52 shows the finite element mesh used for the analysis. The backfill is discretized by using 280 elements. The soil parameters are given in Table 4. The retaining wall is modelled by using 12 linear beam elements with  $\rho = 2.76 \cdot 10^3 \text{ kg/m}$  (mass per unit length),

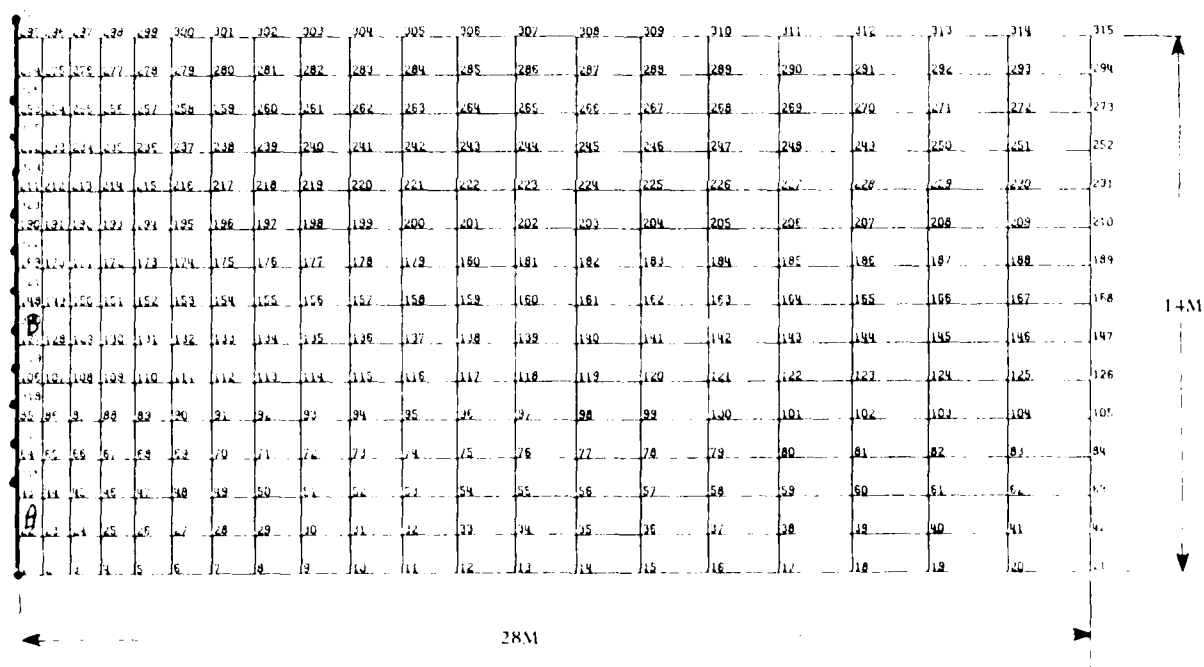


Figure 52. Undeformed mesh used for retaining wall test.

$E = 1.70 \times 10^{10} \text{ N/m}^2$  (Young's modulus),  $G = 6.54 \times 10^9 \text{ N/m}^2$  (shear modulus),  $I = 1.44 \times 10^{-1} \text{ m}^4$  (bending moment of inertia); and  $A = 1.20 \text{ m}^2$  (cross-section area). The soil and wall subdomains are interfaced by using 14 slide line elements, with  $K = 10^{10}$  (penalty parameters). Also, the interface between the wall and the backfill is assumed frictionless.

The bottom boundary is assumed rigid and the side boundary smooth in the vertical direction.

The computed wall crest deflection under gravity load is 4.55 cm, which compares favorably with the measured test value (4.7 cm).

In order to simulate the dynamic test conditions, the same sinusoidal horizontal acceleration was imposed on the bottom boundary nodes and the soil right side boundary, with a maximum acceleration = 0.20 g and a frequency of 0.75 Hz for 16 seconds (12 cycles).

Figure 53 shows the computed horizontal acceleration time histories at the bottom (Figure 53(a)) and at the top (Figure 53(b)) of the wall. Note that as the result of the interaction with the nonlinear soil mass, the computed response at the top of the wall is amplified and exhibits superharmonics (typical of nonlinear systems). Figure 54(a) shows the computed horizontal displacement at the top of the wall. The amplitude of alternating crest deflection is 3.725 cm which compares most favorably with the recorded amplitude ( $0.50 \times 80 = 4 \text{ cm}$ ) in the test (Ref 22).

Figure 54(b) shows the computed vertical displacement of the top soil element at the interface with the wall. Although sinusoidal in shape, this motion occurs with a much longer period (about 12.5 seconds) than the input horizontal motion (1.33 seconds).

Figure 55 shows the computed vertical, horizontal, and shear stress time histories, normalized by dividing them by the initial vertical stress, close to the base of the wall (Figure 55(a), element A in Figure 52) and at midheight (Figure 55(b), element B in Figure 52). At midheight, initially, an active state of stress prevails and  $K_a = 0.40$ . As a result of the stress concentration at the corner, initially,  $K = 0.675$  at the bottom, closer to a passive state. As a result of the shaking, the lateral stress fluctuates and exhibits a net decrease at the bottom of the wall ( $K \approx 0.35$  after 12 cycles), but stays about the same at midheight.

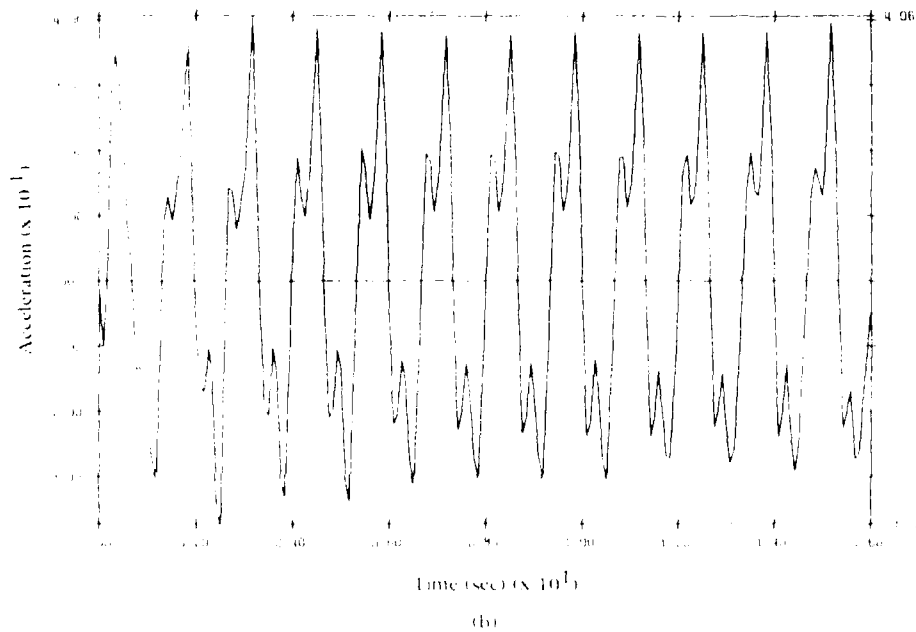
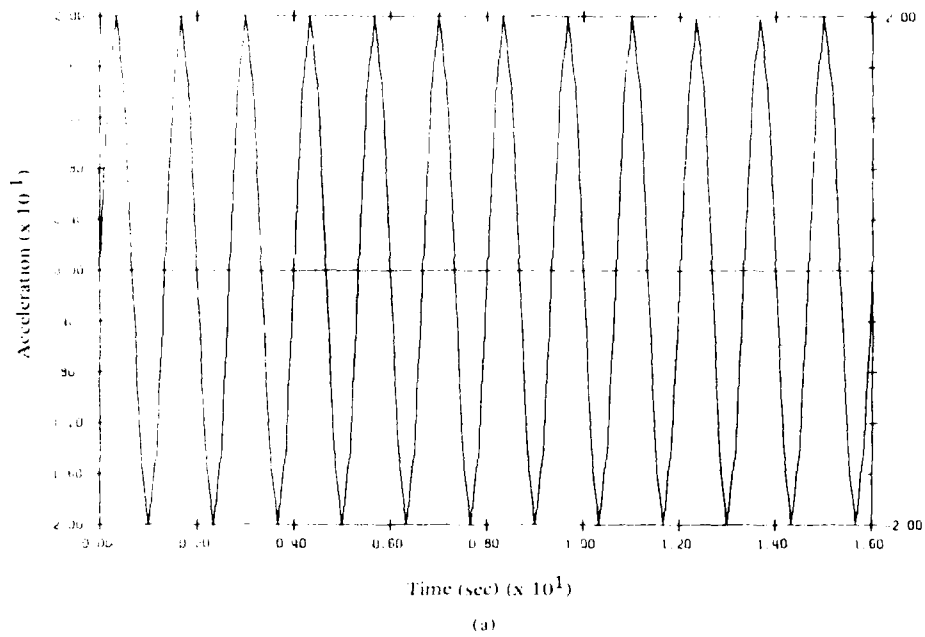


Figure 53. Input horizontal accelerations and resulting accelerations at top of retaining wall.

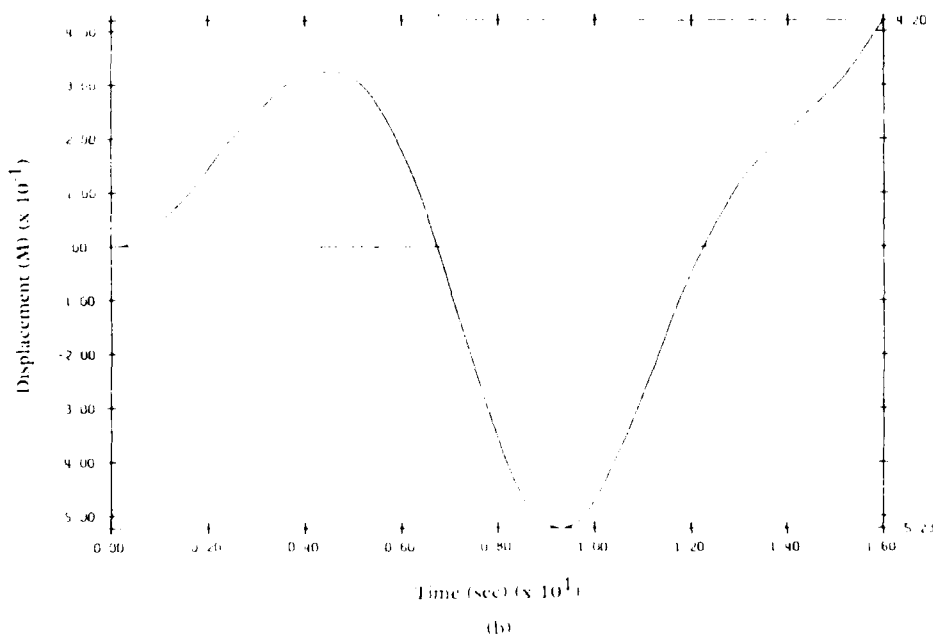
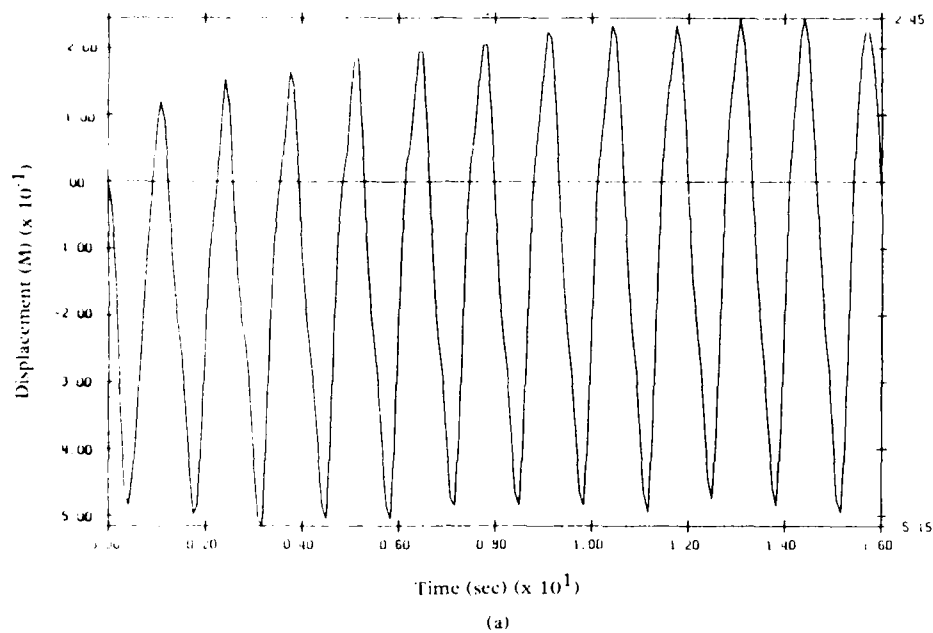


Figure 54. Horizontal displacements at the top of retaining wall and vertical motions in soil-structure contact.

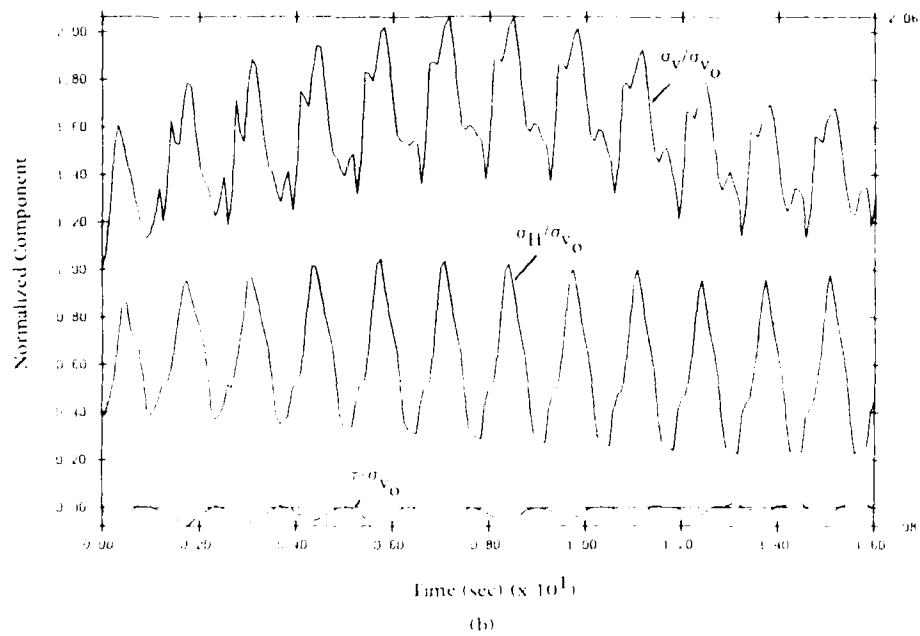
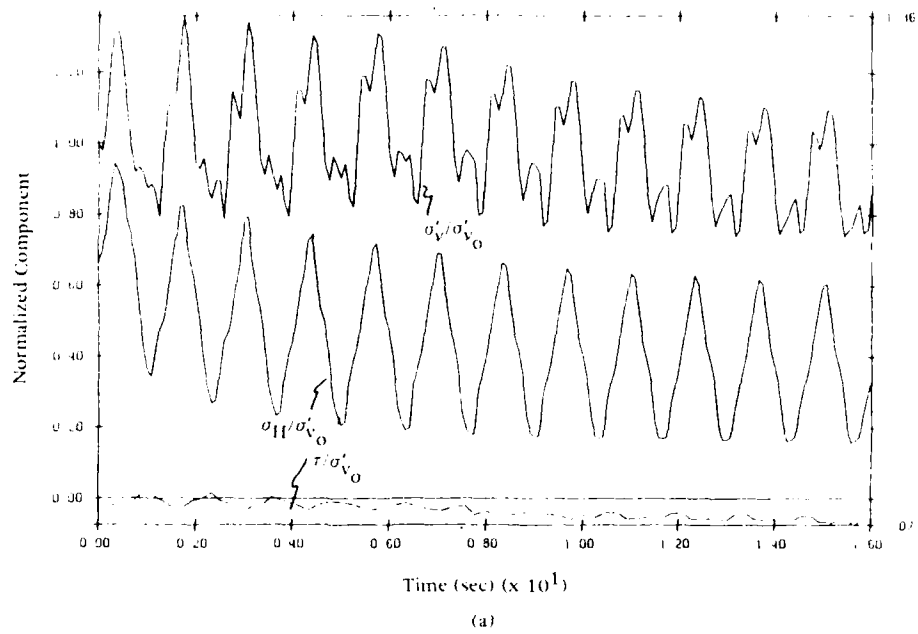


Figure 55. Normalized vertical, horizontal, and shear stresses.

## Storage Tank Test

The centrifuge model consisted of a storage tank placed over a soft foundation strata. The tank model was constructed of rolled aluminum plate, which formed the walls. The base consisted of a flexible, rubber membrane to approximate the conditions of a prototype tank's flexible base. A cross section of the model package is presented in Figure 56.

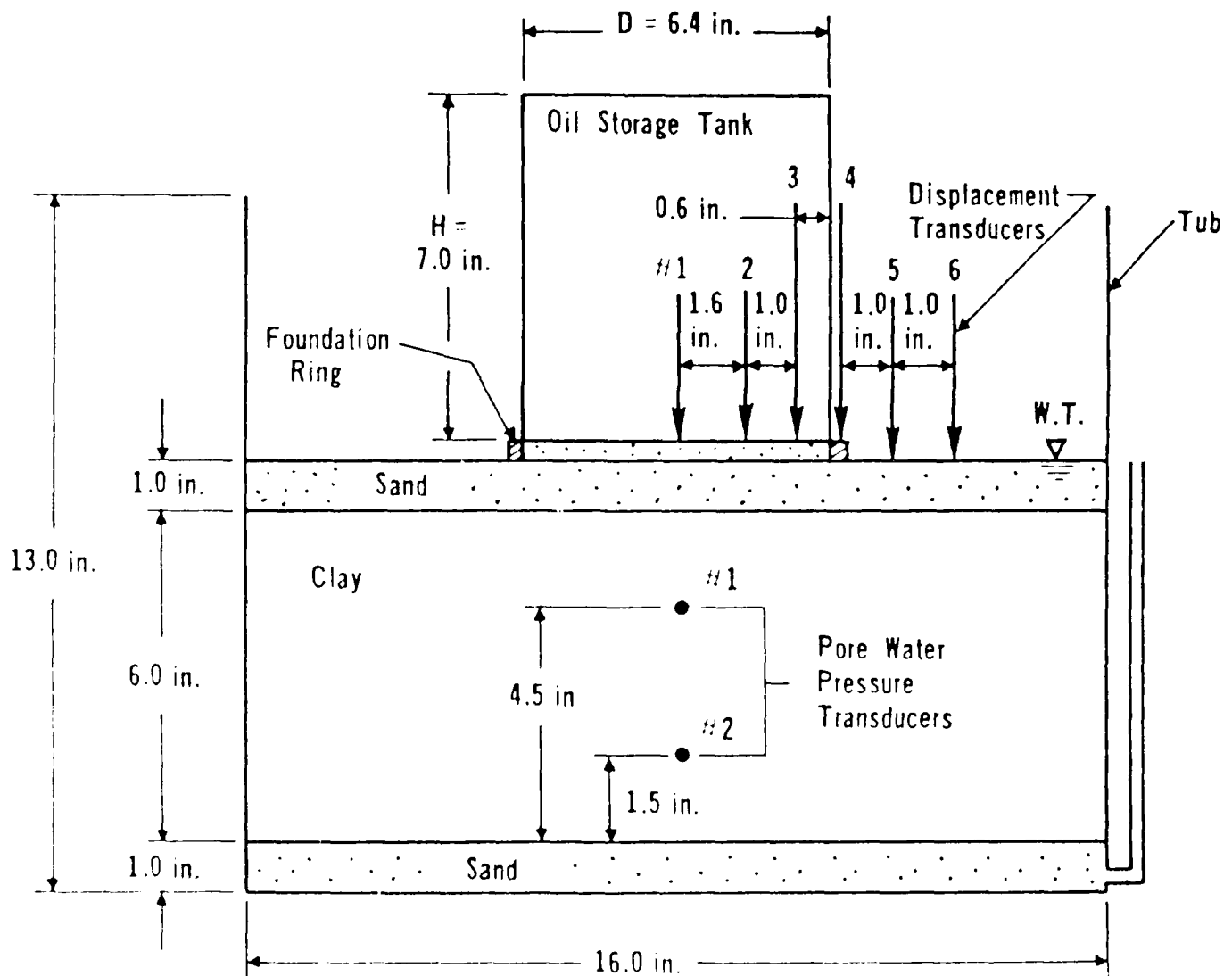


Figure 56. Model tank package.



The model was then mounted on a centrifuge and accelerated to 60 gs. The model was maintained at this acceleration for 6,000 seconds to allow for consolidation to take place. Once hydrostatic conditions were reached, the simulation of the tank loading and unloading began, Figure 56. Pore pressures and surface displacements were recorded through an automated data acquisition system. More detailed information can be found in Reference 44.

The material model properties for the kaolinite simulation were derived from undrained triaxial compression and extension tests presented above. The results of the material model fitting process are shown in Figure 35. The triaxial test data for the extension test was scaled from its original confining pressure to be at the same confining pressure as the compression test as required for input to Program MUD. The effect of this scaling on the final solution was minimal.

The material model properties for the layers of Monterey "0" sand were constructed from test data presented above. Modifications were made to the critical stress ratio, parameters to reflect a somewhat higher relative density, which was back calculated from the weight of the sand used in this test. Triaxial test data were not available for the sand used in this test.

The finite element model consisted of 16 sand and 48 clay elements as shown in Figure 57. The tank loading and unloading was simulated by a uniform pressure distribution over the inner four elements as shown in Figure 57. To properly initiate the stresses and consolidation characteristics of the model, the problem was started at an initial gravity of zero, and then increased to the required 60 level over a time period of 250 seconds. The model was then maintained at this acceleration level throughout the test. After the appropriate time period for consolidation (6,000 seconds) the loading-unloading simulation began. The loading-unloading simulation consisted of three filling and two releasing steps. The entire trace of the loading is shown in Figure 58. Each loading increment consisted of a 125-second load step and 1,875 seconds of dissipation to allow for consolidation time.

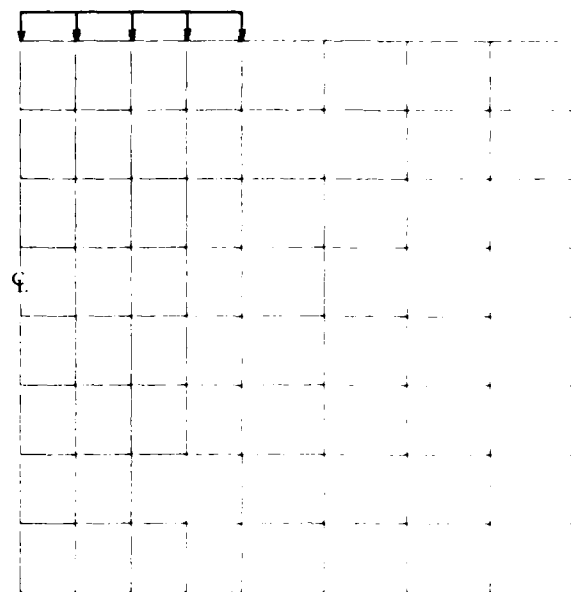


Figure 57. Undeformed mesh used for model storage tank test.

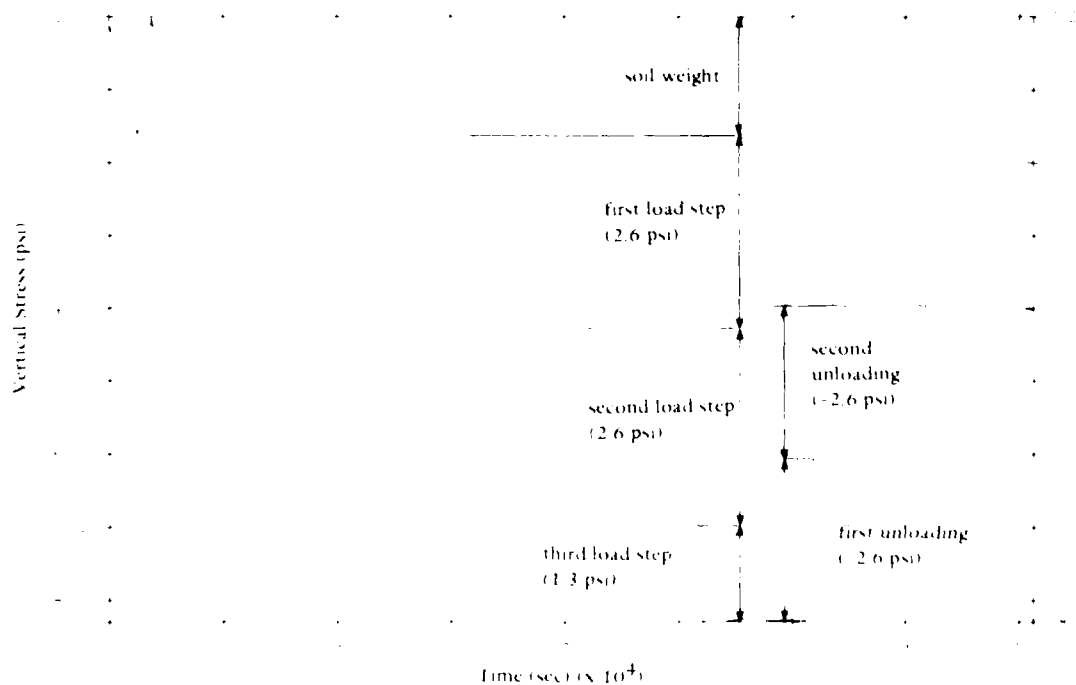


Figure 58. Pressure loading sequence.

Because this is a layered system, which is similar to those found in nature, it is important to correctly capture the effects of all of the layers on the system response. The displacement traces shown in Figures 59 and 60 show the instantaneous settlement of the sand. Displacement characterization overall is in good agreement while the actual measurements are acceptable. There was some difficulty in the degree of rebound that the numerical model exhibited. The errors here are caused by the difficulty in determining the correct input parameters for the material model as well as soil deposit inconsistencies in placement and uniformity acknowledged by the original investigators. The pore-pressure traces (Figure 61) are in excellent agreement with those measured during the test. Dissipation is represented with excellent accuracy in all cases demonstrating Program DYNAFLOW's capability in modeling threedimensional consolidation problems.

Comparing Program DYNAFLOW's prediction and those of the finite element code used by the original investigators (Reference 45) show the Program DYNAFLOW analysis has greater capabilities. This is primarily due to the ability of the Princeton Effective Stress Soil Model to characterize both sands and clays, as opposed to modeling the sand as a quasi-elastic soil as was done in Reference 45. The prototype, as simulated in this configuration, was not highly sensitive to this assumption of elasticity, as the problem is largely dependent on only one parameter--the consolidation coefficient. However, further attempts at modeling more complex and varied systems will require the ability to model all materials present in the system as is done in the Princeton Effective Stress Soil Model.

#### DYNAFLOW ADINA COMPARISON

To evaluate the relative computational efficiency and algorithm accuracy of Program DYNAFLOW, several comparative total stress analyses were run using DYNAFLOW and a well recognized non-linear finite element

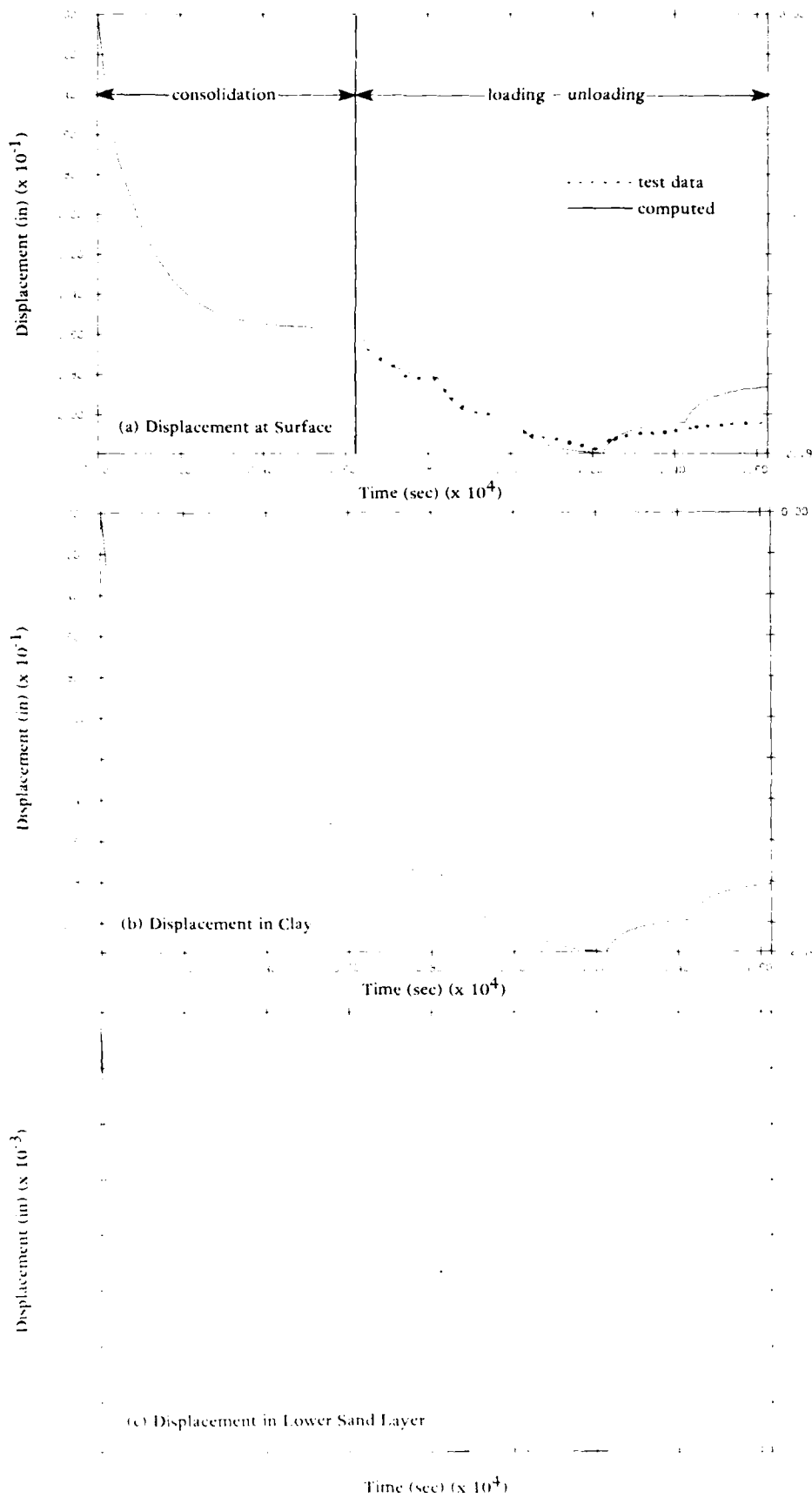


Figure 59. Vertical displacement along centerline.

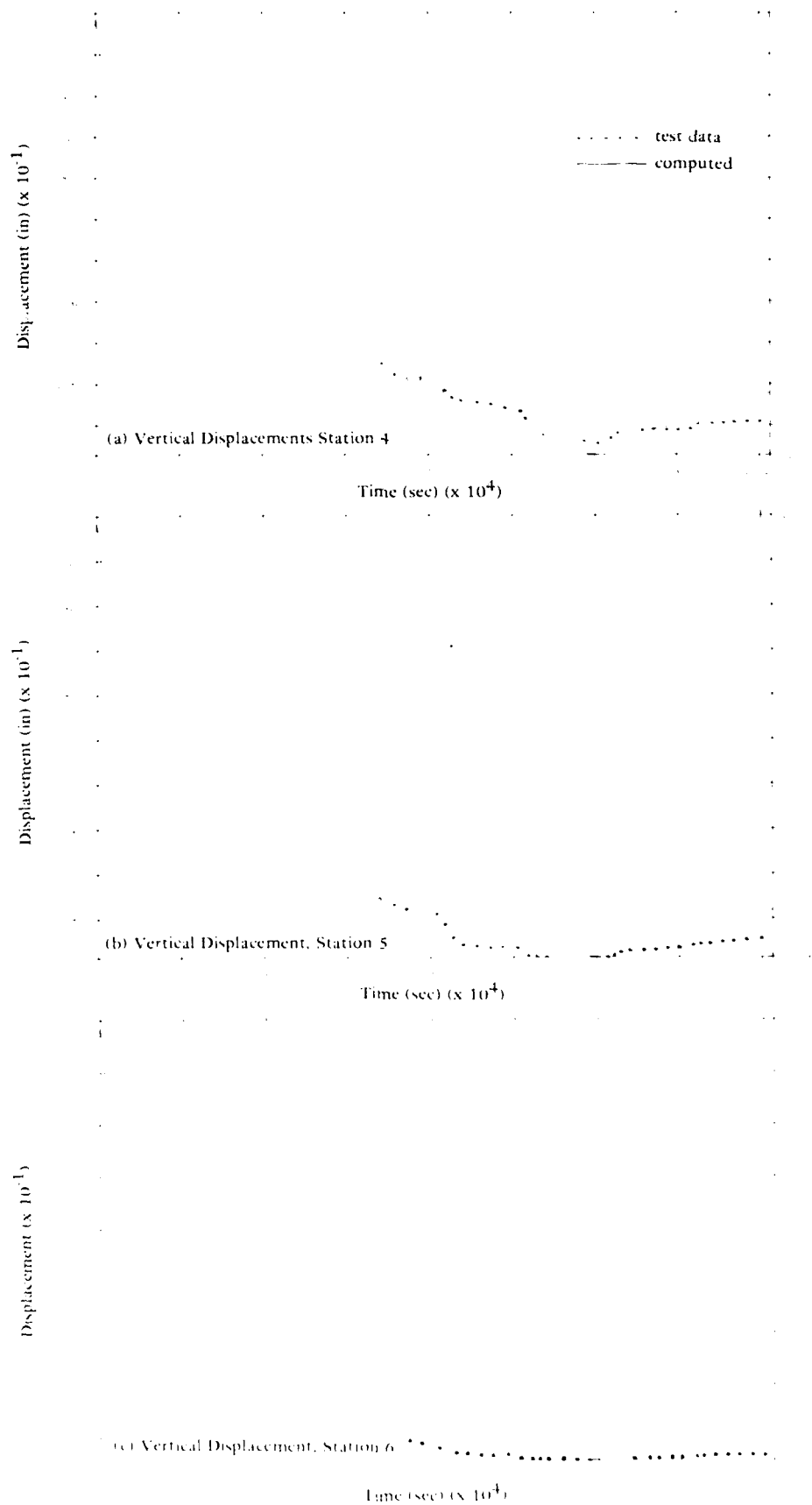


Figure 60. Free-field displacements.

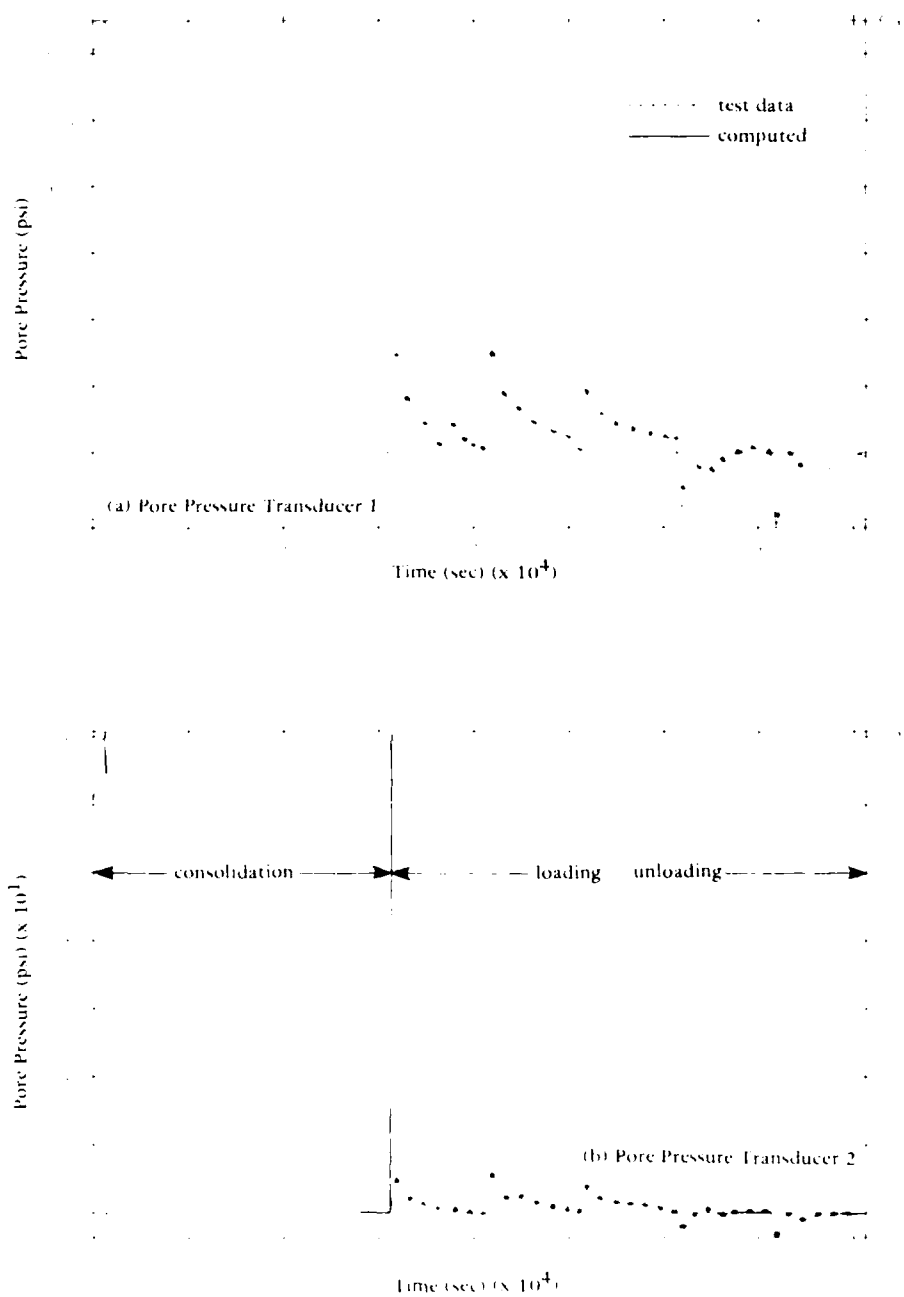


Figure 61. Pore-pressure traces.

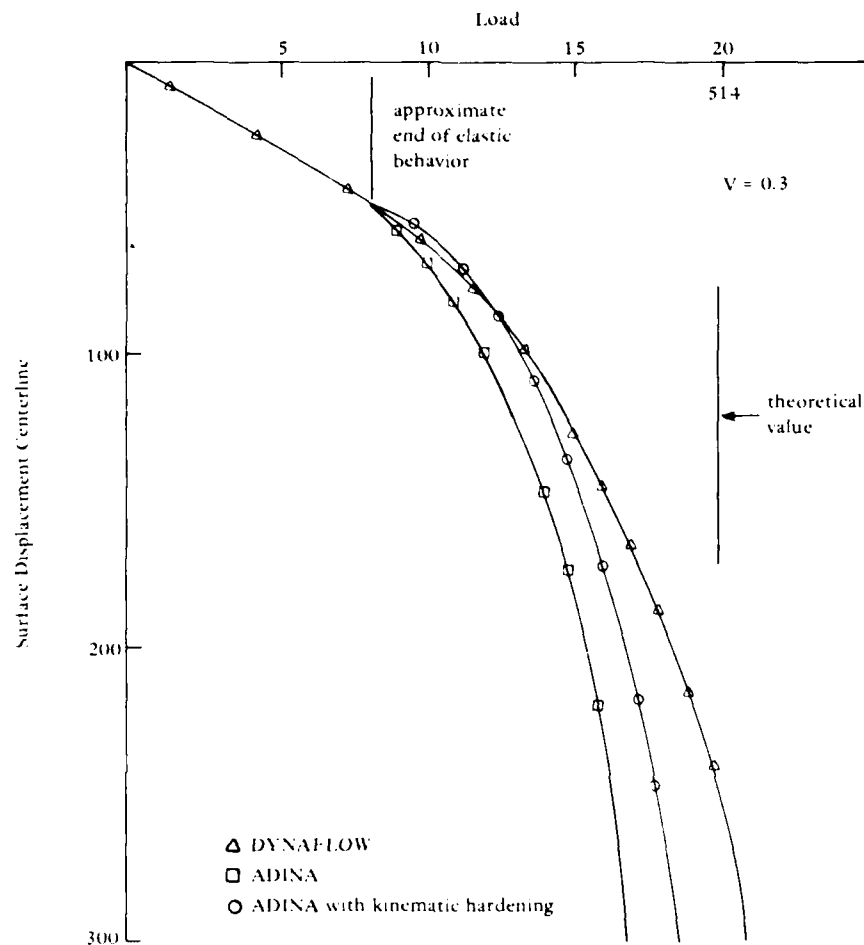


Figure 62. DYNALOW-ADINA comparison load versus displacement, case I.

Program, ADINA. Because ADINA has only total stress capability, a constitutive model other than the Princeton Effective Stress Soil Model had to be selected. The Von Mises model is included in both computer programs and was judged best for a straightforward comparison.

The problem selected for the analyses consisted of a pressure loading over a portion of a semi-infinite elastoplastic half space. The problem is analagous to a flexible mat foundation on which the distributed load is increased incrementally until bearing capacity failure is reached.

The theoretical solution for limit load is given by the equation:

$$P_f = (2 + \pi) C$$

where:  $p_f$  = Failure load per unit area

$c$  = Cohesion, or maximum shear strength of the material

$\pi$  = Pi

The analyses were run in three configurations to determine some of the sensitivities to changes in model parameters. The relative computation times, material parameters, and predicted failure loads are:

Analysis	E	C	v	$P_f$ (theoretical)	Program	$P_f$ (computed)	cpu (seconds)
I	1000.0	100.0	0.3	514.0	Adina Dynaflow	370 540	800 612
II	1000.0	100.0	0.49	514.0	Adina Dynaflow	530 525	633 465
III	5000.0	24.3	0.30	125.0	Adina Dynaflow	120 137	620 418

E = Young's Modulus

C = Cohesion

v = Poisson's Ratio

The resulting load-deformation curves for cases I and II are presented in Figures 62 and 63. Note in Figure 62 an additional analysis using Program ADINA is included with a plastic modulus of 1.0 which adds a significant amount to the total stiffness of the foundation system. In Figure 63 the solutions seem to change their respective "soft versus stiff" relationship present in Figure 62.

This case is a representation of response for a semi-incompressible material (Poisson's ratio = 0.49). The stiffened response in the program ADINA load-displacement history is a result of the locking phenomena generated from incompressible elements. As Poisson's ratio



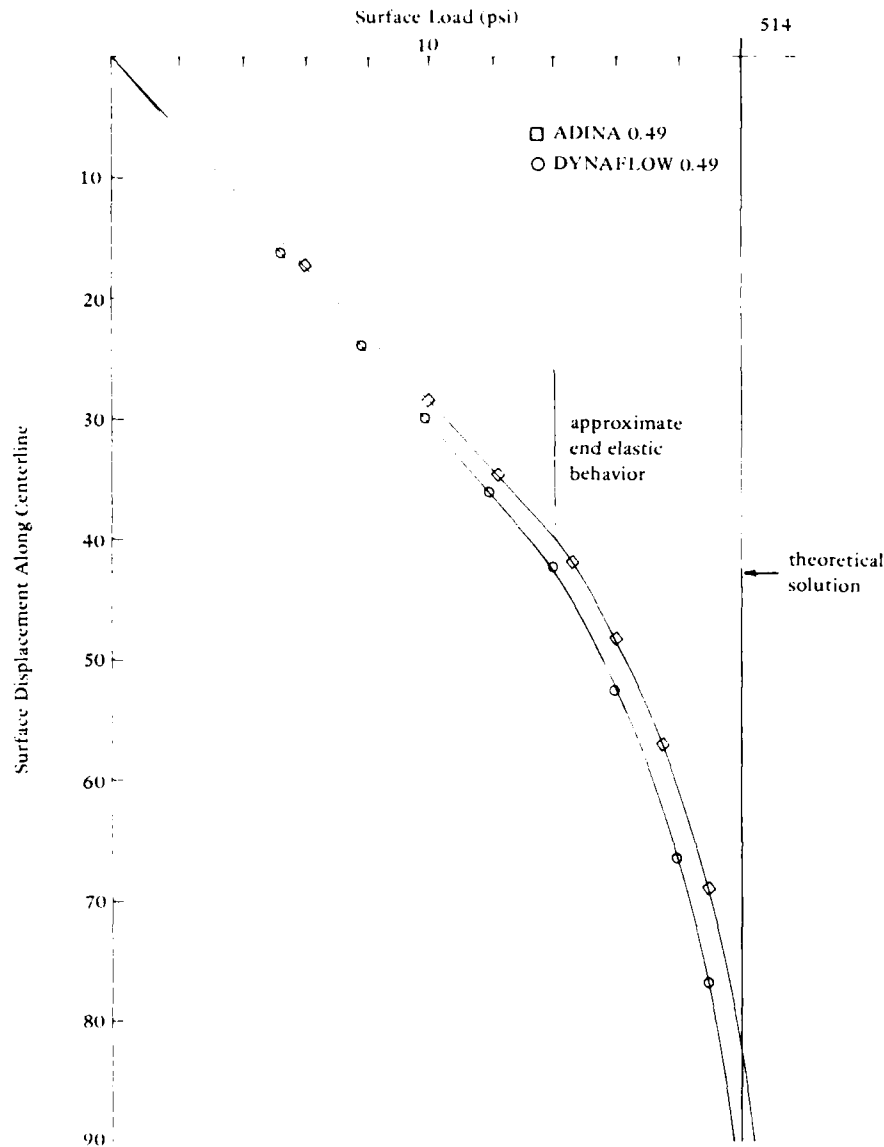


Figure 63. DYNAFLOW-ADINA comparison load versus displacement, case II.

approaches 0.5 the stiffening becomes more pronounced. The solution using Program DYNAFLOW involves a reduced integration on the volumetric stiffness contribution, and prevents the locking phenomena.

Case III is a comparison of the results from ADINA, DYNAFLOW, and a solution presented in Reference 44. Poisson's ratio is again reduced to 0.3 and the differences in the ADINA and DYNAFLOW (Figure 64) solutions become more pronounced. The differences are apparently due to material

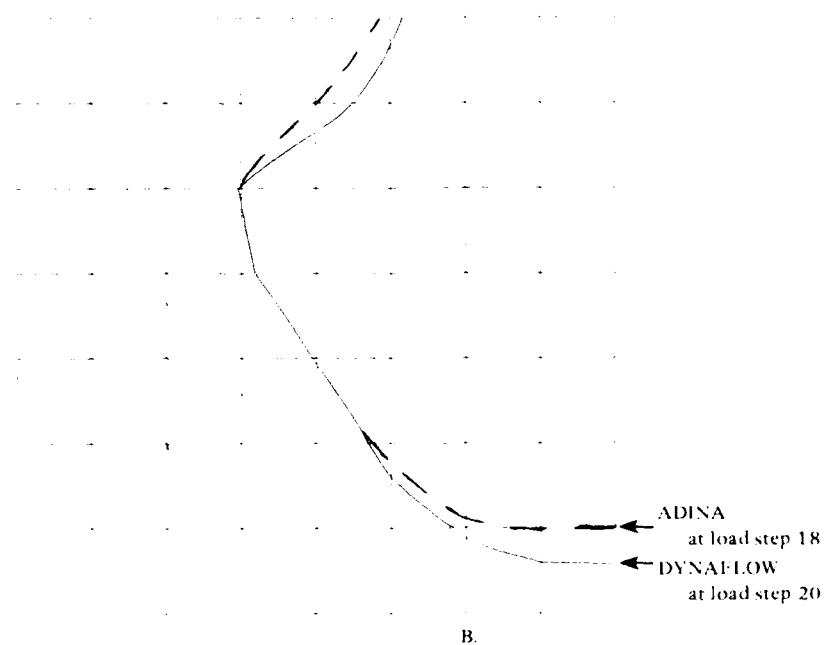
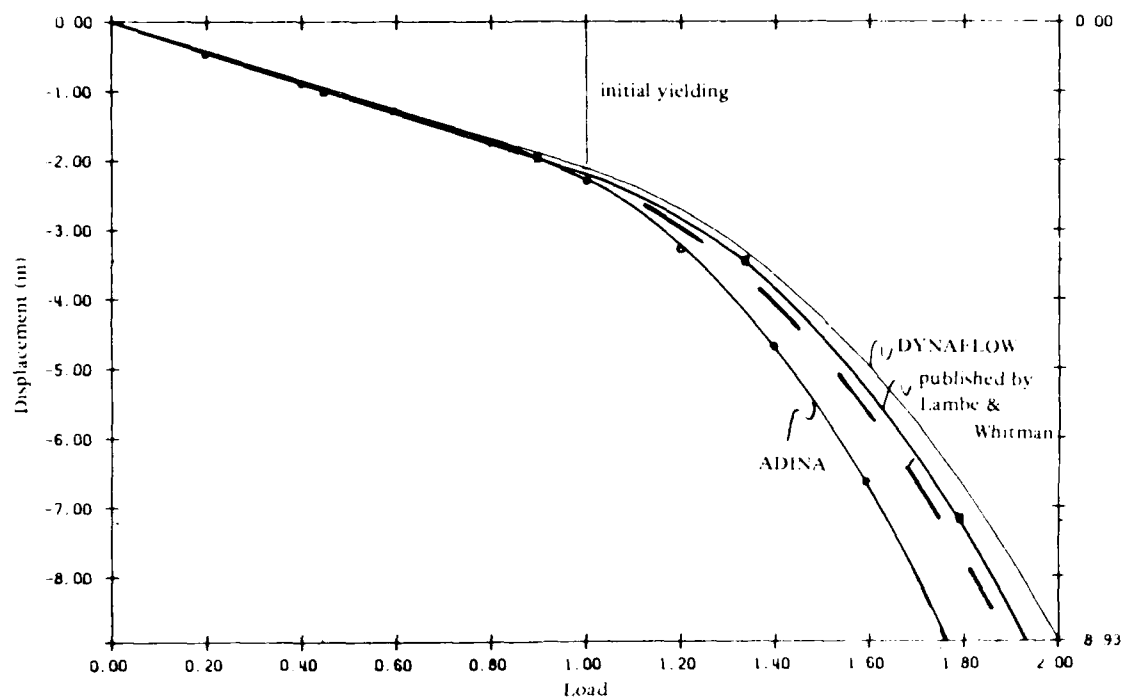


Figure 64. DYNAFLOW-ADINA comparison load versus displacement, case III.

model interpretation in the respective codes. The level of plasticity predicted by each solution is the same, at the same level of vertical deformation, which indicates the agreement of the respective strain level computations (Figure 64(b)). The stress level is however, significantly different past initial yield (Figure 64(a)).

## PILE AND PIER FOUNDATIONS

### Load Capacity

This discussion considers only straight piles driven into homogeneous deposits of cohesionless materials. Experience has shown that when piles are driven into sand, the soil near the pile is compacted to a distance of a few pile diameters. In a homogeneous sand the point resistance and average skin friction increase with depth of penetration up to a critical depth. Beyond the critical depth, the point resistance and skin friction remain almost constant; generally this is caused by soil compressibility, crushing, and arching. The empirical approach to prediction of pile behavior has proven more satisfactory than an analytical bearing capacity approach.

The load transfer mechanism between the pile and the surrounding soil governs the behavior of the pile. The design of a pile requires determination of the proportion of load transferred to the soil by adhesion and friction between the pile and the soil and that transferred by end bearing. This is influenced by the flexibility of the pile, the stiffness of the soil, and the nature of the transfer mechanisms between pile surface and soil.

Through use of instrumented field and model studies, the design of piles and piers has been better understood. Figure 65 illustrates use of pile-driving resistance formulas to estimate individual allowable pile loads. Figure 66 illustrates the calculation of ultimate load capacity of piles in cohesive soils, and Figures 67 and 68 illustrate the calculation of load capacity of piles in cohesionless soils. However, these conventional ultimate design approaches assume the simultaneous and full mobilization of pile shear resistance and base bearing, which is not well founded. Studies have shown that movement of a pile must be present to mobilize its load-carrying capacity.

Reese and O'Neill (Ref 47) show that the division of load between sides and base for a pier on stiff clay is dependent on the total loading (Figure 69). The first two load increments show that almost all of the load is carried by friction; as the load increases, more is carried

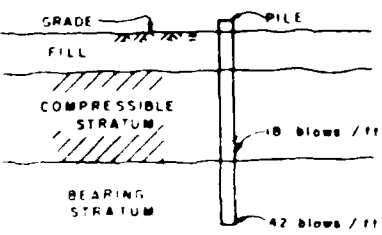
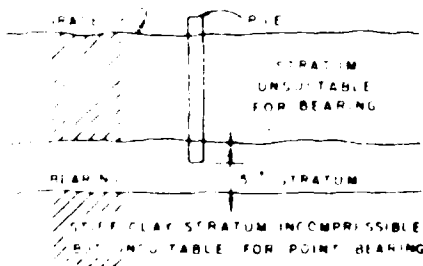
Basic pile driving formulas		
For drop hammer	For single-acting hammer	For double-acting differential hammer
$Q_{all} = \frac{2WH}{S+1}$	$Q_{all} = \frac{2WH}{S+0.1}$ { Use when driven weights are smaller than striking weights. $Q_{all} = \frac{2WH}{S+0.1} \frac{W_D}{W_S}$ { Use when driven weights are larger than striking weights.	$Q_{all} = \frac{2E}{S+0.1}$ { Use when driven weights are smaller than striking weights. $Q_{all} = \frac{2E}{S+0.1} \frac{W_D}{W_S}$ { Use when driven weights are larger than striking weights.
<p> <math>Q_{all}</math> = allowable pile load in pounds  <math>W</math> = weight of striking parts of hammer in pounds.  <math>H</math> = the effective height of fall in feet  <math>E</math> = the actual energy delivered by hammer per blow in foot-pounds  <math>S</math> = average net penetration in inches per blow for the last 6 in. of driving  <math>W_D</math> = driven weights  <math>W_S</math> = weights of striking parts } Note Ratio of driven weights to striking weights should not exceed 3. </p>		
Modifications of basic pile driving formulas		
<p>A. For piles driven to and seated in rock as high capacity end-bearing piles</p> <p>Drive to refusal (approximately 4 to 5 blows for the last quarter inch of driving)</p> <p>Redrive open end pipe piles repeatedly until resistance for refusal is reached within 1 in. of additional penetration.</p>		
<p>B. Piles driven through stiff compressible materials unsuitable for pile bearing to an underlying bearing stratum:</p> <p>Add blows attained before reaching bearing stratum to required blows attained in bearing stratum (see example).</p> <div style="display: flex; align-items: flex-start;"> <div style="flex: 1;">  </div> <div style="flex: 1;"> <p>Example required load capacity of pile <math>Q_{all} = 25</math> tons  hammer energy <math>E = 15,000</math> ft-lb</p> <math display="block">\frac{W_D}{W_S} &lt; 1</math> <p>Penetration(s) as per basic formula = <math>\frac{1}{2}</math>" or 2 blows per inch (24 blows/ft)</p> <p>Required blows for pile <math>24 + 18 = 42</math> blows/ft</p> </div> </div>		
<p>C. Piles driven into limited thin bearing stratum, drive to predetermined tip elevation. Determine allowable load by load test</p> <div style="display: flex; align-items: center;">  </div>		

Figure 65. Pile-driving resistance formulas (Ref 45).

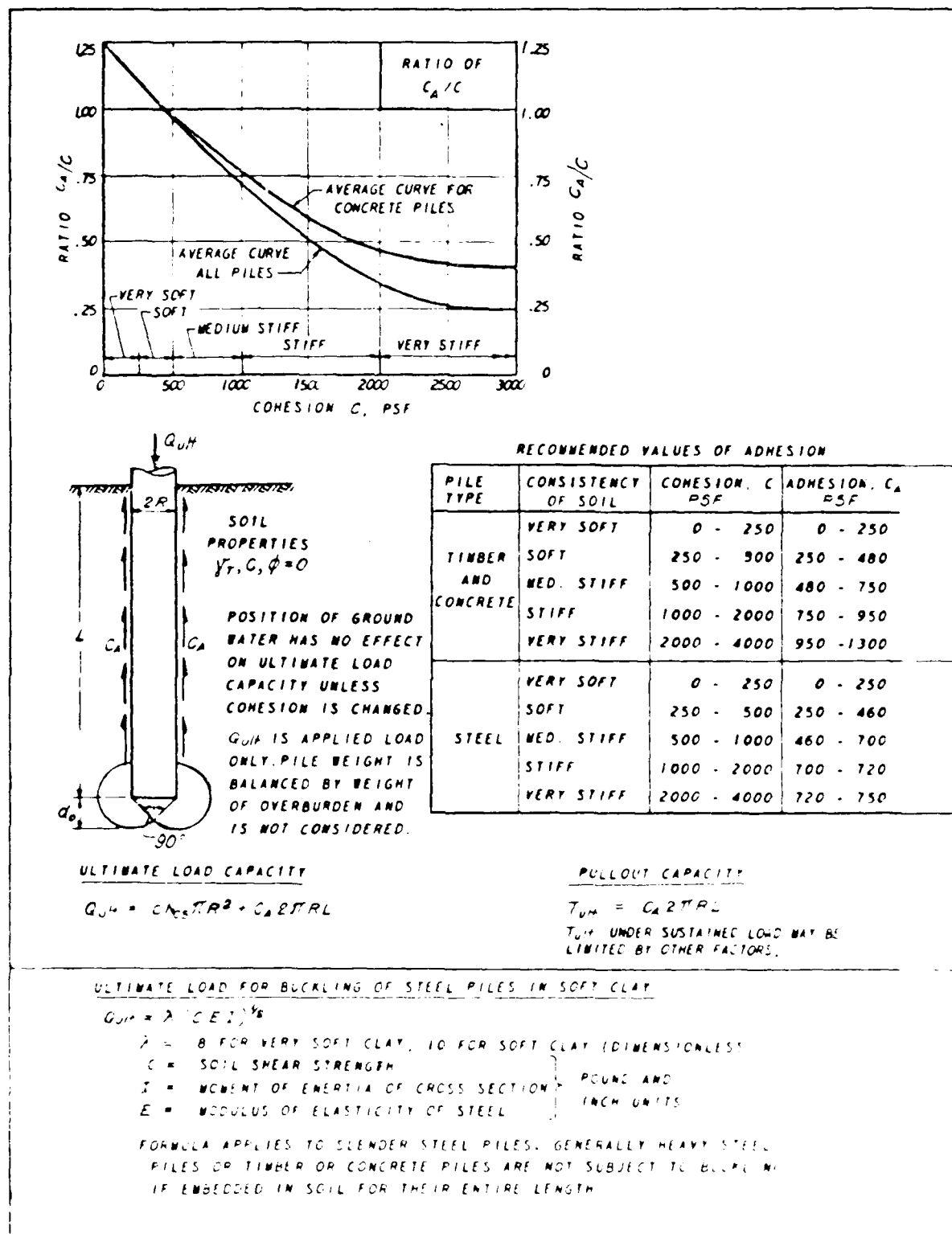
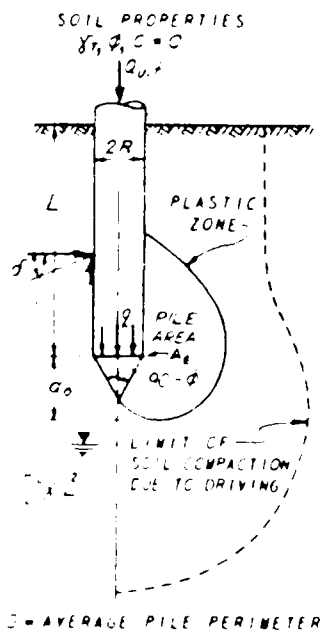
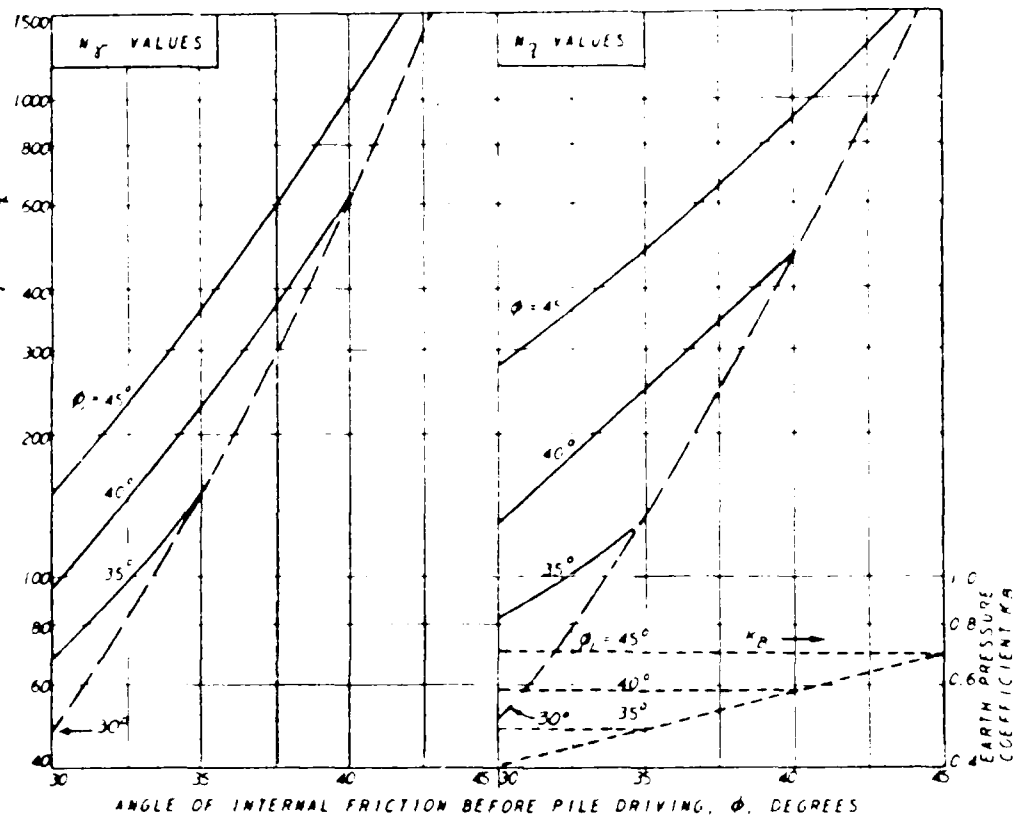


Figure 66. Ultimate load capacity of piles in cohesive soils (Ref 45).



DEFINITIONS:

PILE IS DRIVEN WITHOUT JETTING OR REMOVAL OF MATERIAL WITHIN PILE.

$C_{ult}$  = ULTIMATE LOAD CAPACITY, APPLIED LOAD ONLY

$Q$  = ULTIMATE BEARING CAPACITY AT TIP.

$Q_{UN}$  = ULTIMATE LOAD CAPACITY, APPLIED LOAD ONLY  
 $Q$  = ULTIMATE BEARING CAPACITY AT TIP.  
 $K_H$  = RATIO OF HORIZONTAL TO VERTICAL EARTH PRESSURE  
 ON SIDE OF PILE ABOVE PLASTIC ZONE. AVERAGES  
 0.5 FOR  $\phi = 30^\circ$ , 1.0 FOR  $\phi = 45^\circ$ .

$K_B$  = RATIO OF HORIZONTAL TO VERTICAL EARTH PRESSURE  
ON SIDE OF PILE WITHIN PLASTIC ZONE.

$\phi_1$  = ANGLE OF INTERNAL FRICTION IN COMPACTED ZONE  
AROUND PILE TIP ( $4^\circ$  TO  $5^\circ$  LARGER THAN  $\phi$ ).

$$Q_{UH} = Q_{AS} + \left( \frac{K_H}{2} r_T L^2 \tan \sigma' \right) S \quad (\text{WATER BELOW } \sigma_c)$$

$$G = Y_T R N_T + K_B Y_T L N_2 - Y_T L \quad \text{FOR } L \geq 20R$$

$$Q = \frac{\dot{m}}{20R} (T_{RN_2} + n_2 T_{CN_2}) = 67.2 \quad \text{FOR } L = 20R$$

### EFFECT OF WATER

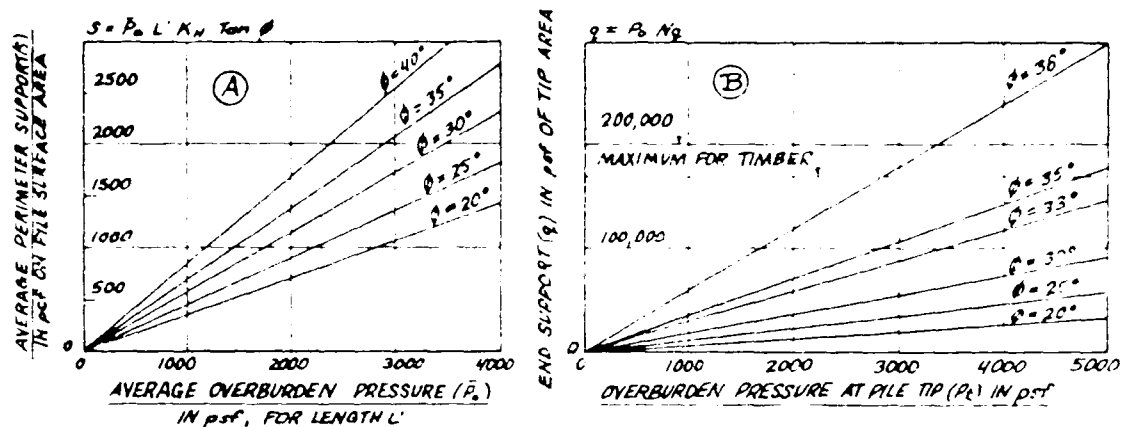
WATER AT GROUND SURFACE

SUBSTITUTE  $Y_{SUB}$  FOR  $Y$ , IN  $\Delta_{11}$

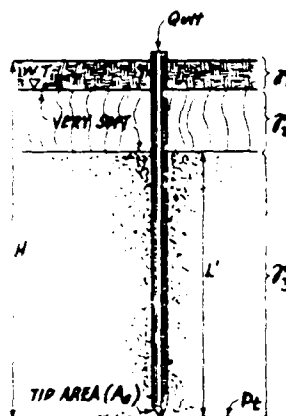
FOR WATER AT INTERMEDIATE LEVEL INTERPOLATE  
BETWEEN LIMITING CONDITIONS

PULLOUT CAPACITY =  $T_{LH} = 9 \left( \frac{1}{2} \pi \right) \gamma_v L^2 \tan \phi'$

116



WHERE :  $\phi$  = ANGLE OF INTERNAL FRICTION OF SOIL.  
 $K_H$  = RATIO OF HORIZONTAL TO VERTICAL EARTH PRESSURE ON SIDE OF PILE  
 TAKEN TO BE EQUAL TO 1.0 IN GRAPH (A)  
 $L'$  = LENGTH OF FIRM EMBEDMENT  
 $N_q$  = VALUES USED IN CHART (B) ARE TAKEN FROM FIGURE 34



EXAMPLE SECTION

#### DEFINITIONS

$Q_{ult}$  = ULTIMATE PILE LOAD CAPACITY.  
 = PERIMETER SUPPORT + END SUPPORT.  
 =  $S \times \text{SURFACE AREA} + q \times \text{END AREA}$ .  
 "S" VALUES IN GRAPH (A) ARE FOR STRAIGHT CONCRETE PILES.  
 FOR TAPERED PILES, DUE TO INCREASED  $K_H$ , USE 2X VALUES IN (A).  
 FOR STEEL OR TIMBER, DUE TO LOWER COEFFICIENT OF FRICTION,  
 USE 0.75 X VALUES IN (A).

$\gamma_1, \gamma_2, \gamma_3$  = UNIT WEIGHTS OF SOIL, BY STRATA.  
 (SUBMERGED WTS BELOW WATER TABLE (WT).)

#### EXAMPLE PROBLEM: DETERMINE $Q_{ult}$

WITH: LENGTH (H) = 40',  $L' = 25'$ ;  $\gamma_1 = 65 \text{ pcf}$   $\phi = 30^\circ$

AVERAGE DIAMETER = 10"  $\gamma_2 = 25 \text{ pcf}$  FOR 13'

TIP AREA = 0.34 sq ft  $\gamma_3 = 80 \text{ pcf}$  FOR 2'

TIMBER PILE (CONSIDERED TAPERED)

$Q_{ult}$  = PERIMETER SUPPORT + END SUPPORT

PERIMETER SUPPORT:

$$\text{AVERAGE OVERBURDEN PRESSURE } (\bar{P}_o) = \frac{(2\gamma_1 + 13\gamma_2) + (2\gamma_1 + 13\gamma_2 + 25\gamma_3)}{2}$$

$$\bar{P}_o = 1297 \text{ psf} \quad \text{ENTER (A) AT } \bar{P}_o \text{ ON } \phi = 30^\circ$$

$$S = 750 \times 2 \times 0.75 = 1125 \text{ psf}$$

$$S \times \text{SURFACE AREA} = 1125 \text{ psf} \times \pi \text{ DL}' = 73,000 \text{ LBS.}$$

END SUPPORT:

OVERBURDEN PRESSURE AT PILE TIP ( $P_t$ )

$$P_t = 2\gamma_1 + 13\gamma_2 + 25\gamma_3 = 160 + 325 + 1625 = 2110 \text{ psf}$$

ENTER (B) AT  $P_t = 2110$  AND  $\phi = 30^\circ$

THEN  $q = 38,000 \text{ psf}$

$$q \times A_o = 38,000 \text{ psf} \times 0.34 \text{ sq ft} = 12,900 \text{ LBS.}$$

$$Q_{ult} = 73,000 \text{ LBS} + 12,900 \text{ LBS} = 86 \text{ K}$$

DESIGN LOAD =  $\frac{Q_{ult}}{\text{SAFETY FACTOR}}$

FOR CAPACITY AS A  
 TENSION PILE, USE  
 STRAIGHT PILES AND  
 USE PERIMETER SUPPORT  
 ONLY IN FIRM EMBEDMENT.

Figure 68. Ultimate load capacity of driven piles in noncohesive soils (Ref 45).

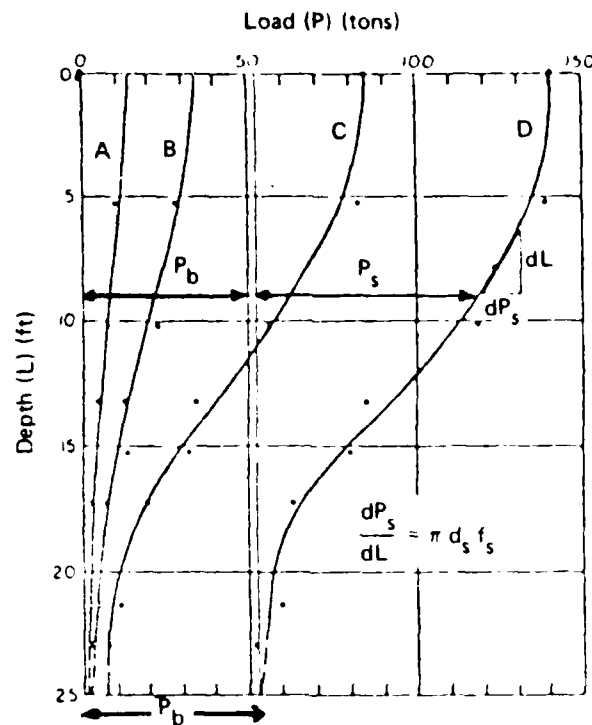


Figure 69. Load distribution for drilled shaft in stiff clay.

by end bearing. Above 80 tons, any additional load is taken by end bearing. Note how curve C simply translates to form curve D, indicating additional load is taken by end bearing. With the information in Figure 69, a typical load transfer relationship can be obtained showing side friction (Figure 70). From the slope in Figure 69, it is evident that frictional effects are greatest in the middle (depth) of the pile., and a reduction in the rate of load transfer occurs in the lower part, particularly just above the base. The distribution of frictional forces depends upon the soil type. Modifications to ultimate strength formulations have been suggested by Reese and O'Neill (Ref 47). Factors include an effective depth concept in lateral earth pressure calculation for granular soils and a friction reduction factor for ultimate resistance in cohesive soils.



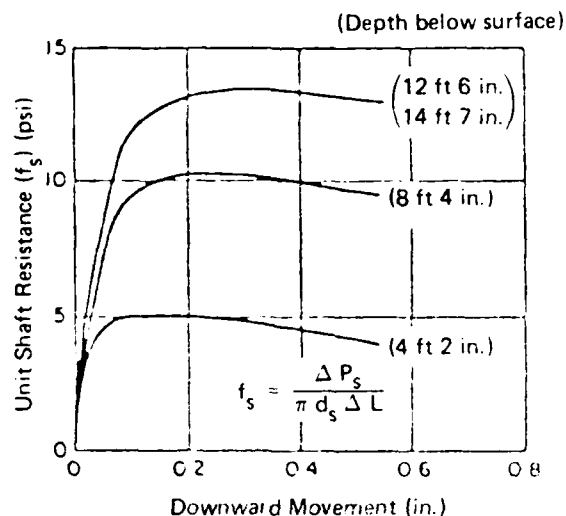


Figure 70. Load transfer to shaft segment versus movement.

A theoretical solution of the load transfer phenomenon can provide considerable insight. For instance, a soil-structure problem would be one in which the nature and mechanism of load transfer is of considerable importance. Solving this problem must focus on the stress strain characteristics of the soil and the behavior of the interface between pile and soil. Using a linear-elastic constitutive model would be a gross simplification of the real material properties. The Princeton University Soil Model offers an opportunity to explore nonlinear relationships.

Several approaches have been used to model the contact problem. Peterson (Ref 48) treats the two contacting surfaces as separate and distinct and joins them mathematically by use of Lagrange multipliers. However, this model does not allow preslip deformation. Herrman (Ref 49, 50, and 51) defines three behavior modes: nonslip, slip, and separation. A compatibility model combining compatibility and equilibrium is used. The compatibility model involves linking the two surfaces

with fictitious bond springs, and the frictional forces are applied as surface tractions. This allows a preslip deformation that would not otherwise be computed.

Another approach simply links two nodes, initially overlapping with nonlinear springs. The procedure is simple to operate but, unfortunately, may produce undesirable numerical characteristics when distinct rapid changes occur in stiffness.

Prevost has formulated a contact element in the Program DYNAFLOW. The contact element may be used to impose inequality constraints between nodes. Either friction (i.e., "stick") or frictionless (i.e., "slip") conditions may be achieved.

A contact element is defined by two nodes: a spring constant or "penalty parameter,"  $k$ , and a fixed direction vector,  $\underline{x}_A + \underline{d}_A$  where  $\underline{x}_A$  is the initial position vector and  $\underline{d}_A$  is the displacement vector. The contact plane passes through the point  $\underline{x}_A + \underline{d}_A$  and is perpendicular to  $\underline{n}$  (Figure 71(a)). The contact/release condition is defined as follows:

$$\sigma > 0 \quad \text{release}$$

$$\sigma \leq 0 \quad \text{contact}$$

where:  $\sigma = \underline{\ell} \cdot \underline{n}$

$$\underline{\ell} = \underline{x}_B + \underline{d}_B - \underline{x}_A - \underline{d}_A$$

The quantity,  $\sigma$ , is a measure of the distance between  $\underline{x}_B + \underline{d}_B$  and the contact plane. When contact is noted, a contact element stiffness and out-of-balance force are added to the global equations.

If  $k > 0$  is sufficiently large, the point  $\underline{x}_B + \underline{d}_B$  will be forced to lie (approximately) on the contact plane. In subsequent steps, only the stiffness is assembled, and the decision to remain in contact or to release is made on the basis of the sign of  $\sigma$ , as above.

For interpreting output, the contact element "displacement" is defined as  $\sigma$ , and the "force" is given by:

$$k\sigma \quad \text{if } \sigma < 0$$

$$0 \quad \text{if } \sigma \geq 0$$

In addition to the contact element, Prevost (Reference 38) has defined a slide element. The slide-line element may be used to impose inequality constraints between nodes. Either friction or frictionless conditions may be achieved.

A slide-line element is defined by three nodes and a spring constant or penalty parameter,  $k$ . The connection from node A to node B defines the slide-line direction, and node C is the contact node (Figure 71(b)).

The projected distance of node C to node A onto the slide-line direction is denoted by  $\alpha$  and is given by:

$$\alpha = \vec{AB} \cdot \vec{AC} / AB^2 \quad 0 \leq \alpha \leq 1$$

where:  $\cdot$  = the dot product of two vectors. The direction of the unit vector  $\vec{n}$  to the slide-line direction is given by:

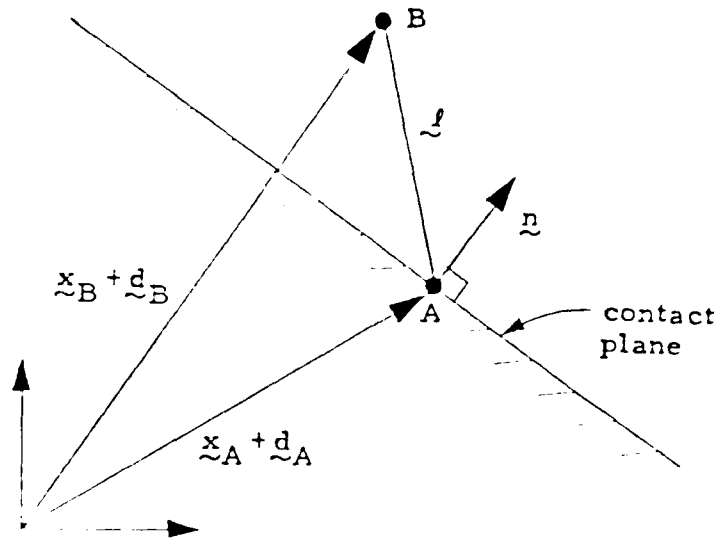
$$\vec{n} = (\vec{AB} \times \vec{AC}) \times \vec{AB} / \left| (\vec{AB} \times \vec{AC}) \times \vec{AB} \right|$$

where:  $\times$  denotes the cross product of two vectors. The local contact stiffness matrix  $\underline{k}$  is given by:

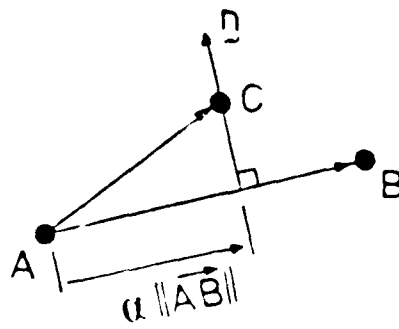
$$\underline{k} = k \begin{bmatrix} (1 - \alpha)^2 & \alpha(1 - \alpha) & -(1 - \alpha) \\ \alpha(1 - \alpha) & \alpha & -\alpha \\ -(1 - \alpha) & -\alpha & 1 \end{bmatrix}$$

where the rows and columns are arranged such that the first, second, and third rows (columns) correspond to nodes A, B, and C, respectively. The contact/release condition is defined as follows: (1) in two dimensions, if  $0 \leq \alpha \leq 1$  and  $\vec{AB} \cdot \vec{n} \leq 0$ , contact (otherwise, release); and (2) in three dimensions, if  $0 \leq \alpha \leq 1$ , then contact (otherwise, release).

If  $k$  is sufficiently large, the point C will be forced to lie (approximately) on the slide-line AB. In subsequent steps, only the contact stiffness is assembled, and the decision to remain in contact or not is made as described above.



(a) Contact element.



(b) Slide element.

Figure 71. Contact and slide line elements.

### Cyclic Behavior of Piles

Poulos (Ref 52) concludes that ultimate load capacity and cyclic stiffness decrease with increasing numbers of cycles and increasing cycle load level. This becomes more significant when the cyclic load approaches one-half the static ultimate load. The cyclic degradation appears to begin at the top of the pile and progresses downward, resulting in a gradual transfer of load to the lower position of the pile. The crucial factor in determining the amount of cyclic degradation is the shear strain for skin friction.

Poulos (Ref 53) conducted a limited investigation of an effective stress approach to determine pore pressure increases with cyclic loading and the resulting modulus degradation factors. Figure 72 shows a compilation of observations (Ref 52) showing degradation as a function of strain ratio, where:

$$\gamma_{ss} = (0.10 \text{ to } 0.25) \gamma_s$$

and

$$\gamma_s = \text{static shear strain to failure}$$

Poulos (Ref 52) reports that "one-way" cyclic loading (i.e., cyclic loading between zero minimum load and a specified maximum) produces "two-way" loading (i.e., loading alternating between tension and compression with zero as a mean value). He points out that degradation will occur at different rates along the pile, depending on local stress level. Even in initially homogeneous soil, a nonuniform distribution of soil modulus and skin friction will result from cyclic loading because nonuniformity of stress distribution occurs along the pile. Degradation occurs in the ultimate skin friction along the length of the pile and also the ultimate base resistance. The major problem in a cyclic response is determining how the degradation factors vary with strain and number of cycles.

The cyclic shear strain in the soil adjacent to the pile,  $\gamma_c$ , can be estimated as:

$$\gamma_c = \frac{2 P_c}{\xi d}$$

where:  $P_c$  = cyclic displacement of pile at a point on the pile shaft

$d$  = pile diameter

$$\xi = \ln [5 \Psi (1 - \mu_s) L/d]$$

$\Psi = 1.0$  homogeneous infinitely deep soil and 0.5 modulus increases with depth

$\mu_s$  = Poisson's ratio

$L$  = embedder pile length

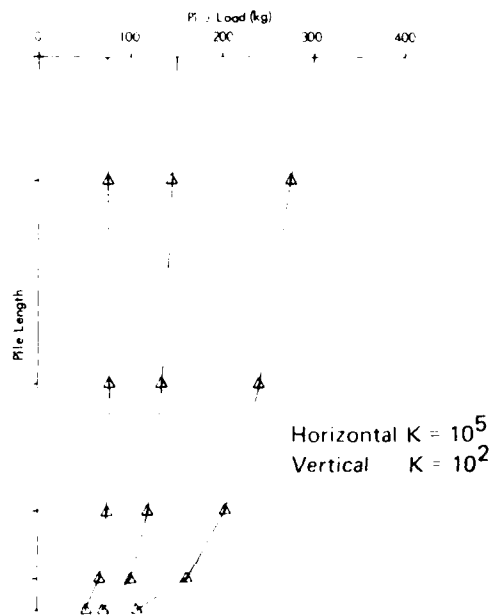


Figure 72. Distribution of force within pile.

The cyclic base strain can be estimated from the above assuming  $\mu_s = 0.5$ ,  $L/d = 100$ .

$$\gamma_c = \frac{0.4 P_{bc}}{d_b}$$

where:  $P_{bc}$  = cyclic displacement of pile base

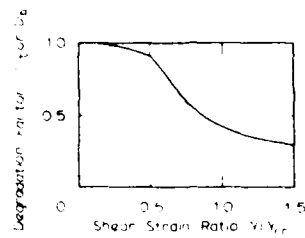
$d_b$  = diameter of pile base.

It is important to note that the above is based on the assumptions of elastic behavior. Typical predictions for pile settlement take the form of Figure 73. Also shown in Figure 73 is the ultimate cyclic load as a function of number of cycles. The settlement problem is the major concern for piles in cohesionless materials.

#### Friction Between Calcareous Sand and Building Materials

Calcareous sediments have proven troublesome to offshore facilities. Piles in calcareous sands have been noted to penetrate and to be extracted with much less effort than predicted by conventional techniques. A research program was previously conducted at NCEL (Ref 54) in which calcareous sediments were collected from three environments: a deep-ocean site, a shallow-ocean site, and coral line sand from an atoll beach. The coefficients of friction of these sands and of a quartz sand (used as a standard) were measured against surfaces of rough and smooth steel and mortar. Volume changes were measured as a function of sliding displacement.

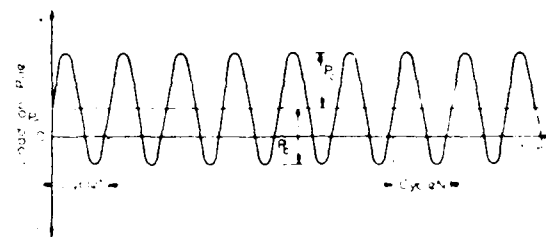
Experience has caused engineers to reduce pile capacities in calcareous materials. This usually results in load capacity reductions to one-fourth that of piles in normal materials. In the past, it was not clearly understood why calcareous materials exhibited inferior pile support. Measured angles of internal friction -- a measure of strength -- are high, 34 degrees or greater. Part of the problem was identified as the low increase in soil effective stress during pile driving, which is thought to result from a crushing or collapse of a cemented soil structure or from the breakup of individual carbonate



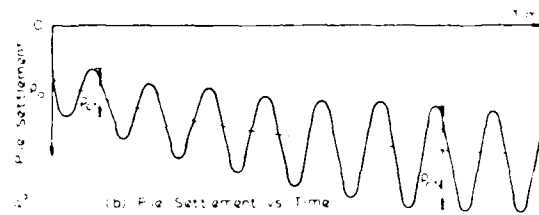
For skin friction ( $D_r$ )  $V_{s0} = V_{ss}$  (vertical shear strain for skin friction)

For base resistance ( $D_r$ )  $V_{s0} = V_{ss}$  (static lateral strain for triaxial compression)

### (a) Degradation.



(a) Load vs. Time



(b) Pile Settlement vs. Time



grains. This lack of increase in effective stress results in a relatively lower shear strength in the soil mass surrounding the pile. Further, it was thought that the coefficients of friction might be substantially less between calcareous materials and piles. Valent (Ref 54) conducted a friction test program using a modified direct shear test machine in which the lower half of the apparatus contained a building material and the upper half a soil sample. Table 5 summarizes his results.

In general, the results show that the low friction forces in calcareous sediments are not the result of low achievable friction angles, because calcareous sands are comparable to other sands; low friction development then, must be attributable to low normal force. Deep-ocean sand (foraminiferal sand-silt) exhibits one possible cause for low developed normal force. The volume change during testing indicated a considerable volume decrease during development of resisting friction force, probably due to crushing of the skeletal structures and shell fragments. Penetration of a pile in such a material would crush the hollow shell material with only a minimal increase in effective stress of the surrounding material.

Quoting from Valent (Ref 54):

- "1. The calcareous sediments tested, and presumably calcareous sediments in general, develop coefficients of friction against steel and concrete building materials that are comparable to those developed by quartz-type sands. Thus, the possibility of low coefficients of friction being responsible for the observed low friction forces on driven piling and other penetrators in calcareous materials is ruled out.
2. The observed large volume decreases during shear of the foraminiferal sand-silt are probably responsible for the low developed friction forces in these hollow-shelled materials. Such large volume decreases at nonincreasing normal load imply densification in the field without accompanying increases in normal stress on the penetrator surface.
3. Low developed friction forces in other calcareous materials may arise from a similar mechanism involving a hypothesized loose, but cemented, structure for

Table 5. Summary of Friction Test Results (Ref 53)

Test No.	Soil Material	$\mu_{\text{peak}}^a$	$\mu_{\text{residual}}^a$
Base Material <sup>b</sup> : Sand <sup>c</sup>			
1	Quartz sand	0.67 <sup>d</sup>	0.54
2	Coralline sand	0.66	0.56
3	Coralline sand	0.68	0.57
4	Oolitic sand	0.77 <sup>d</sup>	0.61
5	Oolitic sand	0.81	0.62
6	Foram sand-silt	0.64 <sup>d</sup>	0.58
Base Material <sup>b</sup> : Smooth Steel			
7	Quartz sand	0.27 <sup>d</sup>	0.19
8	Coralline sand	0.20	0.17
9	Coralline sand	0.20	0.18 <sup>e</sup>
10	Coralline sand	0.21	0.17
11	Oolitic sand	0.15 <sup>d</sup>	0.13
12	Oolitic sand	0.32	0.31
13	Foram sand-silt	0.40	0.37
Base Material <sup>b</sup> : Rough Steel			
14	Quartz sand	0.60	0.54
15	Coralline sand	0.63	0.55
16	Oolitic sand	0.54	0.51
17	Oolitic sand	0.58 <sub>f</sub>	0.50
18	Foram sand-silt	---- <sub>f</sub>	0.66
Base Material <sup>b</sup> : Smooth Concrete			
19	Quartz sand	0.60	0.54
20	Coralline sand	0.63	0.56
21	Oolitic sand	0.59	0.52
22	Oolitic sand	0.58 <sub>f</sub>	0.54
23	Foram sand-silt	---- <sub>f</sub>	0.67

Table 5. Continued

Test No.	Soil Material	$\mu_{\text{peak}}^a$	$\mu_{\text{residual}}^a$
Base Material <sup>b</sup> : Rough Concrete			
24	Quartz sand	0.69	0.57
25	Coralline sand	0.66	0.59
26	Oolitic sand	0.74	0.57

<sup>a</sup> For direct shear tests,  $\mu = \tan \phi$  where  $\phi$  = angle of internal friction; for friction tests,  $\mu = \tan \delta$  where  $\delta$  = angle of sliding friction.

<sup>b</sup> Soil in bottom shear ring for direct shear tests, or building material in friction tests.

<sup>c</sup> Base material same as soil material for direct shear tests.

<sup>d</sup> These tests run with mechanical measurement system; i.e., proving ring and manual recording of data.

<sup>e</sup> Low value for  $\mu$  reached shortly after  $\mu_{\text{peak}}$ , thereafter  $\mu$  increased with displacement to end of test.

<sup>f</sup> No peak  $\mu$  reached,  $\mu$  increasing through end of test.

the soil material. The application of shear stresses during penetration would cause collapse of this structure to a denser, but still loose, arrangement."

#### Piles in Calcareous Sands

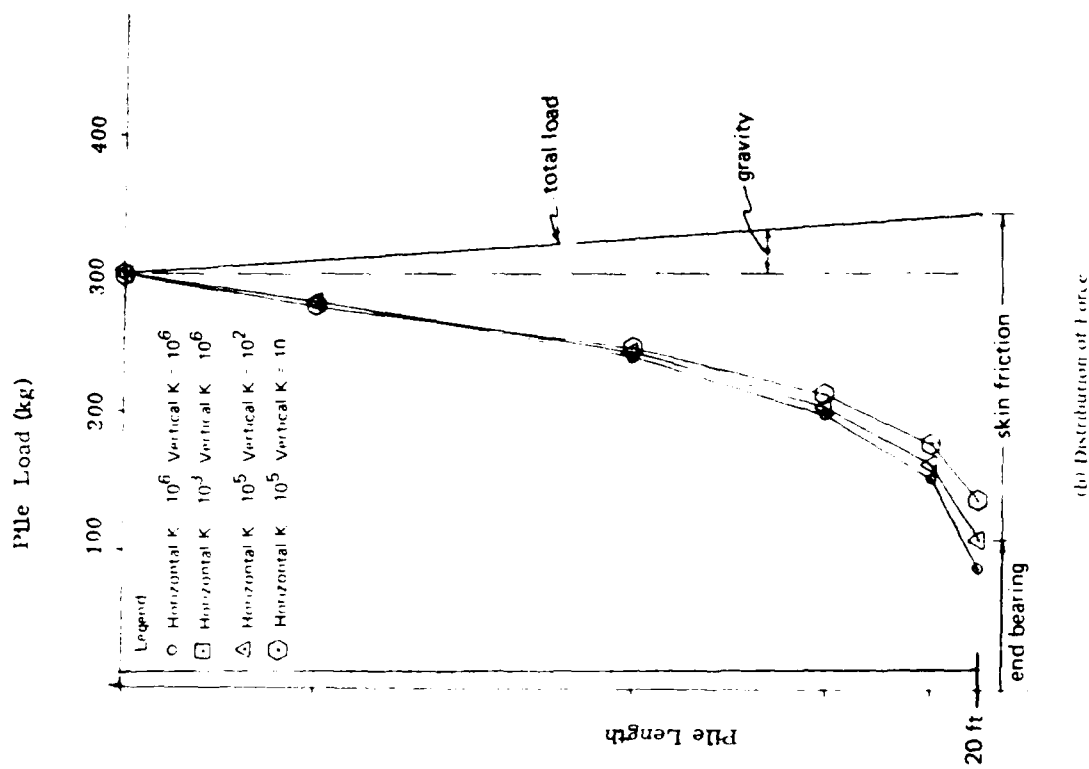
Calcareous sands, as discussed, are noted for loose arrangement of particles lightly cemented to form a structure to support other layers without compacting. However, upon shearing, the structure is destroyed, breaking the cement bonds. The loose-grained structure then compacts and densifies. The sand (silica sand) is a very loose sand (30% relative density) and, as such, is a "manufactured" sand that would not occur in nature. The properties of this material might be expected to represent the constitutive behavior of a calcareous sand.

To analyze a pile's load capacity using the effective stress soil model, the mesh in Figure 74 was used. This mesh simulates a pile already in place (i.e., not the driving of the pile). Horizontal and vertical springs were used to join the pile to the soil field to simulate the interface and allow for pile movement.

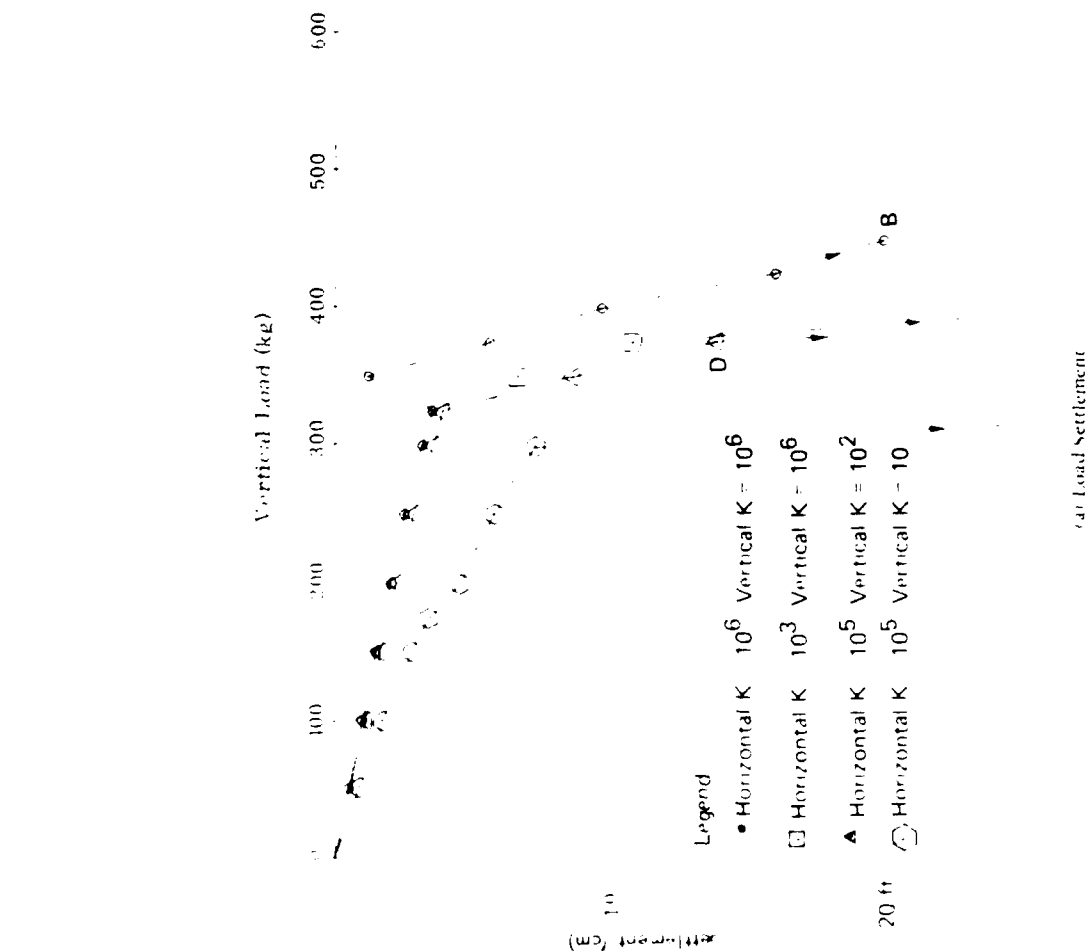
The soil properties used were those of silica sand. The material properties simulate the condition of the soil after placement of the pile. No desiccation occurs, since the pile is in place at the start of the analysis. A prediction of pile capacity was made by using conventional techniques found in Figures 67 and 68 adjusted to the problem conditions but without densification. Results indicated a pile resistance in normal average cohesionless sand of at least 1,500 kg with about 150 kg of that in side friction and the remainder in end bearing.

Load Settlement of the Pile. Figure 75(a) shows the load settlement of the pile. Several values were tried for the spring constants. Results show the pile experienced large settlements between 300 and 400 kg. Figure 72 shows the distribution of force within the pile for three load levels. Note that most of the increase in load is due to skin friction. Figure 75(b) shows the distribution of force along the pile at a point in the loading having a force of 300 kg applied at the top of the pile. The results in Figure 75(b) show about one-half to two-thirds





(a) Load Settlement



(b) Distribution of Force

Figure 75. Load settlement and distribution of force.

of the load is taken in skin friction. The skin friction portion of the load agrees with the predicted values., however, the end bearing is substantially less. It is important to note that the silica sand used had a relative density of only 30% which is so loose it does not occur in nature but is "manufactured" in the laboratory. The level of loading is about one-fourth that of a pile in normal sand, which is the level expected from experience in calcareous sands. Figure 76 shows contours 250 kg

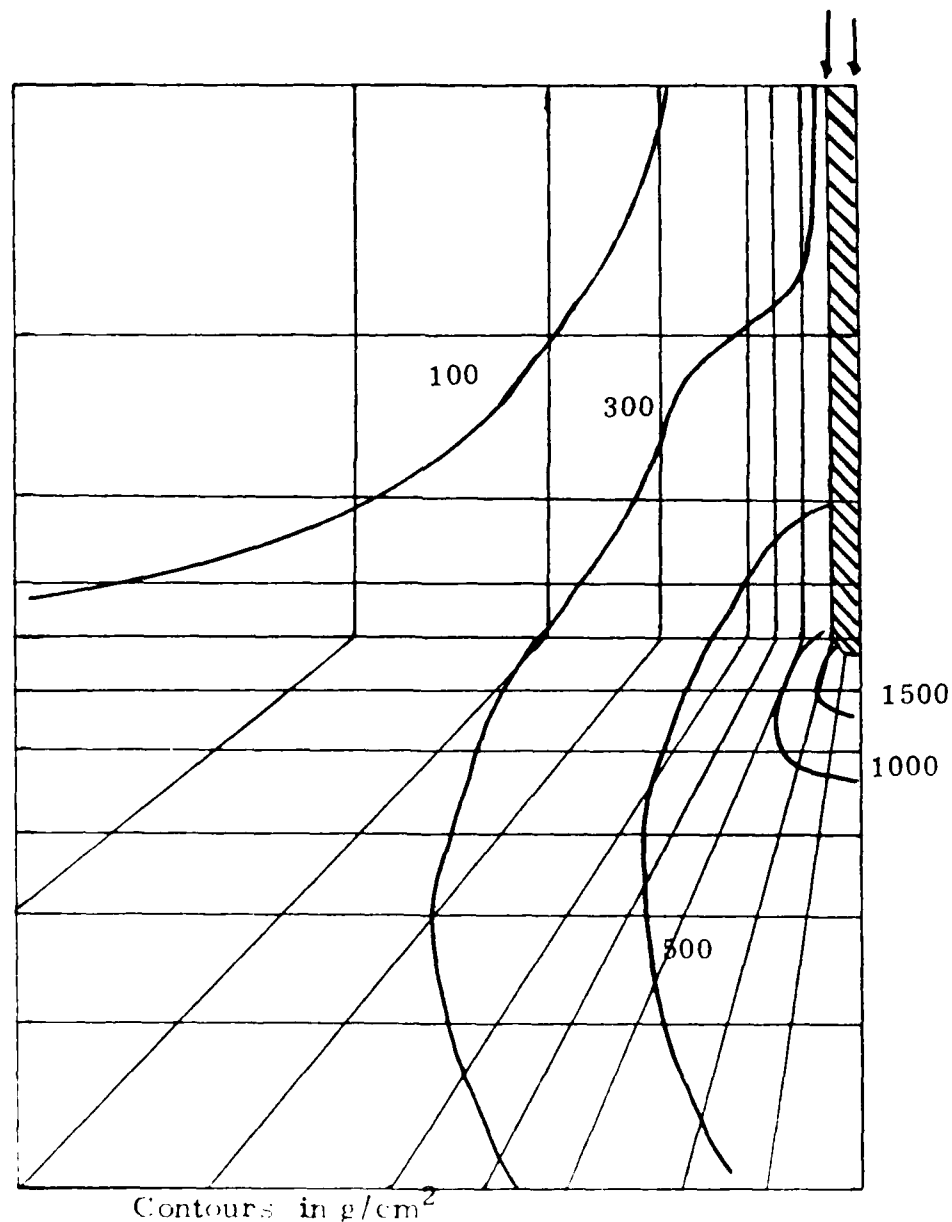


Figure 76. Principal stress contour around pile.

of principal stress around the pile at a typical load step. These show typical patterns, as expected; the level of stress below the pile tip would be on the last surface at yield.

Results show that the order of magnitude of the pile capacity in calcareous materials is predicted correctly. Further, the friction developed on the sides of the pile is at the expected level, not substantially reduced from normal sands. The amount of end bearing is slightly dependent on the vertical spring constant. Use of nonlinear springs would have allowed slip to occur, transferring more load into end bearing when exceeding some local slip level.

Pile Behavior Under Cyclic Loading. Next, pile behavior under cyclic loading was examined. The applied loading consisted of cyclic variation of the vertical load on the pile. In one case, the loading was cycled in "one-way" loading (zero minimum and specified maximum) and in "two-way" loading (alternating compression and tension). The first example was at a relatively low level of loading for the model pile (about one-seventh of yield). Figure 77 shows the stress beneath the pile tip for one-way loading (0 to 50 kg), Figure 78 shows the shear stress contours around the pile (0 to 50 kg). Figure 79 shows the stress beneath the pile tip for two-way loading (50 to 50 kg), the shear stress plot is similar to Figure 80. Note that the tip forces reduce with loading, transferring more to friction to maintain load levels. Figure 80 shows the typical contact element force, a measure of friction between the soil and pile. Note the gradual buildup in the two-way loading case.

The loading was increased to about 40% of yield. Figure 81 shows the distribution of force within the pile for both one-way and two-way loading for the first and fifth cycles. Note the increase in friction loading in the pile with two-way loading, showing the degradation with cyclic loading. Note also that for both cases the friction increases more in the lower half of the pile. Figure 82 represents the typical contact element force, again showing the increase in friction with each cycle. Figures 83 and 84 show the stress beneath the pile tip. Both drop off with each cycle, however, the two-way loading does so at a

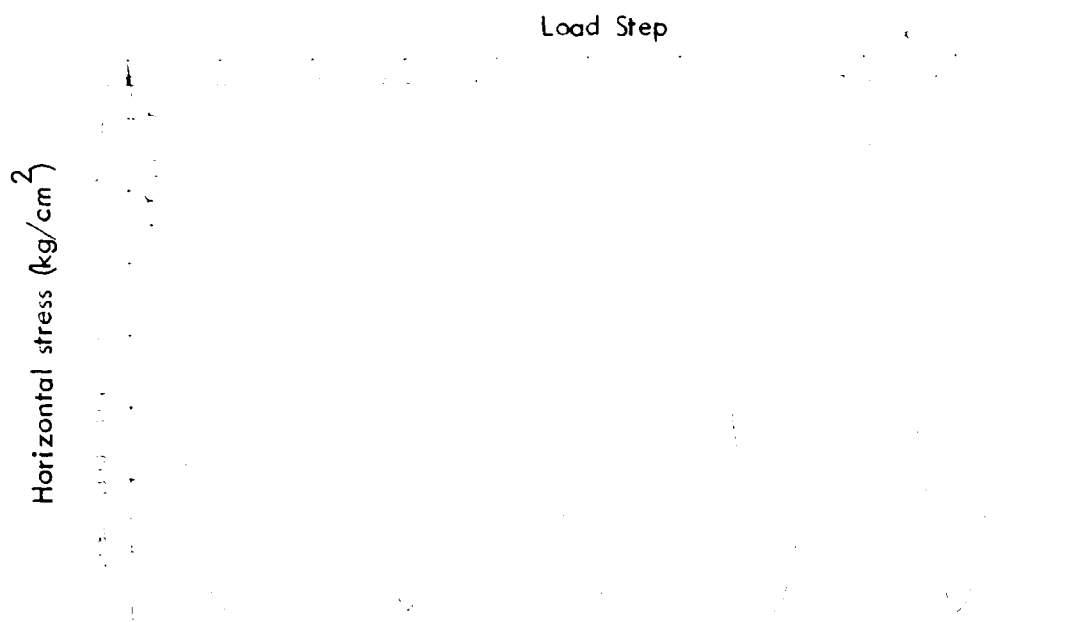


faster rate. Figure 85 shows the pile settlement for both cases. Note that the change in settlement between the first and fifth cycle is over four times greater for the two-way loading. Figure 86 shows the deformed mesh for the one-way loading., the mesh is similar for the two-way loading.

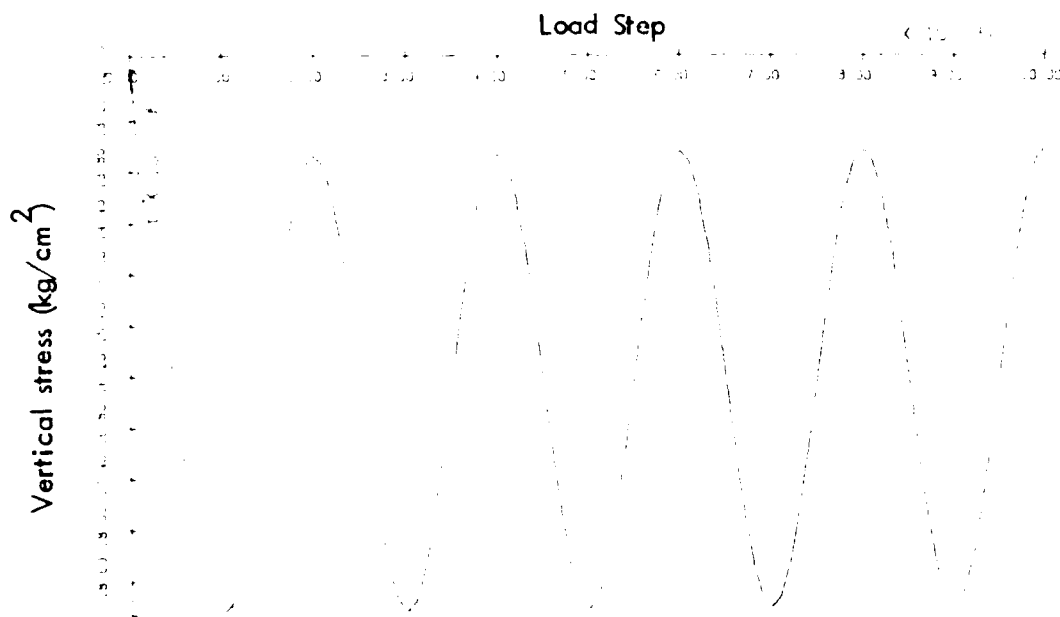
The loading was increased to 80% of pile capacity, and the one-way loading case was tried. This load exceeded the friction capacity so two-way loading could not be used. Figure 87 shows the stress beneath the pile tip, and Figure 88 shows the deformed mesh. Failure occurs between load steps 70 and 80. Figure 89 shows the shear stress contours around the pile at load steps 10 and 70. More load capacity is transferred from end bearing than from side friction.

The cyclic results clearly show the degradation of the pile under cyclic loading. Results show the two-way loading causes more degradation, as expected. The model performed well in predicting the qualitative pile behavior, particularly the settlements (Figures 75 and 85).

The pile problems were repeated for the undrained case in which the water table was at the surface. Figure 90(a) shows the load settlement curve. The original load increment used in the drained problem above was too large for the undrained problem and produced an instability at yielding. The load step was reduced, and the solution proceeded in a satisfactory manner. The pile capacity was about 250 kg, lower than the 350 kg in the drained case. The loading was cycled in one-way and two-way conditions. Figure 90(b) presents the distribution of force within the pile, showing the increase in friction with cycling, as with the drained case. Friction is slightly greater in this case. Figures 91 and 92 show the soil stress beneath the pile. The end bearing stress drops off with cycling, showing the shift to friction. The two-way loading has a faster degradation, as clearly shown in Figure 93, which shows the settlement. The two-way loading produces more permanent differential settlement after the fifth cycle. Figure 94 shows the pore pressure in the soil beneath the pile tip. The pore pressure rises to about three-quarters of the confining stress and then drops off as the load is shifted to friction along the pile. Figure 95 shows the friction force. Note the degradation effects with cycling as the load transfer drops off with each cycle.



(a) Horizontal stress.



(b) Vertical stress.

Figure 77. Horizontal and vertical stress of pile in soil field - 0 to 50 kg.

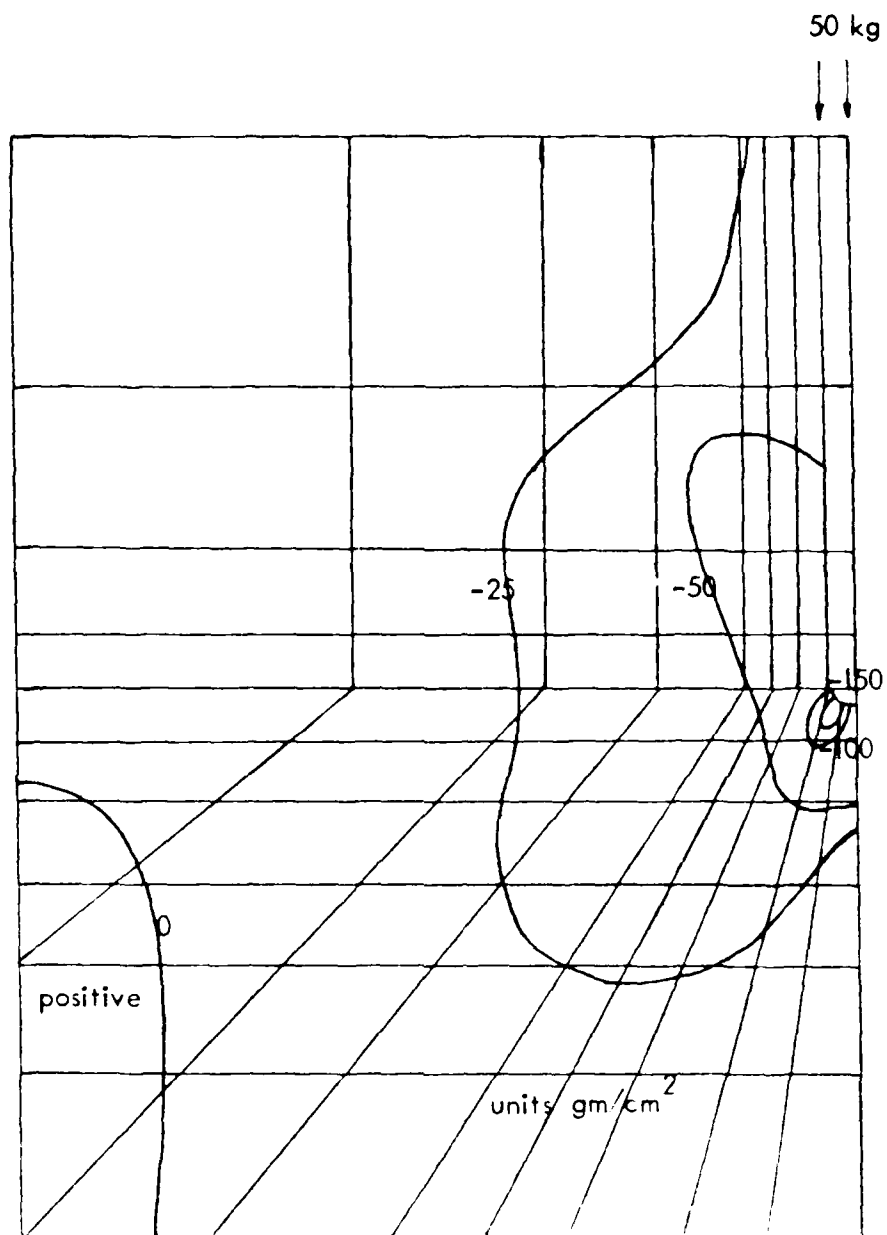


Figure 78. Shear stress contours of pile in soil field - 0 to 50 kg.

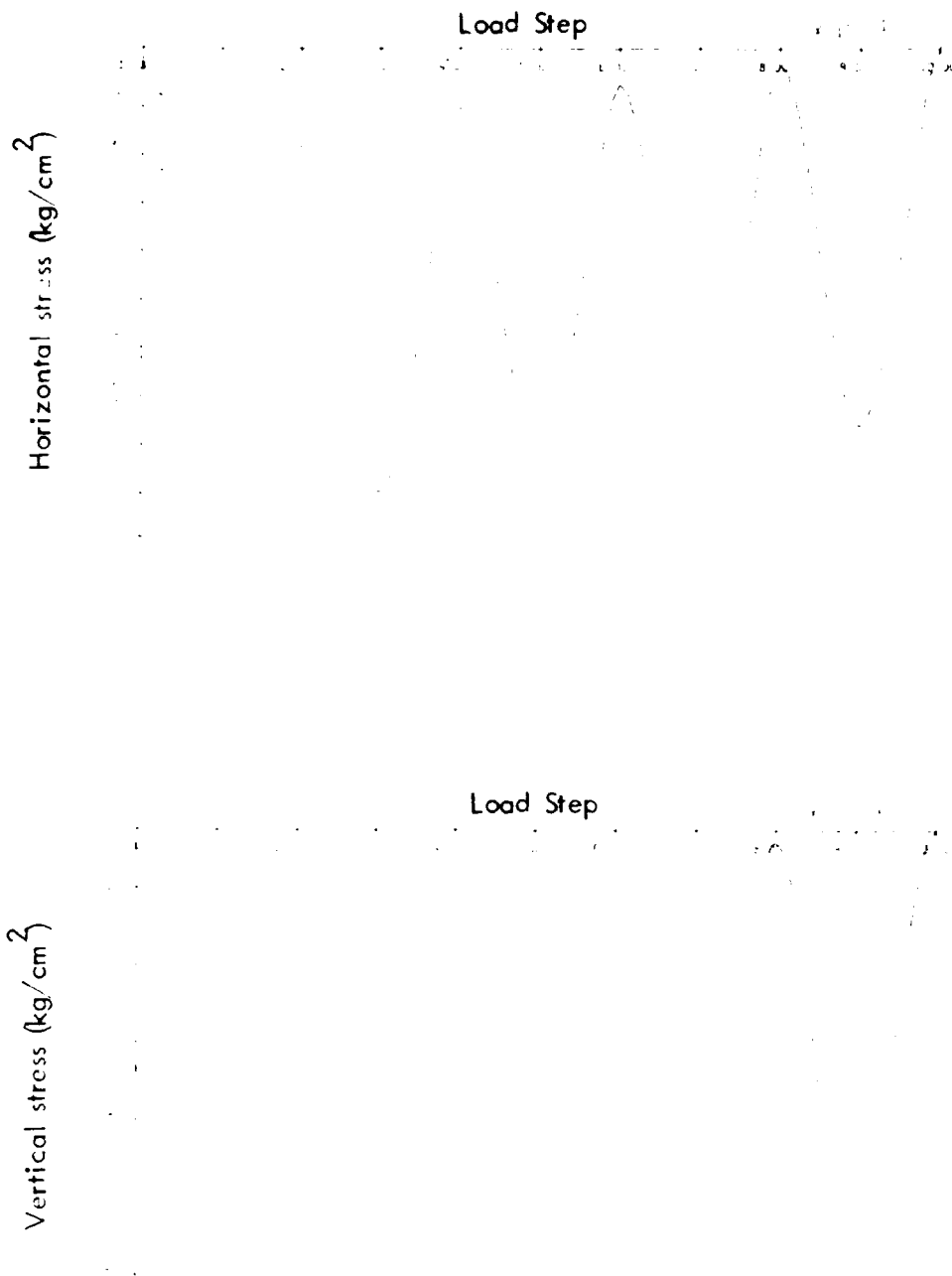


Figure 79. Horizontal and vertical stress of pile in soil field - -50 to 50 kg.

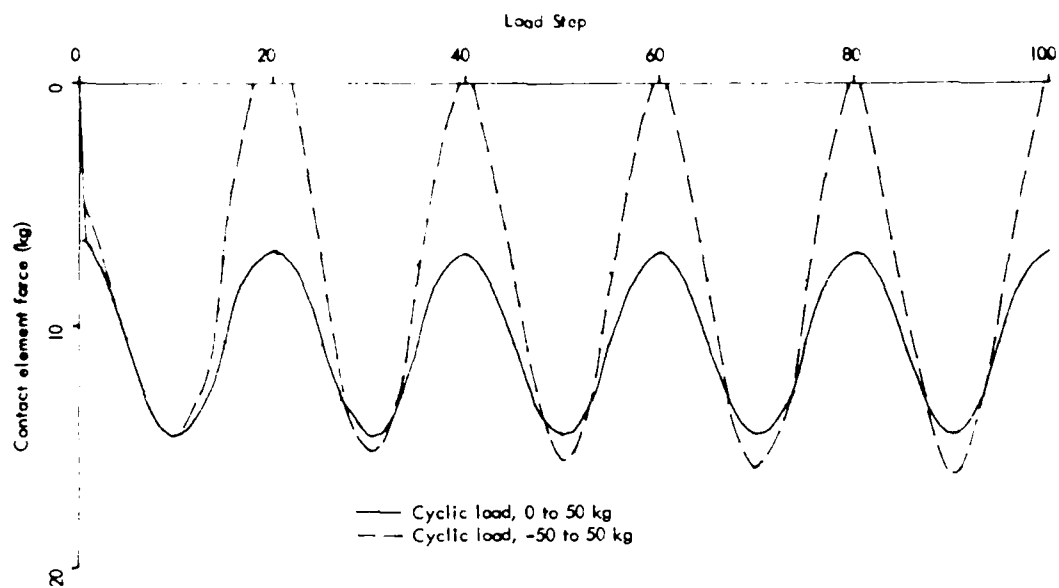


Figure 80. Friction force in pile in soil field - 0 to 50 kg.

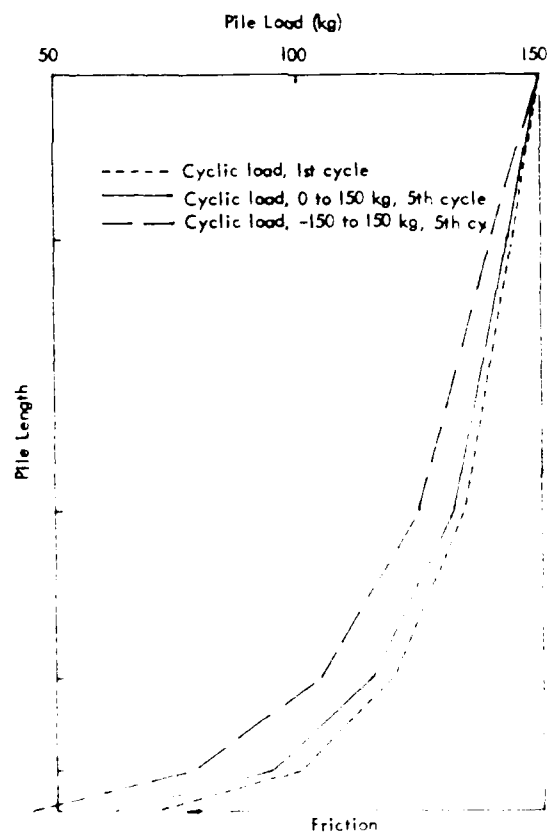


Figure 81. Distribution of force within pile, first and fifth cyclic loads.

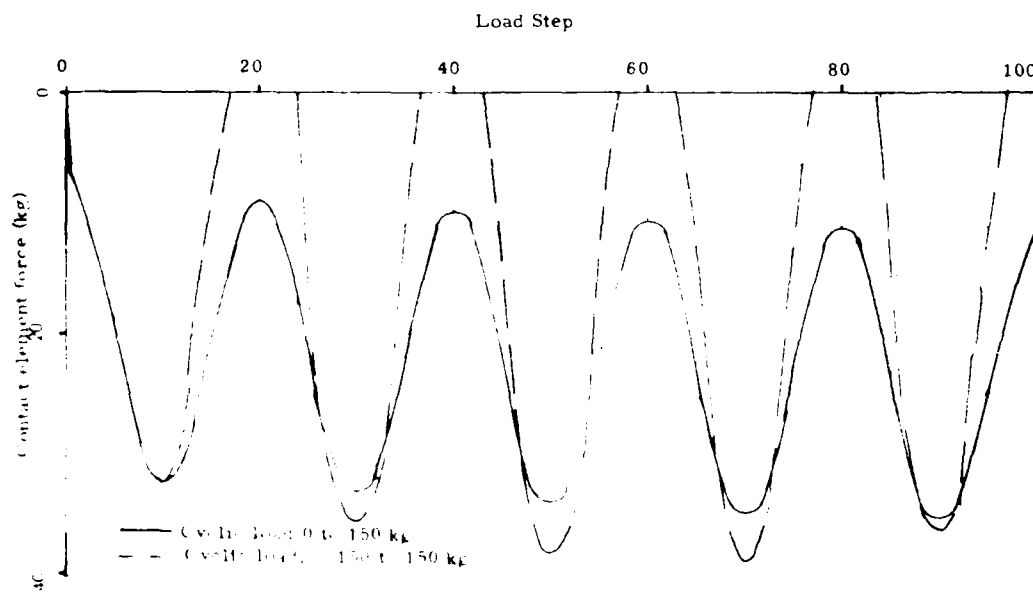


Figure 82. Friction force of pile in soil field - 0 to 150 and -150 to 150 kg.

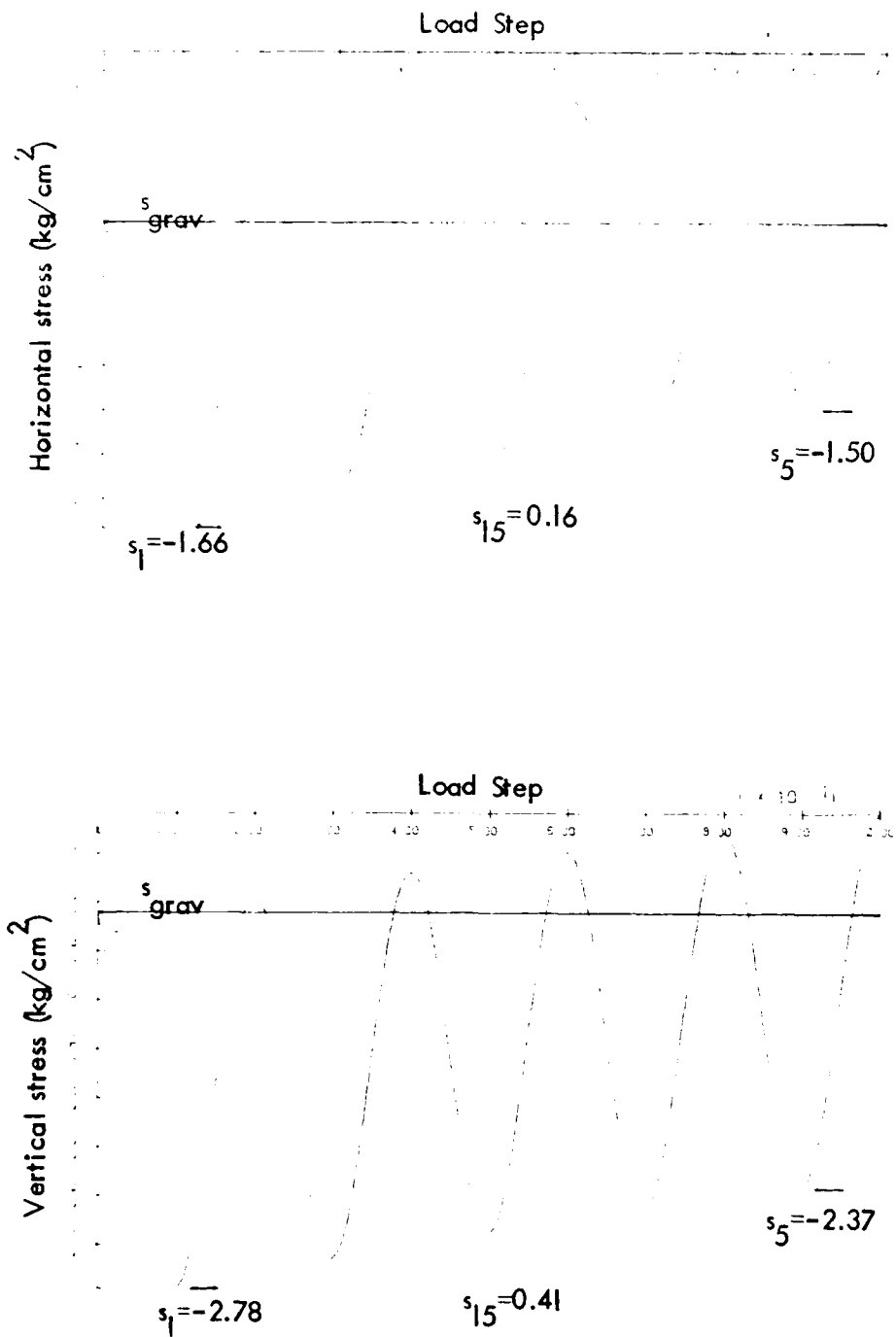


Figure 83. Horizontal and vertical stress of pile in soil field, 0 to 150 kg.

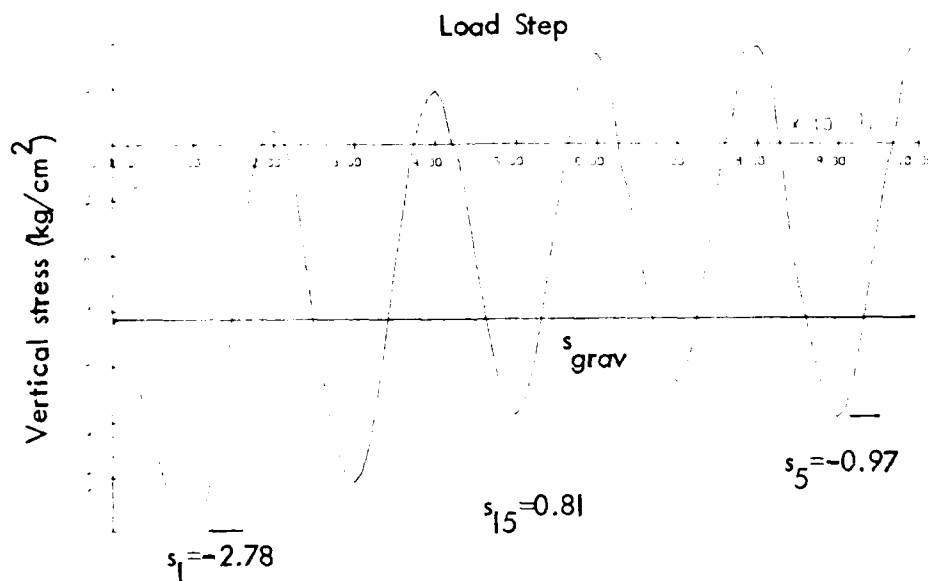
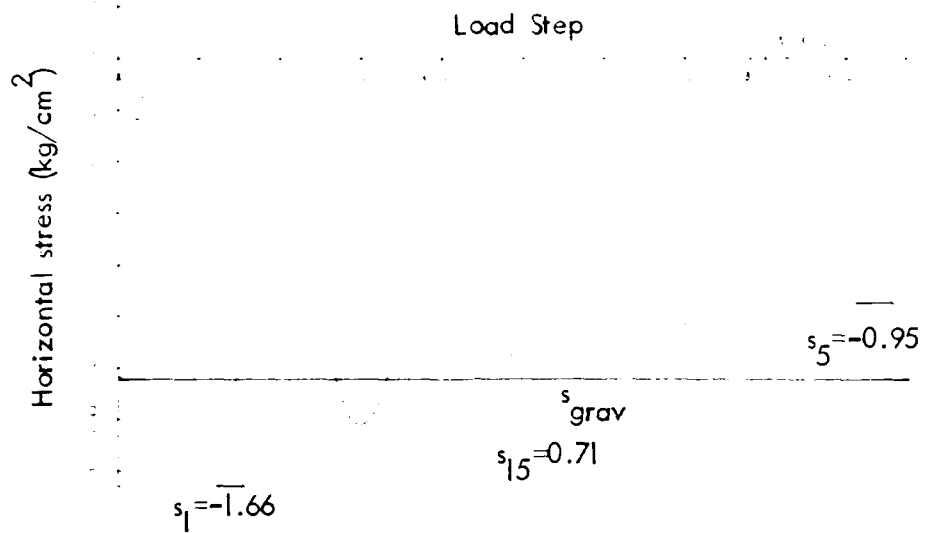


Figure 84. Horizontal and vertical stress of pile in soil field, -150 to 150 kg.



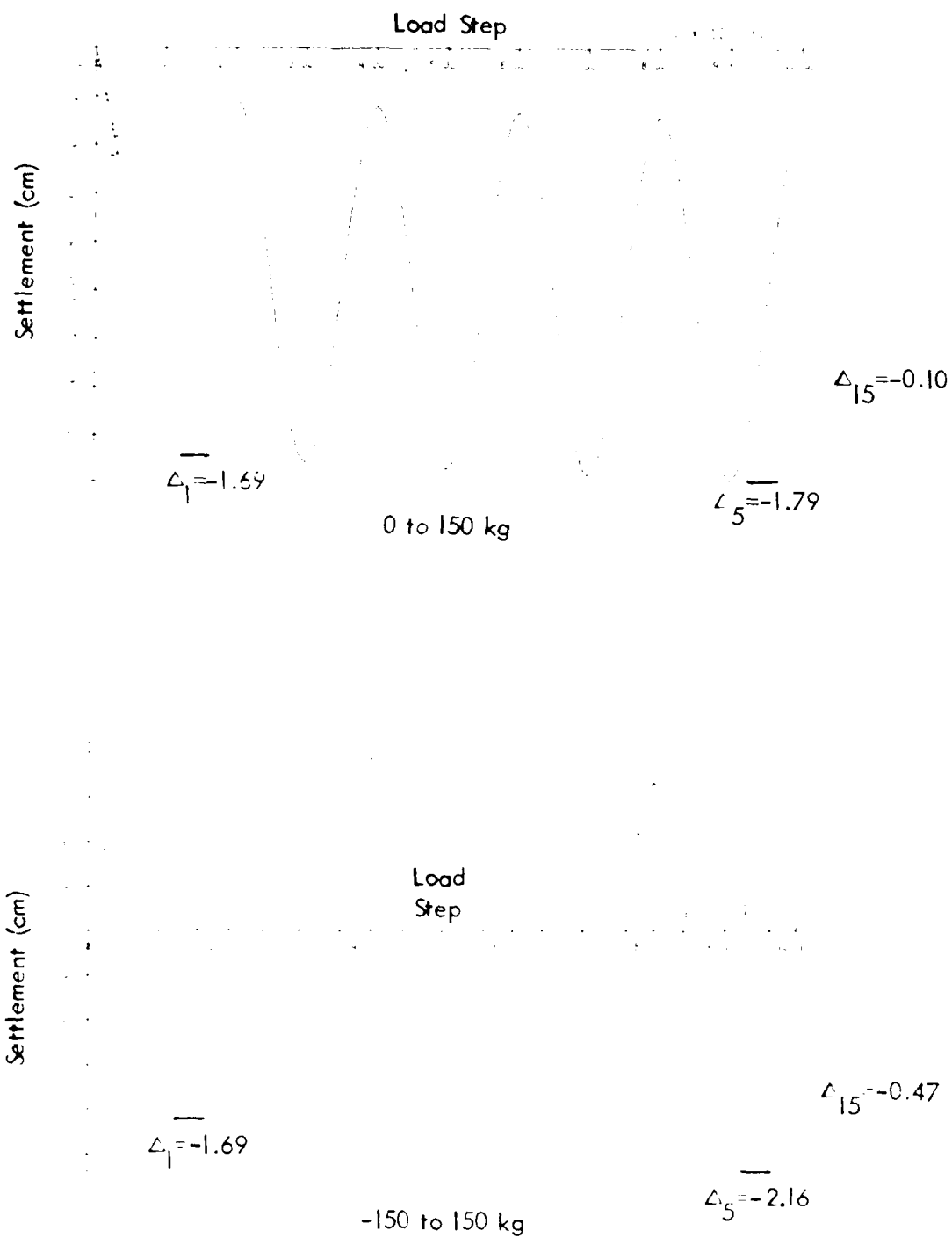
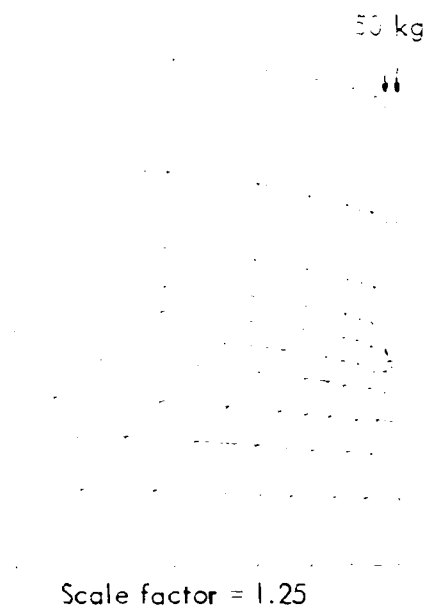
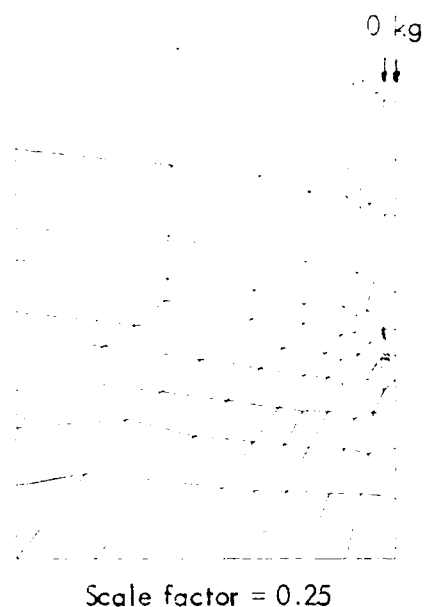


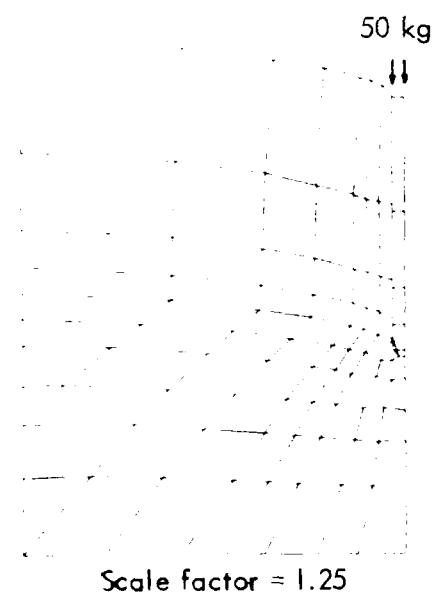
Figure 85. Horizontal and vertical settlement stress of pile in soil field.



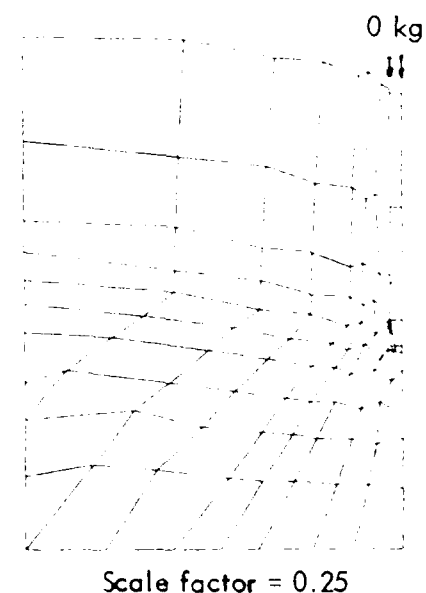
(a) Step 10.



(b) Step 20.



(c) Step 30.



(d) Step 40.

Figure 86. Deformed mesh, cyclic load - 0 to 50 kg.

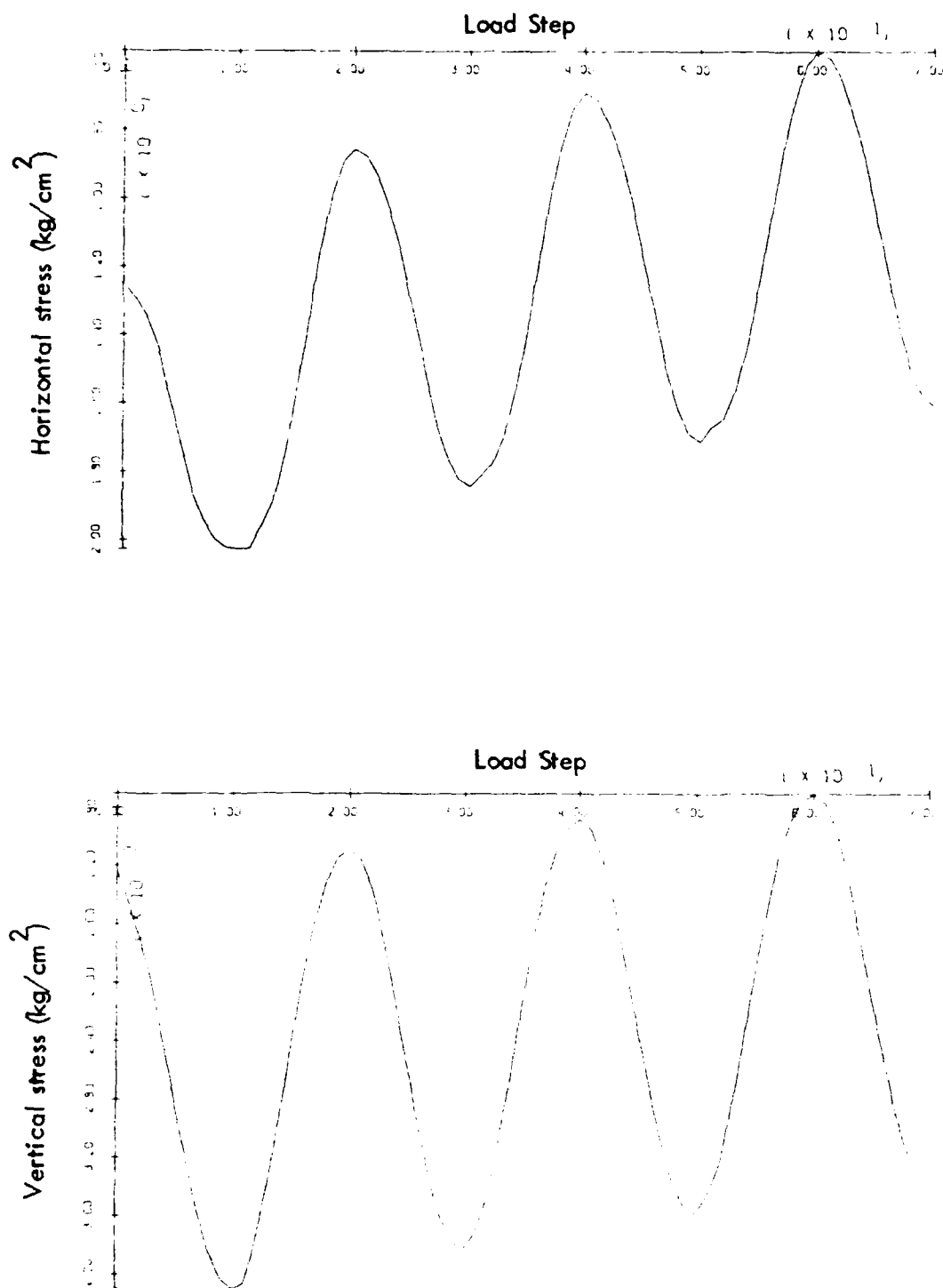
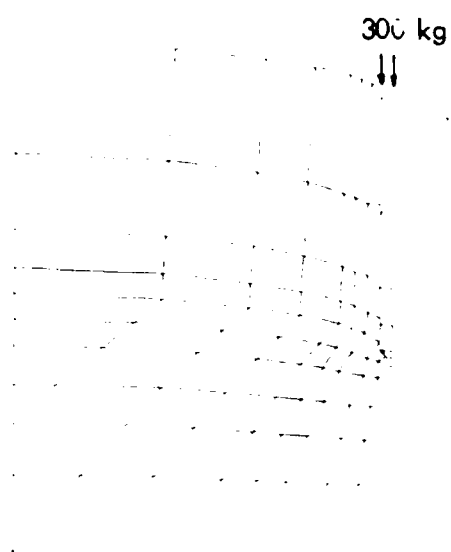
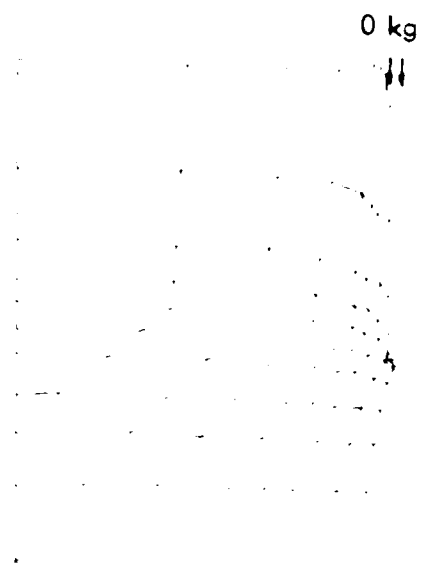


Figure 87. Horizontal and vertical stress of pile in soil field, 0 to 300 kg.



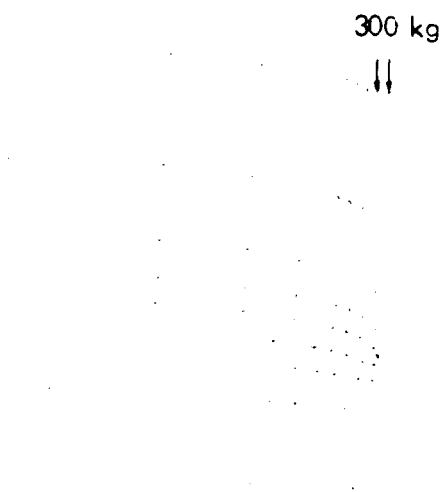
Scale factor = 7.05

(a) Step 10.



Scale factor = 1.13

(b) Step 20.



Scale factor = 7.36

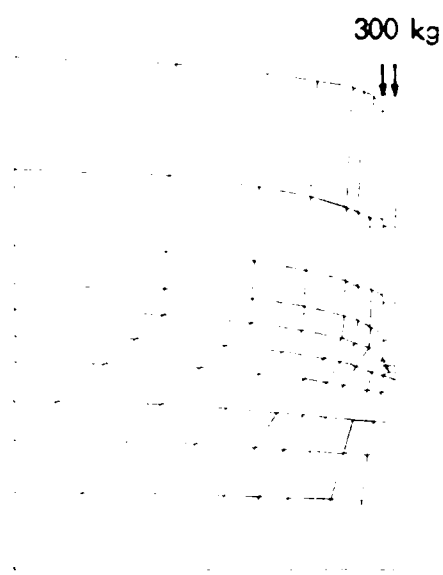
(c) Step 30.



Scale factor = 1.33

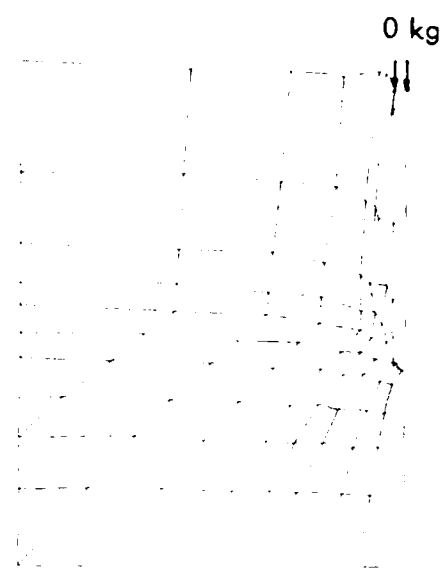
(d) Step 40.

Figure 88. Deformed mesh, cyclic load - 0 to 300 kg.



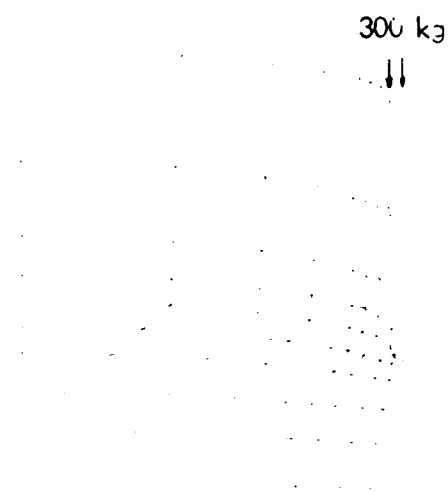
Scale factor = 7.58

(e) Step 50.



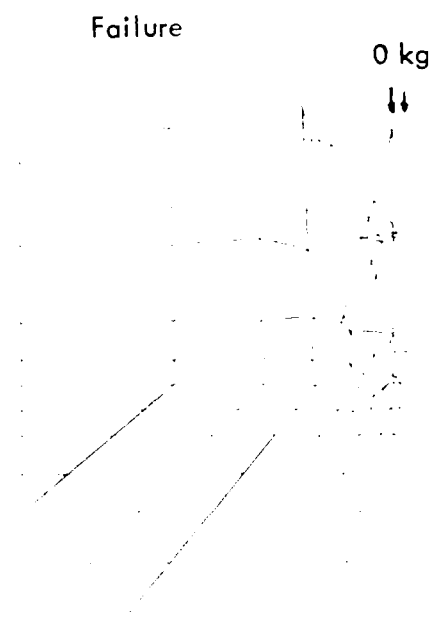
Scale factor = 1.52

(f) Step 60.



Scale factor = 7.79

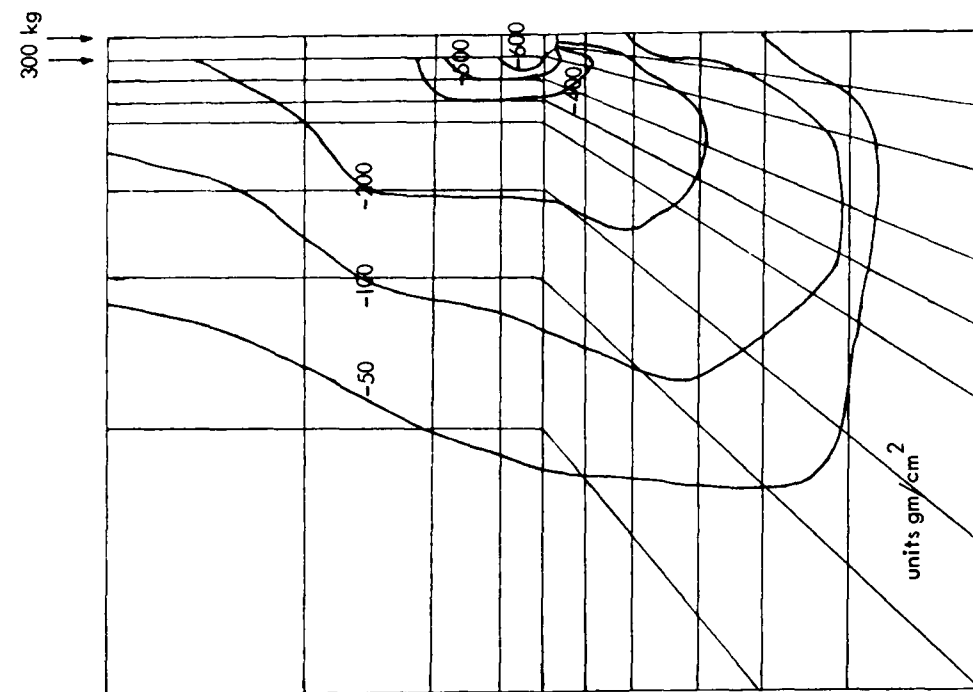
(g) Step 70.



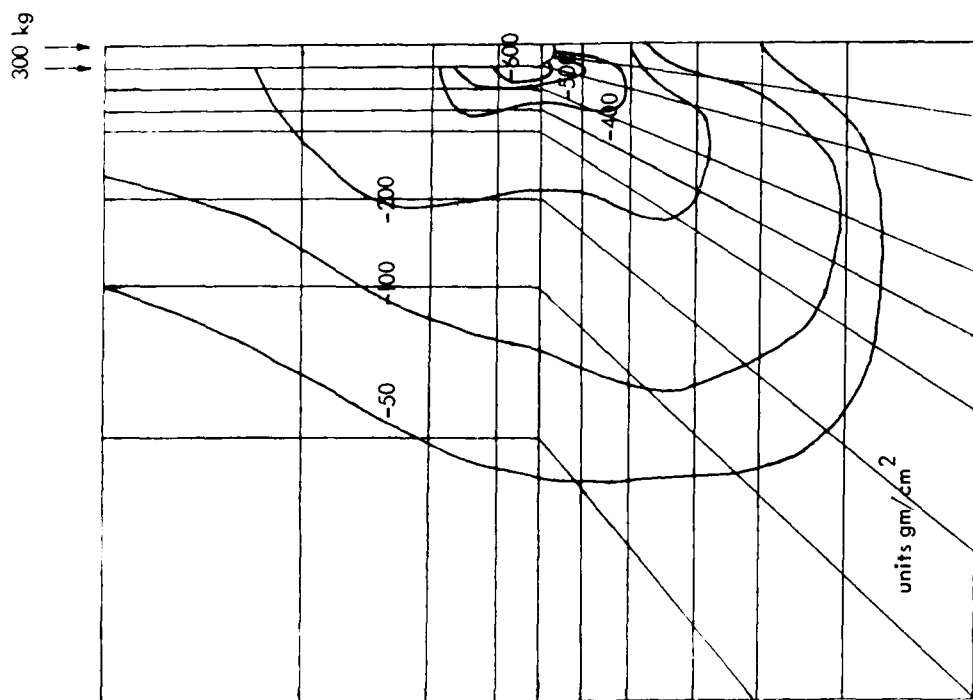
Scale factor = 1550

(h) Step 80.

Figure 88. continued

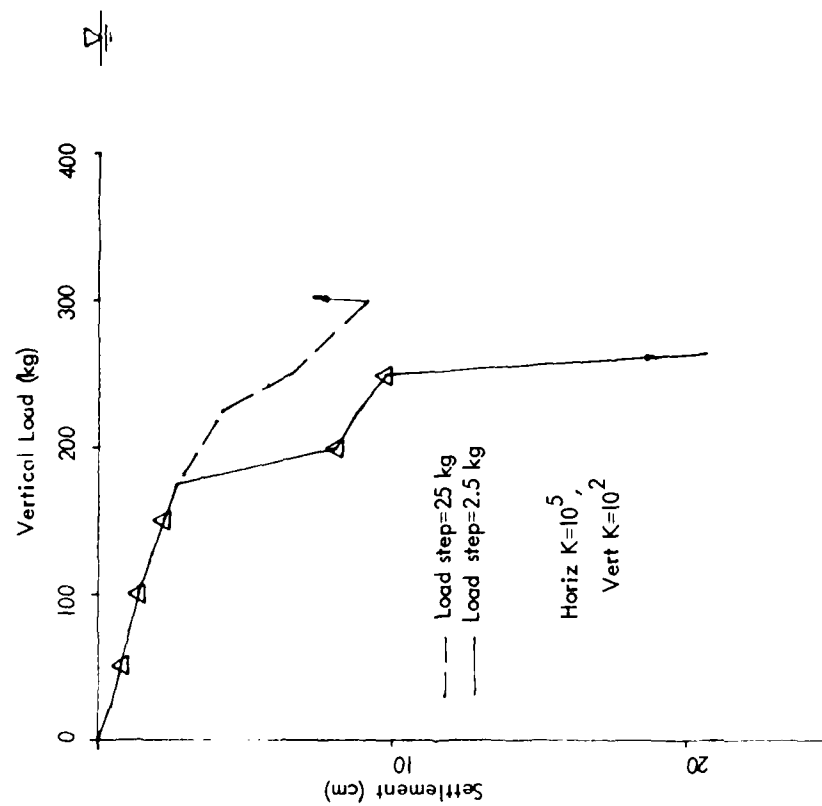


(a) Step 10.

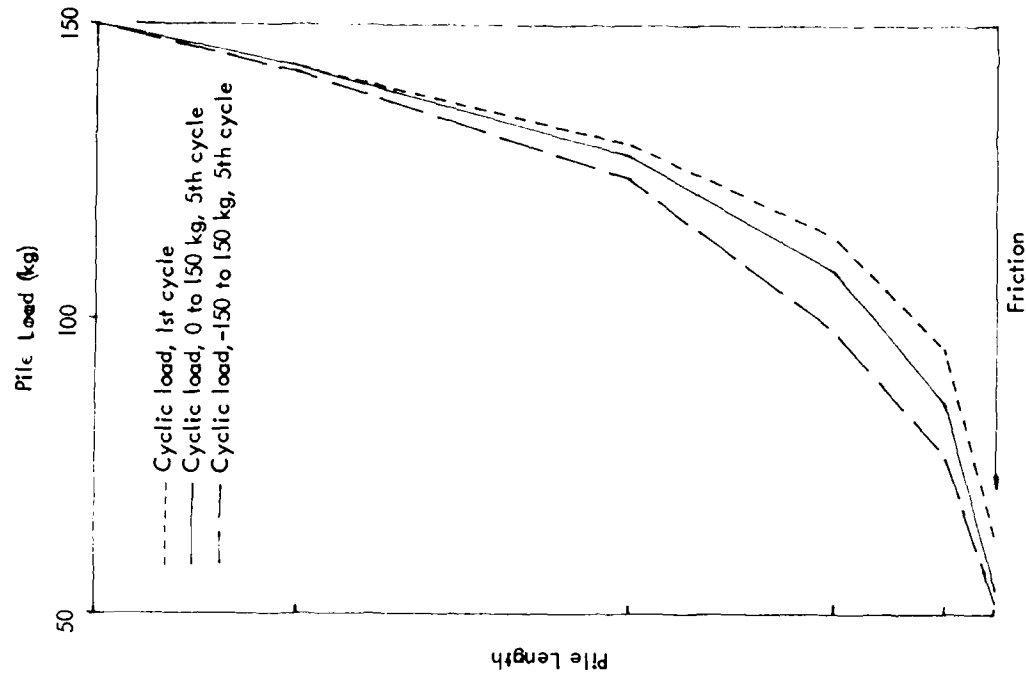


(b) Step 70.

Figure 89. Shear stress contours of pile in soil field - 0 to 300 kg.



(a) Load Settlement



(b) Distribution of Force

Figure 90. Load settlement and distribution of force within the pile (with water table).

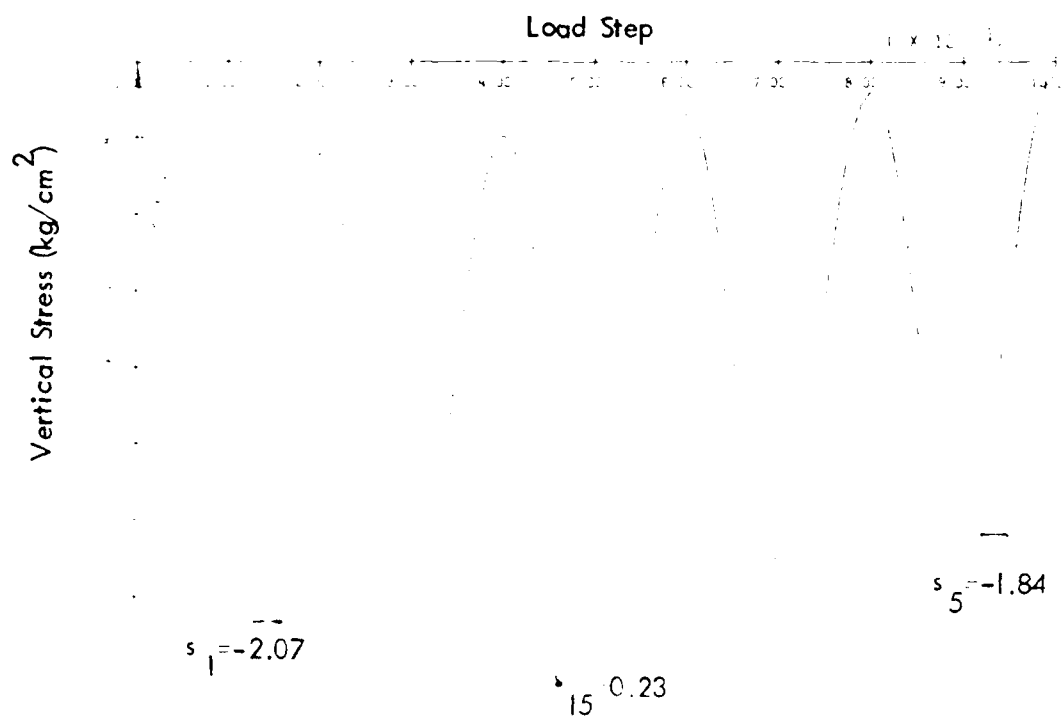
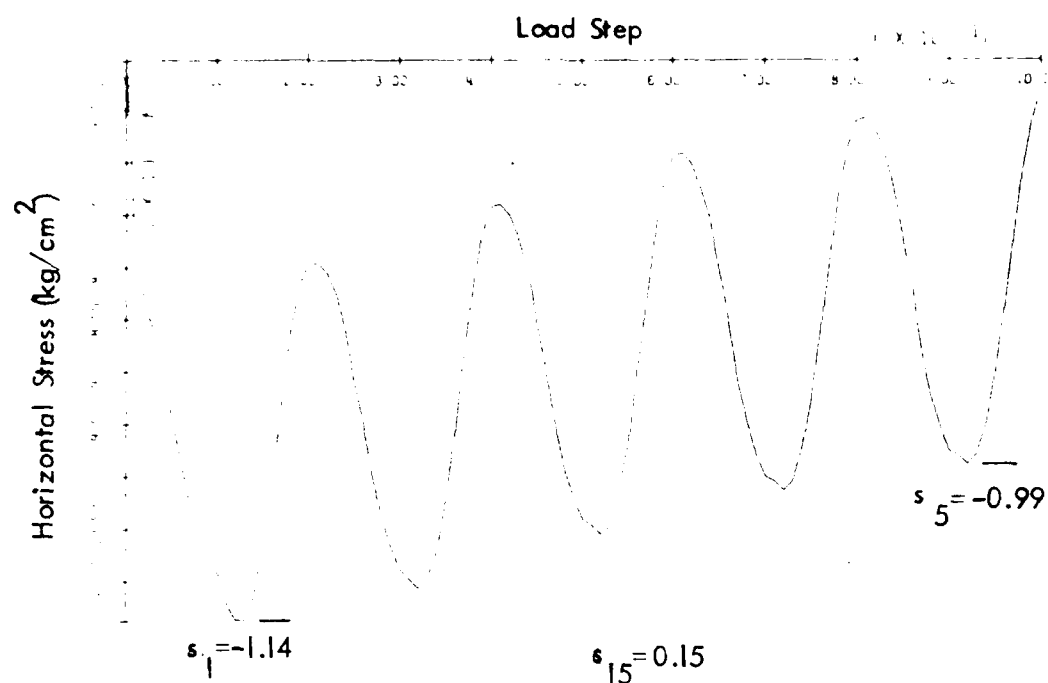


Figure 91. Horizontal and vertical stress of pile in soil field - 0 to 150 kg (with water table).



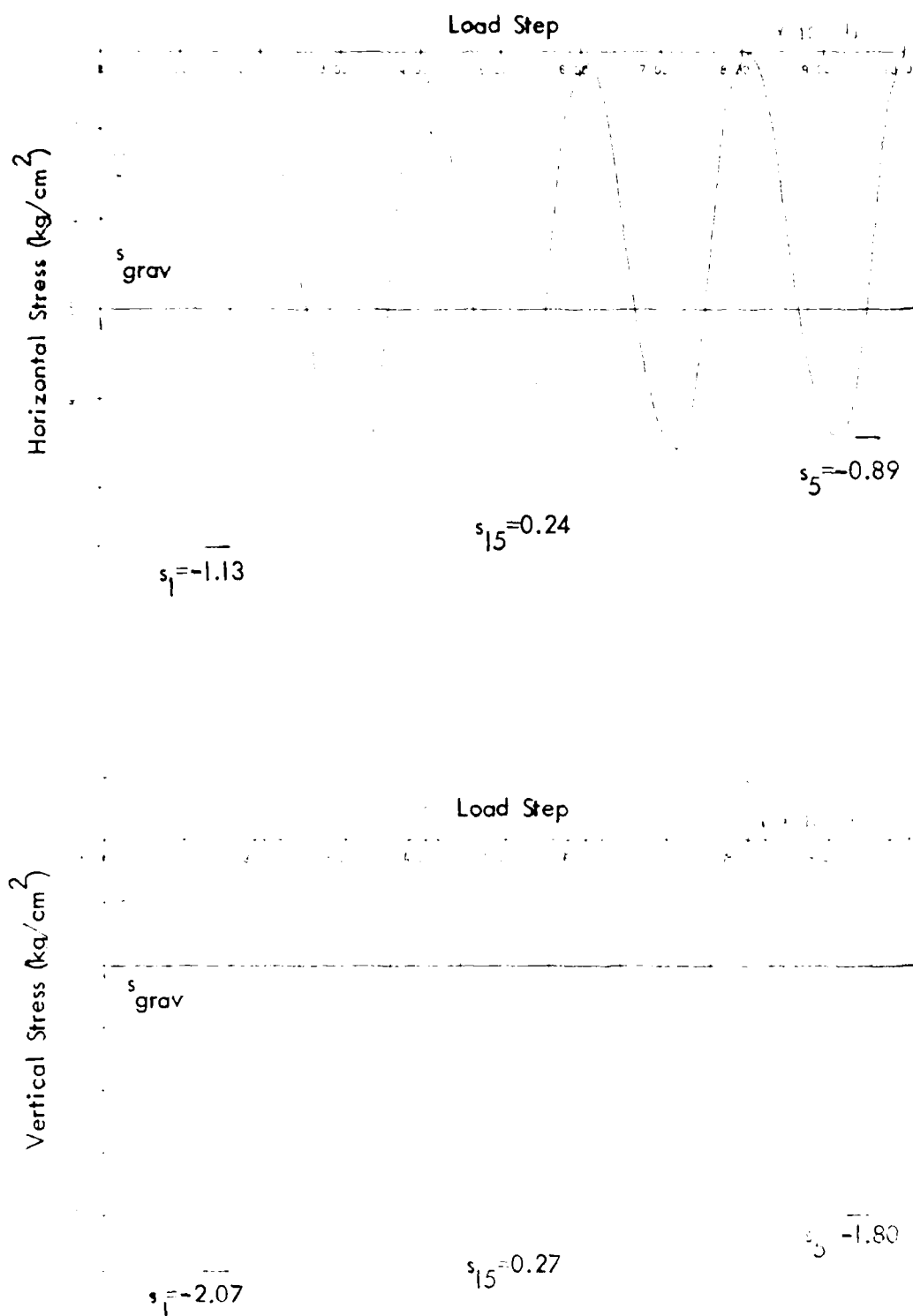


Figure 92. Horizontal and vertical stress of pile in soil field - -150 to 150 kg (with water table).

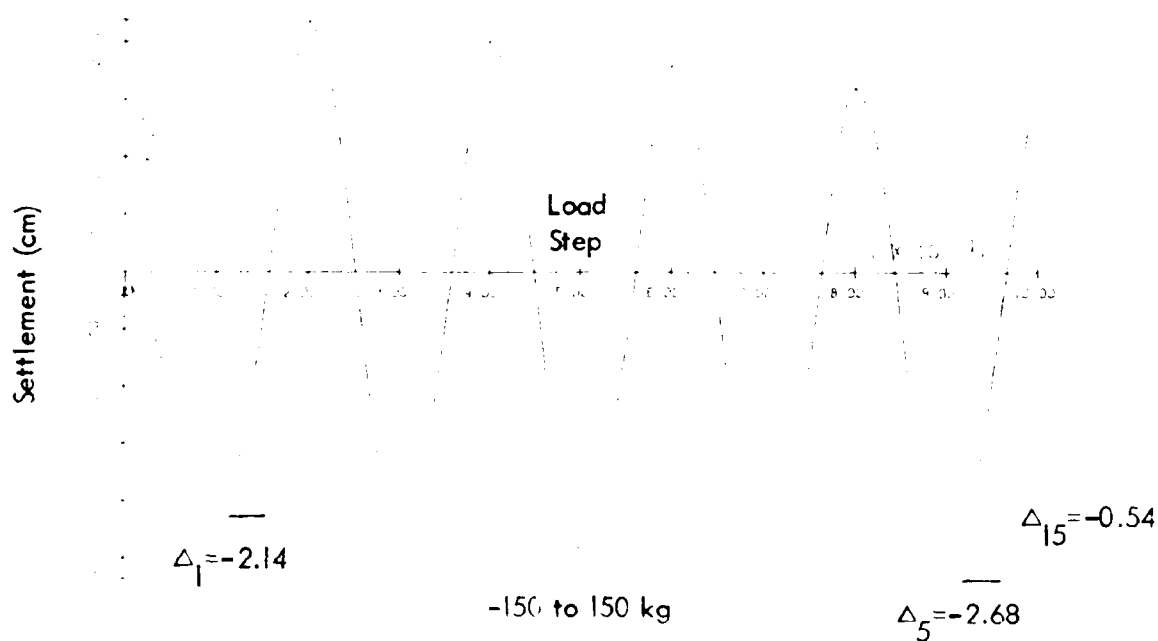
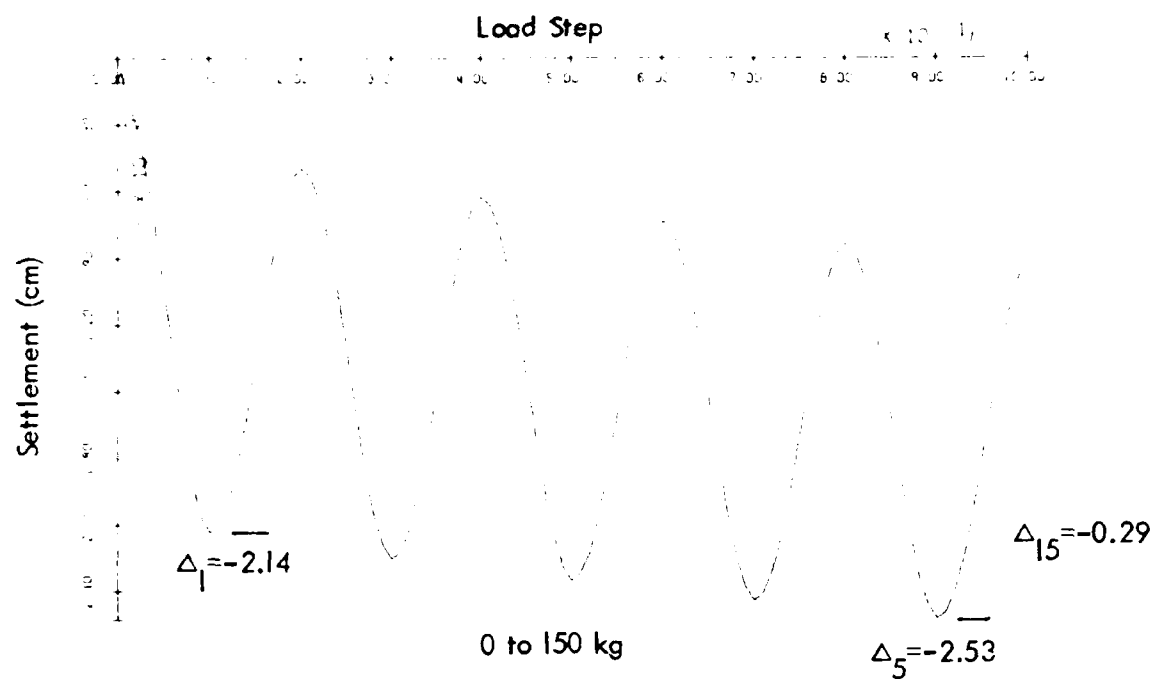


Figure 93. Pile settlement under cyclic load (with water table).

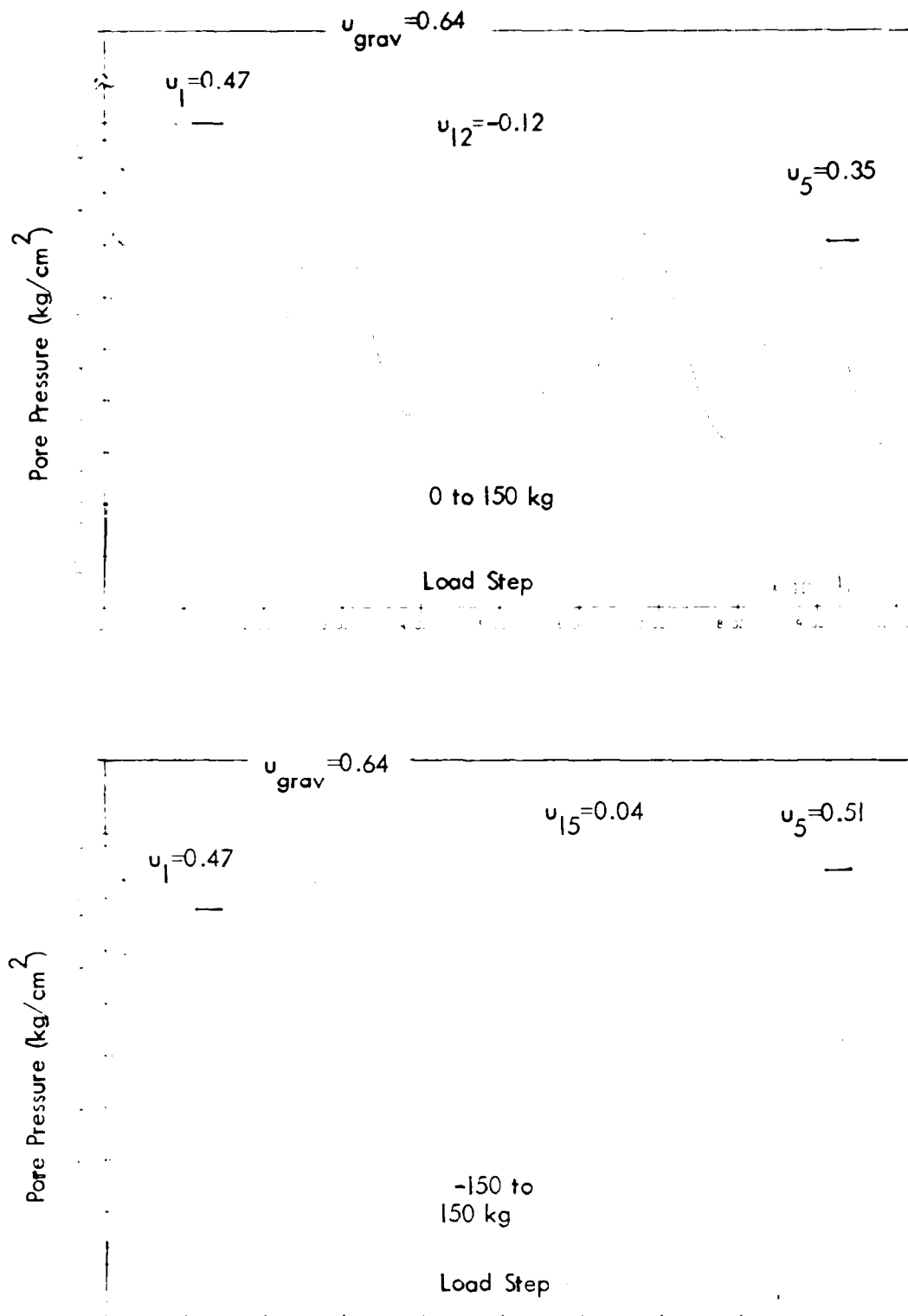


Figure 94. Pore pressure of pile in soil field (with water table).

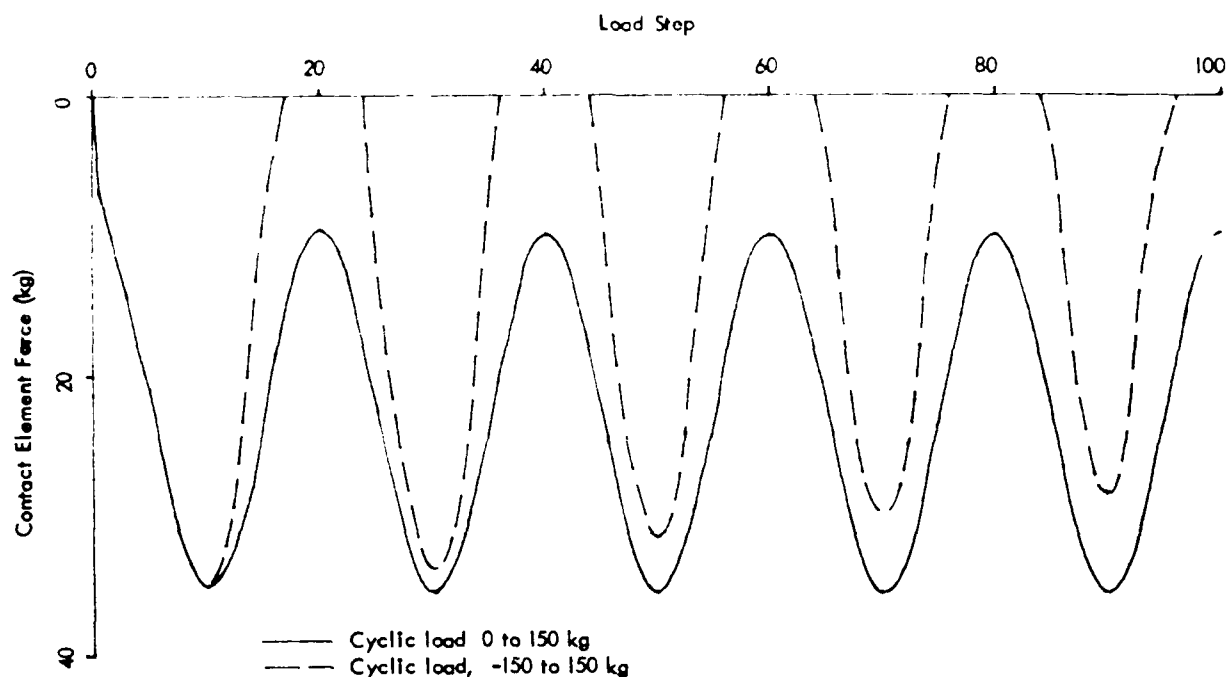


Figure 95. Friction force of pile in soil field (with water table).

#### CONCLUSIONS/RECOMMENDATIONS

An efficient finite element procedure to analyze dynamic transient phenomena in dry and/or fluid-saturated porous soil media is presented. The saturated porous medium is modeled as a two-phase system consisting of a solid and a fluid phase. Time integration of the resulting semi-discrete finite element equations is performed by using an implicit-explicit algorithm. In order to remove the time step size restriction associated with the presence of the stiff fluid in the mixture, the fluid contribution to the equations of motion is always treated implicitly. The procedure allows an optimal selection of the time step

size independently of the fluid. Depending upon the particular applications (seismic, blast loading, etc.) the fluid may be assumed incompressible or compressible.

Accuracy and versatility of the proposed procedure are demonstrated by applying it to a number of dynamic soil and soil-structure interactions tests performed in centrifuges. The hysteretic stress-strain behavior of the soil skeleton is modeled by using the effective-stress elastic-plastic model reported in Reference 31. The model is an extension of the simple multi-surface  $J_2$ -plasticity theory and uses conical yield surfaces. The model accurately describes observed shear nonlinear hysteretic soil behavior, shear stress-induced anisotropy effects, and reflects accurately the strong dependency of the shear dilatancy on the effective stress ratio in granular cohesionless soils. The model is applicable to general multi-dimensional stress-strain conditions, and its parameters can be derived entirely from the results of conventional triaxial soil tests.

The proposed procedure allows a complete and rational analysis of complex dynamic soil-structure interaction problems including important effects such as hysteretic nonlinear effective stress-strain behavior, coupling between shear and volumetric deformations, coupled effects in saturated two-phase soil systems.

The soil model has been validated by comparison with laboratory test data, predicting drained tests, undrained tests, and tests at differing stress paths. The model has been further validated by comparison of computed results to results obtained in centrifuge model tests.

#### REFERENCES

1. Biot, M.A., "Theory of propagation of elastic waves in a fluid-saturated porous solid," Journal of Acoustical Society of America, vol 28, 1956, pp 168-191.

2. Van der Kogel, H., "Wave propagation in saturated porous media," PhD Thesis, California Institute of Technology, Pasadena, Calif., 1977.
3. Nikolaevskii, V.N.; Vasniev, K.S.; Gorbunov, A.T.; and Zotov, G.A. Mechanics of saturated porous media, Nedra, Moscow, 1970, 335 pages.
4. Garg, S.K.; Brownell, D.H.; Pritchett, J.W.; and Herrmann, R.G., "Shock-wave propagation in fluid-saturated porous media," Journal of Applied Physics, vol 46, no. 2, 1975, pp 702-713.
5. Garg, S.K.; Nayfeh, A.H.; and Good, A.J., "Compressional waves in fluid-saturated elastic porous media," Journal of Applied Physics, vol 45, no. 5, 1974, pp 1968-1974.
6. Ghaboussi, J. and Dikmen, S.U., "Liquefaction analysis of horizontally layered sands," Journal of Geotechnical Engineering Division, American Society of Civil Engineers, vol 104, no. FT3, 1978, pp 341-356.
7. Liou, C.P.; Specter, V.L.; and Richard, F.E., "Numerical model for liquefaction," Journal of Geotechnical Engineering Division, American Society of Civil Engineers, vol 103, no. GT6, 1977, pp 589-606.
8. Bowen, R.M. and Lockett, R.R., "Inertial effects in poroelasticity," Journal of Applied Mechanics, American Society of Mechanical Engineering Transactions, vol 50, 1983, pp 334-342.
9. Mei, C.C. and Foda, M.A., "Wave-induced responses in a fluid-filled poro-elastic solid with a free surface: A boundary layer theory," Geophysics Journal, Royal Astronomical Society, vol 66, 1981, pp 597-631.
10. Ghaboussi, J. and Wilson, E.L., "Variational formulation of dynamics of fluid-saturated porous elastic solids," Journal of Engineering Mechanics Division, American Society of Civil Engineers, vol 98, no. EM4, 1972, pp 947-963.

11. Lysmer, J., "Analytical procedures in soil dynamics," in Proceedings of the American Society of Civil Engineers, Geotechnical Engineering Division, Specialty Conference on Earthquake Engineering and Soil Dynamics, Pasadena, Calif., vol 3, June 1978, pp 1267-1316.
12. Prévost, J.H., "Effective stress analysis of seismic site response," International Journal for Numerical Analytical Methods in Geomechanics, Dec 1985.
13. Prévost, J.H., "Wave propagation in fluid-saturated porous media: An efficient finite element procedure," International Journal of Soil Dynamics in Earthquake Engineering, Nov 1985.
14. Prévost, J.H., "Nonlinear transient phenomena in soil media," in Mechanics of Engineering Materials, Chapter 26, Editors: C.S. Desai and R.H. Gallagher. New York, N.Y., Wiley and Sons, 1984, pp 515-533.
15. Prévost, J.H., "Implicit-explicit schemes for nonlinear consolidation," Computer Methods in Applied Mechanics Engineering, vol 39, no. 2, 1983, pp 225-239.
16. Prévost, J.H., "Nonlinear transient phenomena in saturated porous media," Computer Methods in Applied Mechanics Engineering, vol 30, 1982, pp 3-18.
17. Zienkiewicz, O.C. and Shiomi, T., "Dynamic behavior of saturated porous media; the generalized biot formulation and its numerical solution," International Journal for Numerical Analytical Methods in Geomechanics, vol 8, no. 1, 1984, pp 71-96.
18. Hughes, T.J.R. and Liu, W.K., "Implicit-explicit finite elements in transient analysis: Stability theory," Journal of Applied Mechanics, American Society of Mechanical Engineers Transactions, vol 45, 1978, pp 371-374.

19. Hughes, T.J.R. and Liu, W.K., "Implicit-explicit finite elements in transient analysis: Implementation and numerical examples," Journal of Applied Mechanics, American Society of Mechanical Engineers Transactions, vol 45, 1978, pp 395-398.
20. Prévost, J.H., "Study of the capabilities of a soil model to predict axial drained/undrained responses of two sands," Report to NCEL, June 1985.
21. Arulanandan, K.; Anandarajah, A.; and Abghari, A., "Centrifugal modeling of soil liquefaction susceptibility," Journal Geotechnical Engineering, American Society of Civil Engineers, vol 109, no. 3, Mar 1983, pp 281-300.
22. Bolton, M.D. and Steedman, R.S., "Centrifugal testing of micro-concrete retaining walls subjected to base shaking," in Proceedings of the Soil Dynamics and Earthquakes Engineering Conference, Southampton, U.K., 1982, pp 311-329.
23. Lambe, P.C., "Dynamic centrifugal modelling of a horizontal sand stratum," Sc. D. Thesis, MIT, Cambridge, Mass., 1981.
24. Whitman, R.V. and Lambe, P.C., "Liquefaction: Consequences for a structure," in Proceedings of the Soil Dynamics and Earthquakes Engineering Conference, Southampton, U.K., 1982, pp 941-949.
25. Terzaghi, K., Theoretical soil mechanics. New York, N.Y., Wiley and Sons, 1943.
26. Bowen, R.M., "Theory of mixtures," in Continuum Physics, vol III, edited by A.C. Eringen, Academic Press, 1976, pp 1-127.



27. Eringen, A.C., and Ingram, J.D., "A continuum theory of chemically reacting media I and II," *International Journal of Engineering Science*, vol 3, 1955, pp 197-212, and vol 5, 1967, pp 289-322.
28. Green, A.C. and Naghdi, P.M., "A dynamical theory of interacting continua," *International Journal of Engineering Science*, vol 3, 1965, pp 231-241.
29. Bowen, R.M., "Compressible porous media models by use of the theory of mixtures," *International Journal of Engineering Science*, vol 20, no. 6, 1982, pp 697-735.
30. Hill, R., "A general theory of uniqueness and stability in elastic-plastic solids," *Journal of Mechanics and Physics of Solids*, vol 6, 1958, pp 236-249.
31. Prévost, J.H., "A simple plasticity theory for frictional cohesionless soils," *International Journal of Soil Dynamics in Earthquake Engineering*, vol 4, no. 1, 1985, pp 9-17.
32. Prévost, J.H., "Plasticity theory for soil stress-strain behavior," *Journal of Engineering Mechanics Division, American Society of Civil Engineers*, vol 104, no. EM5, 1978, pp 1177-1194.
33. Zienkiewicz, O.C., "The finite element method," 3rd Edition, London, McGraw-Hill, 1977.
34. Hughes, T.J.R. and Belytschko, T., "A precis of developments in computational methods for transient analysis," *Journal of Applied Mechanics, American Society of Mechanical Engineers Transactions*, vol 50, no. 4b, 1983, pp 1033-1041.
35. Hughes, T.J.R.; Pister, K.S.; and Taylor, R.L., "Implicit-explicit finite elements in nonlinear transient analysis," *Computer Methods in Applied Mechanics Engineering*, vol 17/18, 1979, pp 159-182.

36. Newmark, N.M., "A method of computation for structural dynamics," Journal of Engineering Mechanics Division, American Society of Civil Engineers, vol 85, no. EM3, 1959, pp 67-94.
37. Hilber, H.M., "Analysis and design of numerical integration methods in structural dynamics," Report No. EERC 76-29, Earthquake Engineering Research Center, University of California, Berkeley, Calif., Nov 1976.
38. Prévost, J.H., "DYNAFLOW: A nonlinear transient finite element analysis program," Department of Civil Engineering, Princeton University, 1981. (Last revision Aug 1985)
39. Atkin, R.J., "Completeness theorems for linearized theories of interacting continua," Quarterly Journal of Mechanics and Applied Mathematics, vol 21, 1968, pp 171-193.
40. Bowen, R.M. and Reinicke, K.M., "Plane progressive waves in a binary mixture of linear elastic materials," Journal of Applied Mechanics, American Society of Mechanical Engineers Transactions, vol 45, 1978, pp 493-499.
41. Bowen, R.M. and Chen, P.J., "Waves in a binary mixture of linear elastic materials," Journal of Mécanique, vol 14, no. 2, 1975, pp 237-266.
42. Bathe, K.J. and Wilson, E.L., "Numerical methods in finite element analysis," Englewood Cliffs, N.J., Prentics-Hall, 1976.
43. Malkus, D.S. and Hughes, T.J.R., "Mixed finite elements methods - Reduced and selective integration techniques," Computer Methods in Applied Mechanical Engineering, vol 15, no. 1, 1978, pp 63-81.
44. Lambe and Whitman. Soil mechanics, Wiley, New York, 1969.

45. Shen, et al, Centrifuge Consolidation Study for Purposes of Plasticity Theory Validation, University of California, Davis, 1985.
46. Naval Facilities Engineering Command. DM 7. Soil mechanics, foundation and earth structures. Alexandria, Va., Mar 1971.
47. Reese, L.C. and O'Neill, M.W., "Field tests of bored piles in Beaumont clay," American Society of Civil Engineers Annual Meeting, Chicago, Ill., 1969. (Preprint 1008)
48. Peterson, H. "Application o finite element method in the analysis of contact problems," in Proceedings of the International Conference on Finite Elements in Nonlinear Solids and Structural Mechanics, Geilo, Norway, vol 2, Aug 1977.
49. Herrman, L.R., "Nonlinear finite element analysis of frictional systems," in Proceedings of the International Conference on Finite Elements in Nonlinear Solids and Structural Mechanics, Geilo, Norway, vol 2, Aug 1977.
50. Herrman, L.R and Al-Yassin, Z., "Numerical analysis of reinforced soil system," American Society of Civil Engineers National Spring Convention and Continuing Education Program, Pittsburg, Pa., Apr 24-28, 1978. (Preprint 3125).
51. Herrmann, L.R., "Finite element analysis of contact problems," Engineers, vol 104, Journal of the Engineering Mechanics Division, American Society of Civil Engineers, no. EM5, Oct 1978.
52. Poulos, H.G., "Cyclic axial response of single pile," Journal of the Geotechnical Engineering Division, American Society of Civil Engineers, vol 107, no. GT1, Jan 1981.

53. \_\_\_\_\_. "Development of an analysis for cyclic axial loading of piles," Third International Conference on Numerical Methods in Geomechanics, Aachen, Germany, vol 4, Rotterdam, 1979.

54. Civil Engineering Laboratory. Technical Note N-1541: Coefficient of friction between calcareous sands and some building materials, and their significance, by P.J. Valent. Port Hueneme, Calif., Jan 1979.

## DISTRIBUTION LIST

AF HQ PREES Washington DC  
 AF AFITDET, Wright-Patterson AFB, OH  
 AFB AFSC DEEQ (P Montoya), Peterson AFB, CO; HQ MAC DEEE, Scott AFB, IL; SAMSO MNND,  
 Norton AFB CA  
 AFESC DEB, Tyndall AFB, FL; HQ AFESC TST, Tyndall AFB, FL; HQ RDC, Tyndall AFB, FL; HQ TST,  
 Tyndall AFB, FL  
 AF HQ ESD OCMS  
 ARMY-ARADCOM STINFO Div, Dover, NJ  
 ARMY Comm Cmd, Tech Ref Div, Huachuca, AZ; ERADCOM Tech Supp Dir. (DELS-D), Ft Monmouth,  
 NJ; FESA-EM (Krajewski), Ft Belvoir, VA; HQDA (DAEN-ZCM)  
 ARMY CERL CERL-ZN, Champaign, IL; Library, Champaign IL  
 ARMY CORPS OF ENGINEERS HNDED-CS, Huntsville, AL; HNDED-SY, Huntsville, AL; Library, Seattle,  
 WA  
 ARMY CRREL Library, Hanover, NH  
 ARMY EWES Library, Vicksburg MS; WESCV-Z (Whalin), Vicksburg, MS; WESGP-E (Green), Vicksburg,  
 MS  
 ARMY ENGR DIST Phila. Lib, Philadelphia, PA  
 ARMY MAT & MECU RSCH CEN DRXMR-SM (Lenoe), Watertown, MA  
 ARMY MISSILE R&D CMD Ch. Does, Sci Info Ctr, Arsenal, AL  
 ARMY-BELVOIR R&D CTR STRBE-AALO, Ft Belvoir, VA; STRBE-BLORE, Ft Belvoir, VA;  
 STRBE-CFLO, Ft Belvoir, VA; STRBE-WC, Ft Belvoir, VA  
 BUREAU OF RECLAMATION D-1512 (GW DePuy), Denver, CO  
 CBC Tech Library, Gulfport, MS  
 CNO Code NOP-964, Washington, DC; Code OP-987J, Washington, DC  
 COMBLANT Code S3I, Norfolk, VA  
 COMNAVSURFLANT Code N42A Norfolk, VA  
 COMOCEANSYSLANT Fac Mgmt Offr, PWD, Norfolk, VA  
 COMERALANT SCE, Norfolk, VA  
 DIA DB-6E1, Washington, DC; DB-6E2, Washington, DC; VP-TPO, Washington, DC  
 DIRSSP Tech Lib, Washington, DC  
 DISIE Army Logistics Mgt Center, Fort Lee, VA  
 DNA STITL, Washington, DC  
 DOE Wind Ocean Tech Div, Tobacco, MD  
 DHC Alexandria, VA  
 DINSRDC Code 4111, Bethesda, MD; Code 172, Bethesda, MD  
 FAA Code APM-740 (Tomita), Washington, DC  
 EMFLANT CEC Offr, Norfolk VA  
 FOREST SERVICE Engrg Staff, Washington, DC  
 GIDEP OIC, Corona, CA  
 GSA Code FAIA, Washington, DC  
 IRE-IITD Input Proc Dir (R. Danford), Eagan, MN  
 LIBRARY OF CONGRESS Sci & Tech Div, Washington, DC  
 MARCORPS FIRST FSSG, Engr Supp Offr, Camp Pendleton, CA  
 MCDEC PWO, Quantico, VA  
 MCLB PWO (Code B520), Barstow, CA  
 NAS Fac Plan Br Mgr (Code 183), NL, San Diego, CA  
 NATL BUREAU OF STANDARDS R Chung, Gaithersburg, MD  
 NATL RESEARCH COUNCIL Naval Studies Board, Washington, DC  
 NAVCOASTSYSCEN CO, Panama City, FL; Code 2360, Panama City, FL; Code 423, Panama City, FL; Tech  
 Library, Panama City, FL  
 NAVCONSTRACEN Code 00U15, Port Hueneme CA  
 NAVFACENGCOM Code 03, Alexandria, VA; Code 03T (Essoglou), Alexandria, VA; Code 04M, Alexandria,  
 VA; Code EPO-3C, Alexandria, VA; Code 09M124 (Tech Lib), Alexandria, VA; Code 1002B, Alexandria,  
 VA; Code 113C, Alexandria, VA  
 NAVFACENGCOM - CHES DIV Code 101, Washington, DC; Code 405, Washington, DC; Code 406C,  
 Washington, DC; Code 407 (D Scheesele) Washington, DC; Code EPO-1C, Washington, DC; Code  
 EPO-1PL, Washington, DC  
 NAVFACENGCOM - LANT DIV Br Ofc, Dir, Naples, Italy  
 NATL BUREAU OF STANDARDS Bldg Mat Div (Rossiter), Gaithersburg, MD  
 NAVFACENGCOM - LANT DIV, Library, Norfolk, VA  
 NAVFACENGCOM - NORTH DIV Code 04, Philadelphia, PA; Code 04AL, Philadelphia, PA; Code 408 AF,  
 Philadelphia, PA  
 NAVFACENGCOM - PAC DIV Code 101 (Kyi), Pearl Harbor, HI; Code 09P, Pearl Harbor, HI; Code 2011,  
 Pearl Harbor, HI; Code 402, RDT&E LnO, Pearl Harbor, HI; Library, Pearl Harbor, HI

NAVFACENGCOM - SOUTH DIV. Code 1112, Charleston, SC; Code 405, Charleston, SC; Code 406, Charleston, SC; Geotech Section (Code 4022), Charleston, SC; Library, Charleston, SC  
 NAVFACENGCOM - WEST DIV. Code 04B, San Bruno, CA; Library (Code 04A22), San Bruno, CA  
 RDI&E, Inc., San Bruno, CA  
 NAVFACENGCOM CONTRACTS AROICC, Quantico, VA  
 NAVOCEANO Code 6200 (M. Page), Bay St. Louis, MS  
 NAVOCEANSSCEN Code 541 (Bachman), San Diego, CA; Code 964 (Tech Library), San Diego, CA; Code 9642B (Bayside Library), San Diego, CA  
 NAVPGSCOL Code 61W1 (O. Wilson), Monterey, CA  
 NAVSCOLCECOFF Code C35, Port Hueneme, CA  
 NAVSLASYSOM Code 06H4, Washington, DC; Code CFI-1D23, Washington, DC  
 NAVSHIPYD Code 2024, Long Beach, CA  
 NAVSTA Dir., Engr. Div., PWD (Code 18200), Mayport, FL  
 NAVSURFWPNCEN Code E211 (C. Rouse), Dahlgren, VA  
 NAVWARCOL Fac. Coord (Code 24), Newport, RI  
 NAVWPNCEN Code 2636, China Lake, CA  
 NOVA Joseph Vadus, Rockville, MD  
 NORDA Head, Geotech Br. (Code 363), Bay St. Louis, MS  
 NRI Code 5800, Washington, DC  
 NSC Code 541, Norfolk, VA  
 PMIC Code 1018, Point Mugu, CA  
 PWC Code 101 (Library), Oakland, CA; Code 123-C, San Diego, CA; Code 420, Great Lakes, IL; Library (Code 134), Pearl Harbor, HI; Library, Guam, Mariana Islands; Library, Norfolk, VA; Library, Pensacola, FL; Library, Yokosuka JA; Tech Library, Subic Bay, RP  
 US DEPT OF INTERIOR Bur. of Land Mgmt (Code 583), Washington, DC; Nat'l Park Svc, RMR PC, Denver, CO  
 US GEOLOGICAL SURVEY Marine Geology Ofce (Pitelek), Reston, VA  
 USDA Ext. Serv. (J. Maher), Washington, DC; Forest Serv., Reg. 8, Atlanta, GA  
 USNA Chairman, Mech. Engr. Dept., Annapolis, MD; Mgr., Engrg., Civil Specs. Br., Annapolis, MD  
 CALIF. DEPT OF NAVIGATION & OCEAN DEV. G. Armstrong, Sacramento, CA  
 CALIFORNIA STATE UNIVERSITY Energy Tech. Dept. (Kohani), Menlo Park, CA  
 CITY OF LIVERMORE Project Engr. (Dawkins), Livermore, CA  
 CLARKSON COLL. OF TECH. CE Dept. (Batson), Potsdam, NY  
 COLORADO SCHOOL OF MINES Dept. of Engrg. (Chung), Golden, CO  
 COLORADO STATE UNIVERSITY CE Dept. (Nelson), Ft. Collins, CO; CE Dept. (W. Charlier), Fort Collins, CO  
 CORNELL UNIVERSITY Library, Ithaca, NY; Civil & Environ. Engrg. (E. Kulhawy), Ithaca, NY  
 DAMS & MOORE LIBRARY Los Angeles, CA  
 FLORIDA ATLANTIC UNIVERSITY Ocean Engrg. Dept. (McAllister), Boca Raton, FL; Ocean Engrg. Dept. (Su), Boca Raton, FL  
 FLORIDA INSTITUTE OF TECHNOLOGY CE Dept. (Kalapan), Melbourne, FL  
 GEORGIA INSTITUTE OF TECHNOLOGY Arch. Col. (Bentoni), Atlanta, GA; CE Scol. (Kahn), Atlanta, GA; CE Scol. (Mazanti), Atlanta, GA  
 INSTITUTE OF MARINE SCIENCES Library, Port Aransas, TX  
 IOWA STATE UNIVERSITY CE Dept. (Handy), Ames, IA  
 LAWRENCE LIVERMORE NAT'L LAB. EL Tokarz, Livermore, CA  
 LEHIGH UNIVERSITY CE Dept., Hydraulics Lab., Bethlehem, PA; Underman Libr., Ser. Cataloguer, Bethlehem, PA; Marine Geotech Lab. (A. Richards), Bethlehem, PA  
 MICHIGAN TECHNOLOGICAL UNIVERSITY CE Dept. (Haasi), Houghton, MI  
 MIT Engrg. Lib., Cambridge, MA; Lib., Tech. Reports, Cambridge, MA; RV Whitman, Cambridge, MA  
 NY CITY COMMUNITY COLLEGE Library, Brooklyn, NY  
 PENNSYLVANIA STATE UNIVERSITY Gotski, University Park, PA; Rsch. Lab. (Snyder), State College, PA  
 PURDUE UNIVERSITY CE Scol. (Mitschach), Lafayette, IN; CE Scol. (Leonard), Lafayette, IN; Engrg. Lib., Lafayette, IN  
 SAN DIEGO STATE UNIV. CE Dept. (Krishnamoorthy), San Diego, CA; CE Dept. (Noorani), San Diego, CA  
 SEATTLE UNIVERSITY CE Dept. (Schwaegler), Seattle, WA  
 SOUTHWEST RESEARCH INST. Energetic Sys. Dept. (Spitzer), San Antonio, TX; J. Hokanson, San Antonio, TX; King, San Antonio, TX; R. DeHart, San Antonio, TX  
 STATE UNIV. OF NEW YORK CE Dept., Buffalo, NY  
 TEXAS A&M UNIVERSITY CE Dept. (Edbetter), College Station, TX; CE Dept. (Niedzwecki), College Station, TX; Ocean Engr. Proj., College Station, TX  
 UNIVERSITY OF CALIFORNIA CE Dept. (Gerwick), Berkeley, CA; CE Dept. (Mitchell), Berkeley, CA; Engrg. (Williamson), Berkeley, CA; Trans. Engrg. Dept. (Duncan), Berkeley, CA  
 UNIVERSITY OF ILLINOIS CE Dept. (Hall), Urbana, IL; CE Dept. (W. Gambler), Urbana, IL; Library, Urbana, IL; M.E. Davison, Urbana, IL; Metz Ref. Rm., Urbana, IL

UNIVERSITY OF MASSACHUSETTS ME Dept (Heroneumus), Amherst, MA  
 UNIVERSITY OF MICHIGAN CE Dept (Richart), Ann Arbor, MI  
 UNIVERSITY OF NEBRASKA-LINCOLN Ross Ice Shelf Proj, Lincoln, NE  
 UNIVERSITY OF NEW MEXICO NMERI (Falk), Albuquerque, NM  
 UNIVERSITY OF NOTRE DAME CE Dept (Katona), Notre Dame, IN  
 UNIVERSITY OF RHODE ISLAND CE Dept (Kovaes), Kingston, RI  
 UNIVERSITY OF TEXAS AT AUSTIN Breen, Austin, TX; CE Dept (R Olson), Austin, TX; CE Dept  
 (Thompson), Austin, TX  
 UNIVERSITY OF WASHINGTON CE Dept (Mattock), Seattle, WA; RI Terrel, Everett, WA  
 UNIVERSITY OF WISCONSIN Great Lakes Studies, Ctr, Milwaukee, WI  
 AMERICAN CONCRETE INSTITUTE Library, Detroit, MI  
 AMTEK OFFSHORE RSCH Santa Barbara, CA  
 ATLANTIC RICHFIELD CO RE Smith, Dallas, TX  
 AUSTRALIA Sydney Univ, Scol CE & Mine (Poulos), Sydney  
 BATHLE D Frink, Columbus, OH  
 BETHLEHEM STEEL CO Engrg Dept (Dismuke), Bethlehem, PA  
 BRITISH EMBASSY Sci & Tech Dept (Wilkins), Washington, DC  
 BROWN & ROOT Ward, Houston, TX  
 CANADA Viaireur De Champlain, D.S.A., Matane, Canada  
 CHEVRON OIL FLD RSCH CO Brooks, La Habra, CA  
 CONCRETE TECH CORP A Anderson, Tacoma, WA  
 CONRAD ASSOC Luisom, Van Nuys, CA  
 CONSTRUCTION TECH LABS AE Fiorato, Skokie, IL  
 DRAYO CORP Wright, Pittsburg, PA  
 EVALUATION ASSOC INC MA Fedele, King of Prussia, PA  
 FUGRO INTER, INC Library, Houston, TX  
 GEOTECHNICAL ENGINEERS INC, (R.F. Murdock) Principal, Winchester, MA  
 GRUMMAN AEROSPACE CORP Tech Info Ctr, Bethpage, NY  
 HALEY & ALDRICH, INC, HP Aldrich, Jr, Cambridge, MA  
 NUSC DEL Library (Code 4533) Newport, RI  
 KAMAN SCIENCES CORP D Sachs, Santa Barbara, CA  
 LAMONT-DOHERTY GEOLOGICAL OBSERVATORY McCoy, Palisades, NY  
 LIN OFFSHORE ENGRG P. Chow, San Francisco, CA  
 LINDA HALL LIBRARY Doc Dept, Kansas City, MO  
 MARATHON OIL CO Houston, TX  
 MOBILE R & D CORP Offshore Eng Library, Dallas, TX  
 MUESER RUTLEDGE, CONSULTING ENGRS Richards, New York, NY  
 PROF SVCS INDUSTRIES, INC Dir, Roofs (Lyons), Houston, TX  
 PHILIPS ASSOC P.A. Phelps, Rheem Valley, CA  
 PORTLAND CEMENT ASSOC Corley, Skokie, IL, Rsch & Dev Lab Lib, Skokie, IL  
 RAYMOND INTE INC Soil Tech Dept (F Collet), Pennsauken, NJ  
 SANDIA LABORATORIES Library, Livermore, CA  
 SEATECH CORP Petoni, Miami, FL  
 SHANNON & WILSON, INC Librarian, Seattle, WA  
 SHELL OFFSHORE INC E Doyle, Houston, TX  
 SHELL OIL CO E&P Civil Engrg, Houston, TX  
 TIDEWATER CONSTR CO J Fowler, Virginia Beach, VA  
 TRW SYSTEMS Div, San Bernardino, CA Engr Library, Cleveland, OH  
 WESTINGHOUSE ELECTRIC CORP Library, Pittsburg, PA  
 WISS JANNEY ELSNER & ASSOC DW Pfeiter, Northbrook, IL  
 WOODWARD-CLYDE CONSULTANTS R Cross, Walnut Creek, CA; R Dominguez, Houston, TX; W Reg  
 (Lib), Walnut Creek, CA  
 BROWN, ROBERT University, MI  
 HILTZ, E. Vanc., CA  
 NIEDERDA, AW Houston, TX  
 MURPHY, CW Washington, DC

## INSTRUCTIONS

The Naval Civil Engineering Laboratory has revised its primary distribution lists. The bottom of the mailing label has several numbers listed. These numbers correspond to numbers assigned to the list of Subject Categories. Numbers on the label corresponding to those on the list indicate the subject category and type of documents you are presently receiving. If you are satisfied, throw this card away (or file it for later reference).

If you want to change what you are presently receiving:

- Delete - mark off number on bottom of label.
- Add - circle number on list.
- Remove my name from all your lists - check box on list.
- Change my address - line out incorrect line and write in correction (**ATTACH MAILING LABEL**).
- Number of copies should be entered after the title of the subject categories you select.

Fold on line below and drop in the mail.

Note: Numbers on label but not listed on questionnaire are for NCEL use only, please ignore them.

*Fold on line and staple*

### DEPARTMENT OF THE NAVY

NAVAL CIVIL ENGINEERING LABORATORY  
PORT HUENEME, CALIFORNIA 93043

OFFICIAL BUSINESS  
PENALTY FOR PRIVATE USE, \$300  
1 IND-NCEL 2700/4 (REV. 12-73)  
0930-LL-L70-0044

POSTAGE AND FEES PAID  
DEPARTMENT OF THE NAVY  
DOD-316



Commanding Officer  
Code L14  
Naval Civil Engineering Laboratory  
Port Hueneme, California 93043



## DISTRIBUTION QUESTIONNAIRE

The Naval Civil Engineering Laboratory is revising its primary distribution lists.

### SUBJECT CATEGORIES

#### 1 SHORE FACILITIES

- 2 Construction methods and materials (including corrosion control, coatings)
- 3 Waterfront structures (maintenance/deterioration control)
- 4 Utilities (including power conditioning)
- 5 Explosives safety
- 6 Construction equipment and machinery
- 7 Fire prevention and control
- 8 Antenna technology
- 9 Structural analysis and design (including numerical and computer techniques)
- 10 Protective construction (including hardened shelters, shock and vibration studies)
- 11 Soil/rock mechanics
- 13 BEQ
- 14 Airfields and pavements
- 15 ADVANCED BASE AND AMPHIBIOUS FACILITIES
- 16 Base facilities (including shelters, power generation, water supplies)
- 17 Expedient roads/airfields/bridges
- 18 Amphibious operations (including breakwaters, wave forces)
- 19 Over-the-Beach operations (including containerization, materiel transfer, lighterage and cranes)
- 20 POL storage, transfer and distribution
- 24 POLAR ENGINEERING
- 24 Same as Advanced Base and Amphibious Facilities, except limited to cold-region environments

#### 28 ENERGY/POWER GENERATION

- 29 Thermal conservation (thermal engineering of buildings, HVAC systems, energy loss measurement, power generation)
- 30 Controls and electrical conservation (electrical systems, energy monitoring and control systems)
- 31 Fuel flexibility (liquid fuels, coal utilization, energy from solid waste)
- 32 Alternate energy source (geothermal power, photovoltaic power systems, solar systems, wind systems, energy storage systems)
- 33 Site data and systems integration (energy resource data, energy consumption data, integrating energy systems)
- 34 ENVIRONMENTAL PROTECTION
- 35 Solid waste management
- 36 Hazardous/toxic materials management
- 37 Wastewater management and sanitary engineering
- 38 Oil pollution removal and recovery
- 39 Air pollution
- 40 Noise abatement
- 44 OCEAN ENGINEERING
- 45 Seafloor soils and foundations
- 46 Seafloor construction systems and operations (including diver and manipulator tools)
- 47 Undersea structures and materials
- 48 Anchors and moorings
- 49 Undersea power systems, electromechanical cables, and connectors
- 50 Pressure vessel facilities
- 51 Physical environment (including site surveying)
- 52 Ocean-based concrete structures
- 53 Hyperbaric chambers
- 54 Undersea cable dynamics

### TYPES OF DOCUMENTS

- 85 Techdata Sheets
- 86 Technical Reports and Technical Notes
- 83 Table of Contents & Index to TDS

- 82 NCCL Guide & Updates
- 91 Physical Security

☐ None —  
remove my name

PLEASE HELP US PUT THE ZIP IN YOUR  
MAIL! ADD YOUR FOUR NEW ZIP DIGITS  
TO YOUR LABEL (OR FACSIMILE),  
STAPLE INSIDE THIS SELF-MAILER, AND  
RETURN TO US.

(fold here)

**DEPARTMENT OF THE NAVY**

NAVAL CIVIL ENGINEERING LABORATORY  
PORT HUENEME, CALIFORNIA 93043-5003

**OFFICIAL BUSINESS**

PENALTY FOR PRIVATE USE, \$300  
1 IND-NCCL 2700 4 (REV 12-73)  
0030-LL-L70-0044

POSTAGE AND FEES PAID  
DEPARTMENT OF THE NAVY  
DOD-310



Commanding Officer  
Code L14  
Naval Civil Engineering Laboratory  
Port Hueneme, California 93043 5003

END

3-87

DTIC